FIBER-OPTIC MOTION SENSING: DISTRIBUTED ACOUSTIC SENSING, FIBER BRAGG-GRATINGS, AND THEIR LAND AND MARINE SEISMIC APPLICATIONS

by
Ezzedeen Alfataierge

A Dissertation Submitted to

the Department of Earth and Atmospheric Sciences,
College of Natural Sciences and Mathematics

in partial fulfillment of the requirements for the degree of

Doctor of Philosophy

in Geophysics

Chair of Committee: Robert R. Stewart

Committee Member: Yingcai Zheng

Committee Member: Hua-Wei Zhou

Committee Member: Mark E. Willis

University of Houston
December 2019

DEDICATION

I dedicate this to my wife Raeda, thank you for standing by me and supporting me all these years. To my son Rayan, my inspiration and distraction to completing this work. And to my advisor Dr. Stewart, thank you for taking me under your wing and helping me become the scientist I am today.

ACKNOWLEDGMENTS

First and foremost, I thank God for the blessing of health and family, and the blessing of good company at the University of Houston. For being a part of the Allied Geophysical Laboratories (AGL) family is a true blessing and resource to completing my dissertation.

I would like to acknowledge funding and support that helped complete this dissertation. Thank you to Saudi Aramco for their sponsorship and support of my education. Thank you to Harold Merry at Aramco Services Company for his training and support with DAS VSP. Thank you to the Geophysics Technology Team in Dhahran for providing me with the “Smart DAS” data that was used in this dissertation. Thank you to the Texas Commission on Environmental Quality (TCEQ), UH Energy, and the Subsea Systems Institute (SSI) for funding the materials and research in fiber-optic sensing at AGL. Thank you to Peter Hayward, Matt McDonald, George Palmer, and all the people at Fotech Solutions for their support and training with using the Helios DAS systems. Thank you to Mark Willis, Michel LeBlanc, Andreas Ellmauthaler, and all the people at Halliburton for hosting us for several tours, for their support of research and development in the field of fiber-optic sensing, and their constant outreach to support in any way possible.

I would like to personally acknowledge all who contributed to my advancement and the completion of this dissertation, from my wife who was my constant support and reminder to keep working, to my advisor who was always there when I needed him. The list will never end, so simply thank you to all the professionals that I met in various meetings and conferences, for their fruitful discussions and insight on topics and matters discussed in this dissertation.

A special thank you goes to Li Chang for welcoming me into AGL, teaching me all about the equipment, and being someone I could depend on with anything. To Dr. Jingjing Zong, for her guidance with seismic data processing and using VISTA. To Dr. Yingcai Zheng, for teaching me how to use MATLAB and how to code programs that contributed to my dissertation. To Dr. Hao Hu, for his assistance with processing some of the data in this dissertation. To Dr. Nikolay Dyaur for his enormous contribution with all the laboratory experiments we conducted together at AGL. To Dr. Michael Ho and Dr. Gangbing Song at the Mechanical Engineering Department, for their early collaboration with our FBG work and support throughout our projects. And to all the members of AGL, for your constructive criticism of my presentations and fruitful discussion of our research topics.

Last but not least, I give special thanks to Dr. Stewart, a great advisor and an excellent mentor. The lessons I have learned from you over the years will not be forgotten, these lessons will pass on to my co-workers and colleges and live on forever.

ABSTRACT

Fiber-optic motion sensing (FOMS) is a topic that has attracted the interest of many over the past decade. Geophysical interests have primarily been in borehole seismic imaging (BSI) via distributed acoustic sensing (DAS), with a recent interest in utilizing the technology for surface seismic imaging (SSI). The technology has potential for many applications. This dissertation investigates some applications while comparing the fiber-optic sensors to conventional sensors that have been used by industry. In an attempt to address some of the limitations of DAS, Fiber-Bragg Gratings (FBGs), which are single-point fiber-optic sensors, are investigated as well. The motivation and objective of this dissertation are presented in Chapter 1, along with a brief introduction to fiber-optic sensing focused on DAS and FBG theory.

FOMS applications in BSI are presented in Chapter 2. Demonstrating the application of DAS VSP first, investigating the influence of seismic sources and optical parameters on DAS measurements in comparison to geophone measurements. Next, testing the application of FBGs in comparison to hydrophones in a VSP field trial. Chapter 3 explores applications of FOMS to SSI. Starting with a novel application of Multichannel Analysis of Surface Waves (MASW) on surface trenched DAS fiber, then demonstrating an application of DAS in urban infrastructure monitoring using existing telecommunication fiber-optic networks. Also, some field trials are presented, investigating the use of FBGs for surface seismic imaging. Then, FOMS applications in a simulated marine environment are explored in Chapter 4, demonstrating applications of DAS and FBGs in pipeline flow assessment and integrity, marine seismic source characterization, and underwater communications. Multicomponent FOMS considerations are made in Chapter 5, where I developed a multicomponent FBG sensor and test it against multicomponent geophones.

A summary of the findings and contributions of this dissertation are finally presented in Chapter 6, followed by a discussion of future work and conclusion in Chapter 7. In conclusion, various applications of FOMS have been demonstrated in comparison to conventional seismic sensors, finding that FOMS demonstrates advantages to conventional sensing systems along with challenges in processing and handling large amounts of data.

TABLE OF CONTENTS

LIST OF TABLES

LIST OF FIGURES

LIST OF ACRONYMS

ADC	Analog-to-Digital Converter
AWD	Accelerated Weight Drop
BSI	Borehole Seismic Imaging
DAS	Distributed Acoustic Sensing
DTS	Distributed Temperature Sensing
DVS	Distributed Vibration Sensing
DSS	Distributed Strain Sensing
EDFA	Erbium-doped Fiber Amplifier
FBG	Fiber Bragg-Grating
FOMS	Fiber-Optic Motion Sensing
GL	Gauge Length
OTDR	Optical Time-Domain Reflectometry
Pg	Pulse Gap
P_w	Pulse Width
PEG	Propelled Energy Generator
PRF	Pulse Repetition Frequency
SNR	Signal-to-Noise Ratio
SSI	Surface Seismic Imaging
VSP	Vertical Seismic Profile/ Profiling
ZVSP	Zero-Offset VSP

CHAPTER I

INTRODUCTION

This chapter discusses the motivations of my research and the objectives of this dissertation. Followed by a brief introduction to fiber-optic sensing, focusing on the two technologies of interest in this dissertation; distributed acoustic sensing (DAS) and fiber Bragg-gratings (FBGs). Then, fiber-optic motion sensing (FOMS) is discussed with regards to the literature on DAS, FBGs, and their applications. Finally, a summary of the dissertation structure and outline is presented.

1.1. Motivations and Objectives

FOMS has gained the interest of many over the past decade, with applications in many fields and disciplines. Generally, the motivations of this dissertation are driven by the recent development of one of the most exciting technologies in geophysics today, DAS. Advances in DAS have been well documented (Mestayer et al., 2011; Mateeva et al., 2012; Dean et al., 2015; Willis et al., 2016) with applications expanding beyond borehole seismic imaging (BSI). However, we still strive to fully understand the limitations of DAS in comparison to our conventional seismic sensing systems (geophones and hydrophones). This drives the primary motive of this dissertation, which is to establish an understanding of FOMS and their various applications, with the objective of quantifying the difference between fiber-optic sensing systems and conventional seismic sensing systems.

Stewart and Disiena (1989) demonstrate the value of VSP in seismic data interpretation and highlight the importance of multicomponent measurements. Thus, the second motivation is to explore ways to achieve multicomponent measurements using fiber-optic sensors. As such technology would expand the applications and value of fiber-optic sensing. The final motivation was driven by the “internet of things” movement, looking at a network of applications that can be achieved from a fiber-optic network. This is addressed in a simulated marine environment, testing various applications of pipeline flow assessment and integrity, marine seismic source characterization, and underwater communication. With the objective of demonstrating the feasibility of such applications and comparing the capabilities of both DAS and FBG systems to conventional sensing systems.

In summary, the objectives of this dissertation are:

- Establish an understanding of fiber-optic sensing systems (DAS and FBGs) in comparison to conventional geophysical sensing systems (geophones and hydrophones). This is done both in the laboratory and the field, by acquiring, processing, and analyzing data simultaneously acquired with the various sensing systems.

- Explore the applications of fiber-optic sensing in surface seismic imaging, marine environments, and demonstrate the feasibility of multicomponent fiber-optic sensing using an FBG system.

1.2. Literature Review

Charles K. Kao and George A. Hockham were the first, in 1965, to promote the idea of using optical fibers for communication. As they demonstrated that the attenuation of 20 dB/km in optical fibers at the time was due to impurities in the glass, and that it could be reduced by using high purity silica glass (Hecht, 1999). Later, Kao was awarded the Nobel Prize in Physics in 2009 for this contribution (The Nobel Foundation, 2009). Since then, the military was first to develop an interest in fiber-optic sensors and set the foundation for many of its applications. After their work was declassified, engineers found potential in applying fiber-optic sensing in fields of medicine, civil engineering, mechanical engineering, and the oil and gas industry.

Over the past decade, FOMS has gained the interest of many, with applications in borehole seismic imaging, surface seismic imaging, earthquake detection, infrastructure monitoring, and much more. Shell in collaboration with QinetiQ have been one of the early pioneers of DAS VSP technology (Mestayer et al., 2011). Followed by the establishment of DAS service companies such as Optasense, Silixa, Fotech, and many more. Oil service providers such as Haliburton, Schlumberger, and Weatherford, started providing fiber-optic sensing solutions using DAS technologies for VSP, fluid flow and hydraulic fracture monitoring, and microseismic characterization.

The interest in FOMS has been driven by their advantages over conventional seismic instruments, such as independence from electromagnetic interference, having compact and lighter sensors, no mechanical parts, and ease of use in higher temperature and pressure environments. Specifically, the appeal of distributed sensing is in the large coverage (large number of “receiver channels”) that is achieved from a single fiber with a minimal footprint. As well as, the wide range of measurements that can be extracted from that fiber (temperature, strain, acoustic, etc.), abbreviated with D_S, with the first letter of the measured attribute fills the blank (_), yielding DTS, DSS, and DAS for temperature, strain, and acoustic sensing respectively.

Distributed sensing is currently limited to measuring a single axial component, Lim and Sava (2016, 2017, and 2018) propose a solution to overcome the limitation of uniaxial DAS measurements, by introducing an elaborate fiber-optic structure that can be used to extract multicomponent measurements. The multicomponent measurements referred to in their study is with respect to the six-components of the strain tensor, not to be confused with the common reference of multicomponent measurements in the geophysical domain that corresponds to the three-components of a three-dimensional Cartesian coordinate system (x, y, and z). I have yet to see any publication of their theoretical solution being tested in application. I believe that it will not be feasible for the near future as their method incorporates multiple optical fibers that would require simultaneous interrogation and synchronized processing, which would be expensive in terms of acquisition and computational processing and require a very small gauge lenght.

Innanen et al. (2019) demonstrate a field test of multicomponent fiber-optic sensing using a unique DAS fiber loop array equipped with helically wound fiber buried in a two-meter trench. Their study demonstrates the complexities associated with achieving multicomponent measurements using a DAS system. Their objective is to extract a six-component strain tensor using a dual-square geometry, such that each segment would be summarized to extract a single-component trace. The acquisition footprint of their geometry is large (~150 m^2), which is designed to overcome the limitations set by a ten-meter gauge length. Although the results of their study appear promising, this method is expensive for commercial applications since it uses a large acquisition footprint to obtain a single-point multicomponent measurement. Replacing the DAS system with an FBG system would significantly reduce the acquisition footprint and allow for more comparable measurements with higher accuracy and fewer limitations (no gauge length). Thus, our secondary objective is to demonstrate the feasibility of using an FBG system to achieve multicomponent measurements.

Wu et al. (2017) demonstrate the limitations of DAS in terms of broad-side sensitivity of the fiber to incident waves, which for P-waves is similar to a single-component geophone sensor. This limitation is key if we are to use DAS for surface-seismic imaging, since the null in the response would eliminate reflection events and only respond to surface waves. Bakulin et al. (2017a, 2017b, 2018a, 2018b, 2018c) demonstrate a "Smart DAS" geometry utilizing a series of near-surface up-holes equipped with a single fiber-optic cable, using such geometry they were able to achieve surface seismic imaging using the vertical DAS arrays but were unable to do so with the horizontal DAS arrays. They show that the horizontal DAS arrays were useful in characterizing the near-surface through refraction tomography, generating near-surface velocity models. The velocity models showed great use in computing statics resulting in better seismic imaging.

1.3. Introduction to Fiber-Optic Sensing

Shroyer and Dria (2017) and Hartog (2017) give an excellent review of fiber-optic sensing, summarizing the wide range of fiber-optic sensors and their applications. As they note, fiber-optic sensors fall into two general groups, intrinsic and extrinsic sensors. Extrinsic sensors use fiber as a communication medium to communicate with a remote sensor (e.g. electrical submersible pumps), whereas, intrinsic sensors use the fiber as a sensing element (e.g. FBGs and DAS). They can also be summarized into three categories (Figure 1.1), single point sensors (intrinsic or extrinsic), quasi-distributed or multipoint sensors (intrinsic or extrinsic), and distributed sensors (intrinsic only). This dissertation focuses on two types of intrinsic fiber-optic sensors for applications of motion sensing: DAS as a distributed sensor and FBGs as single and multi-point sensors.

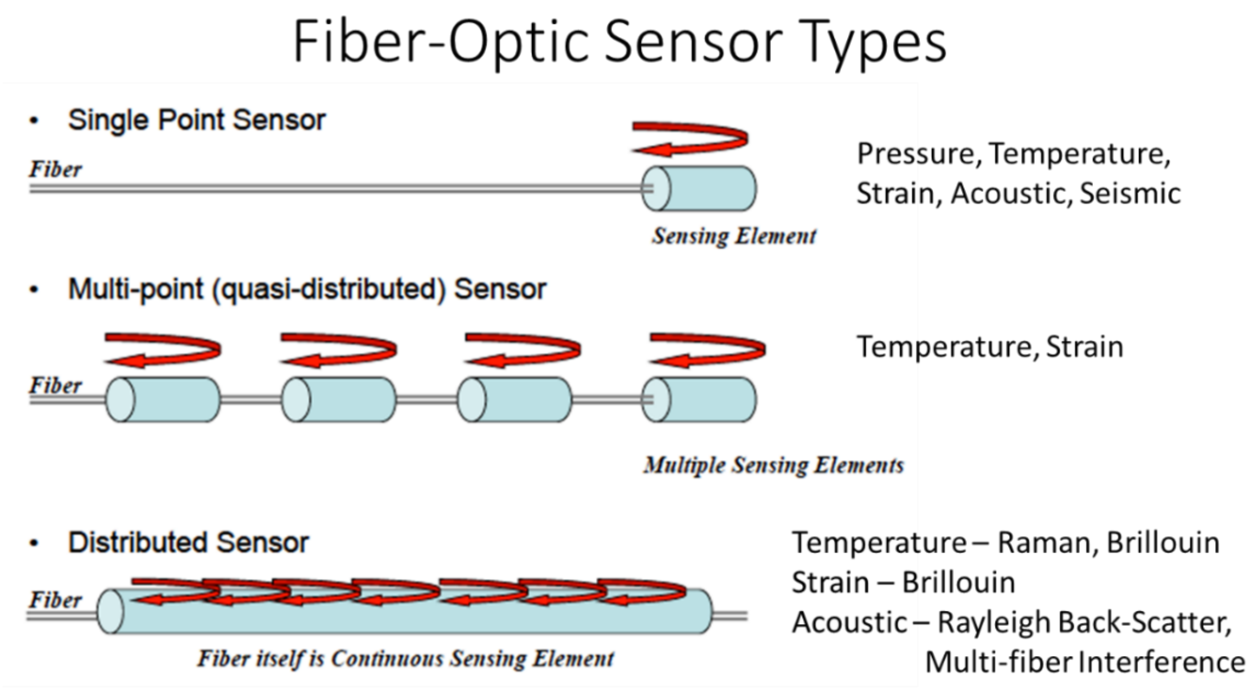

Figure 1.1: Fiber-optic sensor types and their applications.

This figure illustrates the three categories of fiber-optic sensors: single point, multi-point, and distributed sensors, with their sensing applications. Edited from Shroyer and Dria (2017).

1.3.1. Distributed Acoustic Sensing (DAS)

Most methods of distributed fiber-optic sensing are derived from the manipulation of an optical time-domain reflectometer (OTDR) (Hartog, 2017). An OTDR is a device that sends laser pulses into the fiber and monitors the reflected optical backscatter in the time domain. The backscatter occurs from the interaction of the pulsed laser light with the natural imperfections in the fiber. Thus, any change in the fiber length would displace the imperfections and result in a corresponding change in the OTDR backscatter. The change that occurs is in order of intensity of the backscatter amplitude along the fiber. Monitoring these intensity variations is effectively what an intensity-based DAS system does. The major setback of such a method is that the system is non-linear and does not preserve the phase of the signal measured by the fiber (Hartog, 2017). The preferred method of DAS for seismic measurements is a differential phase-based system, such systems preserve linearity of the measurements and the phase of the signals sensed by the fiber thus achieving constant polarity in seismic data.

Hartog (2017) suggests using distributed vibration sensing (DVS) over the commonly used DAS naming. Given that DAS data has been shown to measure elastic events and the term acoustic is typically used in reference to high-frequency (kHz) or rigid (no fluid) media, one is inclined to agree with Hartog (2017). However, “acoustic” has also been used in practice to refer to elastic measurements, sensing both compressional and shear waves. Also, a majority of the publications have been using DAS over the past decade now. Therefore, in this dissertation, the term DAS will be used given the known association of the term with the technology.

The main elements of a DAS system consist of a fiber and an interrogator. First, we look at the fiber and its construction. Telecommunication fiber is commonly manufactured in two types, single-mode and multi-mode fiber (Shroyer and Dria, 2017). Single-mode fiber allows for a single path/mode of light propagation along the fiber, which is achieved by having a small core diameter (9 microns). Whereas multi-mode fiber allows for multiple modes (or paths) of light to propagate along the fiber, this is due to the larger core diameter (50-62 micron). Figure 1.2 illustrates the difference between single- and multi-mode fibers. We can also see the breakdown of a fiber and its elements: the core, cladding, and jacket. The core is the main component of the fiber in which the light propagates, the cladding surrounds the core and is designed with a low refractive index to keep the propagating light inside the core of the fiber, and the jacket that covers the bare fiber and protects it from the environment.

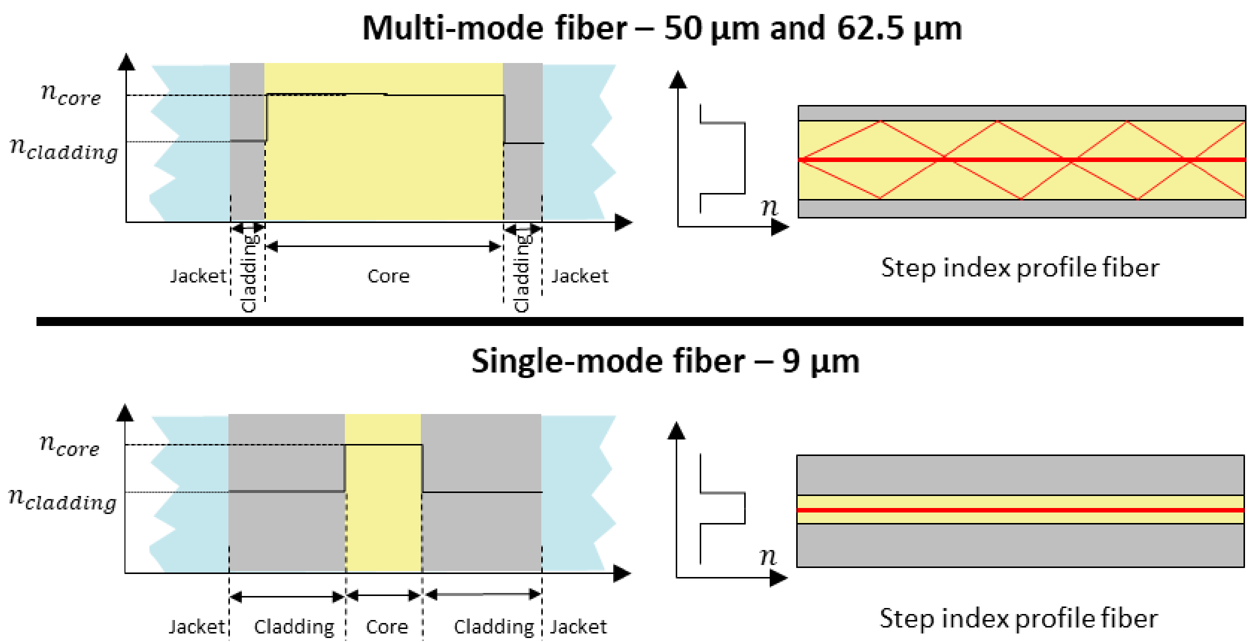

Figure 1.2: Illustration of multi-mode and single-mode telecommunication optical fiber.

Cross-section illustrations of telecommunication optical fibers, the basic components of the fiber consist of the core, which has a relatively higher refractive index, the cladding, which has a lower refractive index, and the jacket, which is a protective material that in capsules the bare fiber. Multi-mode fiber is characterized by its larger core diameter that allows multiple modes of light to propagate, while single-mode fiber has a smaller core diameter that only allows for one mode of light propagation. Edited from Toko (2017).

Most interrogator systems operate on single-mode fiber because it has better signal-to-noise ratio (SNR) in the optical domain and less optical attenuation with distance. When using a single-mode interrogator on multimode fiber, there is a loss of energy in the conversion, think of trying to get water from a large pipe into a smaller pipe without a funnel, so the SNR is lower in multimode data. The interest in multimode fiber is because it is commonly used for DTS and is sometimes installed in older wells for communication purposes with downhole equipment or for DTS applications (Willis et al., 2018). Willis et al. (2018) show that it is possible to acquire DAS VSP using multi-mode fiber at the cost of a reduction in the VSP signal-to-noise ratio SNR.

DAS providers may only provide nominal information about their interrogators to the end users of their measurements due to the competitive nature of the marketplace. The DAS interrogator used in this dissertation was provided by Fotech Solutions, and they were kind enough to disclose information pertaining to the operations of their system. Therefore, we will focus on explaining the operation of their system. Fotech Solutions offers two interrogators, the Helios HSi unit is their intensity-based OTDR system, while the Helios Theta unit is their differential phase-based OTDR system. The HSi unit was designed for DAS applications to urban infrastructure monitoring and acoustic surveillance, while the Theta unit was designed for DAS applications in the seismic realm. Their Theta unit operates via a dual-pulse interferometric approach, interrogating the constructive and destructive interferences of the pulses to infer measurements of strain along the fiber (McDonald, pers. comm., 2019).

Distributed sensing uses what is referred to as the gauge length (GL), the length over which the strain evaluation is made. The GL physically corresponds to the length of fiber over which the laser pulse investigates, or in the case of a dual-pulse system, it is the distance between the two pulses. It can be computed using the pulse width (P_w) in seconds, pulse gap (P_g) as a percentage of the P_w, and the speed of light in the fiber (V) which is defined by the speed of light in a vacuum (C) divided by the refraction index of the fiber (n). Such that a pulse width of 100 nanoseconds and a pulse gap of 80 nanoseconds would correspond to an 8-meter gauge length, which can be computed by equation (1.1) and is illustrated in Figure (1.3).

$$G_L = \left(\frac{P_w + P_g}{4}\right) V \;\; ; \text{where } V = \frac{C}{n} \tag{1.1}$$

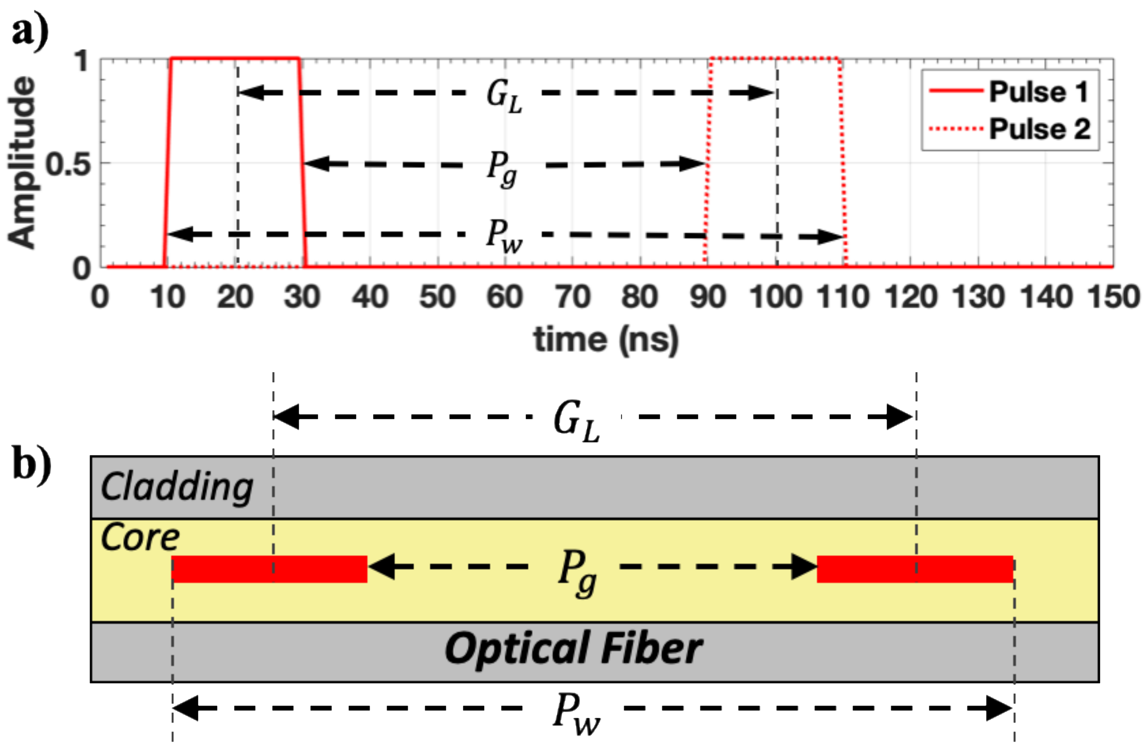

Figure 1.3: Illustration of the gauge length calculation in a dual-pulse interrogation system, with (a) a time-domain display of the signal and (b) a cartoon of the signal in the physical domain.

In a dual-pulse system, the distance between the center of each pulse is the effective gauge length. It is calculated using equation (1.1) given the pulse width and pulse gap.

It is important to understand how the gauge length affects the DAS measurements, Hartog (2017) demonstrates the influence of gauge-length on a synthetic Ricker wavelet with a 50 Hz central frequency. In this example (Figure 1.4), we see how the wavelet becomes wider as the gauge length is increased from 5 m to 25 m. In this case, a velocity of 1000 m/s was used thus the spatial wavelength is 20 meters. It should be noted that for most exploration seismic applications, the P-wave velocity is much greater than water velocity (1500 m/s). Thus, the example overstates the effect of the gauge on the wavelet. However, it is insightful to notice this effect for a P-wave velocity of 1000 m/s, as the gauge length approaches the spatial wavelength of the wavelet (GL = 20 m) the wavelet peak flattens, and once going beyond the spatial wavelength (GL = 25 m) the wavelet becomes a doublet. Thus, selecting the proper gauge length is critical to the preservation of our signal.

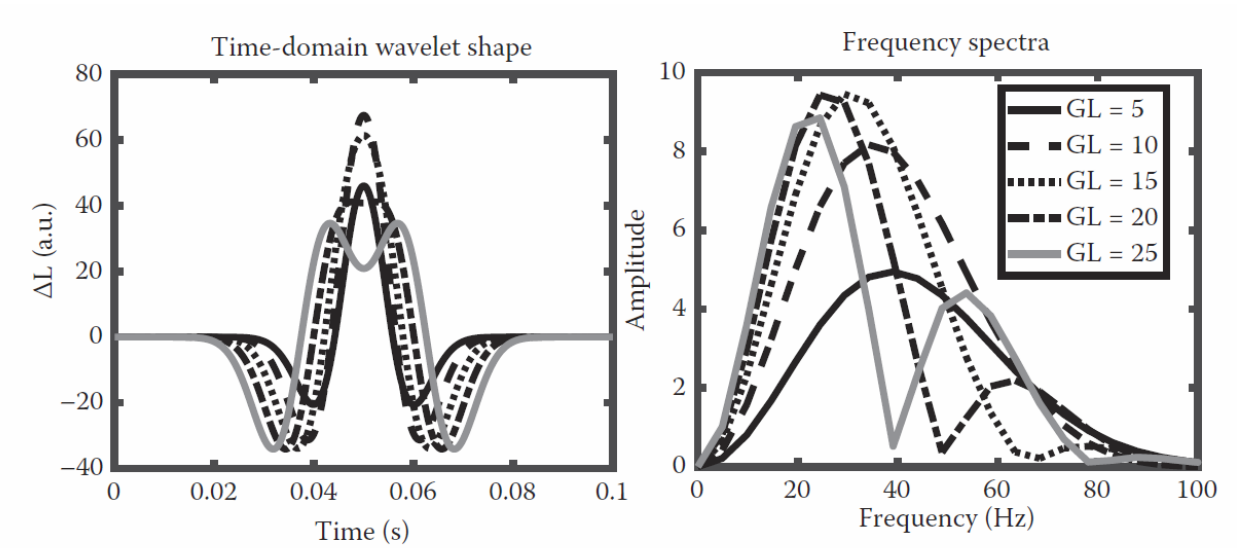

Figure 1.4: Gauge Length (GL) influence on a 50 Hz Ricker wavelet from Hartog (2017).

Hartog (2017) demonstrated how varying the GL influences a Ricker wavelet in the time domain (with respect to acoustic units (a.u.)). As the GL increases, the wavelet becomes wider and an expected peak is seen as a doublet.

Hartog (2017) demonstrates that the GL imposes a spatial resolution on the measurements. Thus, equation (1.2) is formulated to help select the GL during acquisition based on the interest target parameters. Given a maximum expected frequency of 100 Hz and an average velocity of 2000 m/s, the recommended GL is a quarter of the wavelength (i.e. (2000/100)/4 = 5 m).

$$G_L = \lambda/4 \qquad \text{where} \quad \lambda = V/f \tag{1.2}$$

While a smaller GL is always best for preserving the bandwidth of the data, it is not optimal because the SNR will be adversely affected. Thus, knowing the minimum velocity and maximum frequency of the expected data is critical for choosing the appropriate GL.

A simplified schematic of the Helios Theta interrogation system is illustrated in Figure 1.5. The system consists of a transmit chain and a receive chain, the transmit chain consists of the elements used in transmitting the laser signal to the fiber, while the receive chain consists of the elements that are used to process the backscatter measured from the fiber. Both chains are controlled by the digital controller where the user specifies the parameters of the various chain elements. In the transmit chain, the first element is the laser pulser, where the laser signal is generated. The laser signal then goes through the first Erbium-doped Fiber Amplifier (EDFA), each EDFA is followed by an optical filter that helps reduce the optical noise generated by the optical amplification process. Now the amplified signal passes through an optical switch and into the fiber, concluding the transmit chain. The receive chain starts with the backscattered energy coming from the fiber into the optical switch and diverted towards EDFAs 2 and 3. Here the amplification of the backscattered energy is done in two steps to limit the amount of noise generated by the optical amplifiers, while maintaining the integrity of the signal. Finally, the signal is output via the Analog-to-Digital Converter (ADC) as raw backscattered energy.

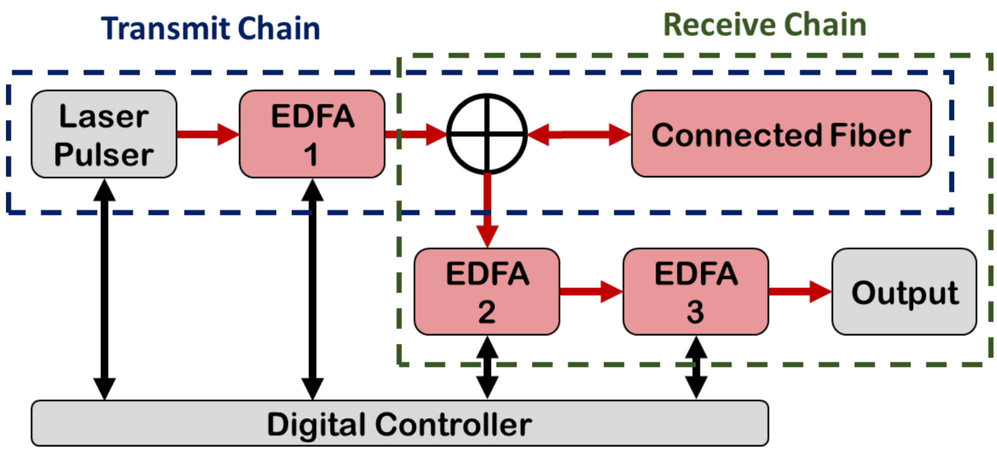

Figure 1.5: Simplified schematic of the Helios Theta interrogation system.

The laser pulser generates the interrogation signal which is amplified by EDFA 1 and sent through the optical switch to the fiber, concluding the transmit chain. Backscatter is generated from the signal interfering with the fiber and it is diverted through the optical switch towards EDFAs 2 and 3 for a two-step amplification process before being output, concluding the receive chain. All elements of the transmit and receive chains are controlled by the digital controller where the user specifies their parameters. Grey rectangles represent electrical elements and red rectangles represent optical elements. The red arrows illustrate the optical signal while the black arrows illustrate electrical signals.

A set of EDFA and ADC values are recommended by the manufacturer, however, the user has the flexibility to adjust these values based on the observed raw backscatter. These values are optimized by adjusting them such that the raw backscatter energy is amplified to two-thirds the digitizer capacity while limiting the amount of data clipping. The default values will typically be lower than the optimized values, setting the values to their maximum amplification power results in clipping of the backscatter energy that result in dead/noisy channels in the receiver domain. Further information is provided in Appendix A as a user instruction manual on operating the Helios Theta system.

1.3.2. Fiber Bragg Gratings (FBGs)

Kersey et al. (1997) review the development of FBGs and explain the theory behind Bragg-grating-based sensing systems. In summary, an FBG can be thought of as a selective wavelength filter, such that when a broadband laser spectrum is injected into a fiber and meets an FBG, the wavelength which corresponds to the grating spacing would be reflected and the rest of the spectrum would pass through. Thus, a single fiber could hold a series of FBGs given that each would filter a different wavelength, limited by the length of the laser spectrum, as illustrated in Figure 1.6.

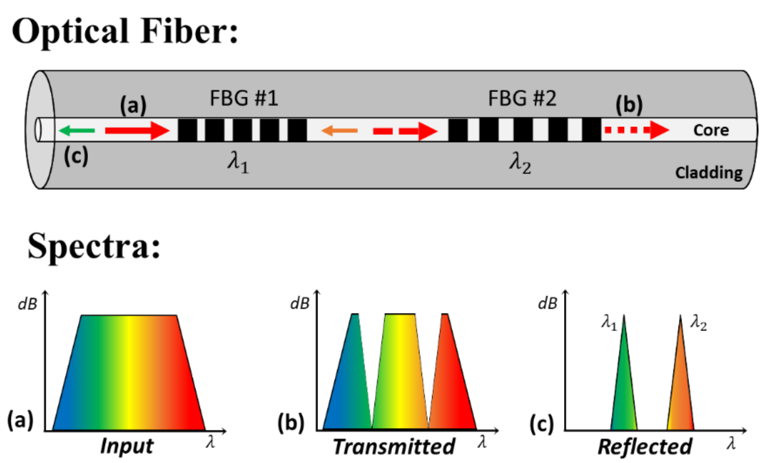

Figure 1.6: An illustration of how a Fiber Bragg-Grating (FBG) works.

When an input laser spectrum (a) meets an FBG, the wavelength (λ) that corresponds to the grating spacing is reflected. Thus, interrogating the fiber from the output port yields the transmitted spectrum (b), and from the input port yields the reflected spectrum (c).

FBG systems are simpler to operate and do not require extensive processing. Their advantages over distributed systems include their higher sensitivity, single-point sensing, and ability to be oriented. A major limitation with FBG systems is the number of sensors that can be deployed on a single fiber, since each FBG will reflect a certain wavelength of the injected laser spectrum, there are only a certain number of available wavelengths given the limited laser spectrum. Additionally, given that the FBGs are specially engineered fibers, they tend to cost more to manufacture and are more fragile compared to telecommunication fiber that is used by distributed systems.

In sensing motion, the FBG wavelength shifts in proportion to the motion straining the FBG along the fiber's direction, where an increase in the wavelength corresponds to stretching the fiber and a decrease corresponds to compressing the fiber. The relationship between the FBG wavelength and the change in temperature and strain is given by this equation (FBGS, 2017):

$$\ln {}^{\lambda}/_{\lambda_0} = \kappa\varepsilon + S_1(T - T_0) + S_2(T - T_0)^2 \qquad (1.2)$$

where λ is the measured wavelength, λ_0 is the nominal wavelength at T_0 with zero strain on the fiber, ε is the strain, T is the temperature, κ is the strain sensitivity coefficient, $S_{1,2}$ are the temperature sensitivity coefficients. The coefficients are typically calculated during the manufacturing of the FBG sensors at a T_0 of ~22.5 ºC.

Given minimal temperature variation observed in the data, the FBG response to temperature is long term (on the order of seconds) whereas the motion/strain response is short term (on the order of milliseconds), thus a linear regression of the data across a one-second window can be used to approximate the temperature response, yielding a linear relationship between the measured wavelength and strain (equation 1.3).

$$\varepsilon = (\ln {}^{\lambda}/_{\lambda_t})/\kappa \qquad \text{where } \lambda_t \text{ is the linear trend of the measured data} \qquad (1.3)$$

Further information on operating the FBG system used in this dissertation is given in Appendix B as a user operations manual.

1.4. Dissertation Structure

The concept of fiber-optic sensing has been introduced in Chapter 1, with a focus on DAS and FBGs. Chapter 2 considers applications to Borehole Seismic Imaging (BSI), analyzing the influence of seismic source types and optical parameters on DAS data in comparison to geophone data, as well as, a field trial of VSP using FBGs in comparison to hydrophones.

Next, surface seismic applications are considered for DAS and FBGs in Chapter 3, where the application of MASW on surface trenched DAS fiber and an example of urban infrastructure monitoring using existing telecommunication fiber networks is undertaken. Additionally, we investigate the application of FBGs in surface seismic imaging.

Chapter 4 explores applications of FOMS in a simulated marine environment. Exploring applications of pipeline flow assessment and integrity, marine seismic source characterization, and underwater communication, using both DAS and FBG systems in comparison to conventional sensing systems.

Chapter 5 considers multicomponent fiber-optic sensing from a theoretical standpoint and presents a multicomponent (3-C) FBG sensor that is developed in the laboratory. Comparing the response of the 3-C FBG to 3-C geophones in a simulated land environment. Testing multiple source types (impulsive and vibratory) and concluding on the 3-C FBG sensor fidelity.

A summary of the dissertation findings and contributions is given in Chapter 6, followed by a discussion of future work in Chapter 7.

CHAPTER II

BOREHOLE APPLICATIONS OF FOMS

This chapter explores applications of DAS and FBGs in BSI. First DAS is considered, investigating the influence of seismic sources and optical parameters on DAS data quality in comparison to geophone data. Next, an FBG array is tested against a hydrophone array in a shallow borehole, to demonstrate the possibility of using FBGs for VSP.

2.1. DAS and Borehole Seismic Imaging:

The motivation of this study is to establish an understanding of the influence of seismic source types and optical sensing parameters on borehole seismic DAS data in comparison to geophone data. With the objective of demonstrating and quantifying the influence of optical parameters of optical amplification and gauge length on data quality, and testing the validity of selecting the optimal gauge length based on the seismic wavelength.

Hardeman-Vooys and Lamoureux (2019) demonstrate the influence of gauge length on synthetic data and show that at larger gauge lengths an expected single peak is detected as a doublet. Dean et al. (2016) also demonstrate this effect on a 50 Hz Ricker wavelet, showing distortion of the frequency content as gauge length increases. They conclude that as the gauge length approaches the spatial wavelength of a wavelet, the wavelet peak flattens. As the gauge length becomes larger than the spatial wavelength, the output wavelet becomes a doublet. This highlights the importance of selecting an appropriate gauge length. The question arises as to why purse larger gauge lengths in the first place? The answer is that a longer gauge length achieves higher signal-to-noise ratio (SNR) in the optical domain. Thus, there is a trade-off between shorter gauge lengths with higher resolution but lower SNR and longer gauge lengths with lower resolution but higher SNR (with wavelet distortion).

This study was conducted at a research facility in Houston, Texas, equipped with a shallow test well (~1500 ft or ~460 m deep). Two seismic source types were used, impulsive and vibratory, while monitoring with two sensing systems, an array of vertical geophones and looped fiber, both cemented behind casing. The optical parameters of the DAS system were varied to investigate the influence of the optical amplifier parameters and gauge length on the VSP data quality.

This section begins with an introduction to the location and geology of the area, followed by a summary of the acquisition parameters and processing workflow. Geophone results are then shown as a benchmark for the DAS results and assess the influence of the two seismic sources on the data. The optimal fold for each source type is presented and the influence of the optical parameters on the data is demonstrated, with respect to optical amplification and gauge length. Then, a comparison between the geophone and DAS processing results is made, with respect to the first-break picks, interval and root-mean-square (RMS) velocity profiles, and corridor stacks. In conclusion, the findings of this study are summarized and recommendations are given.

Location and Geology

This study was conducted at a research facility in Houston, Texas, equipped with a shallow 1500 ft (457 m) test well. The well intersects two minor aquifers in the Gulf Coast major aquifer unit (Figure 2.1a); The Chicot aquifer a Holocene to Pleistocene quaternary system that consists of fluviatile terrace deposits of the Beaumont Clay, Lissie Formation, and Willis Sand (Baker, 1979; Nobel et al., 1996). And the Evangeline aquifer a Pliocene Tertiary system primarily represented by the Goliad sand (Baker, 1979; Nobel et al., 1996). The near-surface layers consist of primarily clastic sediments generally characterized as clays, shales, and sands. Figure 2.1b illustrates the survey geometry, this will be discussed further in the data acquisition section.

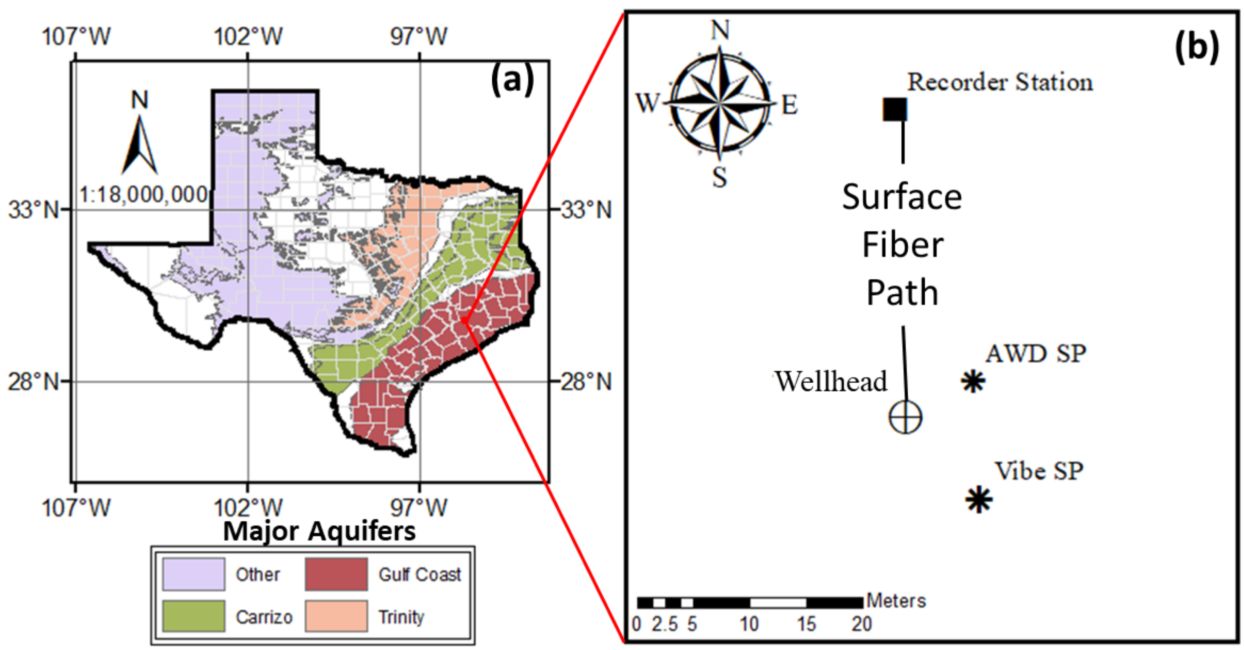

Figure 2.1: (a) Map of Texas with major aquifers indicated. (b) Zoom of the survey location and geometry.

Well logs shown in Figure 2.2a show the Chicot aquifer (green) between 40 and 160 m depth, which consists of six layers characterized by high-resistivity and low gamma-ray, that are interpreted as sand layers interbedded by low-resistivity high-gamma-ray clay layers. They also show the Evangeline aquifer (orange) between 180 m and 360 m, with multiple layers characterized by high-resistivity and low gamma-ray, these layers have higher gamma-ray values than the Chicot sand layers, indicating higher clay content, therefore classifying the layers as dirty sand layers.

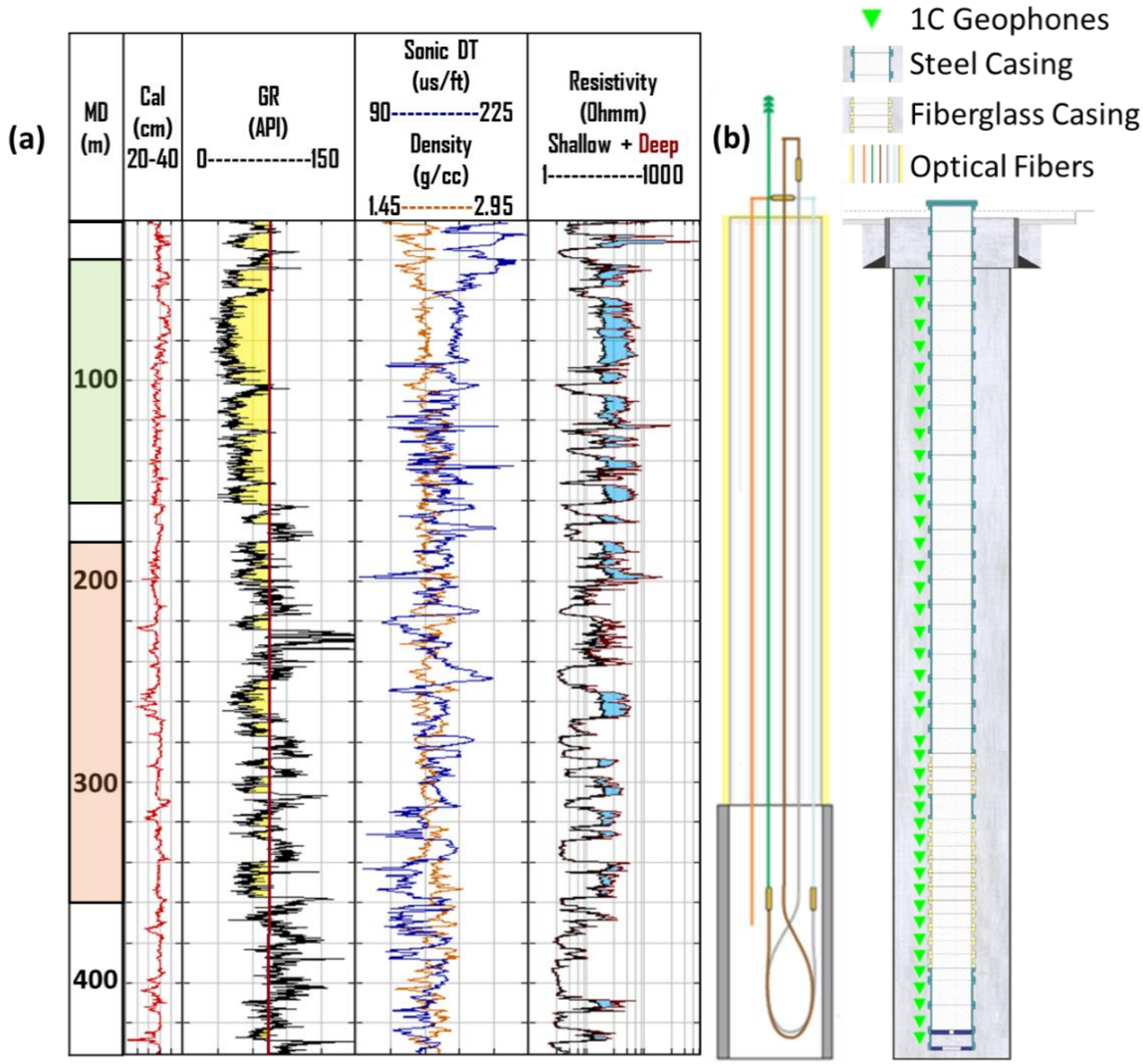

Figure 2.2: a) Caliper (Cal), Gamma-ray (GR), P-Sonic (DT), Density, and Resistivity well logs highlighting the Chicot aquifer in green and the Evangeline aquifer in orange. The Gamma-ray and resistivity logs have been interpreted, highlighting sandy formations in yellow and water saturation in blue. b) The well completion and sensor deployment are illustrated for both geophone and looped fiber.

Data Acquisition

The first survey used an impulsive 80 lb. accelerated weight drop (AWD) source at an offset of 8.5 m from the wellhead and an azimuth of 45º from North. While the second survey used a 34,000 lb. vibratory source (Mini-Vibe Truck), at 10% drive with a 12-second linear sweep from 8 to 120 Hz, at an offset of 11 m and an azimuth of 115º from North. These shot-points are illustrated in Figure 2.1b as AWD SP and Vibe SP, respectively. The recording systems were located in a nearby building, illustrated as Recorder Station on the map in Figure 2.1b. A surface fiber path from the recorder station to the wellhead was necessary to interrogate the fiber. We account for this during the DAS data processing.

The well is equipped with single-component (vertical) geophones and fiber-optic cables cemented behind casing as illustrated in Figure 2.2b. This should allow a fair comparison in terms of sensor coupling and sensitivity. The geophone array consists of two 20-channel strings, the first string has the geophones spaced at 40 ft (~12 m), while the second string has the geophones spaced at 30 ft (~9 m). This spacing was influenced by the different casing types (steel and fiberglass). The fiber-optic cables contain several single-mode fibers that are looped at the bottom of the well and spliced at the surface to create multiple loops of fiber. In this study, DAS data analysis is focused on the first run of fiber from the surface to the bottom of the well.

A summary of the acquisition parameters is given in Table 2.1, highlighting the various source types, source parameters, recording systems, and geophone recording parameters used during the acquisition. The geophone recording parameters were fixed during acquisition, whereas the DAS recording parameters were changed to test the influence of the optical parameters on the data quality.

Table 2.1: Acquisition Parameters

Seismic Source	Source Parameters	Geophone Recording System	DAS Recording System	Geophone Recording Parameters
PEG-40 AWD	36 kg (80 lb.)	Geometrics Stratavisor	Fotech Helios Theta	Sample rate = 1 ms Record length = 3 s
INOVA 34,000 lb. Mini-Vibe	8-120 Hz 12s (Linear) 10% Drive	ISEIS DaqLink 4		Sample rate = 1 ms Record length = 15 s

The interrogator system used in this study (Fotech Helios Theta) uses a phase-based, dual-pulse interferometric approach to measure relative strain along the fiber. Table 2.2 highlights the various optical parameters used during the surveys. Fixed parameters include the pulse repetition frequency (PRF), record length (L), temporal downsampling factor (dT), spatial decimation factor (dS), and refractive index of the fiber (n). While, the pulse width (Pw) and pulse gap (Pg) were manipulated to select different gauge lengths (GL), and the optical power parameters (Erbium-doped Fiber Amplifier (EDFA) and Analog-to-Digital Converter (ADC)) were varied to investigate the influence of default (EDFAs = 590/130, ADC = 0.8), optimized (EDFAs = 720/130, ADC = 0.4), and maximum (EDFAs = 800/180, ADC = 2) settings on the data quality.

Table 2.2: DAS Recording Parameters

Seismic Source	DAS Recording Parameters									
	PRF (kHz)	**Pw (ns)**	**Pg (%)**	**GL (m)**	**L (s)**	**dT (u)**	**dS (u)**	**EDFAs (mA)**	**ADC (V)**	**n (u)**
PEG-40 AWD	15 kHz	40 60 100	33 33 50	2.7 4 7.5	3	21	5	590/130 720/130 800/180	0.8 0.4 2.0	1.468
INOVA Mini-Vibe	15 kHz	30 70 130 130	20 30 40 80	2 4.5 9 12	15	21	1	Optimized		1.468

(u): Unitless

The DAS time sample rate is one-third the PRF, thus a PRF of 15 kHz yields a 0.2 ms sampling rate. A temporal downsampling factor is applied to output a geophone equivalent time sampling rate of 1 ms. The gauge length is defined by the pulse-width and pulse-gap according to equation 1.1. Where the speed of light in the fiber (V) (in meters per second) is equal to the speed of light in a vacuum (C) divided by the refraction index of the fiber (n ≈1.5). The gauge length sets the measurement spatial sampling interval; it will best sample a seismic wavelength longer than four times the gauge length.

Acquisition Guidelines

There are three issues to consider for DAS data acquisition and processing:

The first matter to consider is wellhead fiber calibration, since surface fiber will be required to connect from the wellhead to the recording station, it is important to know where the wellhead lies along the fiber path. This is typically done by means of a wellhead tap test (Ellmauthaler et al., 2016), where a tap is made at the wellhead at the surface and the point is marked on the interrogation window to flag the location for later processing. I have found that this method is not very accurate and leaves room for interpretation error. How to overcome this error is discussed in the DAS processing section.

The second matter is simultaneous triggering of both recording systems with respect to the source excitation time. When acquiring with the AWD a close-contact trigger switch was used to trigger both systems, however, the DAS system required an electrical input trigger, and thus a conversion box was necessary to convert the close-contact signal to an electrical impulse for the DAS to start recording. With respect to the Vibroseis source, an RTM (Radio Trigger Module) box was used to communicate with the Vibroseis and simultaneously trigger both DAS and Geophone systems. We found that both methods worked as expected with no observable issues.

The third matter to consider is geophone and fiber depth calibration, to determine the fiber depth and the location of the geophones along the fiber path. I suggest introducing an electrical current to the geophone array to generate a vibration at each geophone that is then detected by the fiber, thus effectively capturing the location of each geophone along the fiber. I expect that such method would achieve higher accuracy in calibrating the fiber depth in comparison to the conventional method of a tap-test, as there will be more calibration points to tie the fiber-length to the measured depth. Although, the issue of GL will still exist, and thus I would recommend such method be done at the smallest GL possible. This method was not tested during our study but is suggested for future work.

Data Processing

Data format and preconditioning

After some processing is done in the optical domain, DAS data is recorded and written in an optical standardized data format (Hierarchical Data Format. HDF), which is then converted to SEG-Y (using the DAS vendor software). Such processing is necessary to enhance the optical backscatter, unwrap the measured phase, apply temporal and spatial decimation, and limit optical noise. Before writing to SEG-Y, the headers are populated with the seismic parameters and the fiber length is converted to depth, after compensating for optical fiber on the surface from the interrogator to the wellhead. This process is done via a wellhead tap test, where we tap on the wellhead and record the signal to interpret the location of the wellhead along the fiber, the assumption is then made that the distance along the fiber from that point will correspond to the measured depth. The distance along the fiber (Z) is calculated using the travel time (t) and speed (V) of the pulse in the fiber (Shroyer and Dria, 2017), where V is given in equation 1.1. Thus, the refractive index of the fiber plays a major role in the accuracy of the fiber length measurements. I find that this process leads to some inaccuracy in the depth values which needed to be addressed prior to processing the data.

Processing Workflow

A general zero-offset VSP (ZVSP) processing workflow is designed with VISTA seismic data processing software to process the geophone data, with some additional steps added for the DAS data. Figure 2.3 illustrates the general processing workflow that was used in this study. The workflow starts with data imported in SEG-Y format, followed by a quality check (QC) of the headers. For DAS data, common-mode noise is then suppressed, and the data is interpreted for the well top and bottom. I then write the source-receiver geometry onto the headers, taking into account the interpreted well top and bottom, and continue as with the geophone workflow. I then proceed with interactively picking the first-break arrivals in the data, marking the primary downgoing wavefield, which are used for velocity analysis and producing the first VSP product of a time-to-depth curve and a 1D velocity profile. The first-break picks (FBP) are then used to separate the primary downgoing wavefield, which is subsequently used for deconvolution. F-K and median filters and Gain and NMO corrections are applied to the residual deconvolved data to enhance the up-going primary reflections and suppress unwanted waves such as tube and shear waves. Finally, a corridor mute is defined using the FBP as the upper bound mute and drawing the lower bound mute to produce the corridor stack as the final ZVSP product.

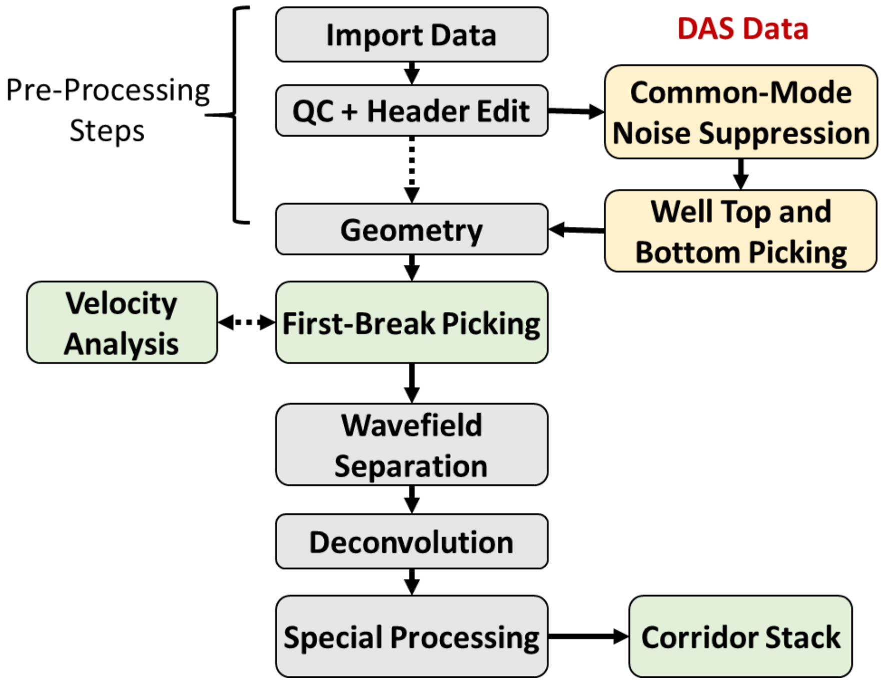

Figure 2.3: ZVSP processing workflow diagram

Geophone Data Processing

The geophone data is processed first to serve as a benchmark and leave a detailed discussion of the events to the results section. Figure 2.4 shows the processing results of the geophone measurements for an 8-fold Vibroseis shot record, starting at the correlated Vibroseis shot-gather (Figure 2.4a), then after separating the primary downgoing (DG) wavefield and deconvolving it from the data (Figure 2.4b), and the final shot stack after suppressing the DG tube waves (Figure 2.4c).

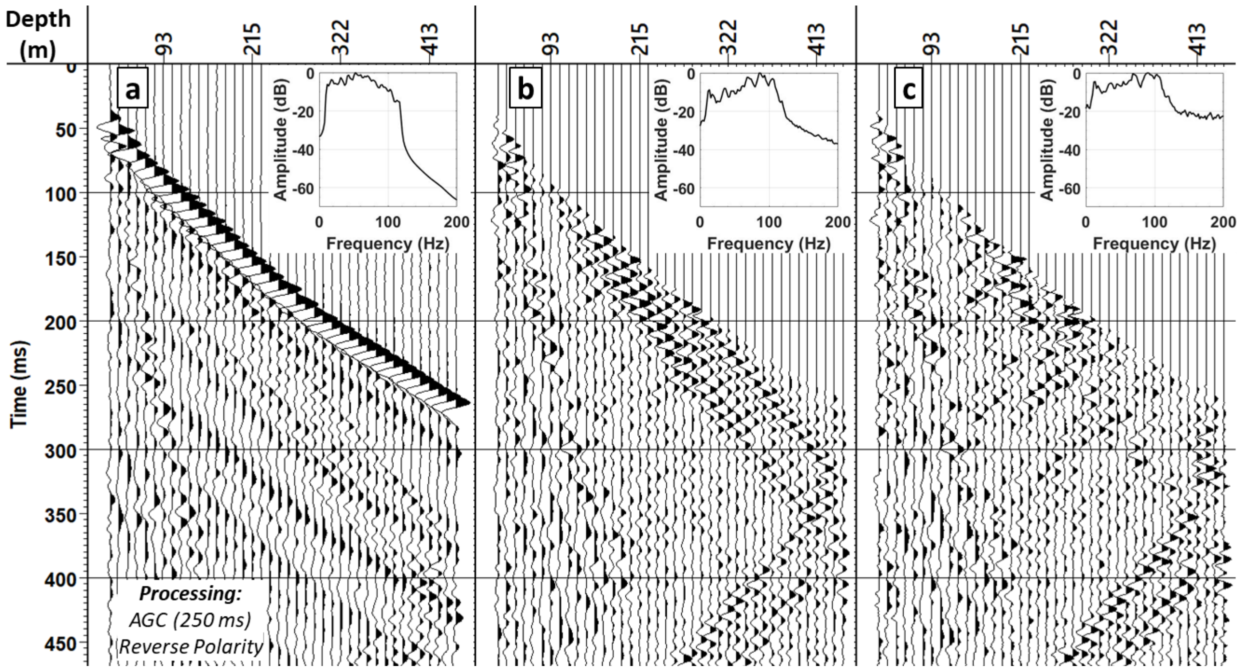

Figure 2.4: 8-fold Vibe Geophone ZVSP Processing results

(a) correlated shot-gather, (b) after separating the primary downgoing wave and deconvolution, (c) after suppressing tube-waves. The average frequency spectrum for each record is shown in the top right corner. The data is displayed with an AGC window of 250 ms and reverse polarity.

Figure 2.5 is the L-plot tying the well logs (Figures 2.5a and 2.5b) to the final shot stack in two-way time (TWT). The corridor mute is annotated with yellow lines, the shot stack (Figure 2.5c) and corridor stack (Figure 2.5d) are then shown next to well-log synthetics (Figure 2.5e) generated using a zero-phase Ormbsy wavelet (5-10-80-120 Hz) with positive and negative SEG. The shot stack depicts the primary reflections with multipath waves, whereas, the corridor stack represents primary reflections only. I find that the top of the Evangeline aquifer generates a reflection at 270 ms (180 m) that ties nicely in the L-plot.

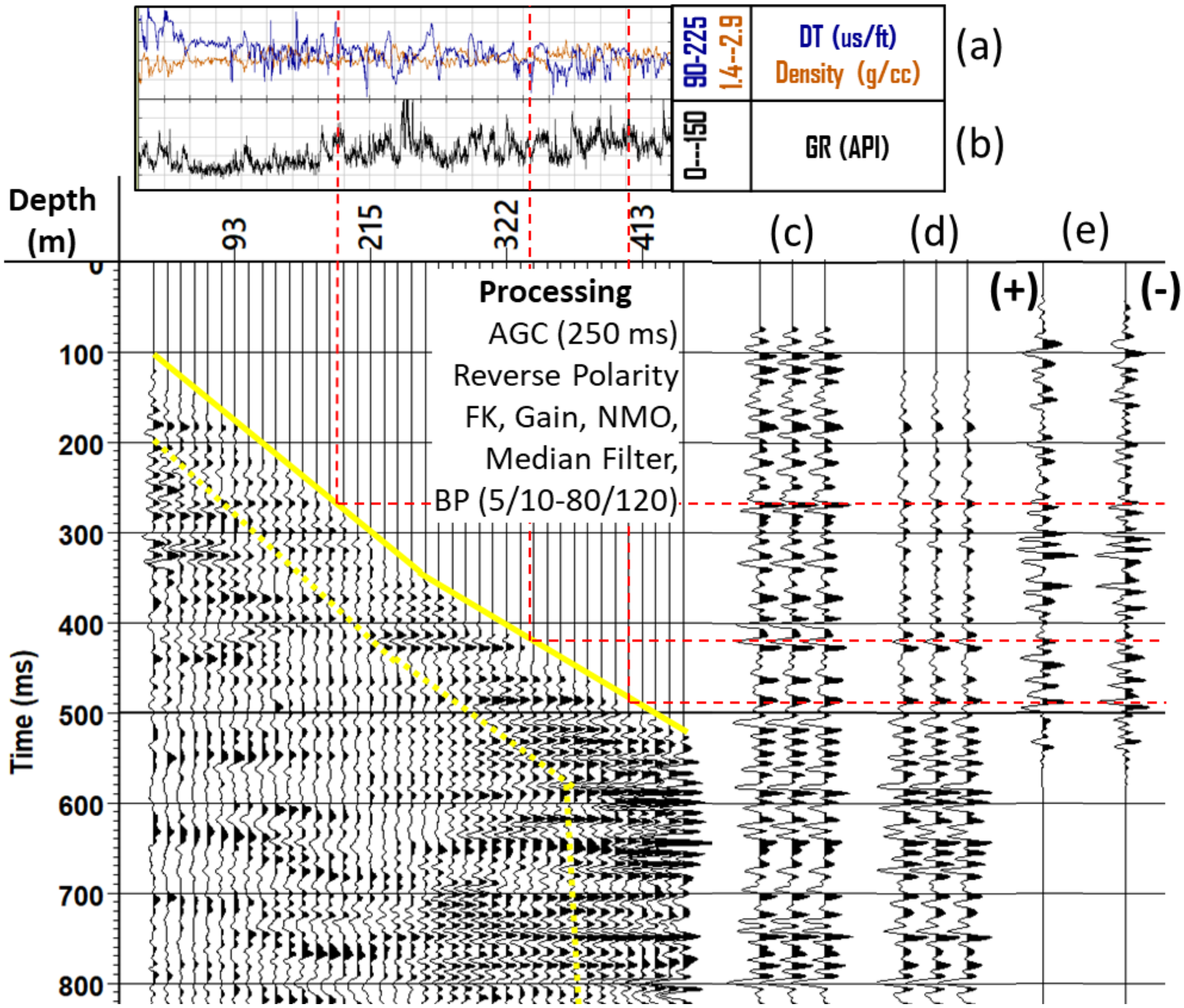

Figure 2.5: 8-fold Vibe Geophone ZVSP post-processing results

(a) Sonic (DT) and Density logs, (b) Gamma-ray log, (c) full-stack, (d) corridor stack, (e) well-log synthetic using a zero-phase Ormsby (5-10-80-120 Hz) wavelet with SEG polarity (+) and reverse-SEG polarity (-).

DAS Data Processing

A majority of DAS processing time is spent on data pre-processing, partially due to the large trace count, but primarily due to the lack of proper header handling when converting the data from the standardized DAS format (HDF) to SEG-Y. The pre-processing steps include checking the headers and populating them with appropriate header values, correcting the fiber length to account for the surface fiber path, and interpreting the well top and bottom to adjust the depth values accordingly.

Figure 2.6 is an example of picking the well top and bottom on a looped fiber geometry. I recommend using the tube waves and first-breaks to assist with picking the well top and bottom. The tube waves travel down and up a fluid-filled well, with the reflecting points marking the fluid contacts. Therefore, the bottom tube wave reflection would point to the bottom of the well and the top tube wave reflection marks the wellhead at the surface. Similarly, we can use the first-break, the first-break from the surface to the depth equivalent of the source offset will consist of refractions and not a direct wave, thus arriving at a later time. This information can be used to guide with picking the well top. As for the well bottom, it will be marked by the latest first-break arrival. In looped fiber geometry, it is easier to verify as that point marks the apex of the first-breaks. In the absence of looped fiber, there will be uncertainty on whether the fiber end marks the end of the well or a break along the fiber.

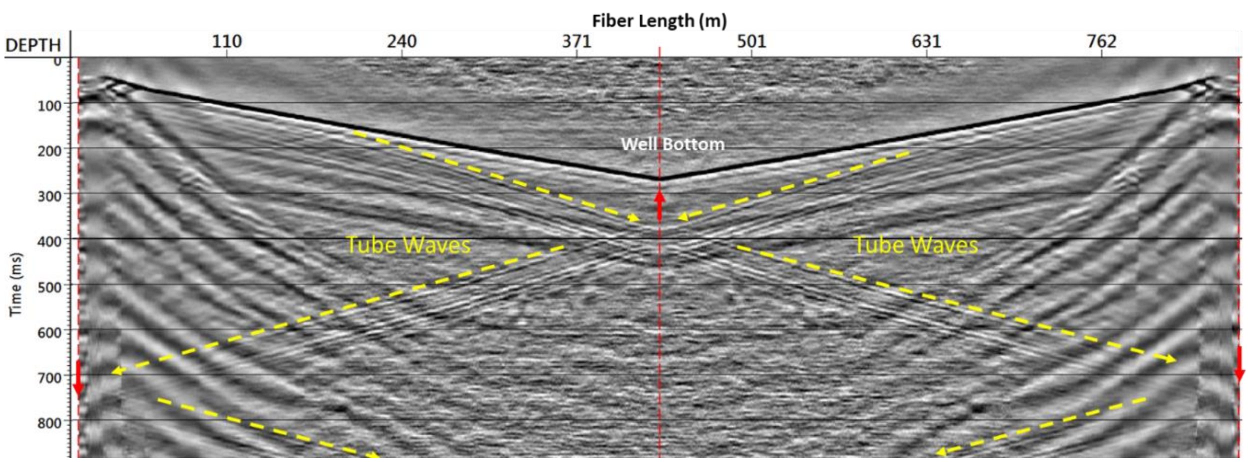

Figure 2.6: Vibe source DAS (4.5 m GL) ZVSP correlated shot gather denoting the recommended method for picking the well top and bottom assisted by the tube waves.

The next step is suppressing the instrument noise that is observed on the data. Common-mode noise (CMN) is manifested as horizontal events along the record. These signals are generated by ambient noise at the DAS interrogator and has a constant imprint across the fiber. We remove the CMN by first applying a large window median filter to enhance the CMN and then subtract it from the data. Figure 2.7 shows the results of this process. The following processing step is applicable to looped fiber, where we extract the first run (fiber from the surface to the bottom) for further analysis. At that point, we proceed with the conventional geophone processing workflow, updating the source-receiver geometry and picking the first-breaks for further processing.

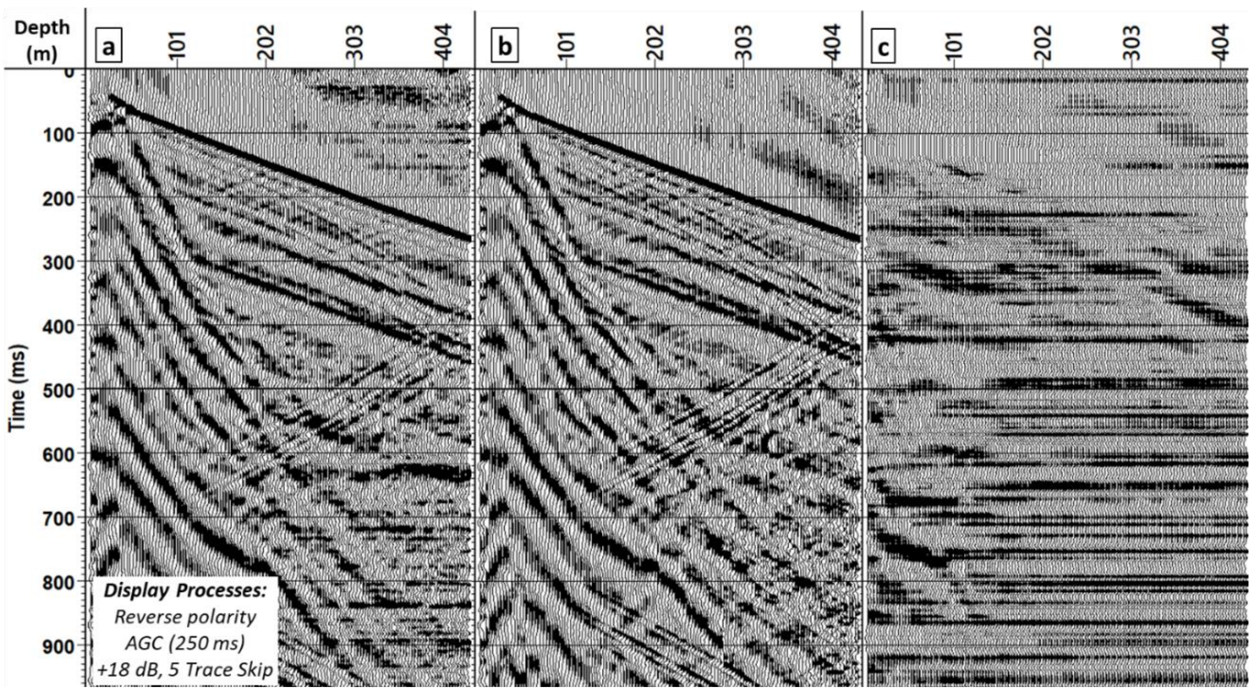

Figure 2.7: Vibe source DAS (9 m GL) ZVSP correlated shot-gather (a) before and (b) after processing the (c) CMN.

Results

Figure 2.8 displays the interpretation of several events that are evident on a DAS shot-gather in the time and frequency domain. The first event of interest is the first-break which marks the primary downgoing wave (Figure 2.8a). From the first-break picks (FBP), we obtain a time-depth relationship that is used to compute the interval and RMS velocities. We also use the FBP throughout the processing workflow for separating the wavefields, deconvolution, and finally converting the record to two-way time. Table 2.3 describes the various events that have been identified in Figure 2.8, with respect to their apparent velocity and their dominate frequency.

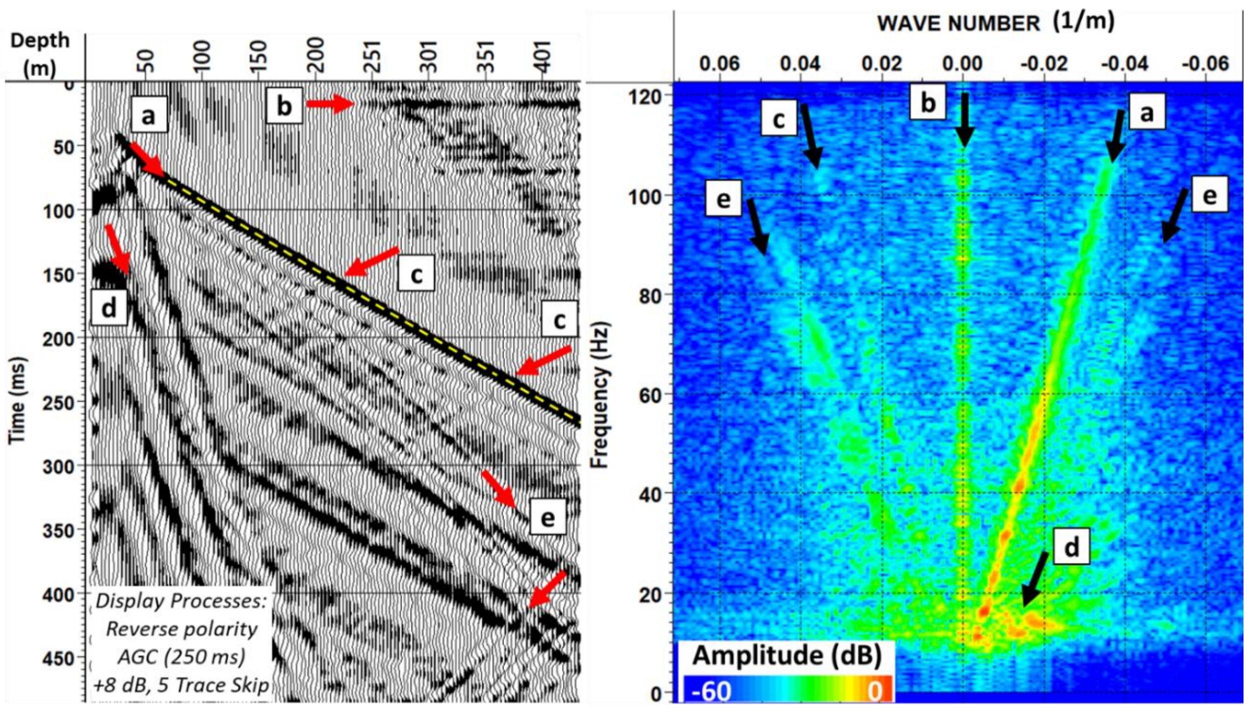

Figure 2.8: Interpretation of events on raw shot-gather in the time (left) and frequency domain (right).
The shot-gather shown in this figure is from DAS vibe data recorded at a 9 m GL, AGC has been applied with a 250 ms window, a constant gain of +8 dB has been applied, and the polarity of the data has been reversed. Annotated events are described in Table 2.3.

Table 2.3: Description of annotated events in Figure 2.8.

Event	Description	Velocity (km/s)	Dominant Freq. (Hz)
a	Downgoing P-Wave	1.9 – 2.3	40 – 60
b	Common-mode Noise	n/a	Variable
c	Primary Reflections	1.8 – 2.2	40 – 60
d	Downgoing S-Wave	0.4 – 0.6	8 – 12
e	Tube Waves	0.9 – 1.3	40 – 60

The SNR is used as an indicator to help quantify our observations and findings. It is estimated (Figure 2.9) by computing the ratio of the average amplitude spectrum at the first break to the average amplitude spectrum prior to the first-break. Similarly, the SNR can be estimated by subtracting the average spectra at the first-break from the average spectra prior to the first break in the dB scale. Thus, in Figure 2.9 the estimated SNR would be around 20 (-70 + 90 dB, or 400k/20k).

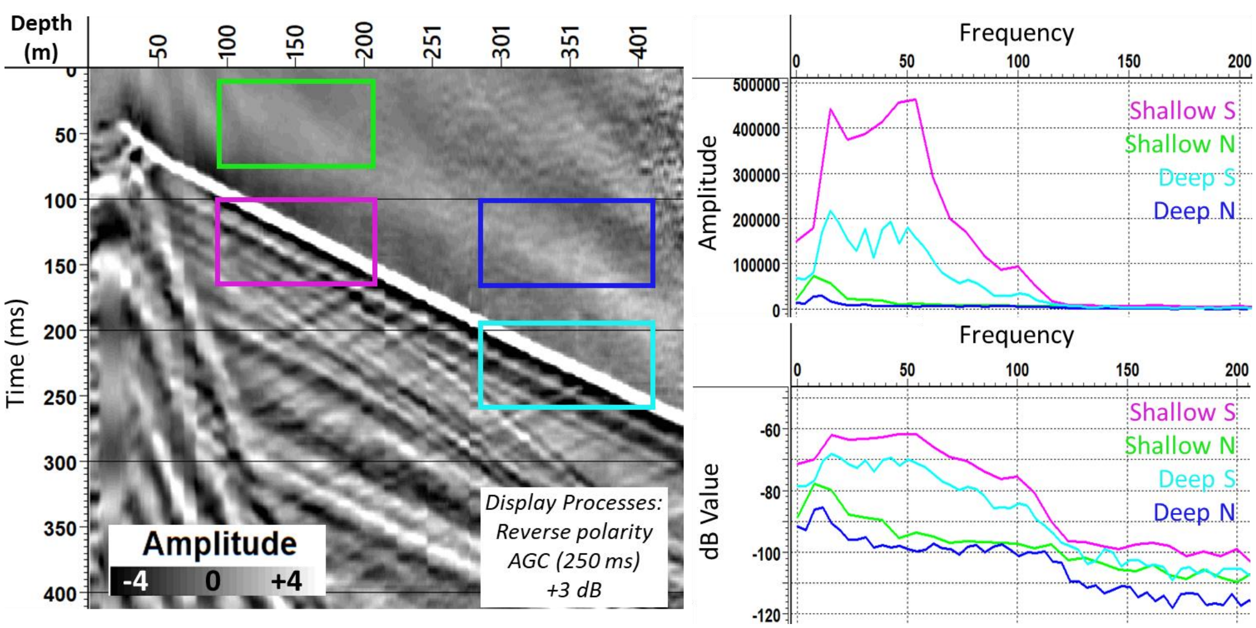

Figure 2.9: Example of SNR estimation by taking the ratio of the average amplitude spectrum prior to the first-break and at the first-break at different areas in the shot record (left image).

The corresponding amplitude spectra are shown in the two right images (top: power spectra, bottom: spectra in dB scale) for each rectangle drawn on the left image.

2.1.1. Influence of source type and fold

From the AWD shot gathers (Figure 2.10), we observe that for the geophone data a vertical shot stack (SS) of 16 is sufficient to produce an image with SNR of 10 where the up-going reflections are strong enough to appear through the noise floor (ambient and coherent noise). The DAS data fails to have observable up-going reflections but begins to image the first-break to the bottom of the well at a SS of 21 with an SNR of 3. However, the results from the Vibroseis source (Figure 2.11) show a significant improvement in SNR. I find that at SS of 8 we obtain an SNR of 25 and are able to pick multiple up-going reflections in the data, while the DAS data requires a SS of 32 to achieve SNR of 20. However, the high trace density in the DAS data provides more interpretable data and higher resolution than the geophone. The results are summarized in Figure 2.12 showing the relationship between the shot fold and the increase in SNR in comparison to the relationship of square root the number of shots as suggested by Dean and Sweeney (2019). I find that the Vibroseis DAS measurements best follow this relationship while the geophone measurements show a higher order of increase in SNR. The AWD measurements, on the other hand, both show a lower-order increase in SNR.

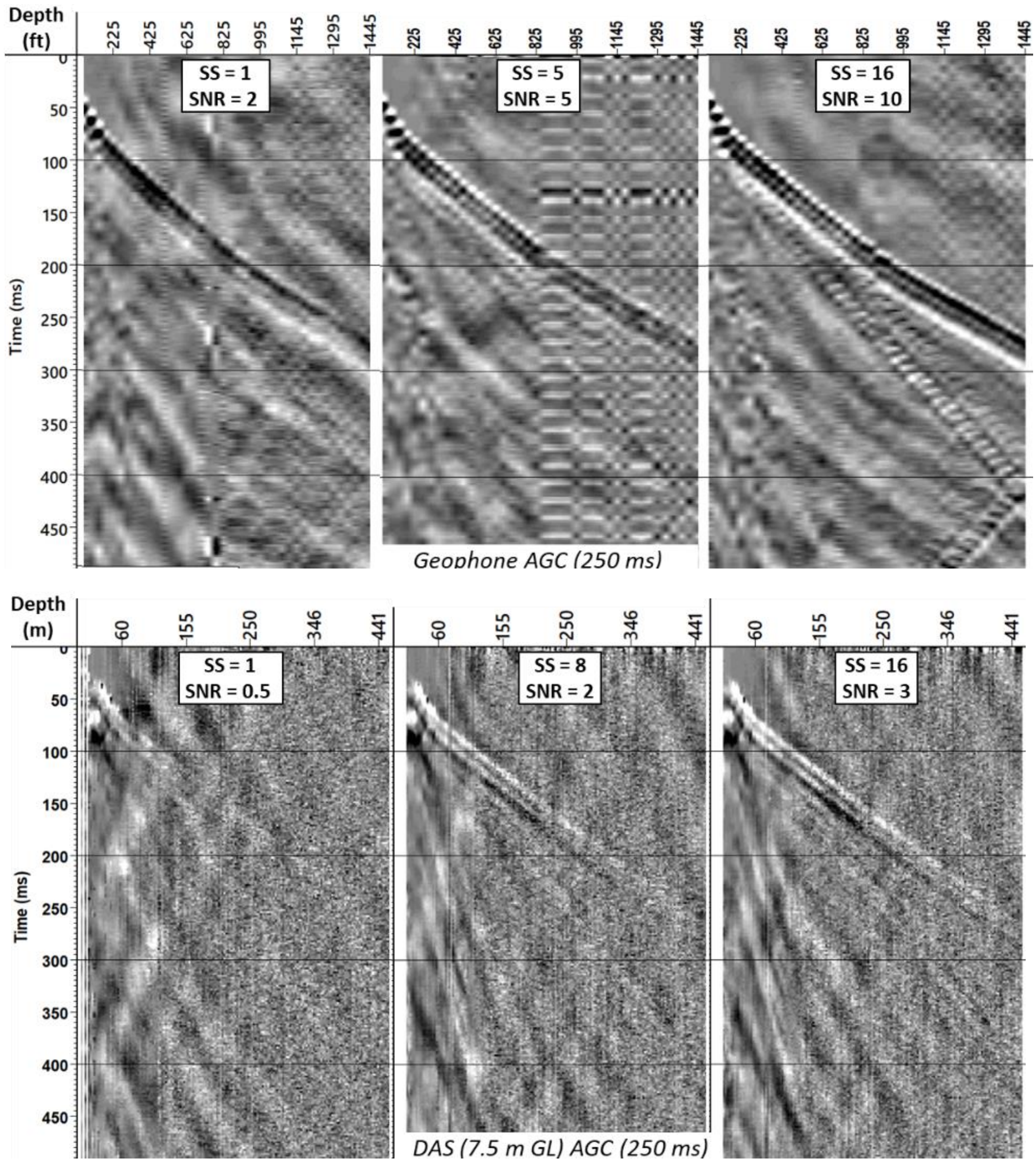

Figure 2.10: AWD shot fold results

Geophone results are shown in the top three panels with respect to a shot stack (SS) of 1, 5, and 16 respectively. DAS (7.5 m GL) results are shown in the bottom three panels with respect to SS of 1, 8, and 16 respectively. AGC with a 250 ms window has been applied to the data for visual enhancement.

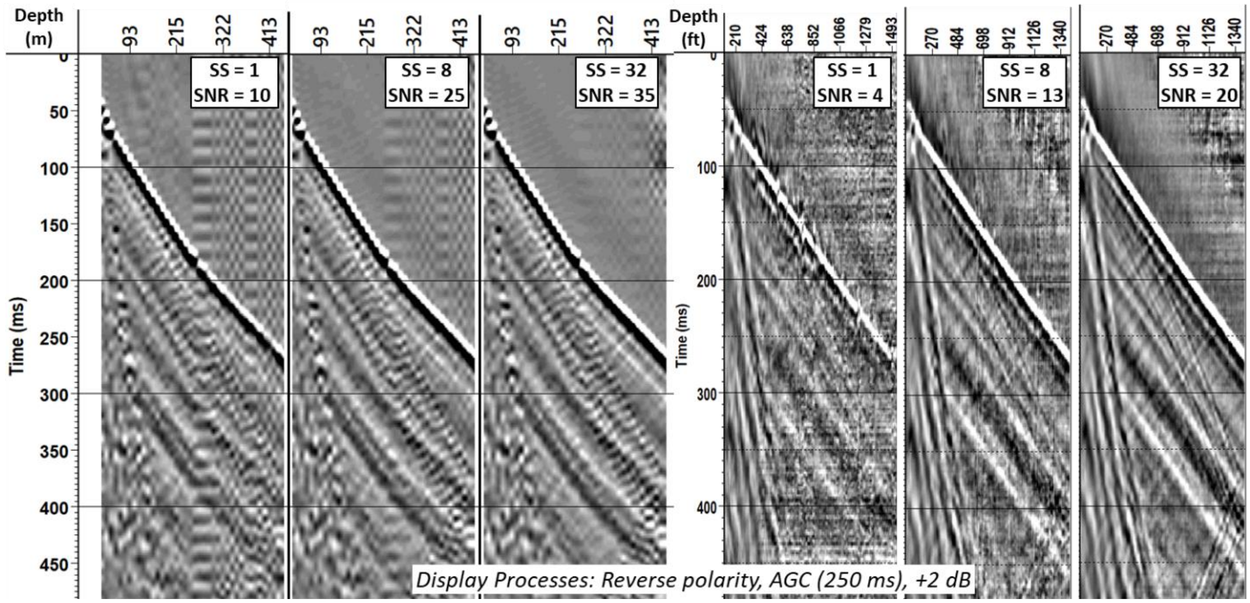

Figure 2.11: Vibe shot fold results

Geophone results are shown in the three left panels with respect to an SS of 1, 8, and 32 respectively. DAS (9 m GL) results are shown in the three right panels with respect to SS of 1, 8, and 32 respectively. AGC with a 250 ms window has been applied to the data with a +2 dB constant gain for visual enhancement.

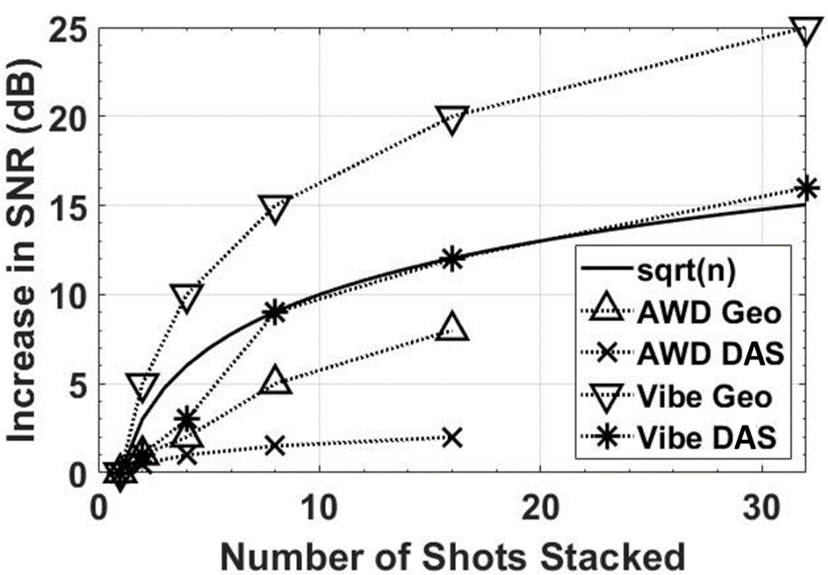

Figure 2.12: Fold SNR analysis for AWD and Vibroseis data with respect to both geophone and DAS sensing systems.

The interpreted SNR values are plotted against the theoretical relationship of the square root of n (the number of shots stacked).

2.1.2. Influence of optical parameters

Optical parameter tests were carried during the AWD survey with respect to varying the optical power amplification and gauge length. Three optical power settings were tested, the first using the default settings recommended by the manufacturer, then maximizing the permissible optical power while avoiding clipping the raw backscatter, and finally optimizing the parameter such that the average raw backscatter is 2/3 the digitizer capacity. Figure 2.13, highlights the results of these tests. I find that increasing the gauge length allowed for higher SNR, similar observations were made by Dean et al. (2016). I also find that optimizing the optical power doubled the SNR, while maximizing the optical power resulted in some dead channels and coherent noise that results from clipping (overpowering the optical digitizer) the raw optical signal.

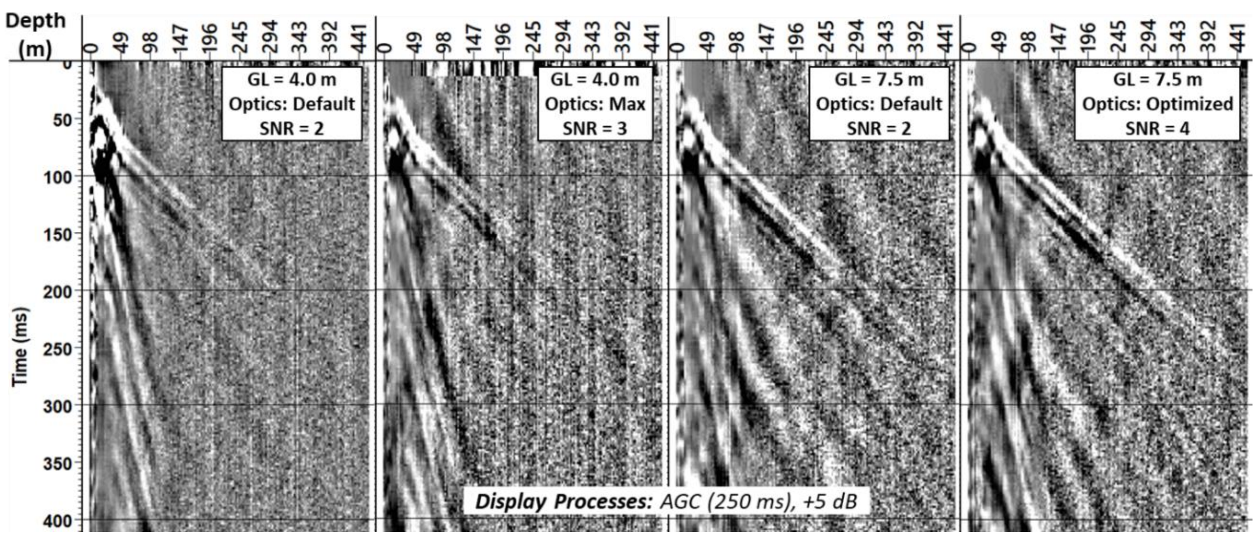

Figure 2.13: Influence of gauge length and optical amplifiers on AWD DAS data.

With respect to the Vibroseis survey, we find a significant improvement in data quality. Referring to Figure 2.14, the highest SNR is achieved at 4.5 m GL, however, when separating the downgoing wavefield and deconvolving the data, the highest SNR is found at 12 m GL (Figure 2.15). Naturally, SNR is not the only evaluator of image quality, as it does not consider the resolution of the image. The 4.5 m GL data demonstrate higher resolution in the sense that there is more detail in the data. The 2 m GL has the poorest data quality due to decreased sensitivity with shorter gauge lengths and the increase of optical noise.

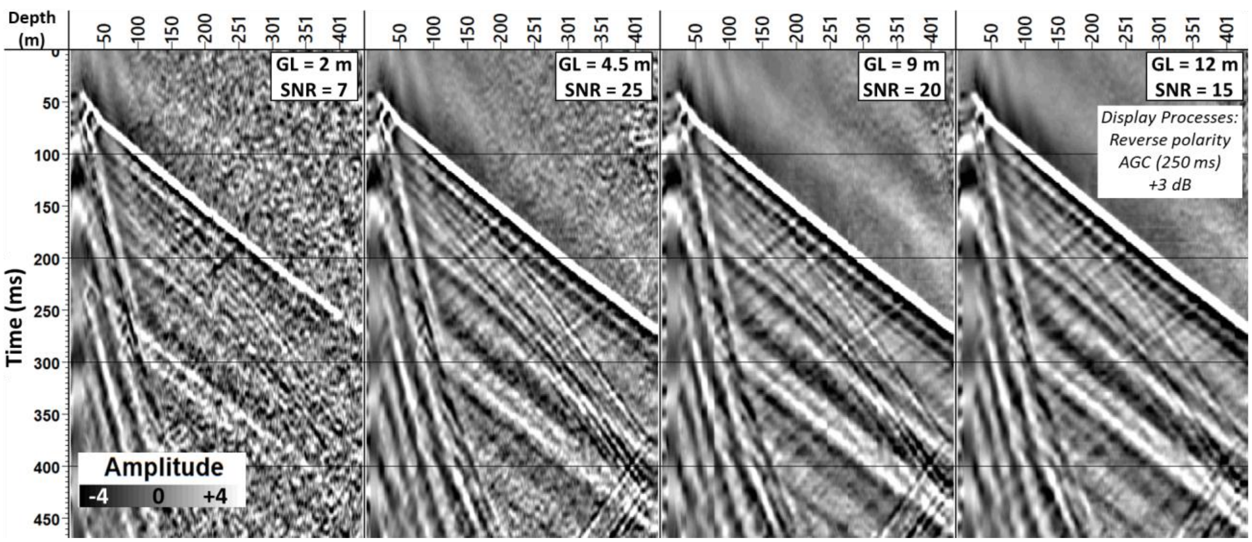

Figure 2.14: Vibe source DAS ZVSP correlated shot gathers at various gauge lengths (GL) after removing the CMN.

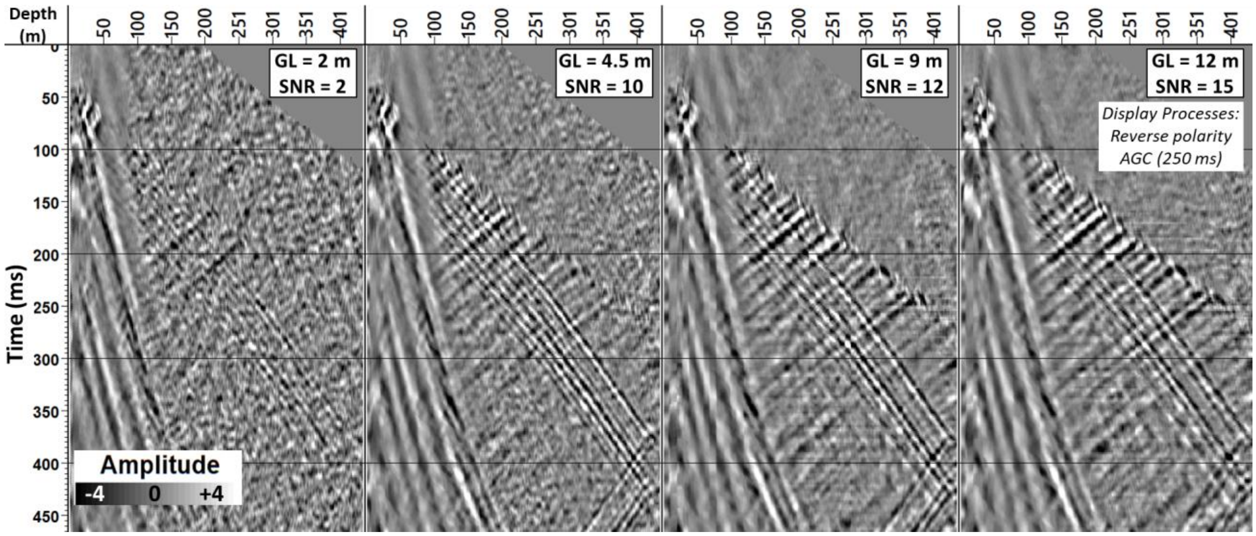

Figure 2.15: Vibe source DAS ZVSP correlated shot gathers at various gauge lengths (GL) after wavefield separation and deconvolution.

By investigating the final gather in two-way time (Figure 2.16) and the corridor stacks (Figure 2.17), we establish a correlation between the imaging result of the ZVSP in comparison to the geophone corridor stack and synthetic seismic traces generated using the density and sonic logs. We cross-correlate the geophone corridor stack (reverse polarity) with all the records to quantify the similarity between the traces. I find that the 4.5 m GL produces the highest cross-correlation value of 0.65 in comparison to the other records. A phase shift is noticed between the DAS and Geophone data, similar observations have been made by Gordon et al. (2018).

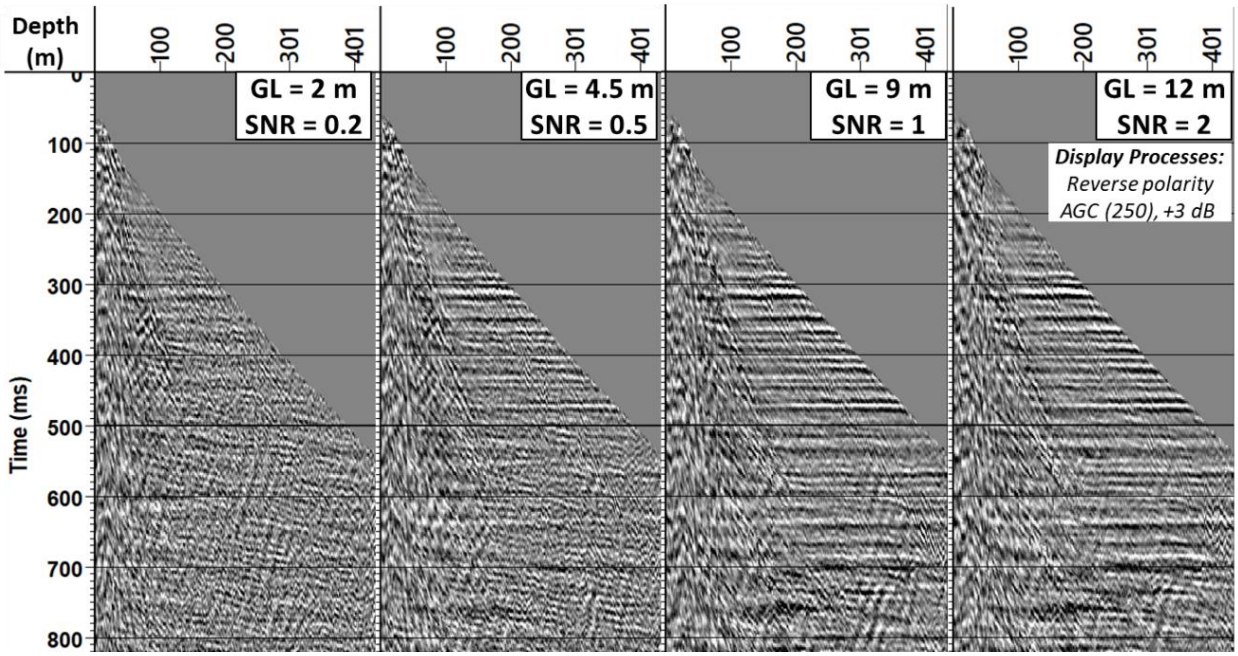

Figure 2.16: Vibe source DAS ZVSP correlated shot gathers at various gauge lengths with respect to the final record in two-way time.

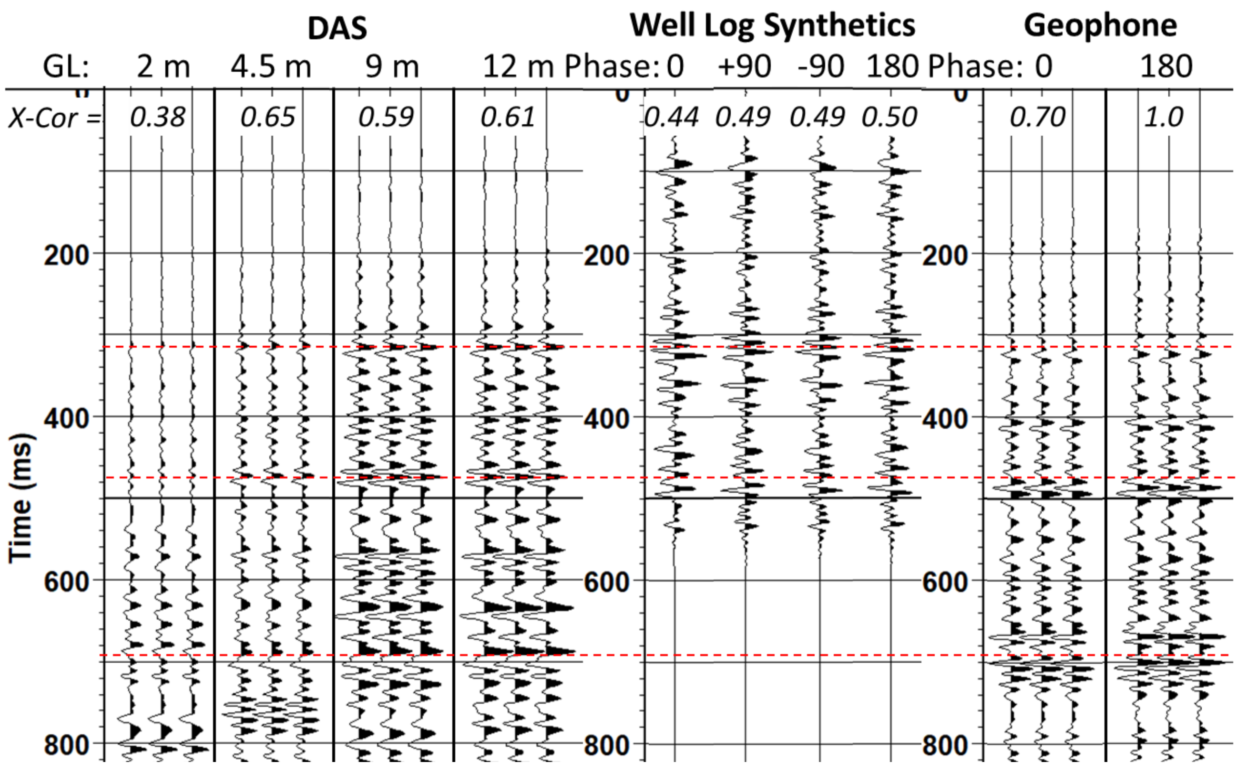

Figure 2.17: Corridor stack analysis of DAS and geophone results in comparison to well log synthetics. *Cross-correlation values for each trace in comparison to the 180-phase geophone trace are shown.*

Analysis:

First-breaks were picked based on the source type: the leading zero-crossing was picked in the AWD data; whereas, with the Vibroseis source, the peak amplitude was picked for positive SEG polarity data. The first-breaks provide the first product of VSP which is a time-to-depth curve, this is used to produce the second product which is a velocity profile. Figure 2.18 plots all first-breaks picked with respect to the various seismic sources and DAS gauge lengths. We find that there is a difference in the FBP (10 ms) with respect to the different sources due to the wavelet pick. Our second observation is that the DAS FBP matched better with a reverse polarity geophone FBP from the surface to around 200 m depth, but then transitioned to match a standard polarity geophone FBP. This effect is due to changes in the first-break wavelet phase that is seen in the data. The third observation is that with respect to different gauge lengths, a variation of ± 2 ms is seen. This is about the expected single-channel time pick error expected for our signal and noise values and a 100 Hz maximum frequency (Stewart, 1984).

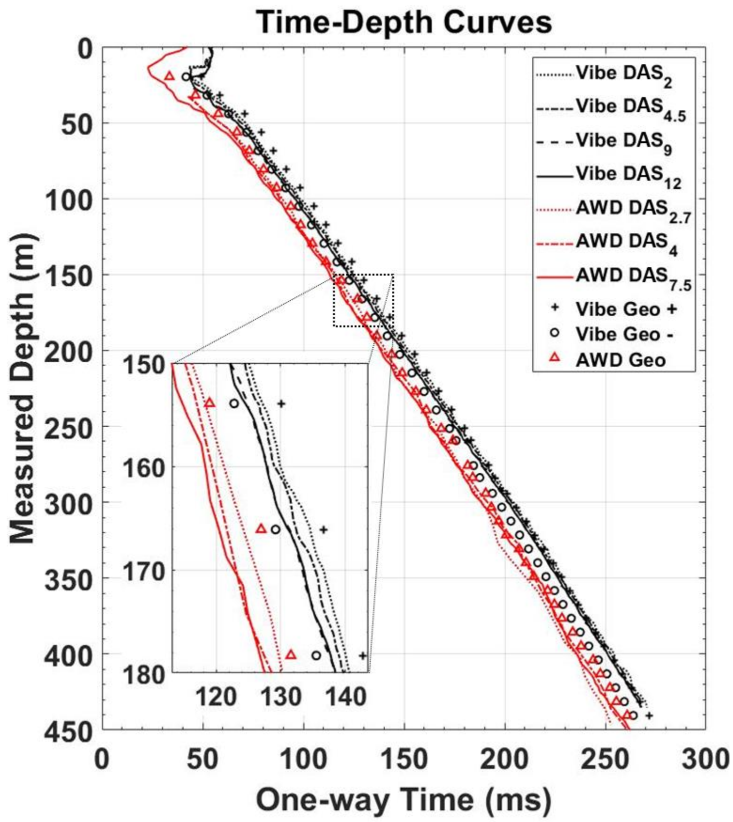

Figure 2.18: Time-to-depth curves analysis for Vibe data (black) and AWD data (red), comparing the results from geophones and DAS at various gauge lengths.

The FBP are used along with the trace spacing to compute interval velocities along the borehole. These calculations were done by the VISTA software and are presented in Figure 2.19, with regards to the AWD and Vibroseis seismic sources while comparing the geophone and DAS results at various gauge lengths. I find that the dense spatial sampling of DAS data with FBP errors yields an error of ±1500 m/s, which is reduced to ±100 m/s when spatially decimating the DAS data to the spatial sampling of the geophone measurements. Recall that the AWD data had been spatially decimated in the field to 2.7 m channel spacing while the Vibroseis data was left at 0.67 m channel spacing. That is why the AWD DAS results do not exhibit the same amount of error seen in the Vibroseis DAS results. I also find that the variation between the results of the DAS interval velocities at different GL is very minimal once decimated (±20 m/s).

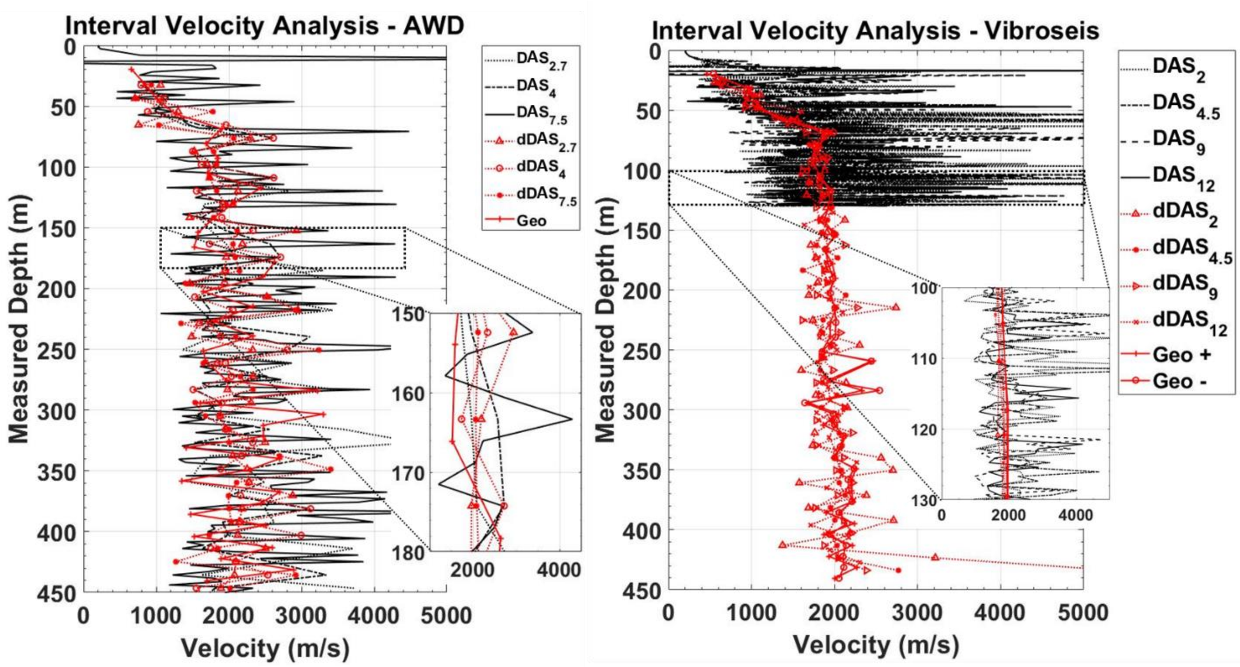

Figure 2.19: Interval velocity calculations for AWD data (left) and Vibroseis data (right).

We can see that the dense spatial sampling of DAS data results in ±1500 m/s of error, which is reduced to ±100 m/s when spatially decimating the DAS data to the spatial sampling of the geophone measurements.

Next, the RMS (root-mean-square) velocity is computed using the calculated interval velocities to produce a 1-D velocity profile along the borehole. Figure 2.20 illustrates the results of the RMS velocity analysis for both geophone and DAS data with respect to the AWD and Vibroseis sources. We observe a similar response with respect to the dense sampling of the DAS data, yielding a variation of 150 m/s between the DAS and geophone RMS Velocities. When spatially decimating the DAS data down to the geophone spatial resolution, we find that the results match up with a minimal variation of ±20 m/s. This is due to a cumulative error in the interval velocity calculations that were shown in Figure 2.19.

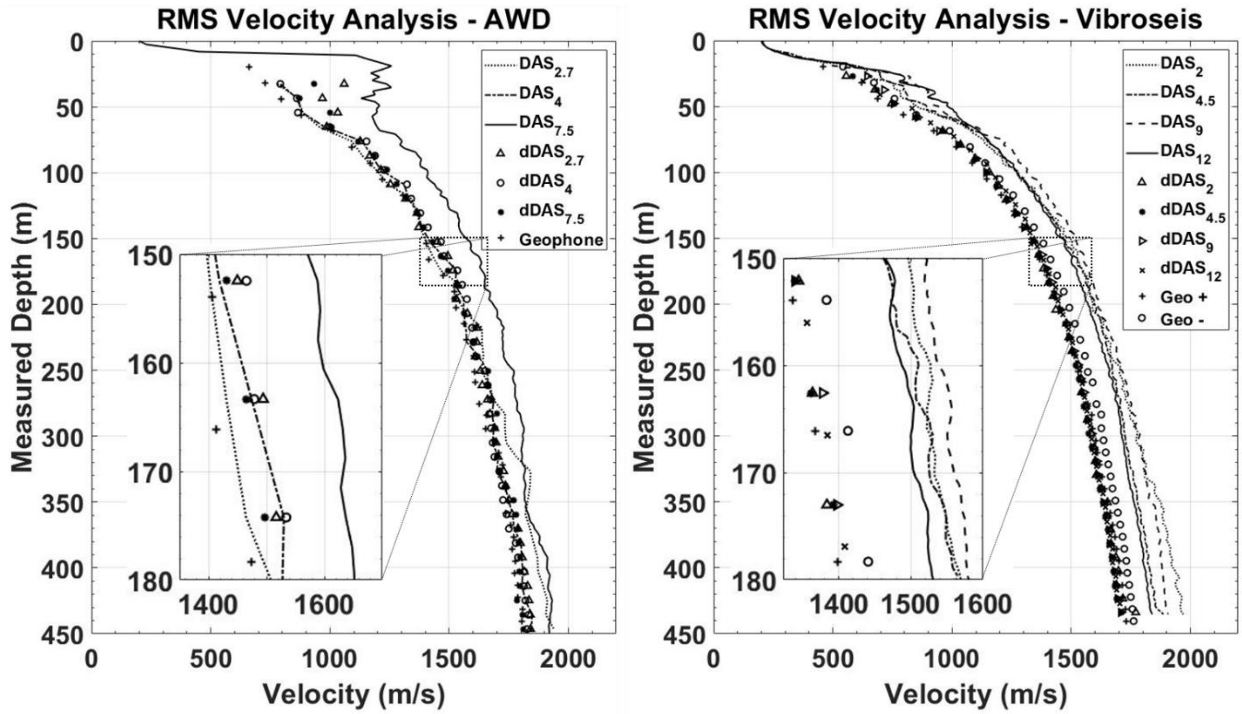

Figure 2.20: RMS velocity analysis of AWD (left) and Vibroseis (right), geophone and DAS, data. *Results show a variation between DAS and geophone results around 150 m/s that is due to the high spatial sampling of the DAS data. When decimating the DAS data spatial sampling down to the geophone spatial resolution, we find that the results match up with a minimal variation of ±20 m/s.*

Cheng et al. (2019) demonstrate the impact of channel decimation on DAS VSP data processing, concluding that the decimation of DAS data is necessary with consideration of an anti-alias filter. Additionally, considering that FBP error is at an order of ±1 ms (the recorded sample rate), the DAS receiver spacing is around 0.68 m, and the seismic source wavelength is at the order of 20 m, it is impossible to measure velocity variations at the DAS receiver spacing resolution. Thus, finding that the interval and RMS velocities are corrected by FBP decimation makes sense.

Conclusions:

In summary, a case study has been presented, evaluating the influence of seismic sources and optical parameters on DAS VSP in comparison to vertical geophone measurements. The study's findings show that AWD was not favorable to the quality of the data for both geophone and DAS measurements, requiring a high fold (+20 SS) to produce acceptable data. While the Vibroseis data demonstrated significantly better data (SNR = 25) at lower fold (8 SS).

It has been demonstrated that optimizing the optical amplifier parameters increases the SNR. The results showed that a 4.5 m GL (which corresponds to a quarter of our seismic wavelength) produced the highest correlation to geophone measurements (0.65) at corridor stack, and the highest SNR (25) with respect to the initial shot-gather. When comparing the VSP results from the various data I found that the DAS data exhibited variation in FBP with respect to the geophone polarity. The study also shows that the high spatial sampling of DAS data results in large errors in the interval and RMS velocities, which was overcome by decimating the data to the geophone array spatial resolution.

It is necessary to develop a more accurate method of interpreting the wellhead location along the fiber in the field, and recommend such a test be done at the smallest possible gauge length to achieve the highest accuracy in picking the wellhead location. Additionally, pre-processing DAS data is time-consuming and can be avoided by properly populating data headers. In conclusion, DAS technology is shown to be very promising although accompanied by some of its own challenges.

2.2. FBGs and Borehole Seismic Imaging:

A field trial test was conducted at the University of Houston Coastal Center (UHCC) in La Marque, Texas. Testing the feasibility of using an array of FBG sensors for borehole seismic imaging via zero-offset VSP. A hydrophone system was also used to benchmark the FBG measurements. This section will discuss the field setup, results, and lessons learned from this experiment.

Field setup:

The FBG recording system consisted of an FBG interrogator (FAZ Technology FBGS Interrogator), an array of five FBG sensors in a plastic-hardened single-mode fiber, a 10-meter single-mode telecommunication fiber extension cable, a field laptop, a 12-volt battery and an inverter for power supply. The hydrophone recording system consisted of a seismic recorder (Geometrics Stratavisor), a hydrophone array, a hydrophone power supply, and a 12-volt battery to power the seismic recorder. A 10-pound sledgehammer with a steel baseplate was used as the source mechanism. Figure 2.21 highlights the field setup, showing the fiber deployment arm (Figure 2.21a), the FBG recording system (Figure 2.21b), the hydrophone array (Figure 2.21c), and the hydrophone recording system (Figure 2.21d).

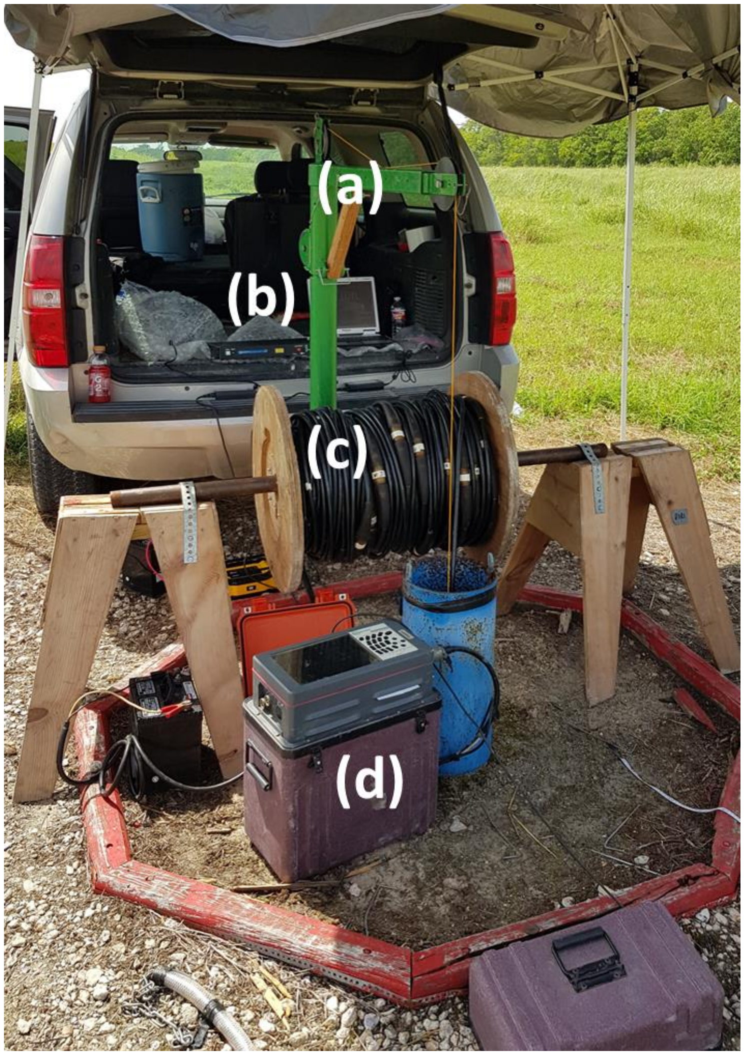

Figure 2.21: Picture of the field setup showing (a) the fiber deployment arm, (b) the FBG recording system, (c) the hydrophone array, and (d) the hydrophone recording system.

A zero-offset survey design was considered, with the source offset 5 meters east of the wellhead. Four hydrophones were deployed to a depth of 16 meters, with a receiver spacing of 4 meters. Five FBGs were deployed to the same depth, however, the FBG receiver spacing is 85 cm. Two fiber-deployments were tested, the first was by attaching a weight to the end of the fiber to weigh the fiber down and ensure contact with the casing. The second deployment setting was by attaching the fiber to the hydrophone cable.

The well was found to be dry, and attempts to fill the well with water were unsuccessful. Due to the limited fiber length and the well condition, the sensors were left in the shallow part of the well that is air-filled. Therefore, we do not expect the sensors to receive any waves through the earth, rather the expect wave is an air blast wave.

Results:

With respect to the first deployment where the FBG fiber was weighed down by a weight attached to the fiber, the results confirm the expected air-blast being received by both hydrophone and FBG sensors (Figure 2.22). The apparent velocity of the direct arrival on the hydrophone data is 342 m/s, while the apparent velocity of the direct arrival on the FBG data is 340 m/s. The hydrophone data shows multiple rounds of the event traveling down and up the borehole, while the FBG data only shows one direct arrival event.

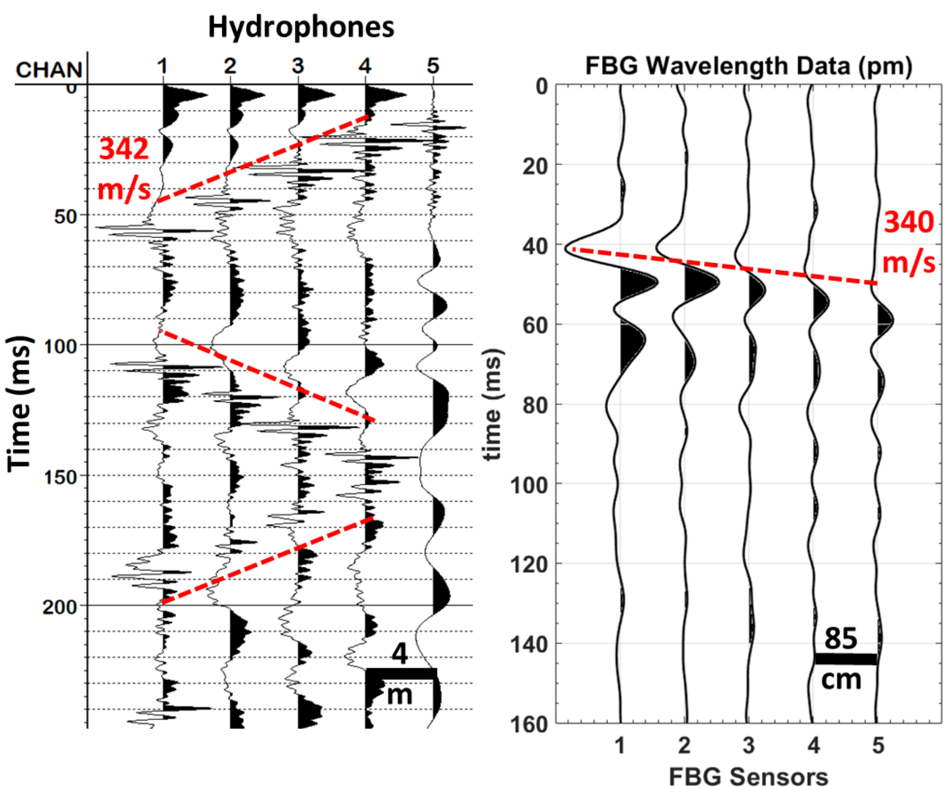

Figure 2.22: ZVSP hydrophone (left) and FBG (right) results with the observed annotated with their apparent velocity. The interpreted event is an air-blast wave with a velocity of 340 m/s.

Both hydrophone and FBG data exhibited high-frequency noise that was processed by applying frequency filters on the data. A band-pass filter of (5-10-500-600) was applied to the hydrophone data presented in Figure 2.22. While the FBG data has a 200 Hz high-cut filter applied to remove high-frequency noise generated by the instrument. Thus, the discrepancy in the visible frequency content of the data is noted. Hydrophone frequency analysis shows a peak frequency response at 1850 Hz, 300 Hz, and 30 Hz (Figure 2.23), while the FBG data shows a peak at 30 Hz and was not sampled high enough to capture the higher frequencies seen by the hydrophone (Figure 2.24).

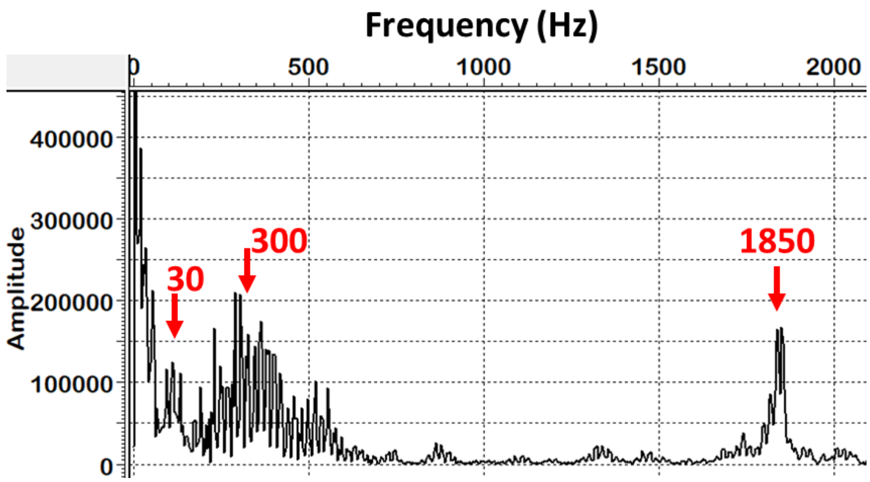

Figure 2.23: Hydrophone raw data frequency spectrum.

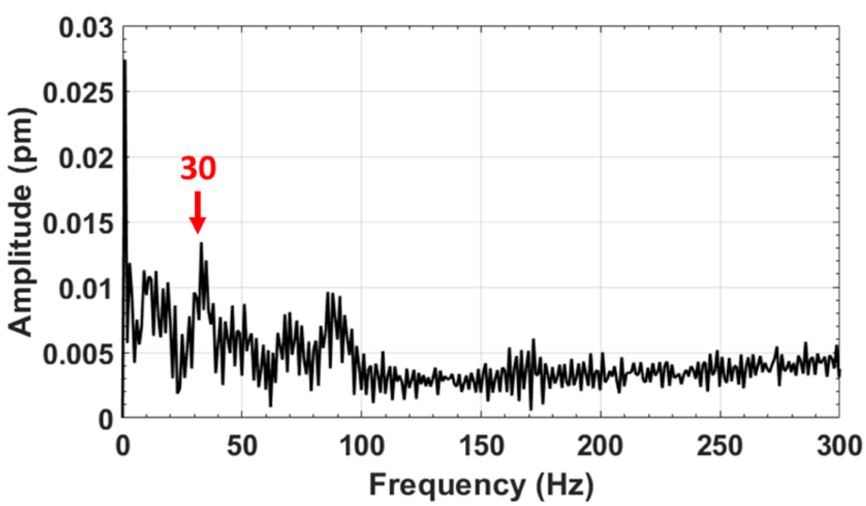

Figure 2.24: FBG raw data frequency spectrum.

The second test setup with the fiber attached to the hydrophone cable didn’t show any results for the FBGs. In this setup it is difficult to ensure contact between the fiber and the borehole, therefore, the FBGs were probably not in contact with the borehole, thus unable to sense any waves.

Lessons Learned:

This field trial demonstrated that the use of FBGs for VSP is feasible, but proper deployment of the fiber is necessary. Additionally, the FBG recording system is not equipped with an external trigger, thus recording is set manually and the recording zero-time is left uncertain. Possible consideration for future acquisition with this system is using GPS time to synchronize the source shooting and receiver recording times. In conclusion, we successfully demonstrate that the FBG is capable of measuring seismic waves even in poor coupling conditions.

CHAPTER III

TESTING SURFACE APPLICATIONS OF FOMS

Many have considered applications of DAS for surface fibers over the past years (Martin et al., 2017; Bakulin et al., 2017; Smith et al., 2019). The Stanford DAS array project uses a horizontal DAS fiber array deployed in telecommunication fiber-optic network conduits, giving examples of earthquake detection, near-surface monitoring, ambient noise interferometry, and passive and active seismic monitoring (Biondi et al., 2017; Martin and Biondi, 2017; Fang et al., 2018; Martin and Biondi, 2018).

This chapter considers applications of fiber-optic motion sensing (FOMS) using fiber in a unique surface geometry (Bakulin et al., 2017a). I use the data for surface wave analysis employing an MASW (Multichannel Analysis of Surface Waves) approach, similar to work done by Cole and Karrenbach (2019). Additionally, I demonstrate an application to urban infrastructure monitoring via DAS on telecommunication fibers in an existing telecommunication fiber-optic network. I conclude with a field trial of surface seismic imaging using FBGs.

3.1. DAS and Surface Seismic Imaging

Bakulin et al. (2017; 2018) demonstrate an application of DAS for surface seismic imaging using a “Smart DAS” geometry. The geometry consists of a single fiber-optic cable trenched at the surface, connecting several shallow upholes (50-150 m deep) (Figure 3.1). Data from their survey is used in this chapter, analyzing and interpreting the raw data (shot-gathers). Then, I test surface wave suppression techniques, comparing a conventional approach using f-k filters to a novel data-driven method of surface-wave removal based on nonlinear signal comparison (Zheng and Hu, 2017; Hu et al., 2019; Hu and Zheng, 2019).

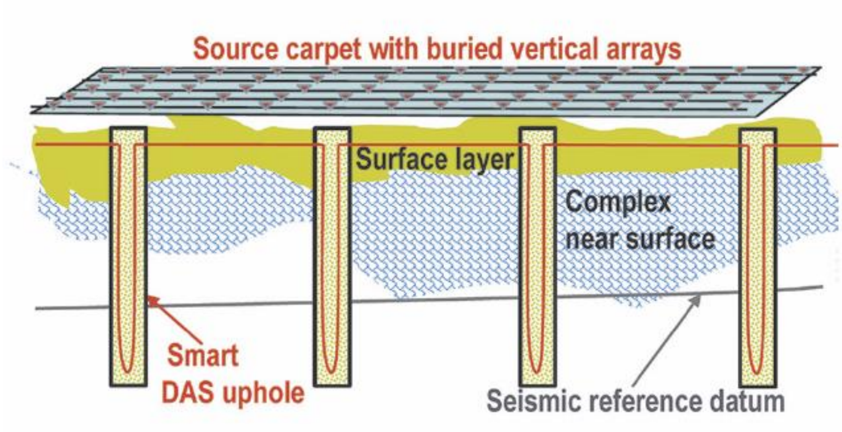

Figure 3.1: Schematic of the Smart DAS fiber geometry from Bakulin et al. (2017a).

3.1.1. "Smart DAS" Data Analysis

Bakulin et al. (2017a) demonstrate the capabilities of generating a 2D seismic image using the vertical segments of the Smart DAS array in comparison to a legacy geophone 2D seismic line (Figure 3.2). I take into consideration the target formation highlighted around 800 ms when processing the horizontal segments of the Smart DAS array. Willis et al. (2016) note the broadside insensitivity of DAS. Hornman (2017) attempts to overcome this limitation by using helically wound fiber to provide a broadside sensitive fiber-optic cable. Given that the Smart DAS array was not a helically wound fiber, the broadside insensitivity will be taken into consideration.

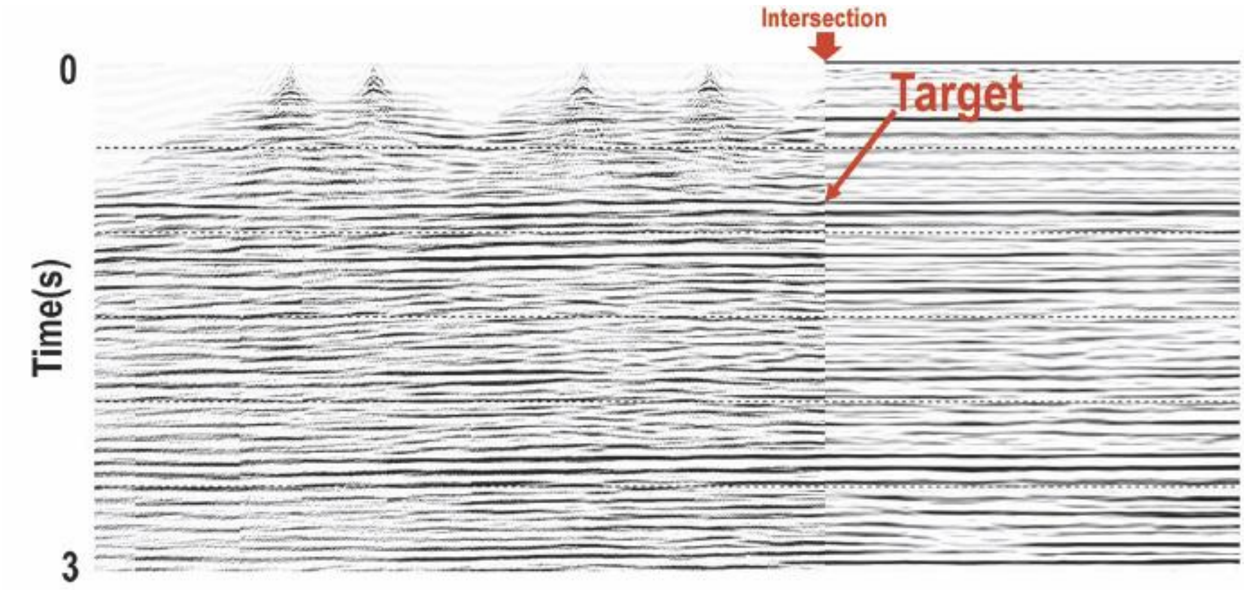

Figure 3.2: 2D Seismic image constructed using the vertical Smart DAS arrays (left) in comparison to a legacy geophone 2D seismic section from Bakulin et al. (2017a).
The target formation is highlighted above around 800 ms.

Survey Parameters

The horizontal segments of the Smart DAS array are stitched together to form a surface 2D line. This is the data that is shared for processing and analysis. The provided data has a 2 ms time sampling rate with a record length of 4 s, 823 live receiver channels in a fixed spread, and three Vibroseis shot lines summed with a linear sweep from 8 to 80 Hz. The summed shot line has a 10 m shot spacing and the receiver line has a 4 m channel spacing (note that the DAS data was acquired with a 7 m gauge length). Figure 3.3 highlights the shot (red dots) and receiver (green dots) geometry and the common mid-point (CMP) fold map.

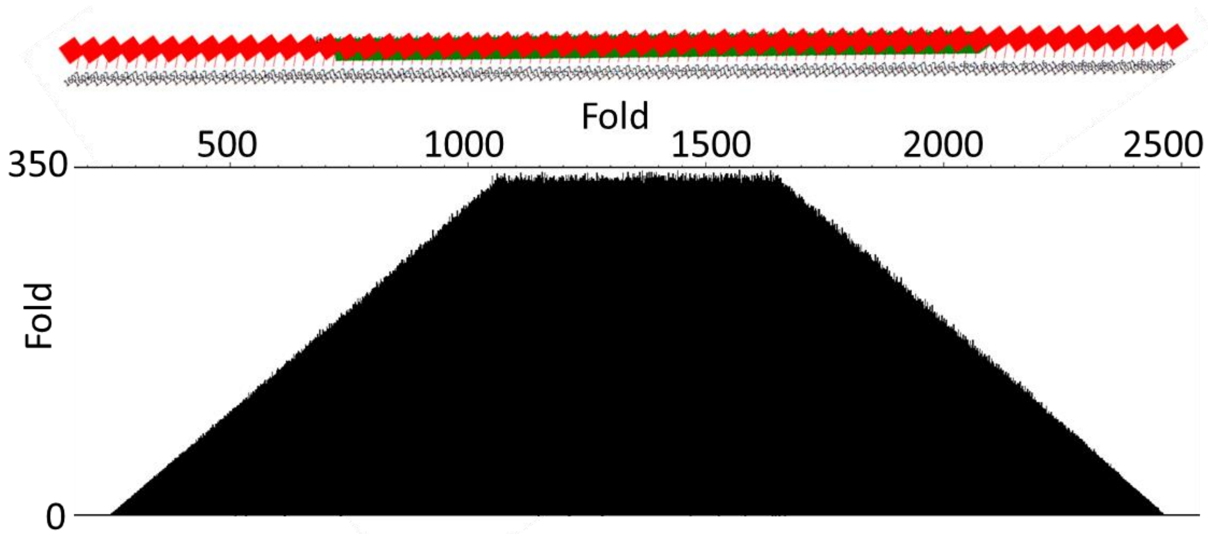

Figure 3.3: Shot-receiver geometry (top) and fold map (bottom) for the horizontal Smart DAS array.
With shot locations in red and receiver locations in green.

Raw Data Analysis

The behavior of the horizontal DAS fiber is expected to be similar to a horizontal geophone. Thus, the possibility of converted wave (P-S) reflections is considered. Upon investigation of the correlated shot gathers in the time domain (Figure 3.4) one possible reflection is evident in the record (around 1 s) with an apparent velocity of 800 m/s. This event is buried beneath the dispersive surface waves. The record shows evidence of both compressional (P) and shear (S) refractions that are annotated in Figure 3.4 as events (a) and (b) respectively. The apparent velocity of these events are around 4000 m/s and 1400 m/s respectively for the P and S wave refractions. Other visible events in the record include the surface waves (Figure 3.4d), with a velocity range between 250 m/s and 740 m/s, and the air-blast (Figure 3.4e), with a velocity around 350 m/s.

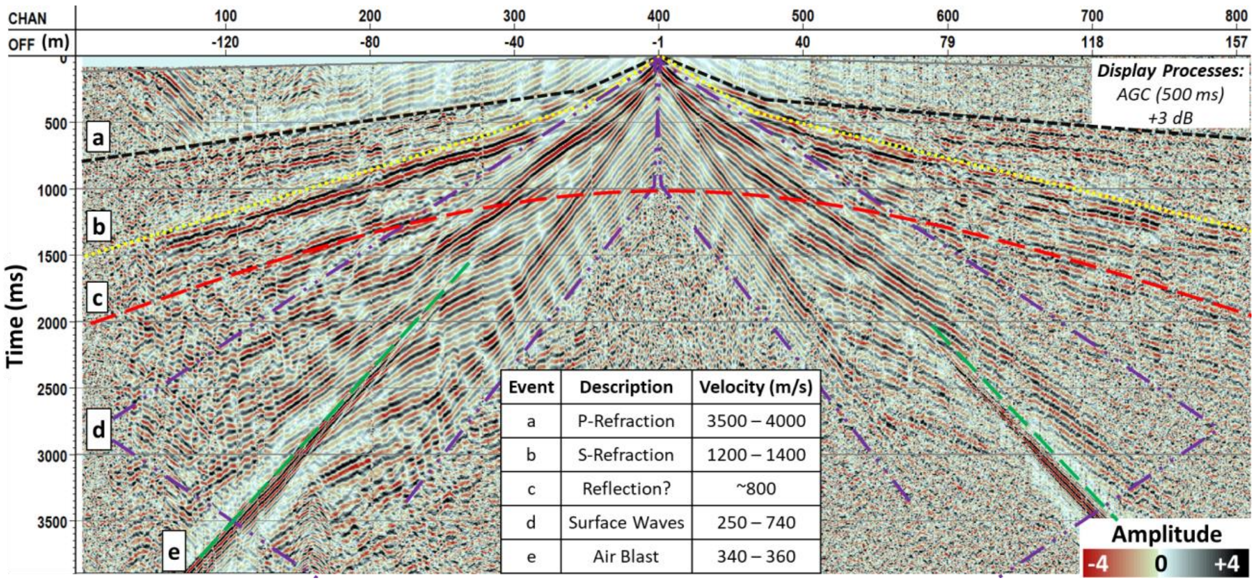

Figure 3.4: Correlated shot gather from the horizontal Smart DAS array with key seismic events annotated and described with their apparent velocities.

a) P-wave refraction (3500-4000 m/s) in dashed black line, b) S-wave refraction (1200-1400 m/s) in dotted yellow line, c) possible reflection (800 m/s) in dashed red line, d) dispersive surface waves (250-740 m/s) inside the purple polygon, and e) the air blast (340-360 m/s) in the dashed green line.

Next, the data is viewed in the receiver and common mid-point CMP domains looking for evidence of reflections (hyperbolic events). Figure 3.5 is a receiver gather for channel 400 with the average frequency spectra displayed. Similarly, Figure 3.6 is a CMP gather in the middle of the spread. Both gathers show the same events that were interpreted in the shot domain but show no obvious reflections. Therefore, surface-wave suppression is considered, in hopes that if any reflection events are hidden in the data beneath the surface waves then they may be evident after removing the surface waves.

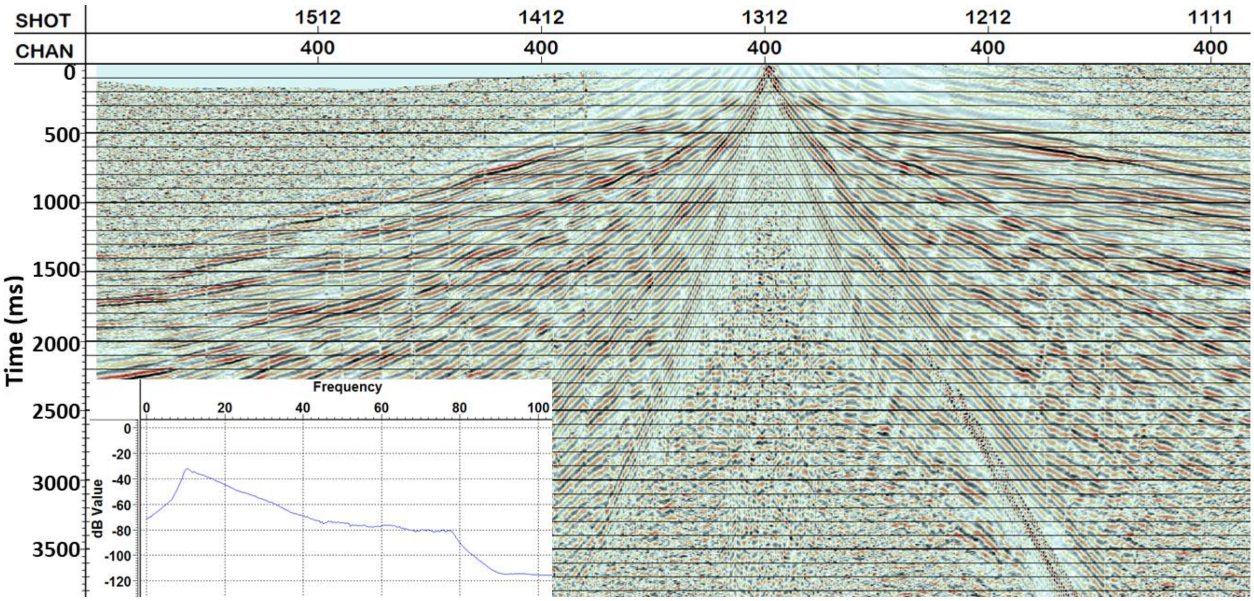

Figure 3.5: Data sorted in the receiver domain, showing the receiver gather for channel 400. No obvious reflections are observed.

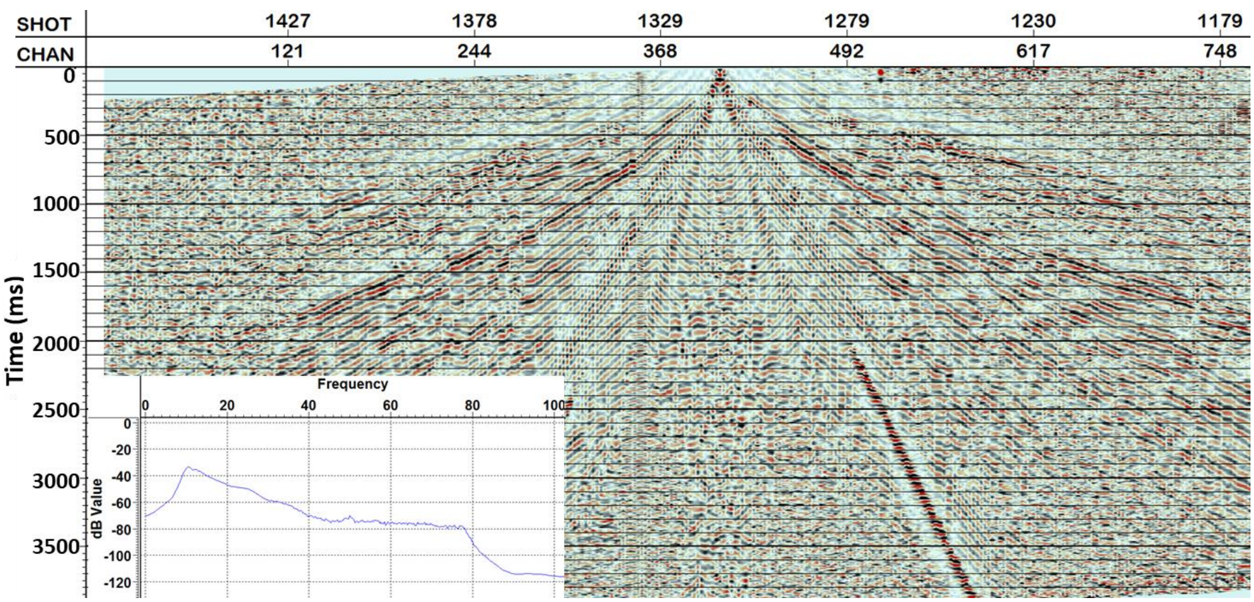

Figure 3.6: Data sorted in the CMP domain, showing the CMP gather in the middle of the spread. No obvious reflections are observed.

3.1.2. Surface-Wave Suppression

Two approaches to suppressing the surface waves are considered. A conventional method of muting the surface waves in the frequency-wavenumber (f-k) domain is considered first. This is done by designing and applying an f-k filter. This method is fast and effective, however, some frequencies that might contain both signal and noise are sacrificed in the process. Additionally, this process is shown to produce artifacts in the data after processing. Therefore, this method is not favorable. Next, a novel method of surface wave suppression via data-driven nonlinear signal comparison (Zheng and Hu, 2017; Hu et al. 2019; Hu and Zheng, 2019) is considered, I will refer to this method as the Zheng-Hu method. This method predicts the surface waves via dispersion curves, then subtracts the predicted surface waves from the original data. This process does not produce any artifacts in the data and effectively suppresses the surface waves without sacrificing any signals that may lay beneath.

Figure 3.7 highlights the results of suppressing the surface wave via f-k filtering. In reference to the f-k filtered output data (Figure 3.7b), a few observations are made: 1) there are still remnants of the surface wave and the air blast, 2) there are no observable reflection events (hyperbolic events). In reference to the difference plot between the initial and filtered data (Figure 3.7c), the majority of the filtered data contains the surface waves along with the air blast, however, there is also energy that has been subtracted in other areas where there is no surface waves or air blast, thus introducing artifacts in the output data.

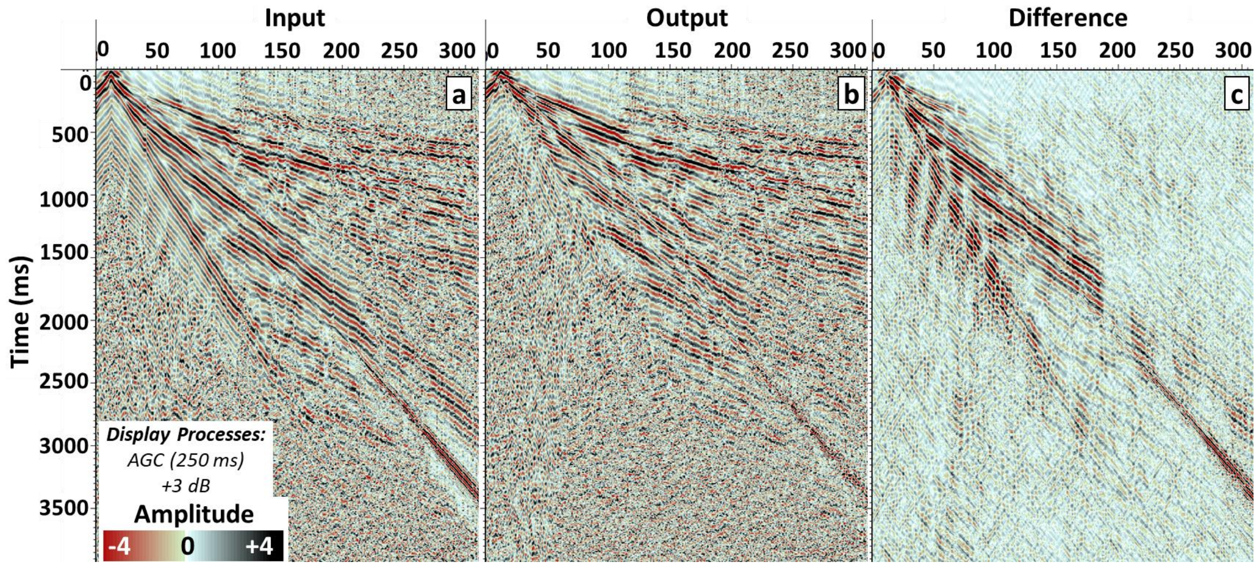

Figure 3.7: Processing results of surface wave suppression via f-k filtering (a) before, (b) after, and (c) the difference between the two datasets, surface waves and the air blast were muted in the f-k domain.

The dispersive nature of the surface waves is explored by plotting the data with respect to the phase velocity at different frequencies (Figure 3.8). The Zheng-Hu method uses the picked dispersion curves to predict and synthesize the surface waves then subtract them from the initial data. Figure 3.9 highlights the results of suppressing the surface waves using the Zheng-Hu method. The results after processing (Figure 3.9b) show an effective suppression of all surface waves including the air blast, and the predicted data (Figure 3.9c) shows that the surface waves were the only events that were suppressed, no artifacts seem to be produced. Inspecting the three datasets in the f-k domain (Figure 3.10) shows that the surface waves were effectively suppressed without sacrificing any other signals. In conclusion, surface waves were best suppressed using the Zheng-Hu method. In both cases no reflection events were observable, thus concluding that the proposed processing of the horizontal Smart DAS data for converted-wave imaging would be challenging at least.

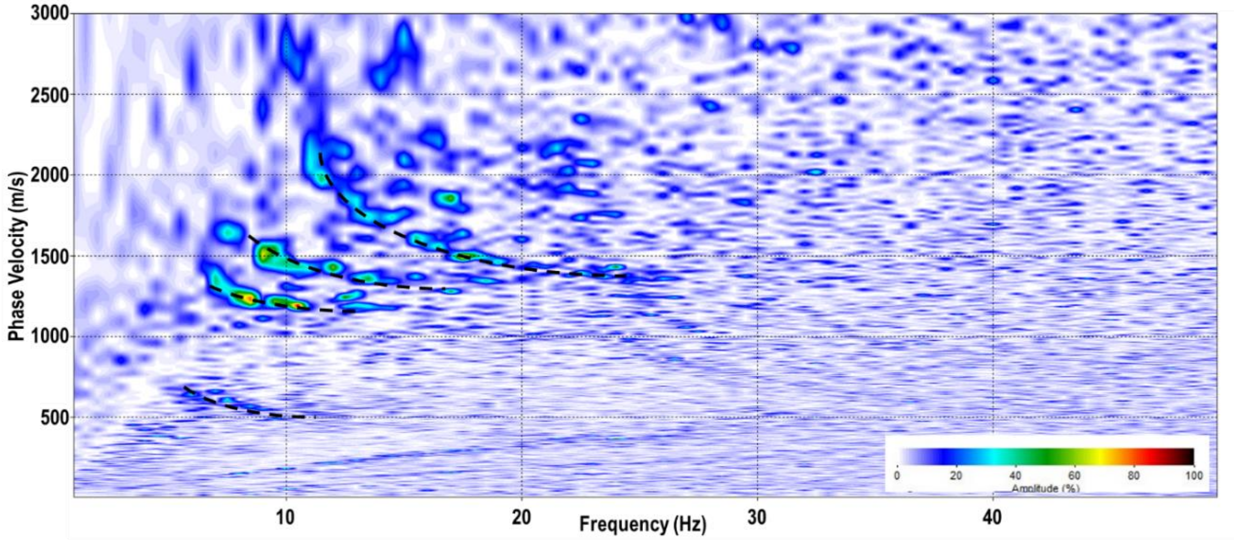

Figure 3.8: Dispersion curve analysis of Smart DAS horizontal surface wave data.

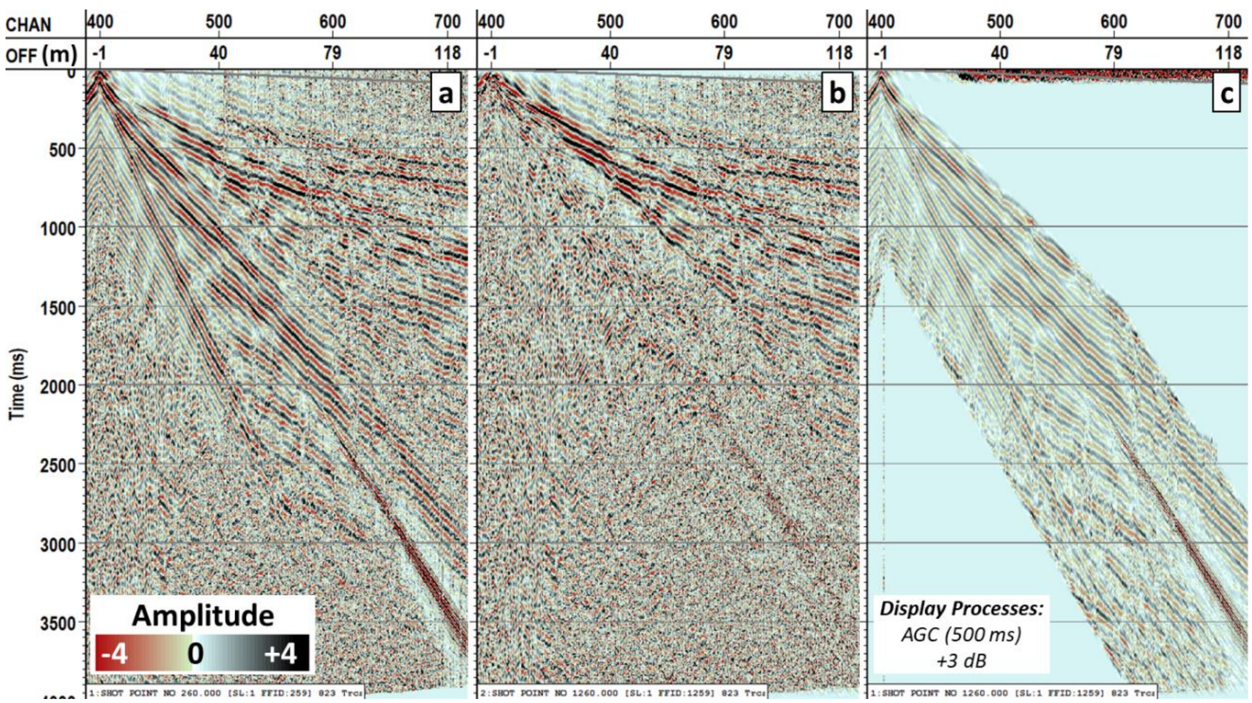

Figure 3.9: Processing results of surface wave suppression via the Zheng-Hu method (a) before, (b) after, and (c) the predicted surface waves that were subtracted.

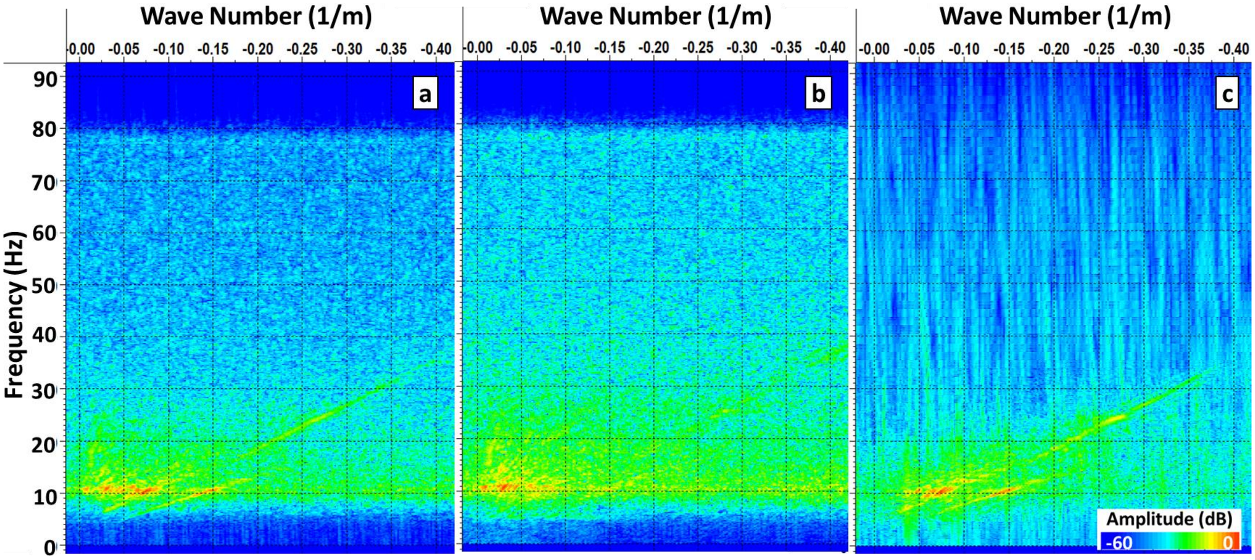

Figure 3.10: Results of the Zheng-Hu method in the f-k domain, showing data (a) before and (b) after the surface wave suppression, and (c) the predicted surface waves.

3.1.3. Multichannel Analysis of Surface Waves (MASW)

A novel application of Multichannel Analysis of Surface Waves (MASW) is considered in this section. Cole and Karrenbach (2019) have demonstrated the application of MASW on surface DAS data, showing that the DAS fiber was able to capture the dispersive surface wave, which was processed to produce a near-surface velocity model. This application is demonstrated on the horizontal Smart DAS data from the previous section.

Figure 3.11 is a schematic of the processing workflow that was used. Standard data pre-processing was applied, including a data quality check (QC), header edit, geometry reading and writing to the headers, killing bad traces, and sorting the data into shot, receiver, and CMP gathers. Next, special data conditioning (spatially decimating the data, applying an f-k filter and top and bottom mutes to enhance and isolate the surface waves) was necessary to provide the best signals for MASW. Then the data is converted from SEG-Y to the KGS (Kansas Geological Survey) format and loaded to the SurfSeis software. The field geometry is then encoded to the data and dispersion analysis is done. Once the dispersion curves have been picked, they are inverted to generate the final product of a near-surface shear velocity model.

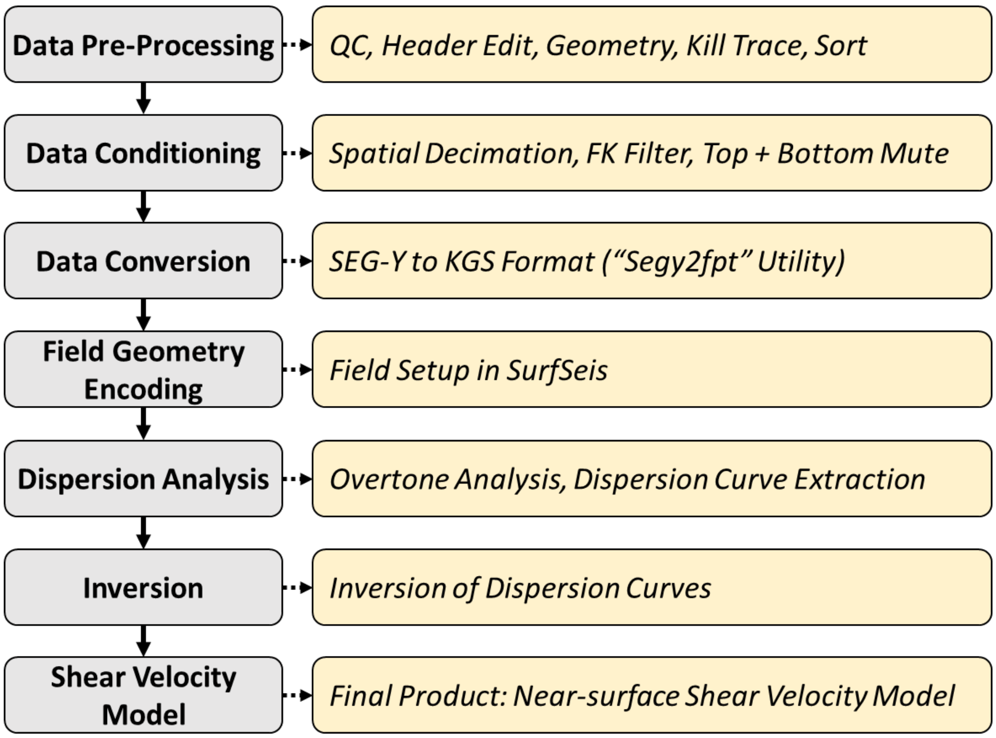

Figure 3.11: Schematic of MASW processing workflow

Ivanov et al. (2008) demonstrate the effect of source and receiver spacing on the dispersion curves. They show that the receiver spread length (L) should be proportional to the longest wavelength (λ_{max}) which is proportional to the maximum depth of investigation (D_{max}) (i.e. $L \sim \lambda_{max} \sim D_{max}$). While the receiver spacing (dx) is proportional to the shortest wavelength (λ_{min}) which is proportional to the minimum depth of investigation (D_{min}) (i.e. $dx \sim \lambda_{min} \sim D_{min}$). Noting that receiver spread lengths over 100 m and receiver spacing larger than 10 m increase the risk of higher mode dispersion curve domination. Therefore, the velocity model depth is bound by the receiver spread length and receiver spacing. In summary, the optimal geometry for MASW is a source offset of 5 m and a receiver spacing of 1 meter for a receiver spread length of 30m. Additionally, the recommended recording parameters are 1 ms time sampling rate and a 2 s record length, with long record lengths (≥5 s) discouraged for active MASW applications.

MASW processing was done using the KGS SurfSeis software, the software requires the shot spacing to be a multiple of the receiver spacing. Thus, spatial decimation of the Smart DAS data was necessary to get the shot and receiver spacing compliant with the software needs. Given that the shot spacing is 10 m and the receiver spacing is 4 m, the lowest common multiple is 20 m. Hence, the data was decimated to 20 m shot and receiver spacing. Therefore, given the discussion of the parameters in the last paragraph, higher-order dispersion curves are expected. Note that the time sampling is 2 ms for a record length of 4 s and a receiver spread of 2000 m, and the data was processed applying a top and bottom mute to isolate the surface waves, similar to what was done by Cole and Karrenbach (2019).

Figure 3.12 and Figure 3.13 are examples of dispersion curves picked on good and noisy data, respectively. The data quality is described by the continuity, coherency, and pick-ability of the dispersion curve. In Figure 3.12, the background noise is very minimal, the first-order dispersion curve is continuous and easy to pick, and a second-order dispersion curve is also evident. While in Figure 3.13 the background noise is very high, the first-order dispersion curve is not continuous, and there are multiple higher-order dispersion curves that are evident. These examples are given to help understand the source of RMS (root-mean-square) error in the final velocity model.

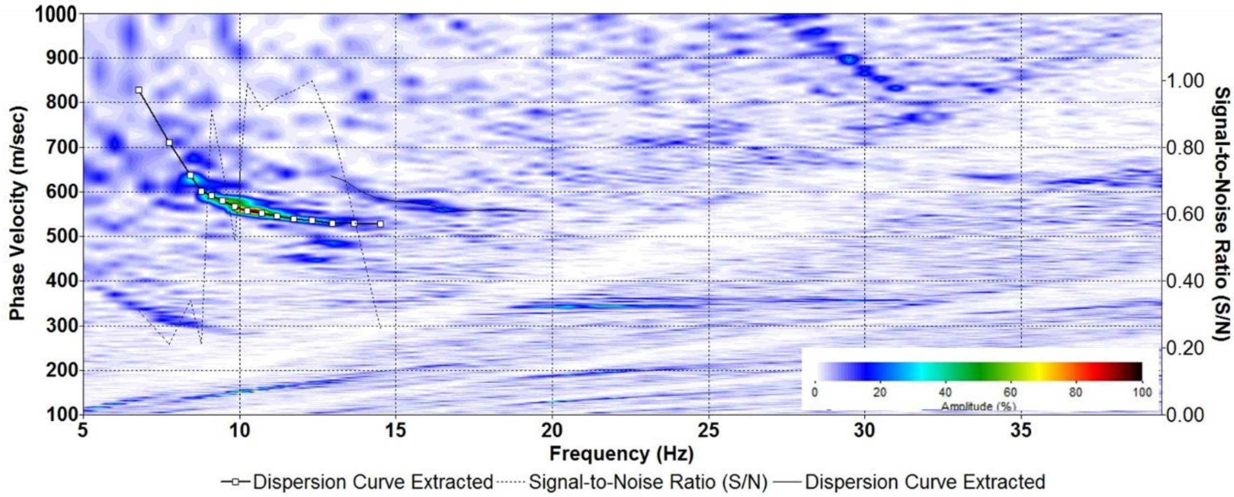

Figure 3.12: Example of good data dispersion curve analysis for Smart DAS decimated data. The first order dispersion curve is picked in line with the high-amplitude coherent signal.

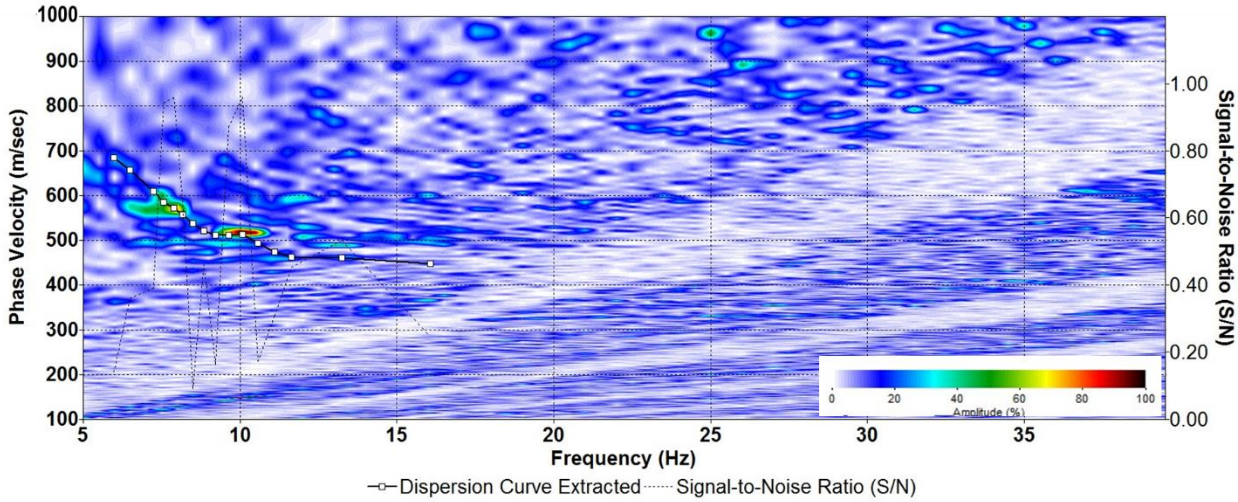

Figure 3.13: Example of noisy data dispersion curve analysis for Smart DAS decimated data. The first order dispersion curve is picked in line with the high-amplitude coherent signal.

The final MASW shear-wave velocity model is presented in Figure 3.14 along with the RMS error of the model. The model generally shows a velocity of 300-400 m/s up to a depth of 15 m, where it transitions to 500- 600 m/s between 15 and 30 m, then to 800-900 m/s between 30-40 m, and ends at a depth of 50 m with a maximum velocity of 1000 m/s, which correlates with values published by Bakulin et al. (2019) on similar analysis done on part of the Smart DAS fiber (Figure

3.15). The RMS error shows high error values at 200, 400, 550, 700, and 950 m surface locations that are due to poor picking from noisy dispersion curves as illustrated in Figure 3.13.

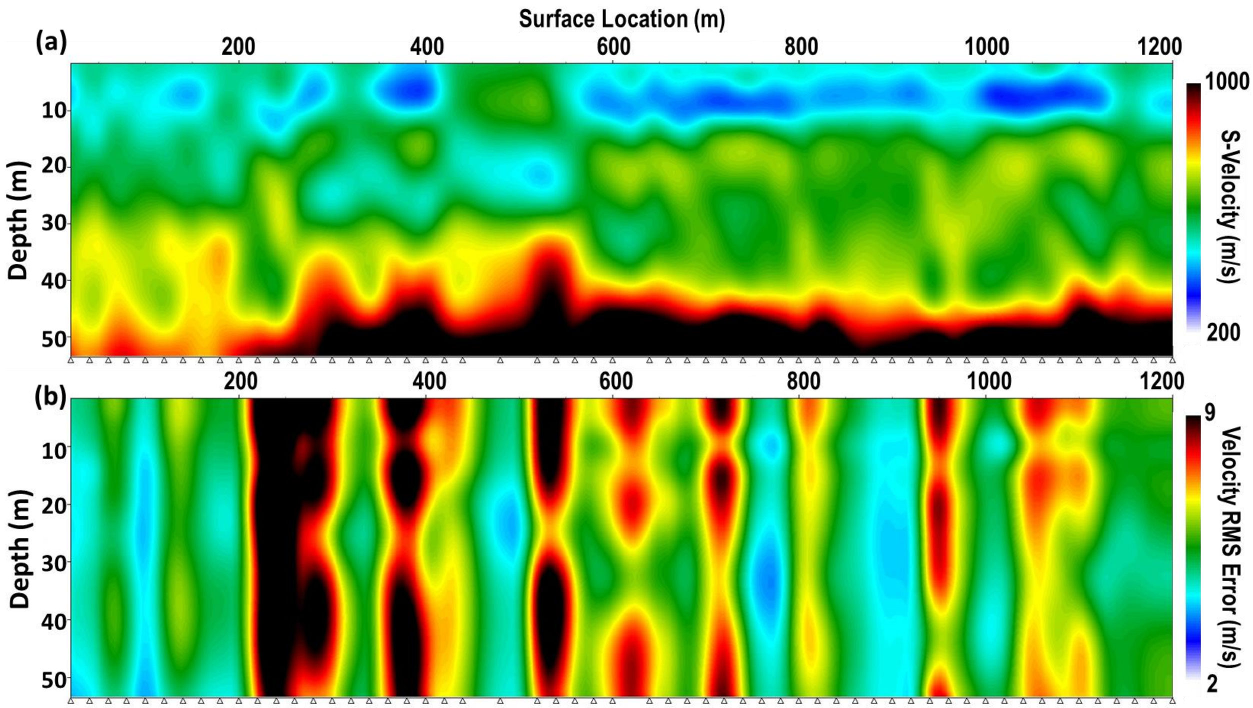

Figure 3.14: Final MASW shear velocity model of the near-surface to a depth of 50 meters with respect to the Smart DAS horizontal data (top) and the corresponding RMS error in the model calculations (bottom).

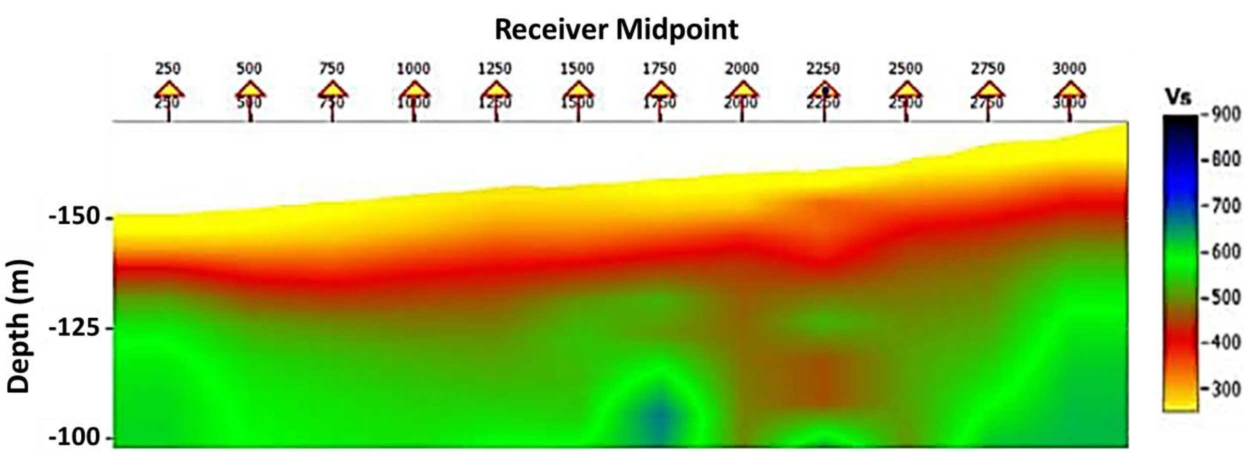

Figure 3.15: MASW shear velocity model edited from Bakulin et al. (2019) for a section of the Smart DAS survey.

3.2. Urban Infrastructure Monitoring

This section addresses preliminary DAS applications to urban infrastructure monitoring motivated by the work done at Stanford (Biondi et al., 2017; Martin et al., 2017; Martin and Biondi, 2017; Fang et al., 2018; Martin and Biondi, 2018) as well as work demonstrated by industry on the use of existing telecommunication fiber networks for sensing (Williams, 2017). The University of Houston (UH) has allocated fibers in their fiber-optic network for research purposes, such that those fibers are unused for communication, they refer to them as "Dark Fiber". The first test was conducted on a stretch of dark fiber that runs from the Philip Guthrie Hoffman Hall (PGH) to the Energy Research Park (ERP) through a substation on the UH campus (Figure 3.16). The substation is a control room where all fibers terminate, it is used as a hub for routing fiber connections across the network. This fiber path was chosen for two main reasons, the first is that it runs by and beneath the train rails in cemented conduits, which would act as an excellent source of seismic energy and has excellent coupling. The second reason is the limited number of substations and jumper cable connections, which is important because increasing fiber connections along the fiber path will degrade the optical signal and introduce optical reflections that harm the interrogation process.

Figure 3.16: Google maps satellite image with the "Dark Fiber" route annotated, with the first segment from PGH to the substation (red) then from the substation to ERP (green).
The red fiber passes beneath the train rails in cemented conduits.

The fiber was interrogated at PGH while looping the fiber at ERP such that a round trip of fiber was interrogated. Figure 3.17 shows the results of the raw optical backscatter, we see a large reflection generated at each location and little backscatter in between. The observed reflections are generated by the telecommunication fiber connectors. Fiber-optic sensing cables are typically terminated with an Angle Polished Connector (or Physical Contact) (APC), whereas telecommunication fibers are typically terminated with Ultra Polished Connectors (or Physical Contact) (UPC). Crawford (2014) presents a technical comparison between APC and UPC connectors. For sensing applications, UPC is not favorable as the reflected interrogation pulse oversaturates the digitizer, blinding the system from seeing any backscatter energy from the fiber. Therefore, the next test was done at the substation where a minimal reflection was visible, and the longer fiber run towards PGH was interrogated.

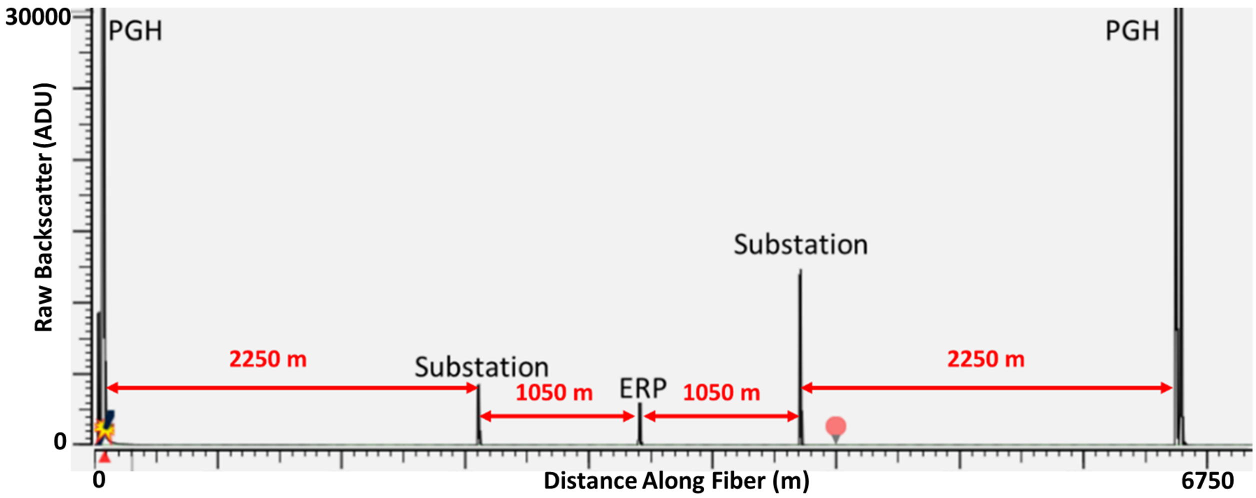

Figure 3.17: Raw optical backscatter of Dark Fiber interrogated from PGH through the Substation to ERP and looped back.

When interrogating from the substation to PGH, some backscatter signals were observed, even though the connector reflections were still visible (Figure 3.18). Unfortunately, the raw backscatter signal was not enough for phase measurements. Upon investigating the acoustic measurements (Figure 3.19), evidence of acoustic signals generated by activity on the train rail was observed. These signals correlated with the presence of a moving train on the rails. The width of the signal (180 m) correlated with the amount of fiber crossing beneath the train rails, the move out of the signal correlated (~ 17 m/s or 38 mph) correlated with the regulated speed limit on the rails (40 mph), and the absence of signal correlated with no activity (no visible trains) on the rails. Other observations were seen with regard to constant coherent signals that are constant through time at a specific location along the fiber. Some of these signals were associated with the connector (Figure 3.19a) while others were unexplainable (Figure 19d).

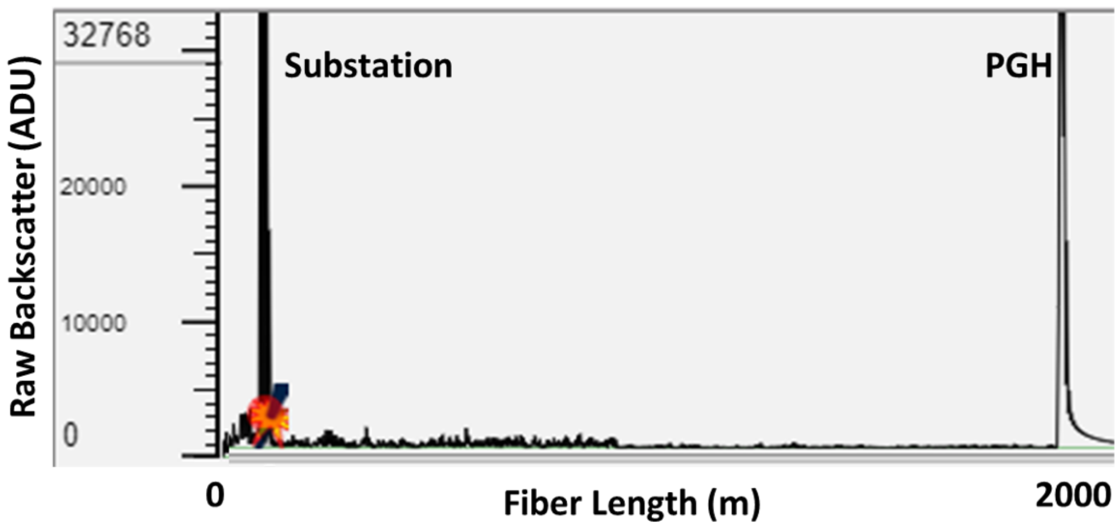

Figure 3.18: Raw optical backscatter of Dark Fiber interrogated from the Substation to PGH.

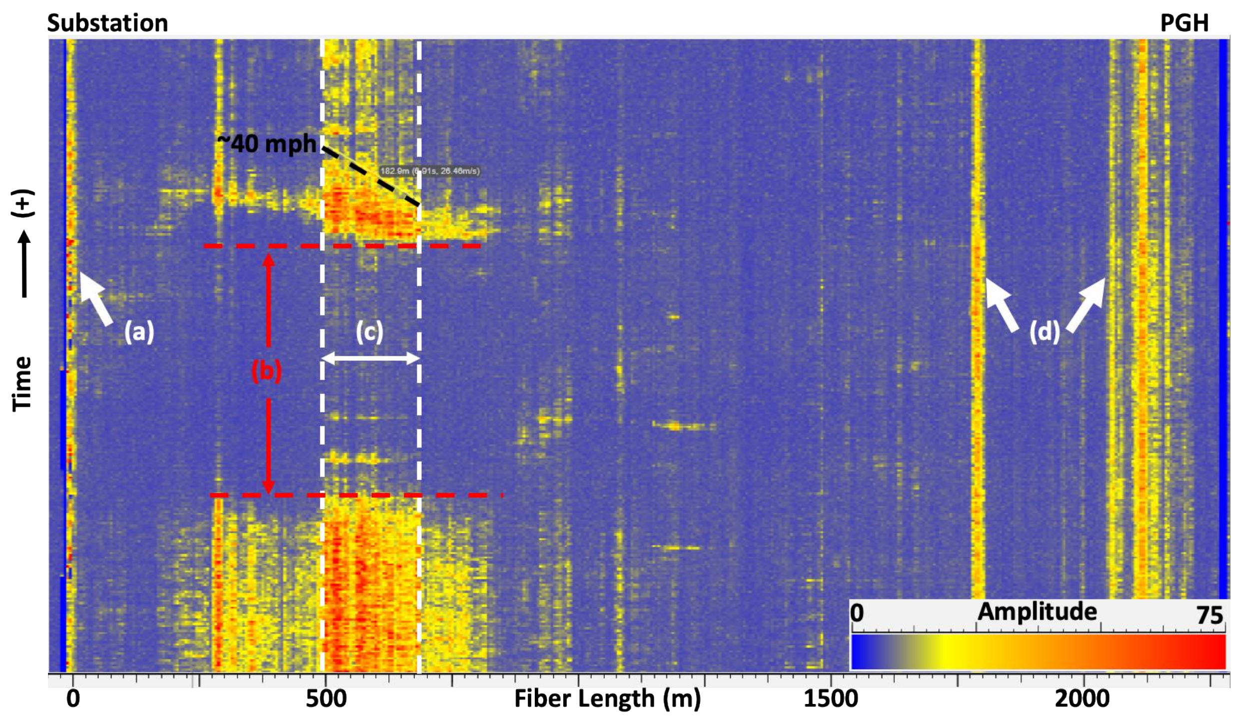

Figure 3.19: Acoustic waterfall display of Substation-to-PGH Dark Fiber.

(a) Noise generated by the large reflection in the backscatter domain, (b) time with no train signal, (c) bounds of train signal around 180 m, and (d) coherent constant signal.

In conclusion, this test demonstrated the feasibility of using the UH telecommunication fiber with a DAS system for urban infrastructure monitoring. Noting that telecommunication fiber connectors make the interrogation process difficult. Thus, future applications would require considering methods to overcome the reflections by eliminating the telecommunication connectors or installing a Large Reflection Card (LRC) module on the interrogation system (Hayward, pers. comm., 2018).

3.3. <u>FBGs and Surface Seismic Imaging</u>

Next, an application of FBGs for surface seismic imaging is tested at the University of Houston Coastal Center in La Marque, Texas. An FBG array was deployed at the surface using wooden logs to help couple the fiber to the ground (Figure 3.19). The FBG array consists of 5 FBGs with an 85 cm receiver spacing. A 10-pound sledgehammer was used as the seismic source at an offset of 15 meters from the fiber end. The source was excited in a shear direction along the fiber direction. Results showed a direct shear wave arrival was measured, with an apparent velocity of 680 m/s (Figure 3.20), a velocity that correlates with a shear wave velocity in unconsolidated sediments. Thus, showing that the FBGs were able to measure a propagating seismic wave.

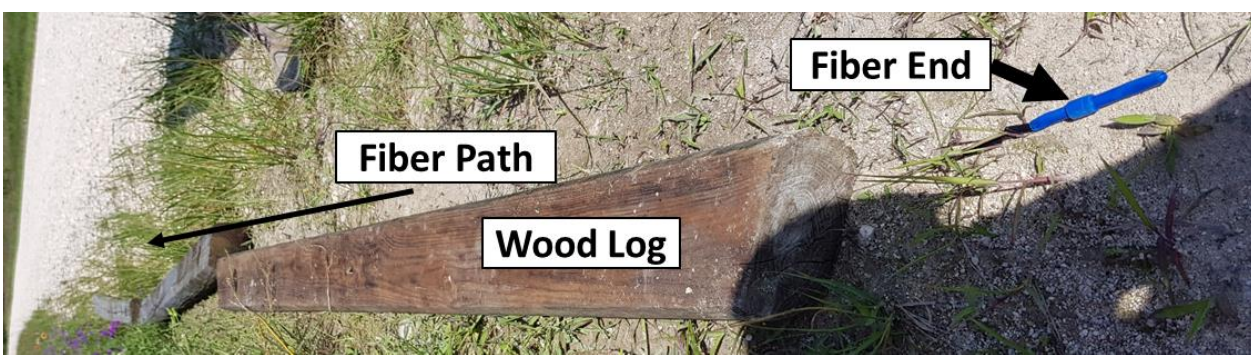

Figure 3.20: Photograph of the fiber deployment in the field. The fiber is deployed on the ground and wooden logs are placed on top to couple the FBG to the ground.

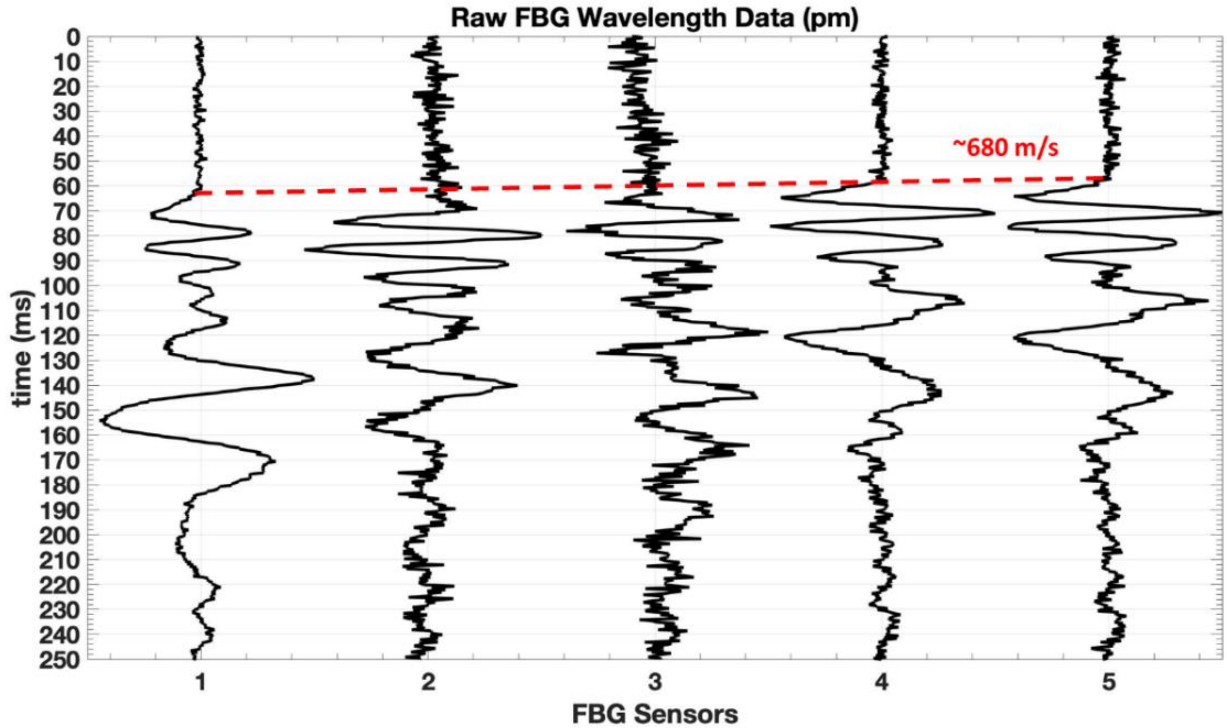

Figure 3.21: FBG results from shear source excitation. Apparent velocity is calculated to be 680 m/s.

Lessons Learned:

This experiment demonstrated the feasibility of using an FBG system for active source seismic sensing. However, there are many lessons learned that must be considered for future applications: 1) The FBG recording system (FAZ-T Interrogator) is not equipped with an external trigger mechanism to measure the source excitation time relative to the recording time. Thus, any acquisition with such system would require synchronized clock measurements to correlate the source excitation time with the sensor recording time. 2) The FBG deployment considered in this experiment was not optimal, optimal deployment would allow for better coupling of the fiber with the medium, either by trenching the fiber in the ground or burying it under sediments. 3) Ambient noise at the interrogator effects measurements, thus the interrogator must be shielded or isolated from the environment to limit ambient noise. 4) The FBG fiber is fragile, during this experiment the fiber broke due to some mishandling, although the used fiber was a plastic hardened fiber.

In conclusion, this chapter has demonstrated several applications of fiber-optic motion sensing using DAS and FBGs. Finding that the technology is mature and has excellent potential for such applications.

CHAPTER IV

APPLICATIONS OF FOMS IN A SIMULATED MARINE ENVIRONMENT

This chapter considers applications of fiber-optic motion sensing (FOMS) in a simulated marine environment, a setup that has been constructed at the Allied Geophysical Laboratories (AGL) at the University of Houston (UH). The laboratory experiments are motivated by several possible applications: pipeline flow assessment and integrity (Alfataierge et al., 2019a), marine seismic source characterization (Alfataierge et al., 2019b), and underwater communications (Alfataierge et al., 2018). Those tests are undertaken using a network of DAS and FBG fibers.

Figure 4.1 is a schematic diagram of the simulated marine environment setup. The setup consists of a flow line that starts at a water reservoir, then passes through a flowmeter and a multicomponent FBG station at the surface, then through a vertical pipe segment, and a horizontal pipe segment equipped with a leak valve, then ends at the main control valve. A series of FBG sensors are deployed on the pipelines and some are left free in the water. Around 30 m of single-mode DAS fiber is deployed on the tank floor as well as the pipelines. Additionally, a hydrophone array is deployed alongside the horizontal pipe segment and fixed to the vertical pipe segment.

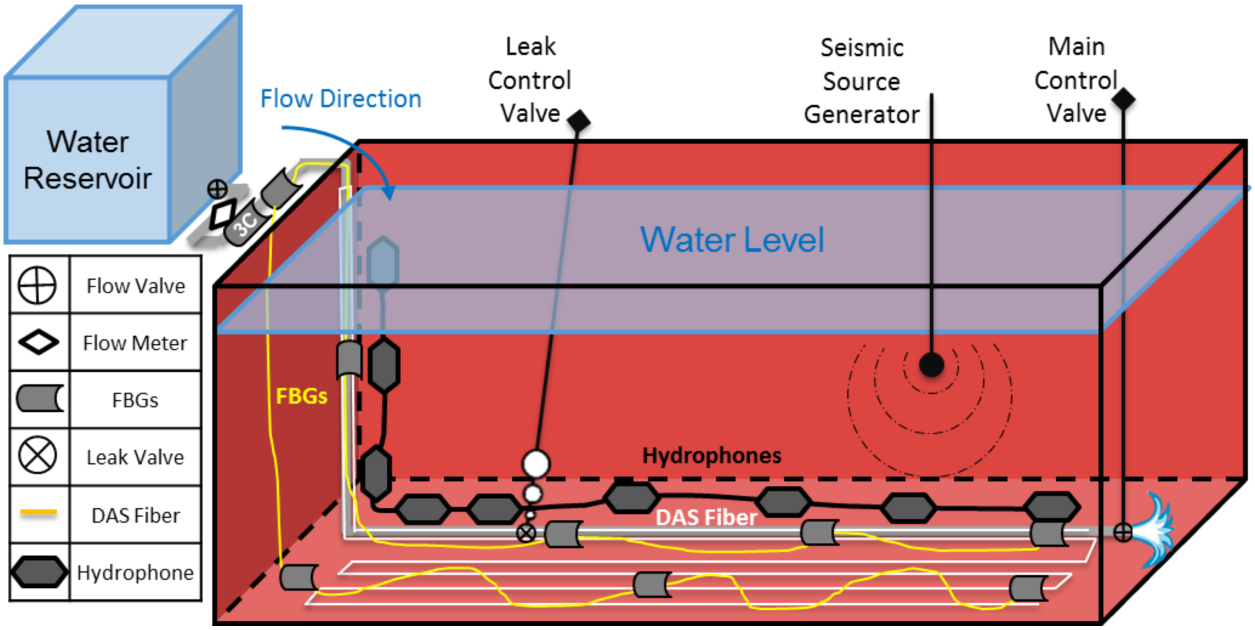

Figure 4.1: Simulated marine environment setup at AGL.
The setup consists of a flow line that starts at the water reservoir, passes through a flowmeter at the surface, then through a vertical pipe segment and a horizontal pipe segment equipped with a leak valve, and ends at the main control valve. A series of FBG sensors are deployed on the pipelines and some left free in the water, ~30 meters of DAS fiber is deployed on the tank floor and on the pipelines. Additionally, a hydrophone string is deployed alongside the horizontal pipe segment and fixed to the vertical pipe segment.

The setup is designed to simulate an offshore environment, where the vertical pipe would simulate a pipe from an offshore riser or facility to the ocean floor, and the horizontal pipe simulates a pipe on the seafloor or horizontal reach in a well. The horizontal pipe segment is equipped with a leak valve that can be controlled during experimentation to simulate a leak in the flow line. Figure 4.2 is a physical image of the schematic in Figure 4.1, annotating the various components of the setup.

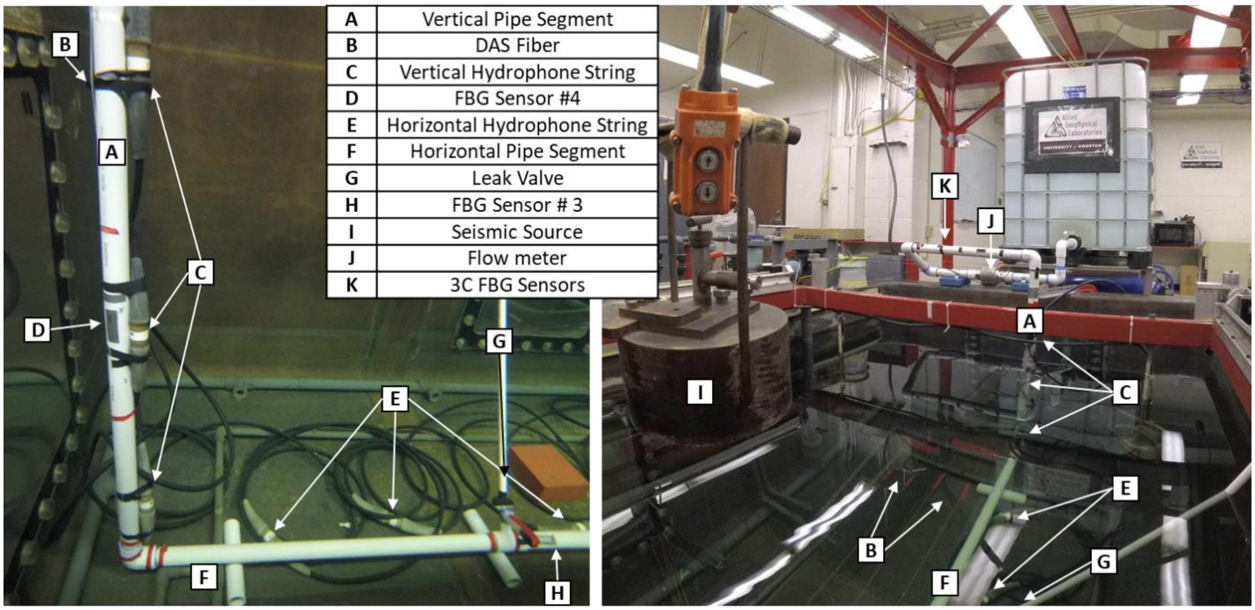

Figure 4.2: Annotated images of the simulated marine setup, below the water (left) and above (right).

4.1. Pipeline Flow Assessment and Integrity

The first application considered is flow assessment and integrity. This is an important topic in the oil and gas industry (Buck, 2017), and it becomes even more critical in offshore environments. By installing fiber on or near pipelines flow can be monitored (Somerville, 2012; Williams, 2012; Hayward & Fryer, 2018). DAS and FBGs are considered in this section, evaluating their abilities in measuring flow rates, detecting and locating leaks, determining flow and flow directionality.

Experiment setup

Two systems were used during this study, an amplitude base DAS system (Fotech Helios HSi) with single-mode telecommunication fiber, and an FBG system (FBGS FAZ-T Interrogator) with an array of FBG sensors in a single fiber. The DAS system outputs measurements in what is called a waterfall display. The waterfall display shows the activity along the fiber while recording in time.

The FBG system outputs measurements of wavelength that correspond to the nominal wavelength of each FBG. These measurements are used to establish a relationship between flow and flow rates. During the flow experiments, water flow starts at the water reservoir and is controlled through a flow valve. It then passes through the flow meter followed by a three-component FBG station, which consists of three FBG sensors that have been glued to the pipe in three orthogonal directions (X, Y, and Z), such that the X component corresponds to the axial component of the pipe and the Y and Z components correspond to the radial component of the pipe. Following the 3-C FBG station is a taped FBG (Sensor 5) oriented in the axial component of the pipe. These stations were analyzed to determine the effect of coupling and orientation on the measurements, which will be discussed in the results section. Next, flow is directed to a vertical pipe segment that transfers flow into a tank, the vertical pipe segment is connected to a horizontal pipe on the bottom of the tank equipped with a leak valve. Flow is expelled from the end of the horizontal pipe segment through a control valve.

Sensor deployment and installation

Three FBG sensors are installed along the horizontal pipe starting with Sensor 1 near the control valve, Sensor 3 near the leak valve, and Sensor 2 in between. Sensor 4 is installed on the vertical pipe segment, and Sensors 6, 7 and 8 are distributed on the tank floor without being fixed. The single-mode DAS fiber is laid out on the tank floor and then loops twice on the vertical and horizontal pipe segments.

FBG coupling and orientation were considered during sensor deployment. Appendix D summarizes the influence of coupling on FGBs, where we find that taping the FBG sensors rather than gluing them is enough for our experiments as the measurements were not compromised. With regard to orientation, we find that the FBGs responded two flow to primary directions (axial and radial). Figure 4.3 further validate these observations, showing a comparison between Sensor 5 (taped) and the X component (glued) with respect to one of the flow experiments. Additionally, Figure 4.3 shows the response of the Y and Z components (radial components) in comparison to the X component (axial component). The typical installation of FBGs is done by gluing the sensor to the pipes, which is a permanent installation. The possibility of temporary installation of the FBGs is tested by taping some of the sensors to the pipes and gluing some to compare the response.

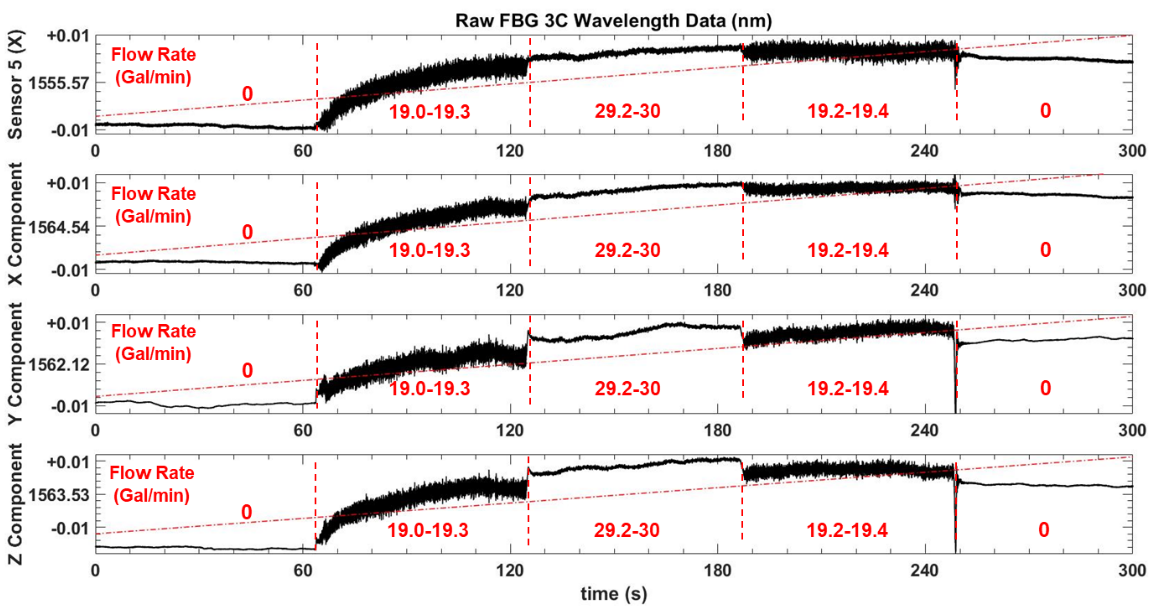

Figure 4.3: 3-C FBG response to flow experiment with flow rate range annotated (Alfataierge et al., 2019a).
Sensor 5 is taped to the pipe and corresponds to the X component of the 3-C FBG station which is glued to the pipe. The response between the glued and taped sensors is comparable. The radial components (Y and Z) respond differently than the axial component (X).

3-C FBG measurements

Figure 4.3 shows the response of the 3-C FBG station to flow test 1 with the average flow rate readings from the flowmeter annotated. The results show that the response of the axial component differs from the radial components, such that the radial components have higher sensitivity to mechanical noise produced by handling the control valve, which is seen at approximately 250 seconds when the flow is shut-in. However, the overall relative shift in the wavelength and fluctuations are comparable. Figure 4.4 is the results from flow test 2 with a different flow pattern, in this test the 3-C FBGs were taped rather than glued to the pipe, a longer flow time was used, and the control of flow was done via the control valve at the tail end of the pipe, whereas the previous test was done using the flow control valve located at the water reservoir. The results show higher mechanical noise produced by shutting in the flow that produces large DC shifts in the measurements that obscure the trend of the data.

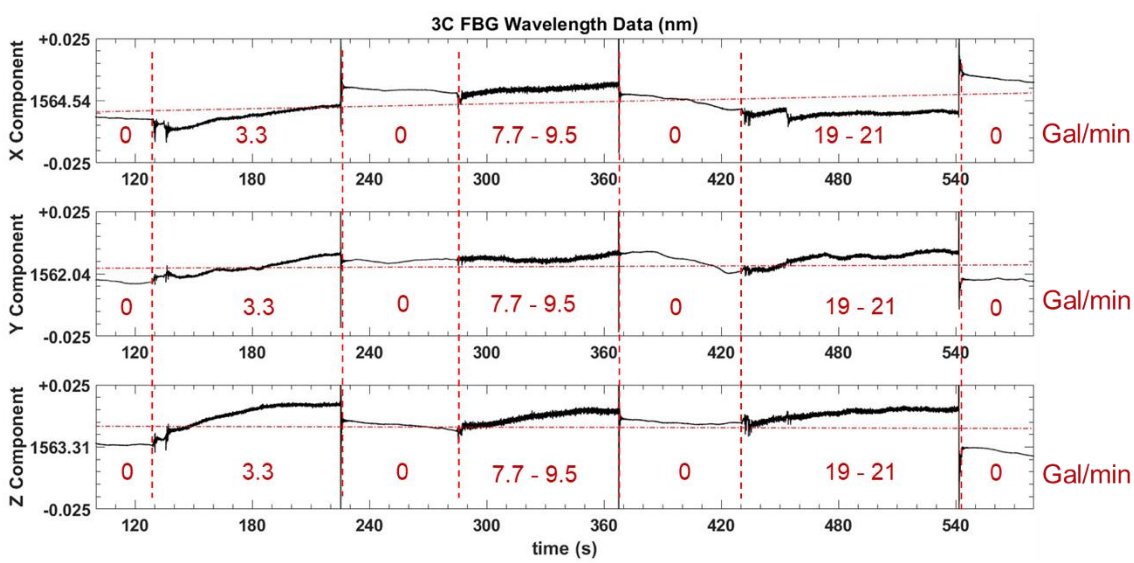

Figure 4.4: Example of 3-C FBG response to flow with the average flow rate range annotated (Alfataierge et al., 2019a).

The radial components (Y and Z) have a slightly different response than that of the axial component (X). However, the response with respect to flow is comparable, such that in the presence of flow we see more fluctuations in the measurements, and the fluctuations increase with respect to the flow rate.

Distributed FBG measurements

Figure 4.5 shows the results of measurements made from the distributed FBG sensors 1-8 with respect to flow test 1. The measurements show that all sensors attached to pipe capture the flow response, while the free FBGs (Sensors 6 and 7) show no response to flow except for Sensor 8 which responds to the flow coming out of the pipe and deflecting of the tank wall to interact with Sensor 8. The flow response in Sensor 5 is different than that on the other sensors because it is above water, therefore the fluctuations are dampened.

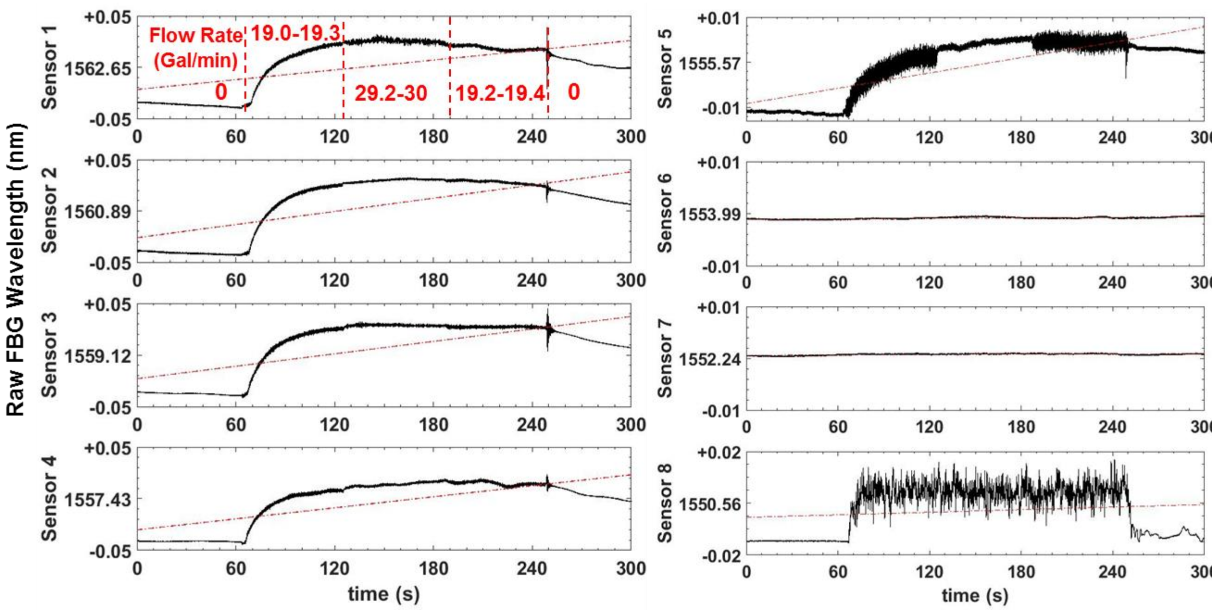

Figure 4.5: Distributed FBG response for flow test 1.
Sensors 1-5 are taped at various locations along the pipe. Sensors 6-8 are not coupled to the pipe but in the water along the tank. Sensor 8 is located near the end of the flow pipe and thus senses the flow current as it exits the pipe and flows in the tank.

Cross plotting the flow rate and the relative wavelength shift of each FBG sensor gives a relationship between the average flow rates and relative wavelength shifts (Figure 4.6). The observed relationship is a positive linear correlation, such that the increase in flow results in an increase in the wavelength shift. This preliminary relationship could be used to estimate flow rates from given FBG wavelength measurements.

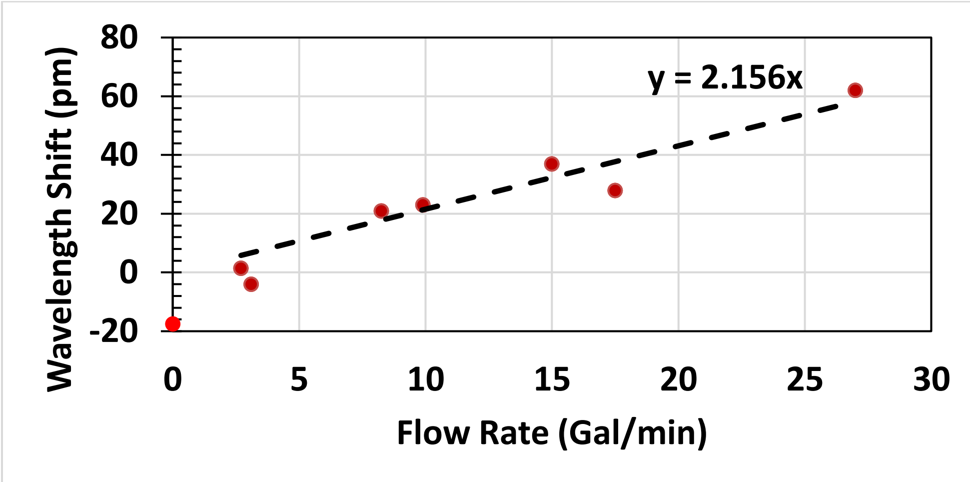

Figure 4.6: Observed relationship between flow rate and FBG wavelength shift.

DAS measurements

Figures 4.7 and 4.8 show the DAS response with respect to flow tests 1 and 2 respectively. We notice that the fiber mounted on the tank floor is insensitive to flow, whereas the fiber on the pipes was sensitive to flow. The DAS amplitude response has an interesting response to the flow rate, such that the DAS amplitudes complemented the noisiness of flow more than the rate of flow. The noisiness of flow is attributed to flow turbulence caused by the flow valve. The control valve used is a ball valve mechanism, which causes the most turbulence when open at 45%, at 90% it is fully open and causes no disturbance to flow, thus producing flow that we interpret as more laminar and associate with less noise (or vibrations).

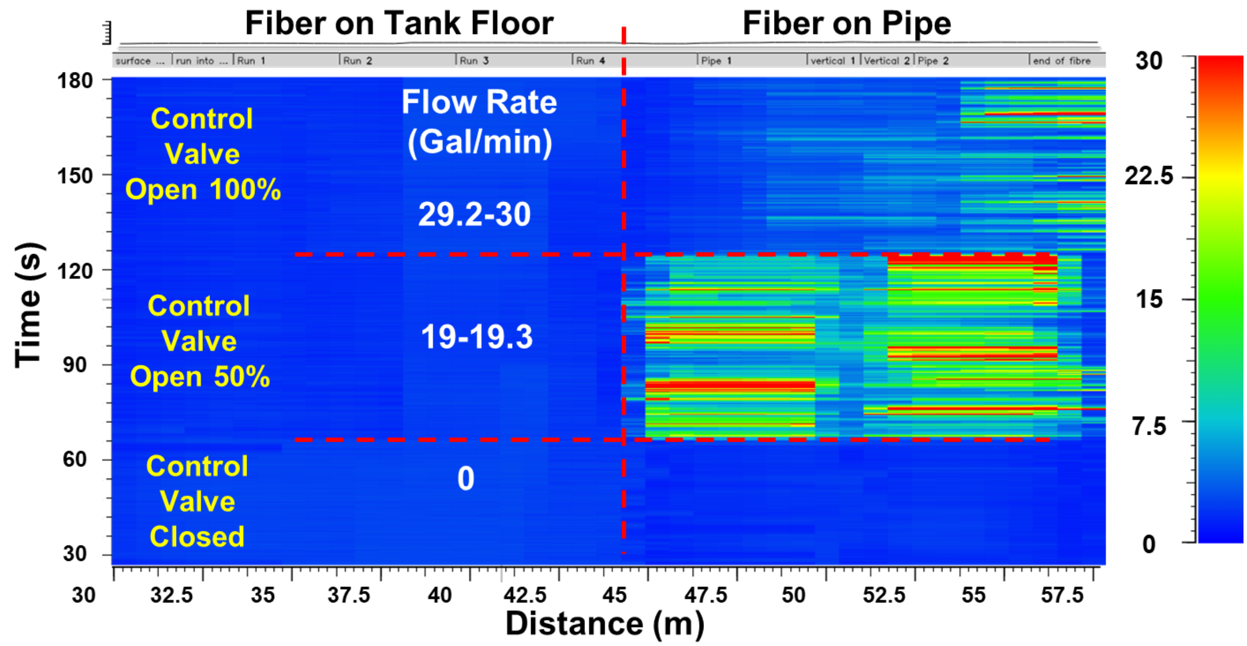

Figure 4.7: Example of DAS response to a flow test.
In this example the measured flow rate doesn't seem to correlate with the amplitudes of the DAS, rather the DAS amplitudes correspond to the flow turbulence introduced by the control valve.

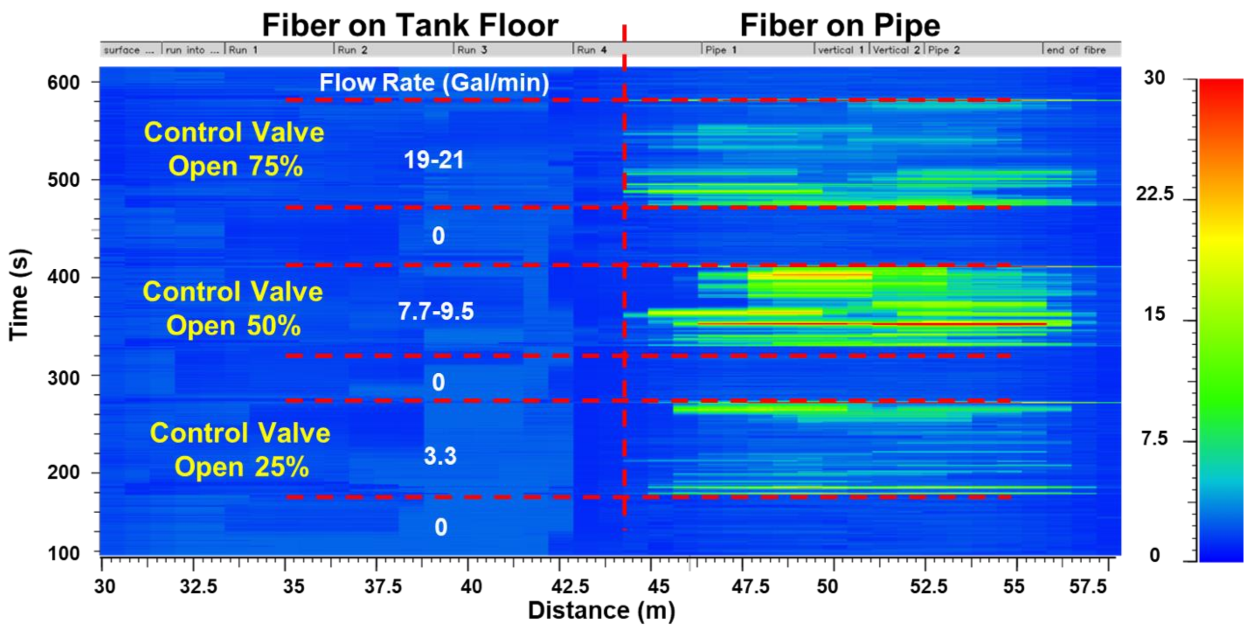

Figure 4.8: Example of DAS response with respect to flow rate.
In this example, the flow was increased in a step-like function such that between each flow increase was a period of no flow. We see here that we can determine the existence of flow using DAS, however, we cannot rely on the amplitudes as an indicator of flow rate.

Leak detection

Experiments conducted with the leak valve showed that the leak added approximately 2 Gal/min to the flow rate. The leak was identified by two characteristics: 1) Mechanical noise, which was used to identify manual intervention in the system, for the DAS system this helped identify the location of the leak source (with a margin of error that was relative to the gauge length). 2) Increase in amplitude (or wavelength shift for the FBG system) this increase was proportional to the increase of flow rate, additionally, engaging the leak added noise to the system which was the source of the increased DAS amplitude. Figure 4.9 is the 3-C FBG response to a leak experiment. In this experiment, the main flow valve was open to produce 10-15 Gal/min, the leak valve was then open after one min of flow and the flow rate increased to 13-17 Gal/min, which correlated to a positive increase in the wavelength shift. When closing the leak valve, mechanical noise was observed in the FBG data due to difficulty in manipulating the leak valve. Once the leak valve was shut, the flow rate dropped back to 10-15 Gal/min, and the FBG wavelengths dropped proportionally. Note that the temperature response was not accounted for in the displayed data, we attribute the low-frequency variations to temperature variation. Additionally, DC shifts in the data that are observed were found to be associated with the mechanical noise produced by manual intervention on the valves.

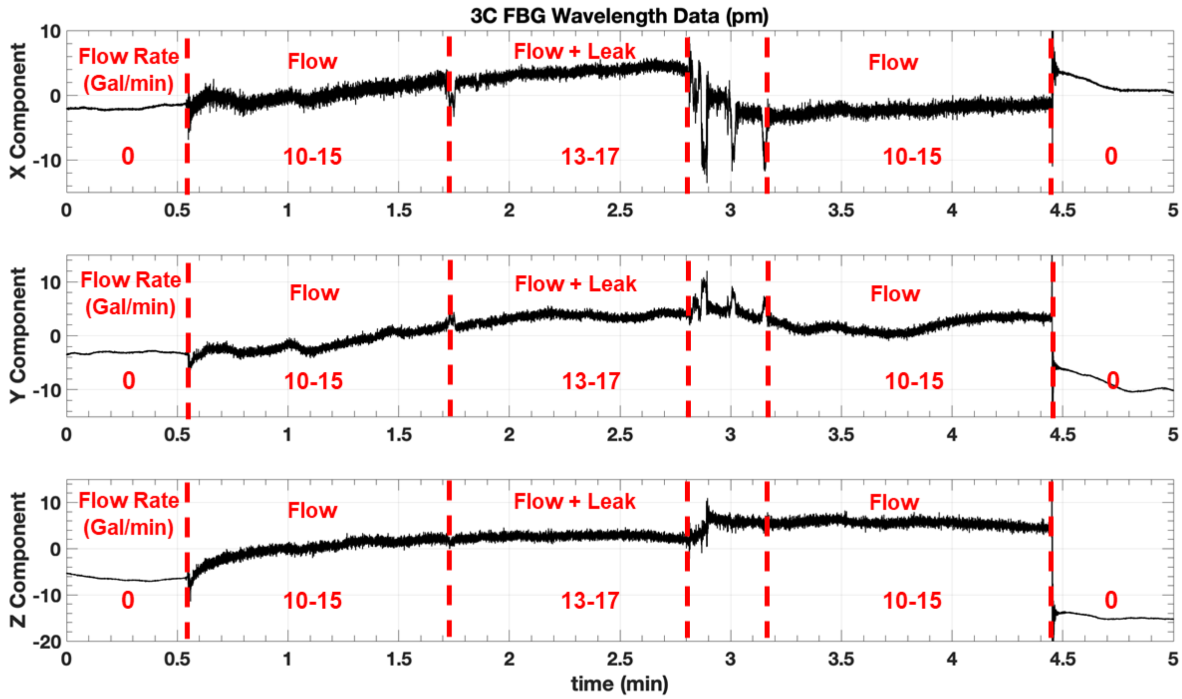

Figure 4.9: 3-C FBG response to a flow experiment with leak introduced.
An increase in the flow rate is seen with respect to the opening of the leak valve, then a decrease when shutting the flow valve.

Figure 4.10 is the DAS response to the same leak experiment. The DAS response shows an increase of DAS amplitudes when opening the flow. The center of the peak amplitude points to the leak valve location, as the energy is spread out across the gauge length (10 m in this case). We note that none of the fiber on the tank floor senses the leak or flow, only the fiber on the pipe was able to sense a response to flow and the leak.

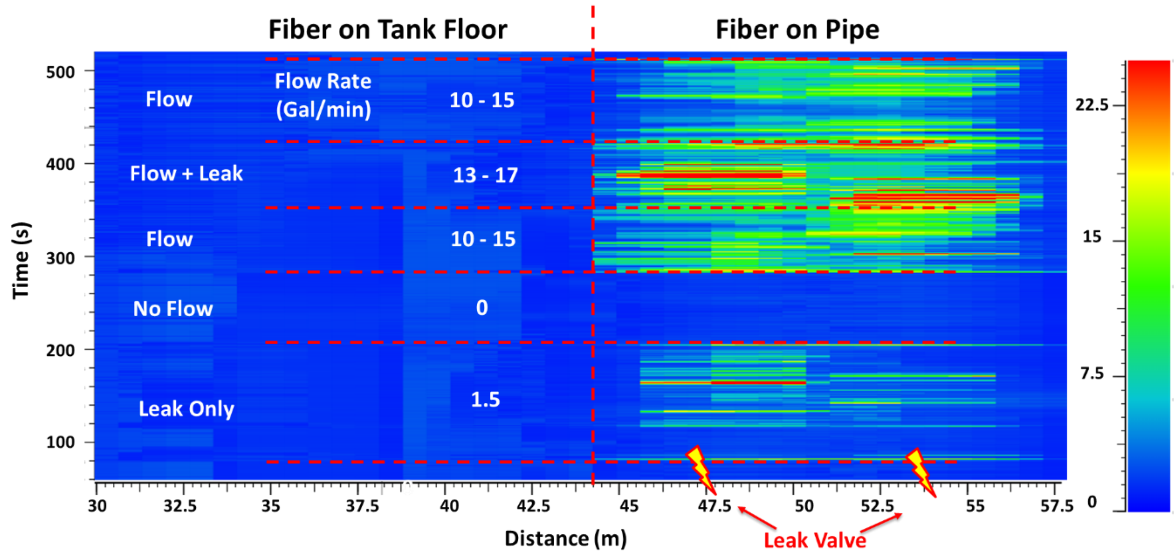

Figure 4.10: DAS response to a flow experiment with leak introduced.
The introduction of a leak during flow resulted in an increase in DAS amplitudes.

Conclusions

Two primary observations are made with regards to the response of FBGs to flow. First, the overall shift in the wavelength correlated with the flow rate, such that an increase in flow resulted in an increase in the wavelength shift. Second, short-term fluctuations in wavelength corresponded to the turbulence in the flow produced by the flow control valve. Similarly, DAS amplitudes corresponded to the turbulence in flow. In conclusion, we find that a fiber-optic sensing system shows considerable promise for monitoring flow in pipes.

Future work is needed to develop a stronger relationship between flow and the fiber-optic sensing systems and explore further applications of fiber-optic systems installed on pipelines. Additionally, a more controlled flow system that allows multi-stage flow and control of flow turbulence would help better understand the response on the fiber-optics sensing systems. Other topics to consider: 1) external flow, flow around the pipe rather than inside the pipe, this is relevant to borehole environments in evaluating cement and detecting a breach behind the casing. 2) flow directionality, evaluating the direction in which flow is propagating. 3) fluid type, determining the type of fluid being flowed is also an important topic, discriminating water from oil from gas is a very important topic to the oil and gas industry.

4.2. Marine Seismic Source Characterization

In this section, we consider the simulated marine environment setup for seismic source characterization. This work serves as a foundation for future work considering marine seismic imaging using fiber-optic sensors, and consideration of fiber-optic streamers. Laboratory tests are carried using the intensity-based DAS interrogator (Fotech Helios HSi) and the FBG system in comparison to the hydrophone system. Multiple source types have been considered using various material, the most successful source types that generated frequencies in the seismic imaging range were the spring source and the air source.

All DAS results are presented as waterfall plots displaying the amplitude response to a series of source tests with respect to time. Future work should consider using a phase-based system in order to generate more comparable measurements. The FBG system consists of a single fiber with an array of FBG sensors that have been deployed and highlighted in the figures (Figures 4.1 and 4.2). FBG measurements with respect to change in wavelength were corrected for the effect of temperature by linear regression of the data. The linear trend observed in the data was considered as the temperature response, given that minor temperature variation is expected and that the temperature response on the fiber has a long wavelength.

Figure 4.11 presents the FBG response of all eight FBG sensors during a source test with multiple excitations (shots). The source was excited six times with roughly 10 seconds between each shot. The source location was in the far end of the tank near the tail of the horizontal pipe segment, then moved approximately 50 cm towards the vertical pipe segment after every shot. The results show that Sensors 1-3 behave similarly with respect to the signal-to-noise ratio of the measurements, which is expected given that these sensors were all located on the horizontal pipe segment and secured the same way on the pipe. Sensors 4 was on the vertical pipe segment and was near the water level surface, thus the measurements exhibit unique noise characteristics between shots, the different orientation of the sensor with respect to the other sensors explains the amplitude variation. Sensor 5 was the only sensor above water and thus has a unique response compared to the other sensors. Sensors 6-8 were underwater but uncoupled, which explains the noisier measurements. The signal referred to here is the large amplitude event that shows consistent time arrival across the sensors and is associated with the source excitation and wavefield generation into the system, whereas, the noise is the low amplitude fluctuations that are due to environmental sources. The amplitude variation seen between shots is due to variation in the amount of energy exerted by each source excitation.

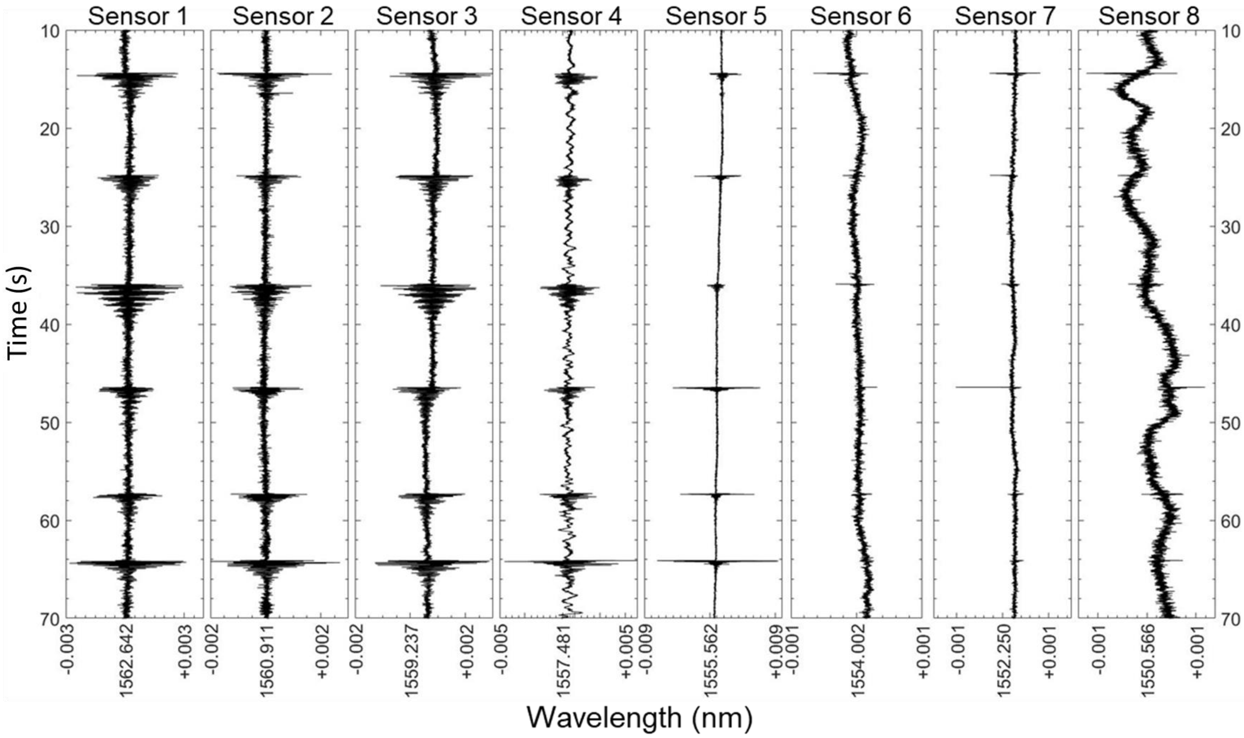

Figure 4.11: FBG response to multiple source excitations with respect to all FBG sensors shown in Figure 4.1. *Sensors 1-5 are taped on the pipe whereas Sensors 6-8 were left floating in the water. During this experiment, the water level was near Sensor 4, and Sensor 5 is above the water level. The source used was a wood plank excited with a rubber hammer by tapping it from a vertical direction as it is submerged in the water.*

FBG vs. Hydrophones:

In this section we consider the two seismic sources that were selected, the first source consists of a spring that was attached to the outer wall of the tank and pulsed to generate a low-frequency wave in the tank. The second source simulates an air-gun type source using inflatable balloons that were burst underwater. 4 FBG sensors were added to the horizontal pipe segment while having the hydrophones as close as possible and parallel to the FBG sensors. And one FBG sensor was left suspended in the water to evaluate the possibility of measuring the seismic wave without the fiber being coupled.

Figure 4.12 displays the results of the spring source on both FBG and hydrophone sensors. An apparent velocity is calculated from the moveout between the nearest and furthest sensor from the source. The apparent velocity on both the FBGs and hydrophones correlates to the velocity of a soundwave in water (1500 m/s). Figure 4.13 provides an analysis of the near and far sensor in the time and frequency domain. The source is characterized by a peak 8 Hz frequency and a bandwidth from 5-25 Hz, which is captured on both FBG and hydrophone systems. The FBG system exhibits high amplitudes with time, whereas the amplitudes decay with time on the hydrophone system. We believe this is due to the FBGs being sensitive to the wavefield as it rings in the tubes.

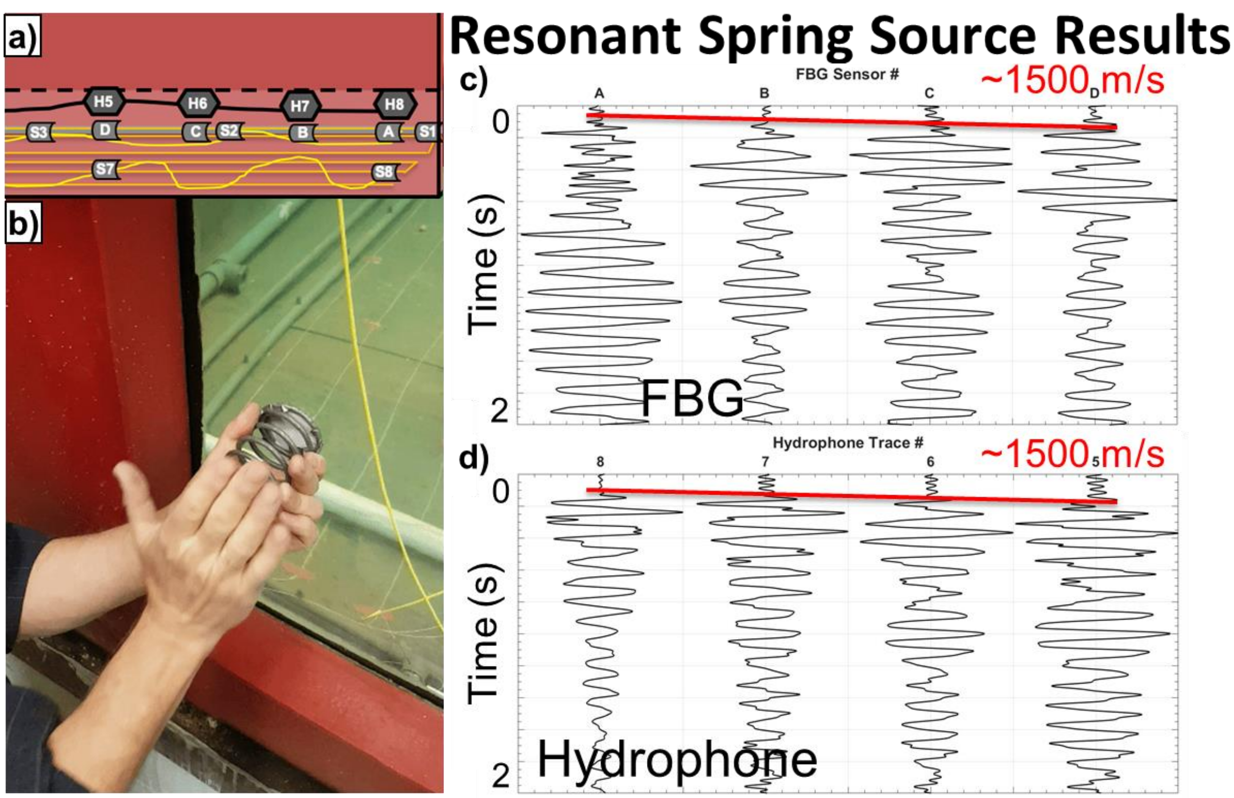

Figure 4.12: Resonant spring source results
a) Geometry of hydrophones and FBG sensors, b) image of spring source during excitation, c) FBG results for all 4 FBG sensor with sensor A (nearest to the source location) and sensor D (furthest from the source location) showing a moveout that corresponds to 1500 m/s, and d) Hydrophone results with Hydrophone 8 (the nearest to the source location) and Hydrophone 5 (the furthest from the source location) showing an apparent velocity of 1500 m/s.

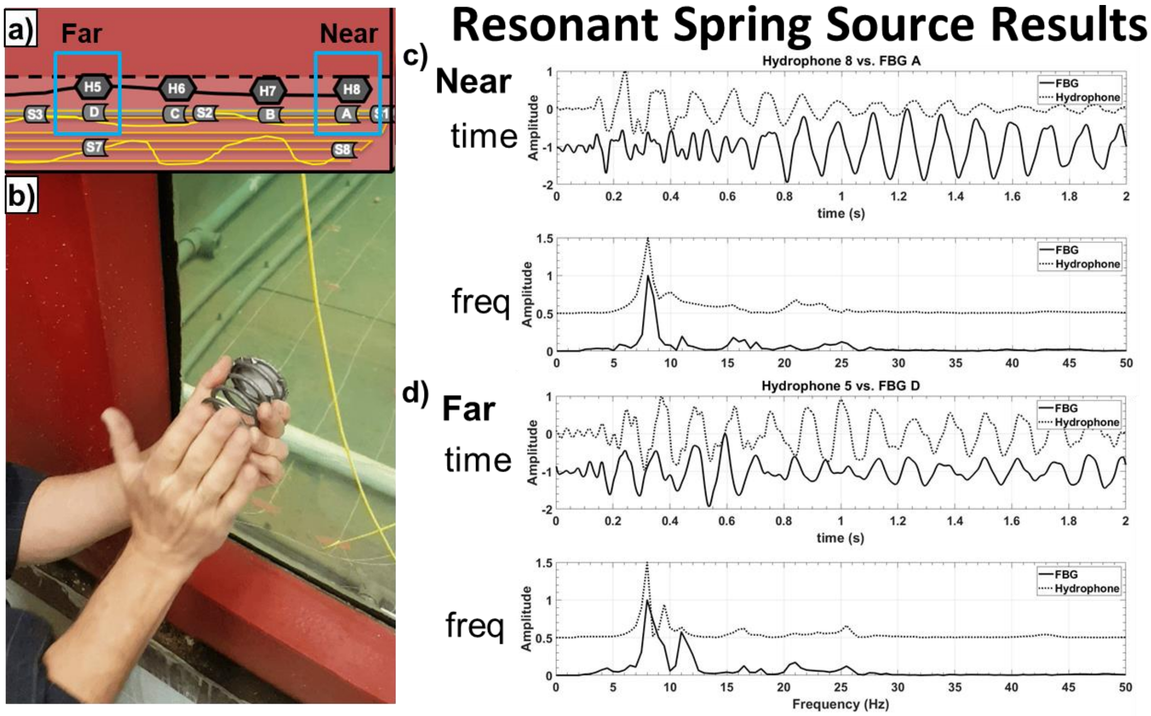

Figure 4.13: Resonant spring source results

a) Geometry of hydrophones and FBG sensors highlighting the near and far sensors, b) image of spring source during excitation, c) FBG (solid line) vs hydrophone (dotted line) results for the sensors near the source, d) FBG (solid line) vs hydrophone (dotted line) results for the sensors far from the source. Results characterize the spring source with an 8 Hz peak frequency and a bandwidth of 5-25 Hz that is captured by both sensing systems.

Similarly, Figures 4.14 and 4.15 show the results of the first air source and Figure 4.16 and 4.17 are the results of the second air source. Both source tests show a similar observation in the time domain with respect to move out that correlated to the velocity of sound in water (1500 m/s). The first air source is an elongated air balloon that was characterized by an 80 Hz peak frequency and a bandwidth of 40-120 Hz. Note that a low-cut filter was applied at 40 Hz due to a high amplitude low-frequency noise interfering with the measurements. The second air source is a spherical air balloon that was characterized by an 8 Hz peak frequency and a bandwidth of 5-60 Hz. Note that a 5 Hz low-cut filter was applied to remove high-amplitude low-frequency noise. In conclusion, the FBG system was capable of sensing the various seismic source types and producing similar measurements to the hydrophone system.

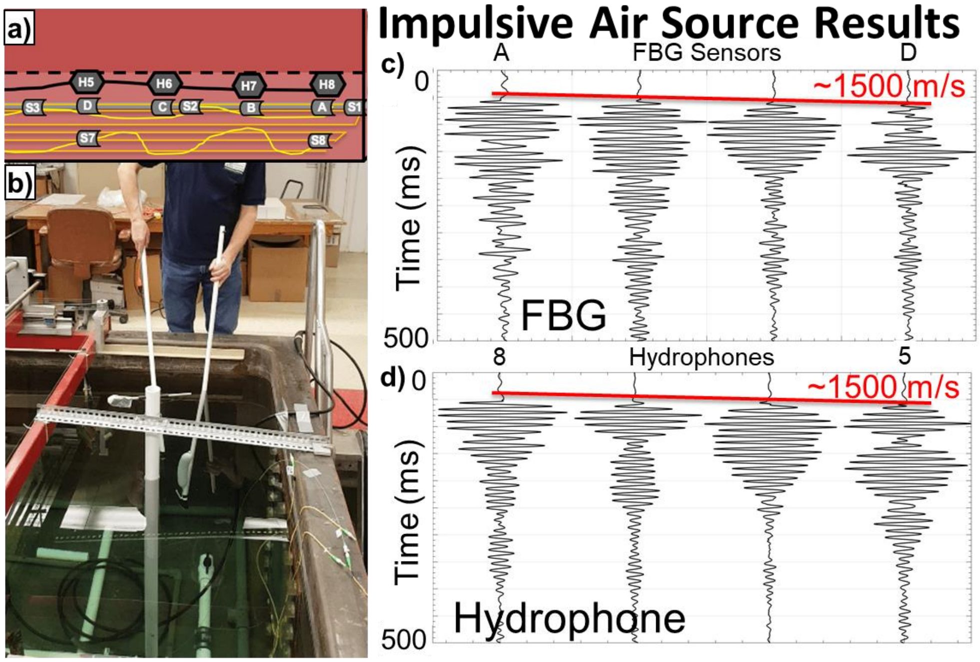

Figure 4.14: Impulsive air source results

a) Geometry of hydrophones and FBG sensors, b) image of spring source during excitation, c) FBG results for all 4 FBG sensor with sensor A (nearest to the source location) and sensor D (furthest from the source location) showing a moveout that corresponds to 1500 m/s, and d) Hydrophone results with Hydrophone 8 (the nearest to the source location) and Hydrophone 5 (the furthest from the source location) showing an apparent velocity of 1500 m/s.

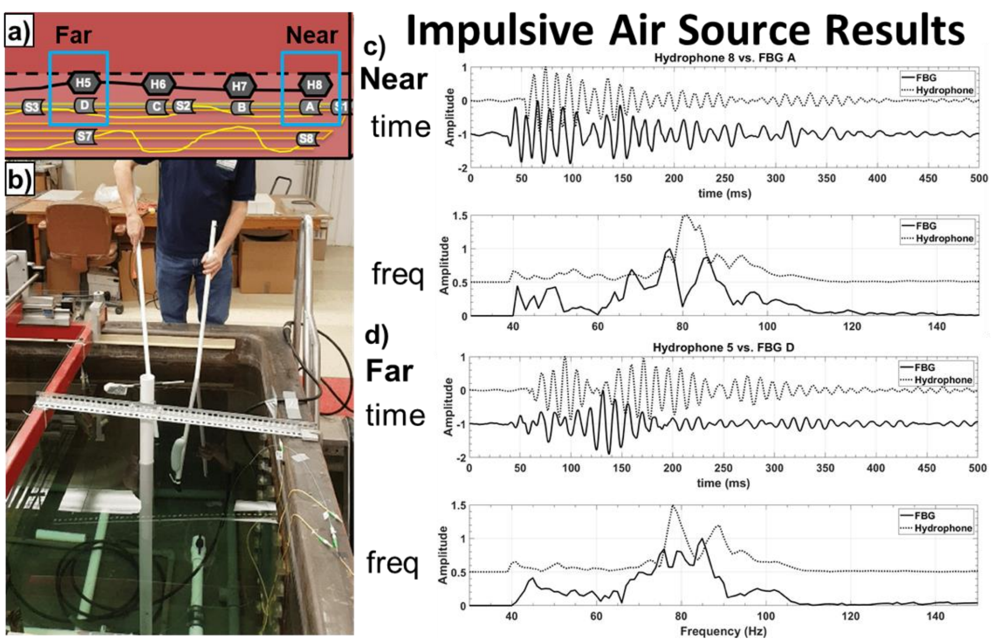

Figure 4.15: Impulsive air source results

a) Geometry of hydrophones and FBG sensors highlighting the near and far sensors, b) image of spring source during excitation, c) FBG (solid line) vs hydrophone (dotted line) results for the sensors near the source, d) FBG (solid line) vs hydrophone (dotted line) results for the sensors far from the source. Results characterize the spring source with an 8 Hz peak frequency and a bandwidth of 5-25 Hz that is captured by both sensing systems.

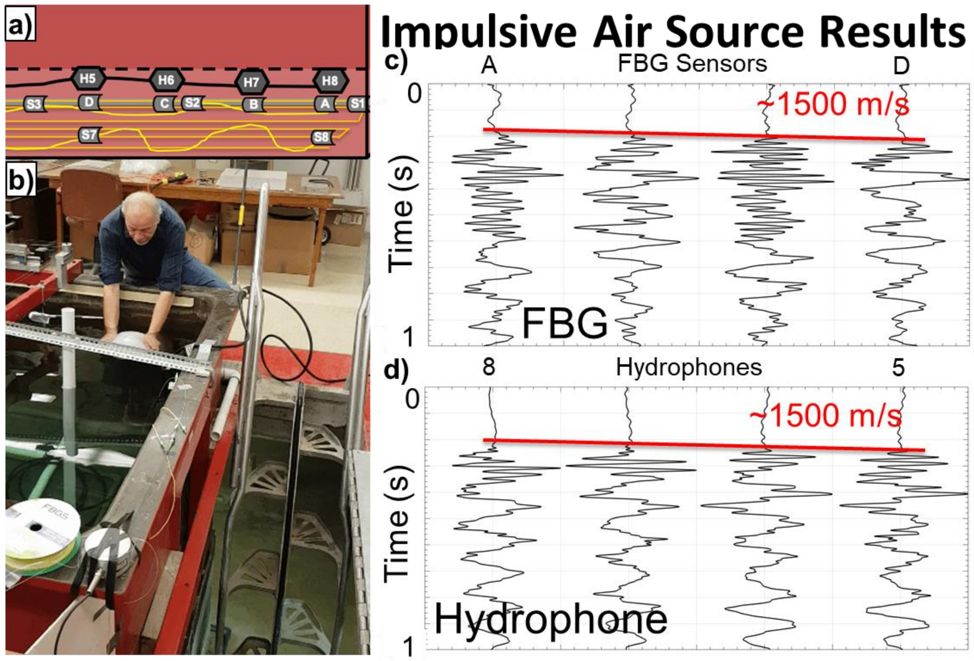

Figure 4.16: Impulsive air source results:

a) Geometry of hydrophones and FBG sensors, b) image of spring source during excitation, c) FBG results for all 4 FBG sensor with sensor A (nearest to the source location) and sensor D (furthest from the source location) showing a moveout that corresponds to 1500 m/s, and d) Hydrophone results with Hydrophone 8 (the nearest to the source location) and Hydrophone 5 (the furthest from the source location) showing an apparent velocity of 1500 m/s.

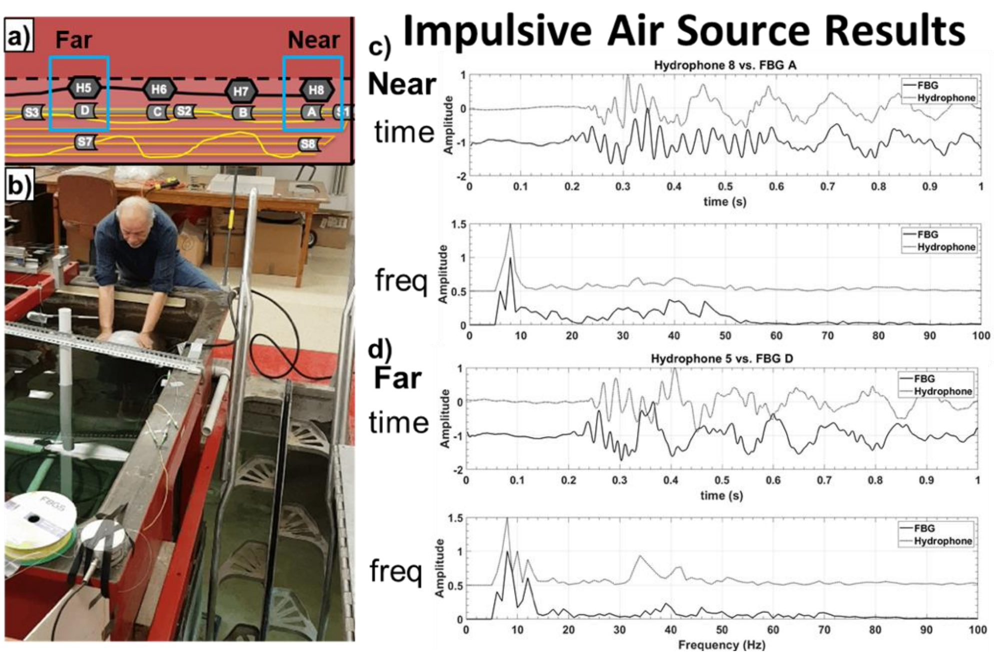

Figure 4.17: Impulsive air source results:

a) Geometry of hydrophones and FBG sensors highlighting the near and far sensors, b) image of spring source during excitation, c) FBG (solid line) vs hydrophone (dotted line) results for the sensors near the source, d) FBG (solid line) vs hydrophone (dotted line) results for the sensors far from the source. Results characterize the spring source with an 8 Hz peak frequency and a bandwidth of 5-25 Hz that is captured by both sensing systems.

Next, we explore the influence of coupling in a simulated marine environment, comparing the response of the FBG that was taped to the FBG that was left suspended in the water, while considering the response of a nearby hydrophone as a benchmark. The results shown in Figure 4.18 are for the elongated air balloon source. The results show that both sensors were able to detect the seismic wave, the suspended sensor exhibits lower signal amplitudes, but the frequency content shows a peak frequency around 80 Hz which matches the hydrophone and pipe secured FBG. Additionally, further comparison of the suspended FBG with the hydrophone data showed more similarity in the time and frequency domain than with the pipe coupled FBG. We believe this is due to the pipe coupled FBG being more sensitive to the wavefield interacting with the pipe.

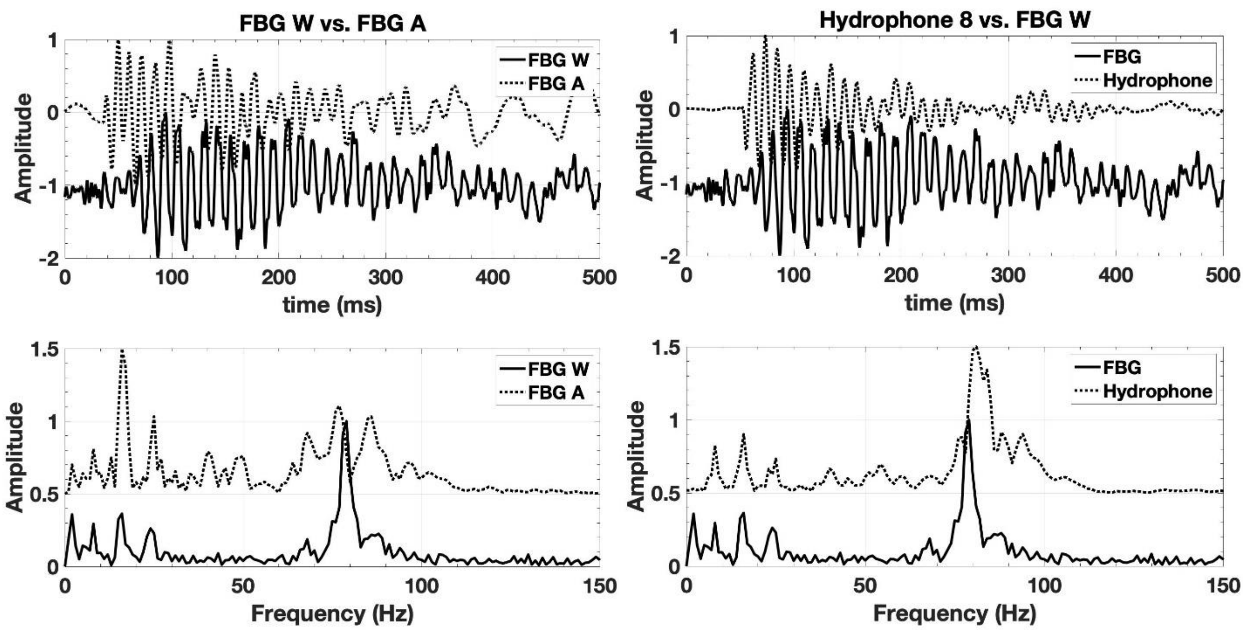

Figure 4.18: Hydrophone and FBG coupling comparison

To the left, a comparison between an FBG sensor suspended in water (FBG W) and an FBG taped to a PVC pipe (FBG A) with respect to time (top) and frequency (bottom) domains. To the right, a comparison between the same FBG W and a nearby Hydrophone. Note: the time and frequency responses have been skewed for display purposes (-1 in the time domain and +0.5 in the frequency domain). The response measured here is from the long balloon source which was found to generate a peak frequency of 80 Hz (Alfataierge et al., 2019b).

Figure 4.19 shows the result of the DAS system to one of the source tests. The results display the amplitude response of the fiber with respect to time and location along the fiber. Some source excitations were detected on the entire fiber, while other excitations were only sensed on part of the fiber. Additionally, the amplitude response varies along the fiber, which helps indicate the location of the source.

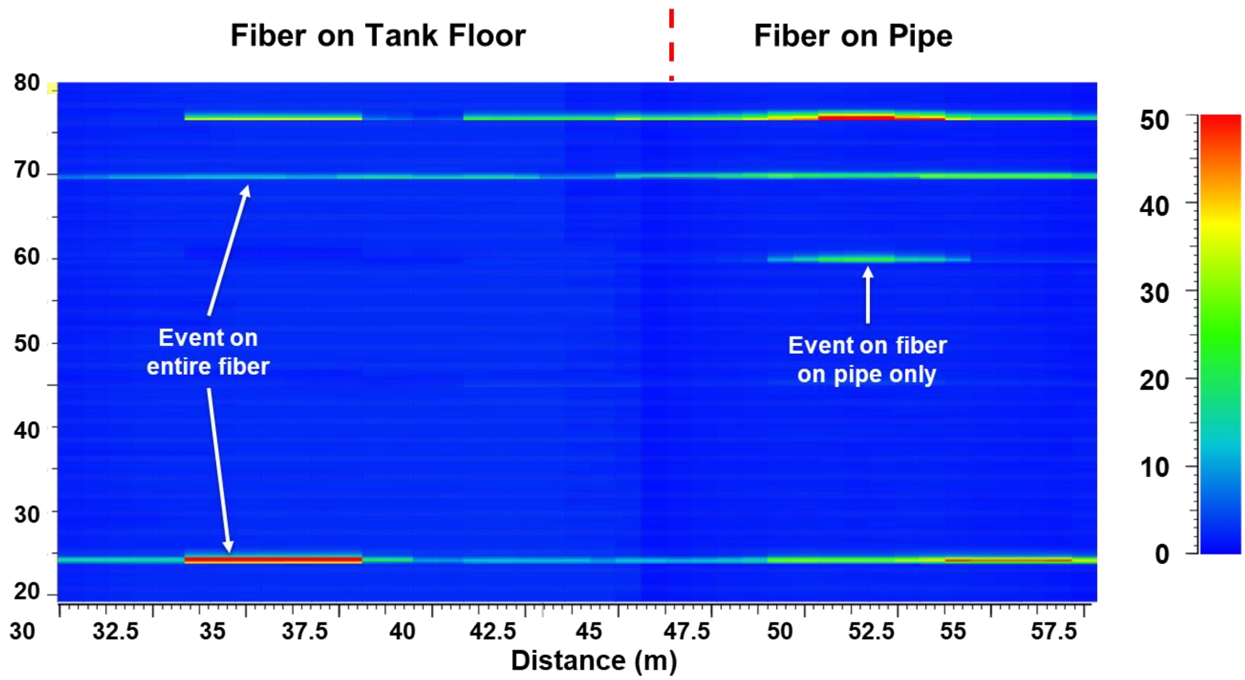

Figure 4.19: DAS response to steel pipe source excitation.
One can see that lack of repeatability in the source as some shots generate events on the entire fiber while some are only detected by the fiber on the PVC pipes.

Figure 4.20 is another example of DAS data using a different source, this source is controlled through a pin mechanism, which gives better repeatability. The source was placed in the corner of the tank near the vertical pipe segment, thus the DAS amplitude response is highest on the fiber mounted on the vertical pipe segment and attenuated as it goes toward the rest of the fiber. The energy produced by this source was not strong enough to be sensed by the fiber on the tank floor.

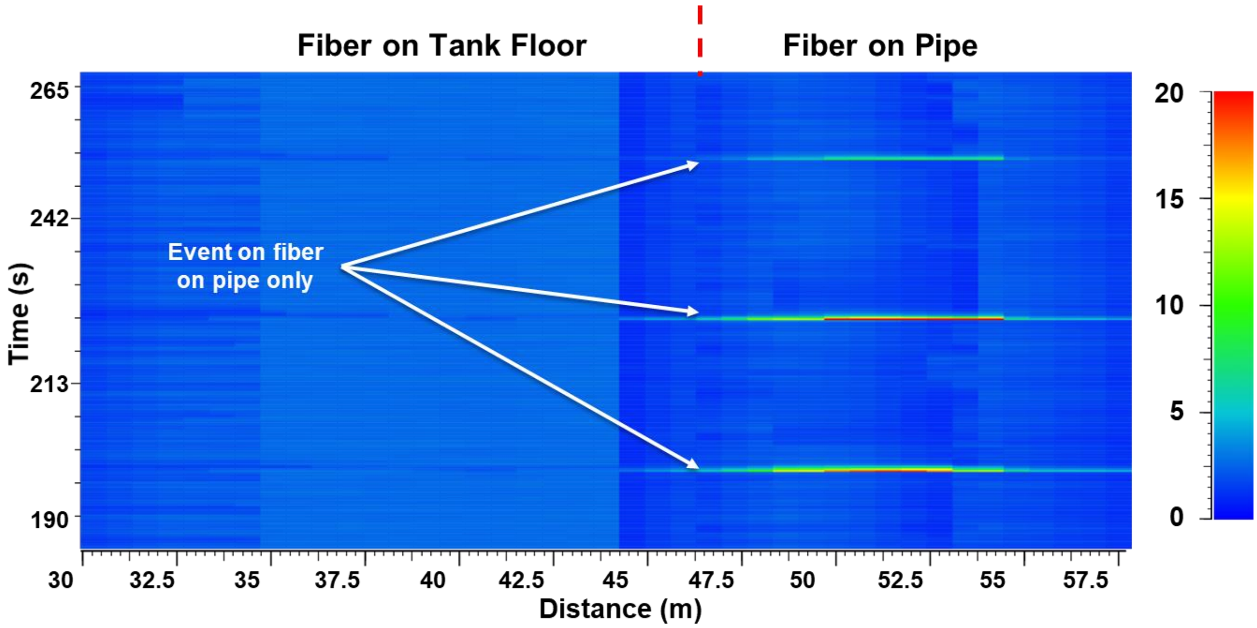

Figure 4.20: DAS response to seismic source positioned at the corner of the tank near the vertical pipe segment. *We see that this source signature is captured by the fiber on the pipe but not the fiber on the tank floor. The amplitude is highest at the vertical pipe segment.*

Conclusions:

In conclusion, the fiber optic sensing systems used in this study were able to sense the seismic sources while preserving the frequency response of the source. FBGs were found to be able to detect seismic sources even when uncoupled from solid support and suspended in water. The experiments conducted in this study show that the fiber-optic sensors can be considered as a marine seismic receiver on the ocean floor and potentially as a streamer.

4.3. Underwater Communication

In this section, underwater communication is considered using Piezoelectric (PZT) transducers and DAS fiber (Figure 4.21). The results of these experiments open the possibilities to underwater communication via coded messages in the frequency domain. The use of underwater communication in marine environments may allow the user to communicate with a remote instrument via a transducer and fiber optic sensors. An example of such application would be with an instrument remotely located on the seafloor that is equipped with a source transducer that is programmed to send a coded signal of a specific frequency, which then can be captured by a nearby fiber that is being interrogated without interrupting the seismic imaging process.

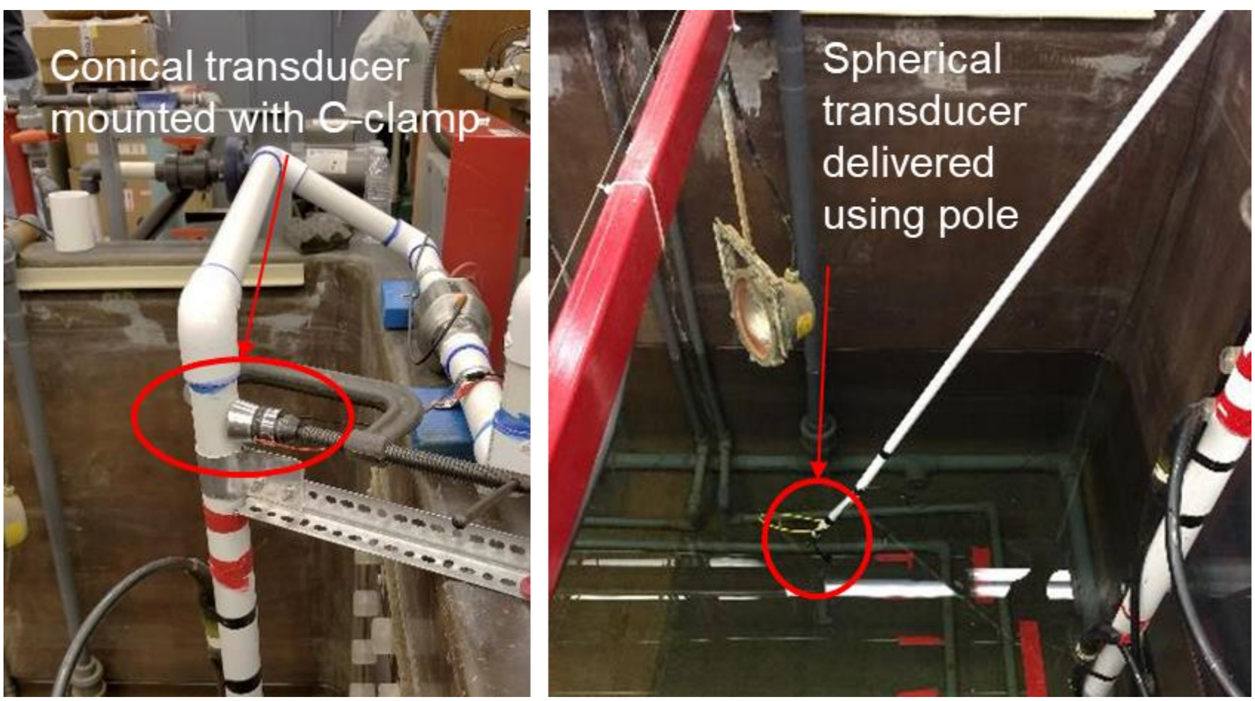

Figure 4.21: Piezoelectric transducers used for the underwater communication experiments, a conical transducer mounted to the PVC pipes (left) and a spherical transducer suspended in the water using a pole (right) (Alfataierge and Stewart, 2018).

Measurements are shown in the frequency domain using a Fast Fourier Transform (FFT) of the DAS data in real-time. Figure 4.22 shows the results of exciting the conical transducer at 2 kHz, the observed signal is isolated to the fiber mounted on the pipe, with no signal observed on the rest of the fiber. Results from the spherical transducer are compiled in Figure 4.23. The source was excited at 5, 10, 15, 20, then 24.5 kHz. The results show that both the DAS fiber in the tank and on the pipes were able to capture and preserve the source frequency. With lower frequencies (less than 5 kHz) the PZT transducer was unable to produce enough energy that could be captured by the fiber. This effect is seen on the 5-kHz results which display less amplitude than the other tests.

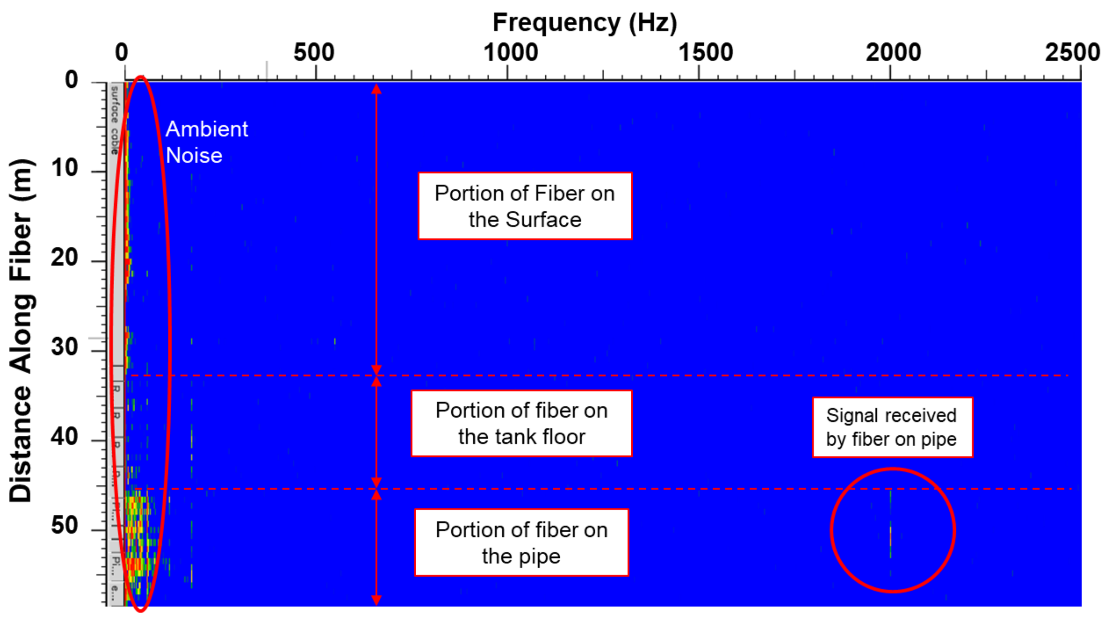

Figure 4.22: DAS frequency spectrum response to the conical transducer excited at 2 kHz (Alfataierge and Stewart, 2018)

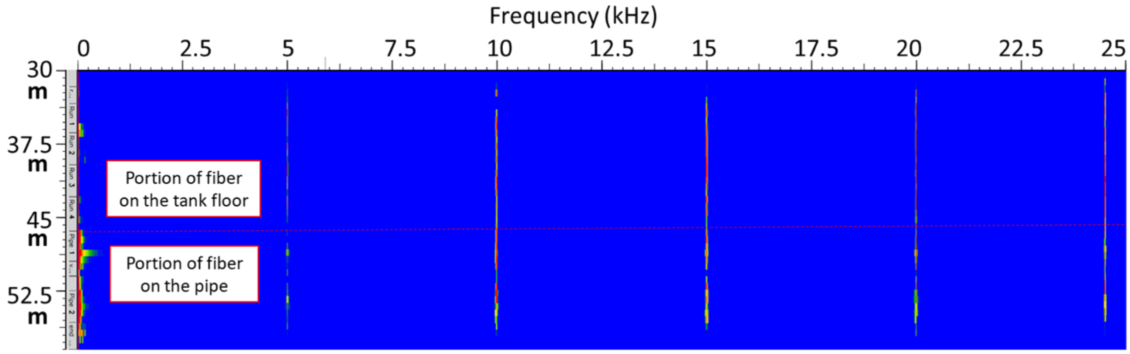

Figure 4.23: DAS frequency spectrum response to the spherical transducer source submerged in water. *The transducer was excited at 5, 10, 15, 20, and 24.5 kHz, and the DAS fiber was able to capture the energy produced on all the fiber in the tank (Alfataierge and Stewart, 2018; Alfataierge et al., 2019b).*

In conclusion, a concept for using PZT transducers and a DAS system for underwater communication in a marine environment is demonstrated, showing that such application would be feasible using frequencies up to 24.5 kHz. Future tests can consider sending coded messages from the transducer and measuring them on the DAS system and decoding them, further demonstrating the feasibility of such application.

This chapter has demonstrated three applications to a single simulated marine environment setup. Finding a relationship between flow and fiber-optic sensors, a positive linear relationship between the flow rate and the FBG wavelength shift and a positive correlation between noisiness of flow and DAS amplitudes. Demonstrating the feasibility of using fiber-optic sensors for marine seismic acquisition, showing that such application could be accomplished via a network of DAS and FBG fibers on the seafloor or on pipelines, or using FBGs suspended in water. Then testing an application of underwater communication using PZT transducers and a DAS system, finding that such application would be feasible using frequencies up to 24.5 kHz.

CHAPTER V

MULTICOMPONENT SEISMIC CONSIDERATIONS

This chapter discusses the possibility of multicomponent fiber-optic sensing. First discussing theoretical solutions that have been suggested in the literature, then presenting some preliminary numerical modeling of strain measurements using an elastodynamic Green's function. Next, a multicomponent solution is suggested using FBGs, it is demonstrated theoretically, then tested in the laboratory using a prototype 3-C FBG cube. Measurements are made assessing the sensor fidelity of the 3-C FBG cube and comparing it to 3-C Geophones in a simulated land environment in the laboratory.

One criticism of fiber-optic sensing is the single-component axial strain measurement that is extracted from the fiber. In borehole seismic imaging, conventional acquisition employs multicomponent geophones, therefore, in the application of DAS less information is obtained on the directionality of the incident wavefield. Direction plays a major role when using DAS for microseismic applications (Willis et al., 2016). An assumption is made in these cases, bounding microseismic events within the injection layer and projecting the events in the direction of the injection well. However, Mateeva (2017) makes a valid point when it comes to multicomponent DAS VSP, typical processing of multicomponent geophone VSP only uses the multicomponent measurements to rotate the geophone data and point it towards the source, and thus the multicomponent measurements do not contribute much beyond the initial processing stage.

Many have considered helically wound fiber as a solution to multicomponent DAS measurements, referring to a multicomponent strain tensor (Lim and Sava, 2016; 2017; 2018; Kuvshinov, 2016; Hardeman-Vooys and Lamoureux, 2019; Innanen, 2017). However, the technology has been limited to numerical modeling and theoretical considerations. Innanen et al. (2019) is one recent study that attempts multicomponent DAS using a complex surface geometry. However, the acquisition footprint of their proposed geometry (~150 m^2) is too large, which was necessary to overcome the large gauge length (10 m) that is too large for most practical applications. Therefore, I feel that at this point multicomponent DAS is not feasible, although with further development of the geometry and advances in the interrogation technology it will be achievable.

Multicomponent measurements referred to in the previous studies are with respect to the six-components of the strain tensor, whereas the common reference of multicomponent measurements in the geophysical domain corresponds to displacement, velocity, or acceleration in three-components (3-C) of a three-dimensional Cartesian coordinate system (x, y, and z). 3-C multicomponent fiber-optic solutions have been demonstrated using FBGs (Fernandez et al., 2001; Suresh et al., 2009). Therefore, this chapter evaluates the use of FBGs for multicomponent measurements in comparison to multicomponent geophones in a laboratory setting.

5.1. Theoretical Considerations

The numerical modeling has been done using MATLAB to simulate the response of a fiber optic system using the elastodynamic Green's function (equations 5.1-5.4). Strain measurements were done by computing the relative strain between two receiver stations using equations (5.5-5.7). This algorithm is used to validate the feasibility of manipulating FBG orientation to obtain multicomponent measurements.

$$G_{nm}\ (\boldsymbol{x}_g|\boldsymbol{x}_s,\omega) = \frac{1}{\rho\omega^2}\left[(k_s^2\delta_{nm} + \partial_m\partial_n)g_s - \partial_m\partial_n g_p\right]; n,m = 1,2,3 \tag{5.1}$$

where

$$g_{s,p}\ (\boldsymbol{x}_g|\boldsymbol{x}_s,\omega) = \frac{1}{4\pi R} exp\left[ik_{s,p}R\right],\ k_{s,p} = \frac{\omega}{V_{s,p}},\ R = |\boldsymbol{x}_g - \boldsymbol{x}_s| \tag{5.2}$$

$$\partial_1 = \frac{\partial}{\partial x_g},\ \partial_2 = \frac{\partial}{\partial y_g},\ \partial_3 = \frac{\partial}{\partial z_g} \tag{5.3}$$

$$\delta_{nm} = \begin{cases} 1 & n = m \\ 0 & n \neq m \end{cases} \tag{5.4}$$

G_{nm} is the elastodynamic Green's response with respect to three-component source and receiver ($n, m = 1,2,3$), where the receiver location is $\boldsymbol{x}_g$, the source location is $\boldsymbol{x}_s$, and the distance between them is R. The function is solved in the frequency domain ω. And the medium dependent parameters are the compressional and shear velocities $V_{p,s}$ and density ρ.

$$\varepsilon = \frac{Change\ in\ length}{Original\ length} \tag{5.5}$$

where

$$Change\ in\ length = \frac{x_{r2} - x_{r1}}{|x_{r1} - x_{r2}|} * (x_{t1} - x_{t2}) \tag{5.6}$$

$$x_t = [t_x \quad t_y \quad t_z]' \tag{5.7}$$

where t is the time trace response for each component (x, y, z).

FBG vs. Geophone Synthetics:

An elastic medium with a compressional velocity of 3000 m/s and shear wave velocity of 1414 m/s calculated via the Mudrock Line (Castagna, 1985) and a density of 2.294 g/cc calculated using the imperial Gardner's relationship was used. Figure 5.1 displays the numerical modeling results highlighting the response of orienting an FBG in the Y and Z components using source excitations in the Y and Z components respectively. We see that orienting the FBG in the direction of the source excitation is effectively measured in comparison to the geophone measurements. Thus, validating the possibility of orienting FBGs for multicomponent sensing.

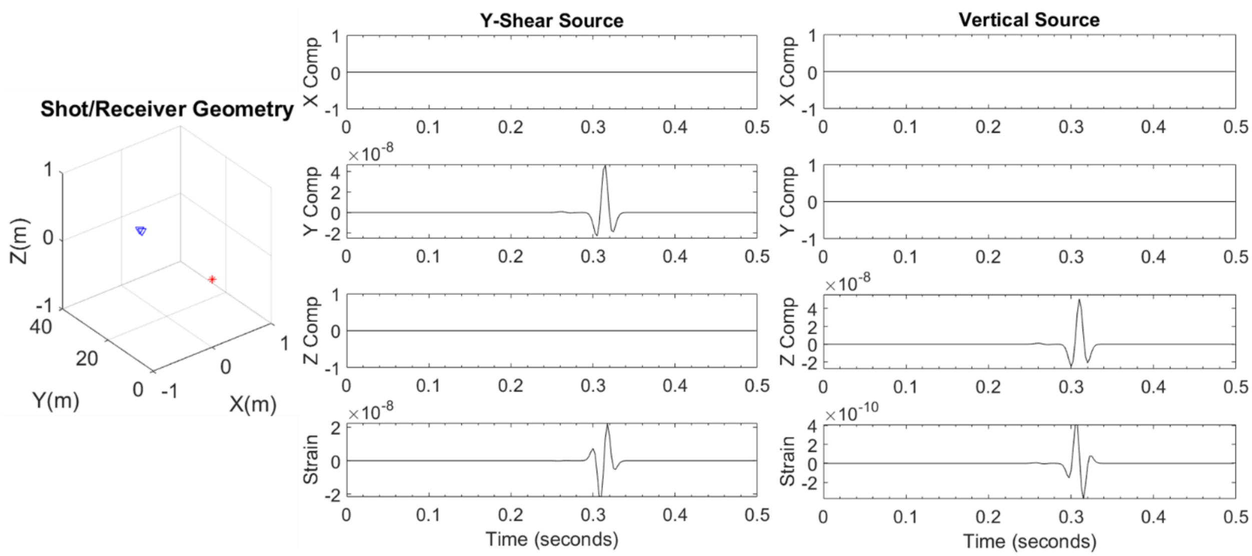

Figure 5.1: Numerical modeling results for shot-receiver geometry with 40-m offset (left), with respect to an FBG oriented in the Y direction and source excitation in the Y direction (center), and an FBG oriented in the Z direction and source excitation in the Z direction, in comparison to the 3-C measurements of a geophone (X Comp, Y Comp, Z Comp).

5.2. Laboratory Experimentation

Preliminary laboratory experiments were conducted on a prototype multicomponent FBG sensor in comparison to multicomponent geophone, using impulsive and vibratory seismic source types in a simulated land environment. First, experiments were conducted on the FBGs assessing the sensor amplitude and frequency fidelity. Next, the 3-C FBG sensor is tested again multicomponent geophones to assess the vector fidelity of the sensor. Then a conclusion is made on the overall sensor fidelity and comparison to geophones.

5.2.1. FBG Sensor Fidelity

The amplitude fidelity of an FBG sensor is assessed using a vibratory source, by introducing vibrations in line with the fiber and varying the gain (amplitude) of the source. The vibratory source used in this experiment is a Mini SmartShaker ™ with an integrated power amplifier (Model K2007E01) manufactured by The Modal Shop (MTS Systems Corporation). The FBG system used is the FAZT I4 Interrogator provided by FBGS International, along with DTG (Draw Tower Grating) FBG sensors manufactured by FBGS International. A function generator application was used on a smartphone to generate the signal frequency, gain manipulation was done by altering the output volume percent.

Results from an amplitude test at 50 Hz is presented in Figure 5.2 with respect to the FBG measurement response in the time and frequency domains. The amplitude test consisted of recording the FBG response with no signal introduced, giving a measurement of the noise floor, then introducing the signal at 25% volume, and increasing the volume by 25% going up to 100 %

volume. Similarly, the experiment was done at 100 Hz (Figure 5.3) however the overall amplitude of the signal was lower than the 50 Hz experiment.

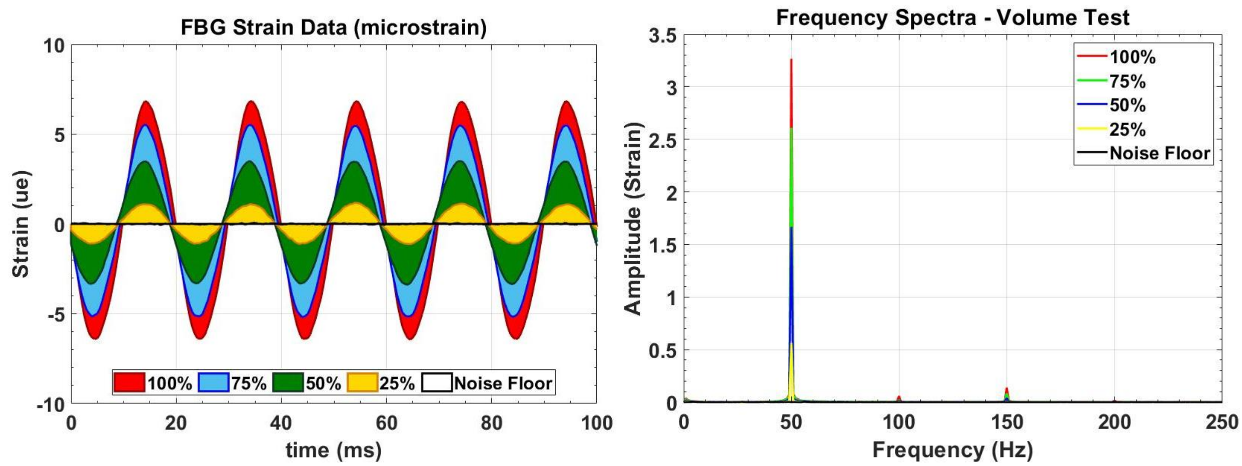

Figure 5.2: Amplitude analysis volume test at 50 Hz for an FBG using the SmartShaker source.
The amplitude response in the time domain is displayed on the left and the frequency domain on the right.

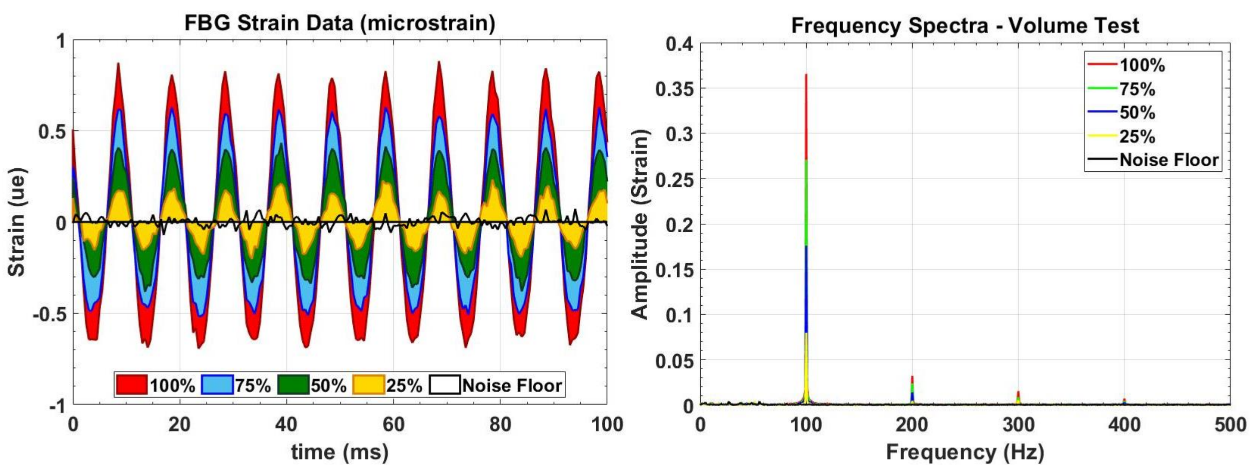

Figure 5.3: Amplitude analysis volume test at 100 Hz for an FBG using the SmartShaker source.
The amplitude response in the time domain is displayed on the left and the frequency domain on the right.

The results show that the FBG response is linear with respect to the amplitude variation, for both the 50 Hz and 100 Hz tests (Figure 5.4). Therefore, we conclude that the FBG sensor has a linear amplitude fidelity.

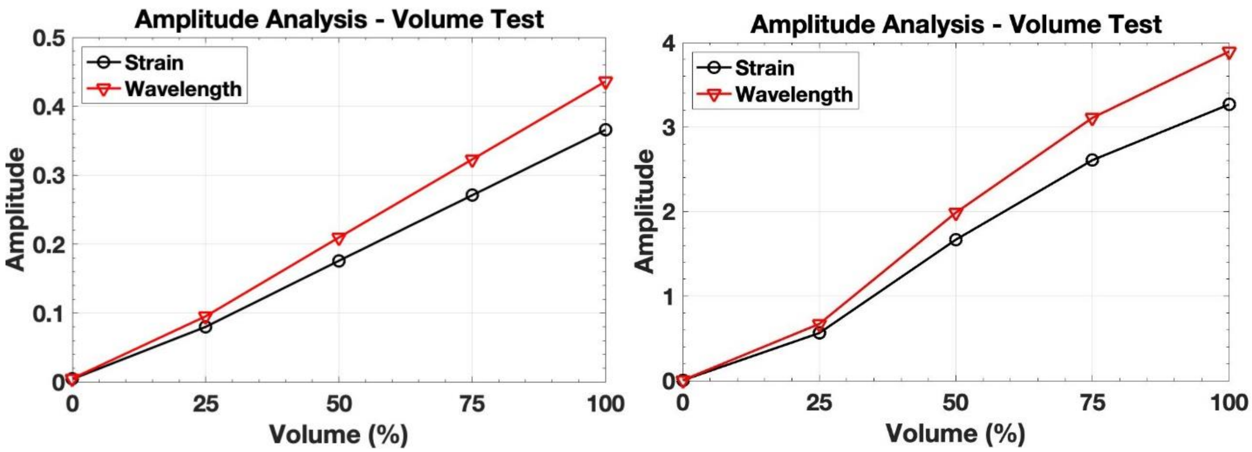

Figure 5.4: Amplitude analysis results for 100 Hz (left) and 50 Hz (right) with respect to measured wavelength shifts (red) and calculated strain (black)

Next, the frequency fidelity of the FBG is tested by measuring the FBG response at various frequencies. A frequency bandwidth of 2-200 Hz was selected Figure 5.5 shows the normalized results from source excitations from 2 Hz up to 200 Hz with an increment of 10 Hz. The time-domain measurements are presented in Figure 5.5. The data shows that the amplitude response varied from one frequency to the next, this was due to human error during the experiment process. Therefore, the amplitudes were normalized for this data, however, this resulted in lower SNR for the experiments that yielded low amplitudes. The frequency-domain response (Figure 5.6) shows a linear correlation in the frequency response. Second and third-order harmonics of the source frequency are evident at certain frequencies, this is observed when the measurements have a low SNR. The harmonics are a product of a non-uniform sinusoidal wave that has been observed by others (LeBlanc, 2000). We conclude that the FBG has linear frequency fidelity and thus we proceed to test the vector fidelity via the multicomponent FBG sensor.

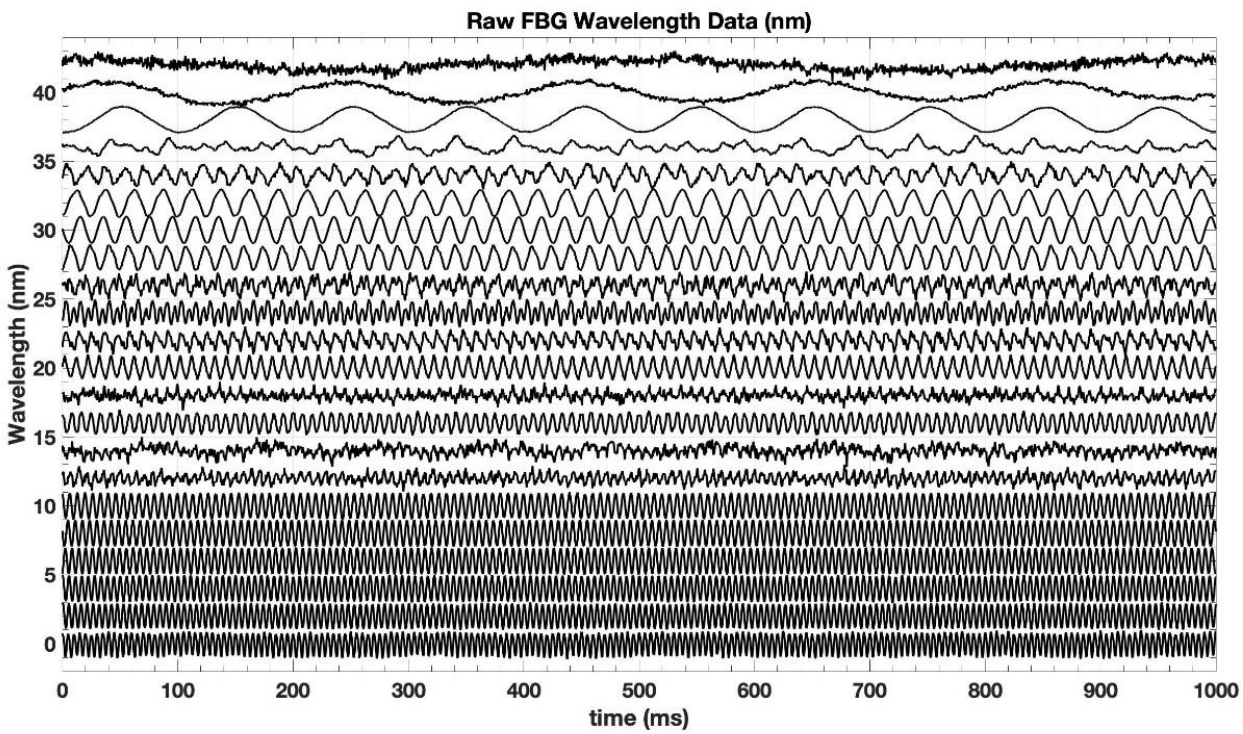

Figure 5.5: Normalized results of sweeps measured by an FBG from 2 Hz (top) down to 200 Hz (bottom)

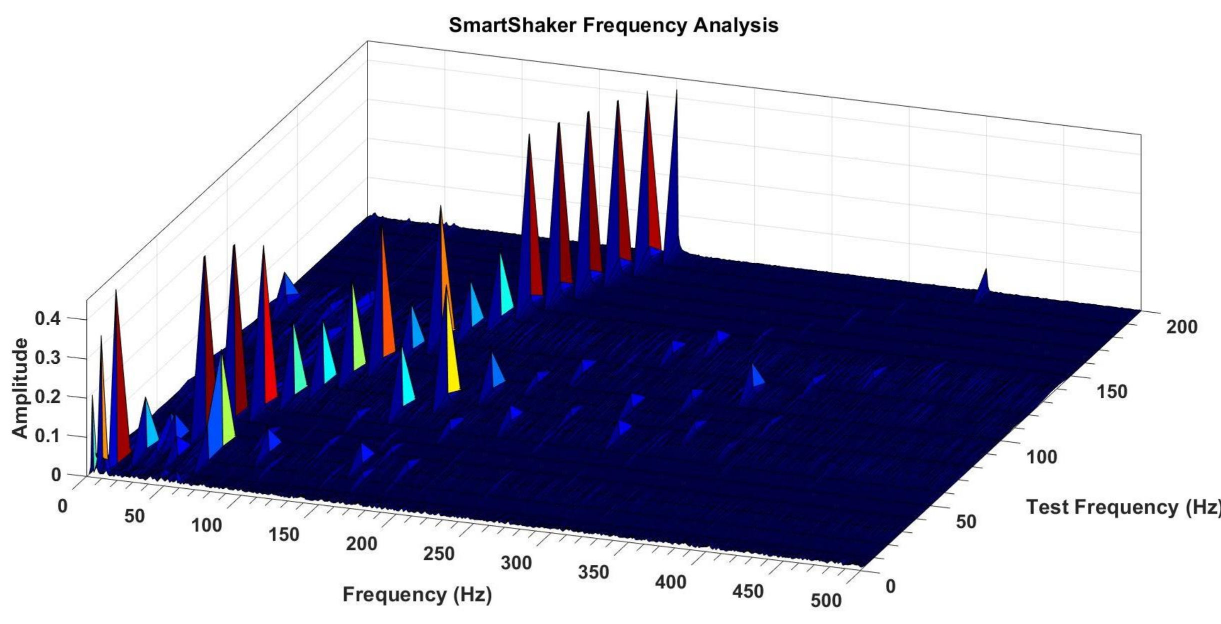

Figure 5.6: Frequency spectra of normalized sweeps presented in Figure 5.5.

5.2.2. 3-C FBG vs. 3-C Geophone

The multicomponent FBG sensor (3-C FBG) was developed using a quasi-distributed FBG array. Three FBGs were fixed to three orthogonal faces of a cube to effectively measure three components of a Cartesian coordinate system (X, Y, and Z). Three setups were considered (Figure 5.7) during the evaluation process to determine the influence of material on the measurements. The results of this evaluation are presented in Appendix E, where we find that materials have no influence on the 3-C FBG measurements with respect to the seismic frequencies that were used. This is supported by the fact that the wavelength of the highest frequency that was used (200 Hz) would be 10 m (assuming a velocity of 2000 m/s). This wavelength exceeds the dimensions of the cube and the setup. Therefore, there is no effective influence of the material on the FBG measurements.

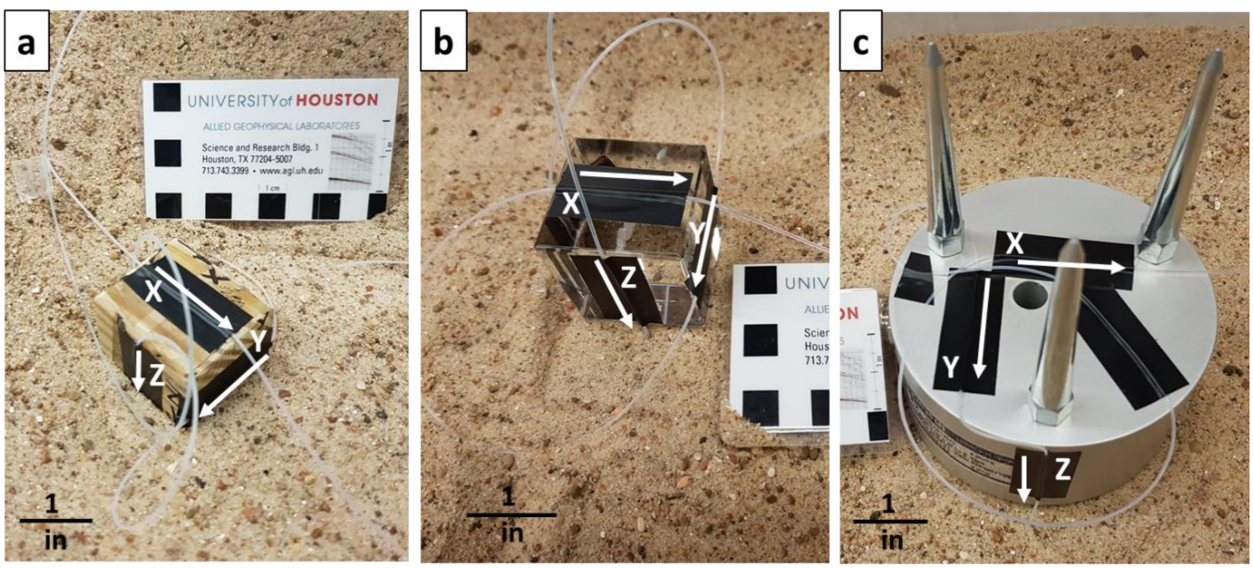

Figure 5.7: Three-component Fiber Optic Sensor (3-C FOS)

It consists of three FBGs in one fiber that have been secured to three orthogonal faces of a) a wooden cube, b) a glass cube, to represent the three primary components of X, Y, and Z. c) 3-C Micromate Geophone with 3-C FBGs taped and annotated.

The 3-C FBG sensor was first evaluated against three different 3-C geophones, an Instantel Micromate/ Blastmate geophone, a Geometrics 3-C geophone, and a Geometrics 3-C marshphone. The geometry of this experiment is illustrated in Figure 5.8, where each sensor was placed near a corner in a sandbox and the source was placed at the center with an equal distance from each receiver. Note that the 3-C FBG was buried in all experiments to maximize coupling with the medium.

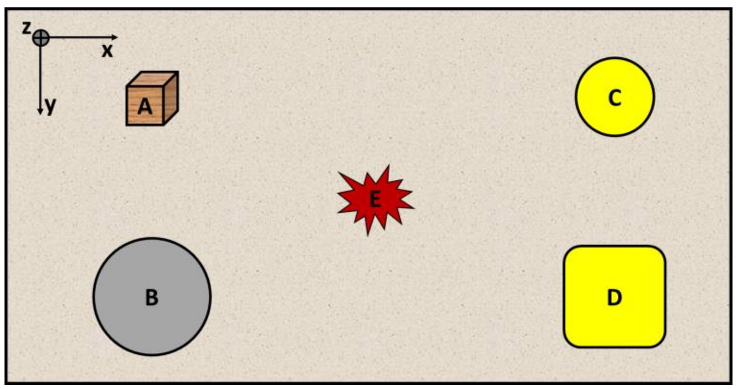

Figure 5.8: Sandbox setup illustration of the four sensing instruments and vibratory source.
A) The 3-C FOS, B) Micromate 3-C Geophone, C) Geospace 3-C Marshphone, D) Geospace 3-C Geophone, E) Source Location.

An ambient noise test is carried first to set a benchmark for the noise floor in the experiment. The results of the ambient noise test for the geophone comparison geometry (Figure 5.8) are presented in Figure 5.9. The results show that the ambient noise was slightly different on the right side of the geometry (Geometric Geophone and Marshphone results) versus the left side (3-C FBG and Micromate Geophone). All sensors capture an ambient noise signal around 60 Hz, 118 Hz, and 185 Hz on one or all components. Additionally, the 3-C FBG results showed lower amplitudes of ambient noise in comparison to the geophone sensors.

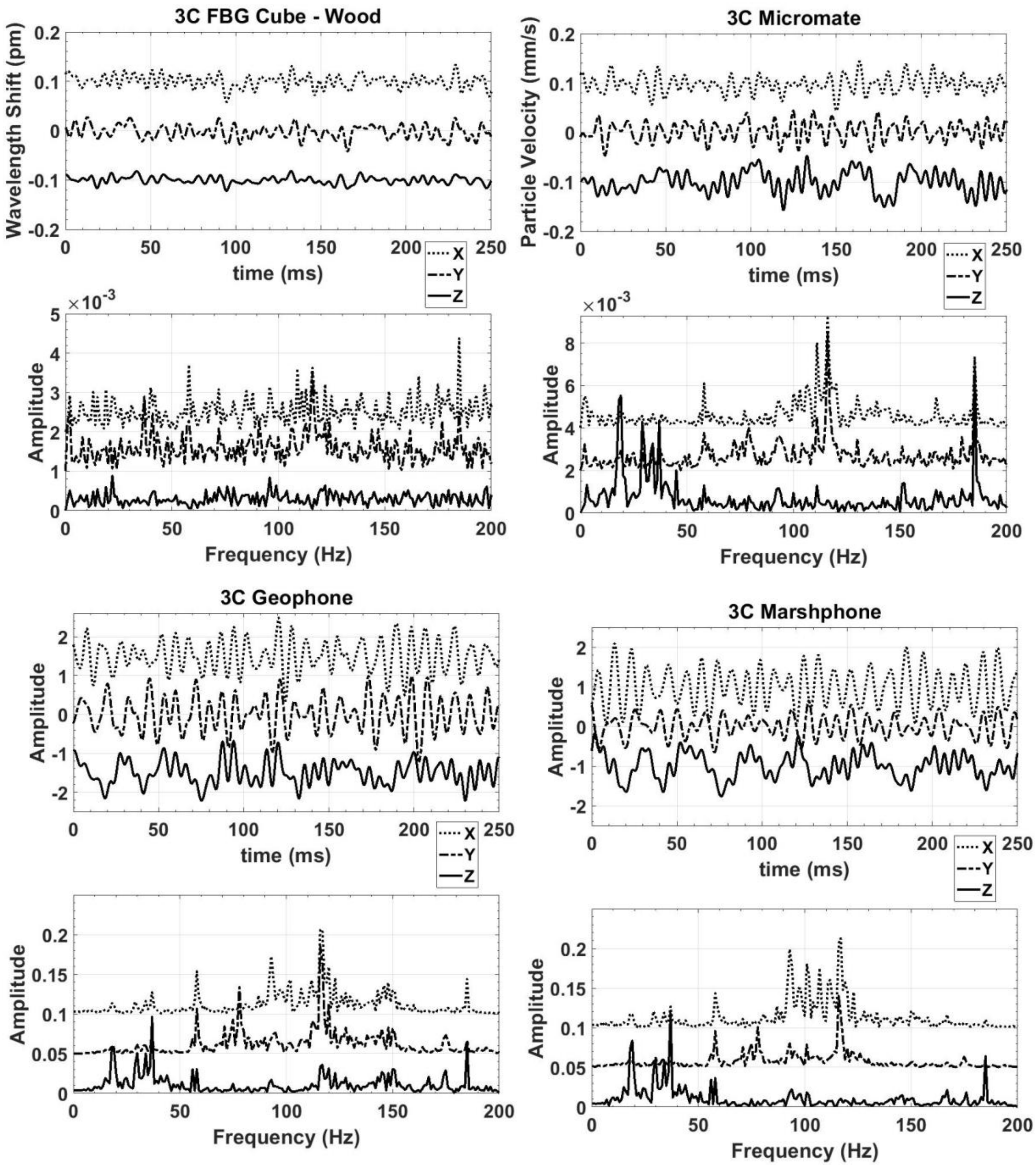

Figure 5.9: Ambient noise response for each sensor in the time and frequency domain.

The frequency content of the 3-C FOS is similar to the 3-C Micromate data, which were both located in the left part of the sandbox. And the 3-C Geophone and Marshphone data are similar and were in the right part of the sandbox. The results of each component have been skewed in the time and frequency domain for better display.

Next, a vibratory source was used to introduce a mono-frequency signal into the system. The results (Figure 5.10) show that all sensors detected the source frequency (86-87 Hz) that exhibited primarily shear energy captured on the X and Y components, with little signal on the Z component. The relative amplitude between the horizontal component and the vertical component was preserved in all sensors. Again, we find that the FBG exhibits harmonics of the source energy (at 172 Hz and 258 Hz), this is also evident in the geophone measurements but at very low amplitude. With this we conclude that multicomponent measurements via the 3-C FBG cube is feasible, preserving the frequency response of the seismic source and the relative amplitude on all three components.

We note that the FBG recording system is operated manually and was set to record first during each experiment. Whereas, the Micromate recording system operates automatically upon detecting an event and was set to record for 2 s after an event with 0.25 s prior to the event. The Stratavisor recording system was set to record manually due to the absence of a trigger mechanism for the source type being used. Therefore, the results of each experiment are not time-synchronized for all recording systems. With the exception of the measurements from the 3-C Geophone and Marshphone, which were recorded on the same system. Thus, the data presented was manually shifted in time in an attempt to line up the events at a similar time. Additionally, velocity information was unattainable since the source zero-time is unknown.

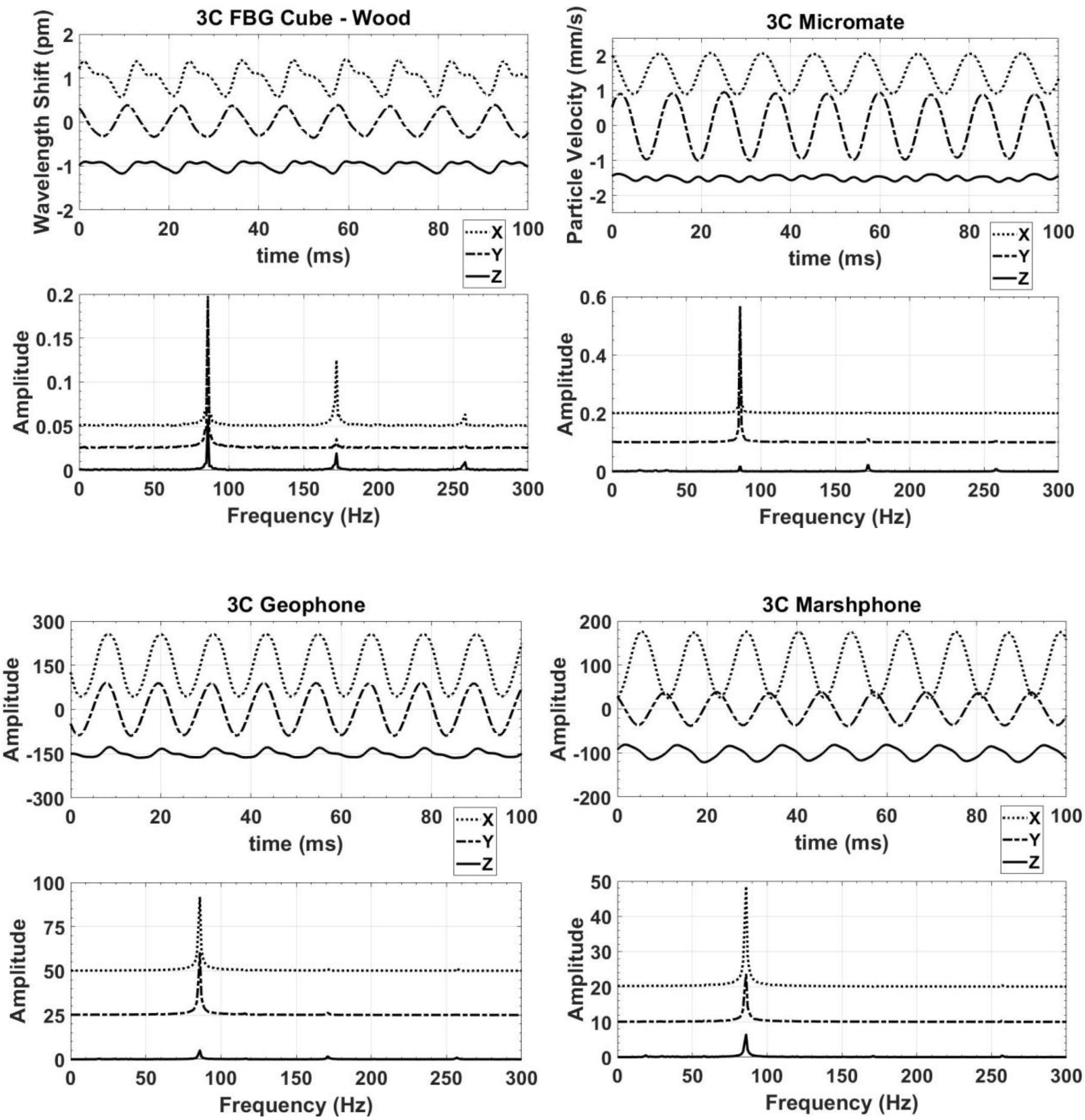

Figure 5.10: Surface vibratory source results on the four sensors in three components, with respect to the time and frequency domain.

The results show that the source has an 86 Hz frequency signature that registers on all three components. The energy spreads along the surface and does not contain a strong response on the vertical component of the sensors. The results of each component have been skewed in the time and frequency domain for better display.

In the next experiment, only the Micromate geophone is considered, given the positive correlation with the 3-C FBG measurements and the higher accuracy and reliability of the system. Additionally, the sensors are relocated to be placed in the same location to minimize the influence of variable ray paths on the data. In the new geometry (Figure 5.11), the 3-C FBG is buried beneath the 3-C geophone, thus the sensors are as close as possible for direct comparison. We will refer to this as the walk-away geometry, since the source station is set at 5 in (12.7 cm) from the receiver and moved away with an increment of 5 in (12.7 cm) to a maximum of 25 in (63.5 cm) of offset.

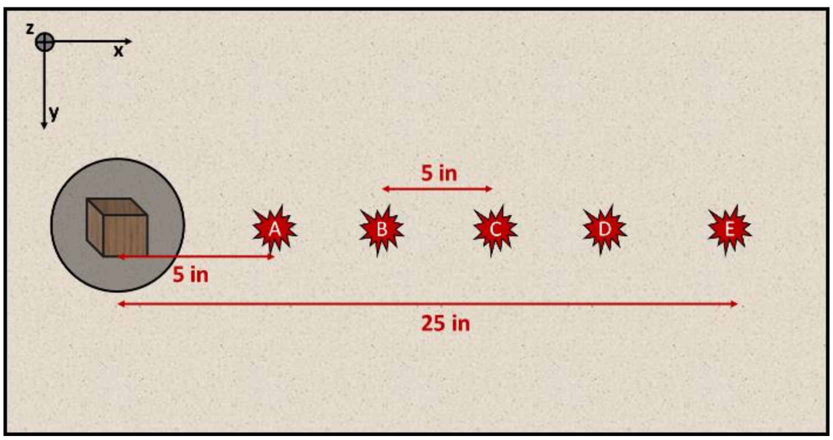

Figure 5.11: Walk-away source-receiver geometry
The source location is depicted in red with an offset increment of 5 in (12.7 cm). The grey circle depicts the 3-C Micromate Geophone with the 3-C FOS buried beneath.

Two source types were used during this experiment a weight dropped from a fixed height (about 30 cm) onto a wooden baseplate and a vibratory source. The results of the walk-away survey are presented in Figure 5.12, with respect to the weight drop source for the X and Z components. The results show an amplitude decay with source offset. The FBG measurements exhibit DC shifts in the data at near offset (5 in) but have comparable measurements on all other offsets. The results highlight a limitation in the 3-C FBG sensor at near offset.

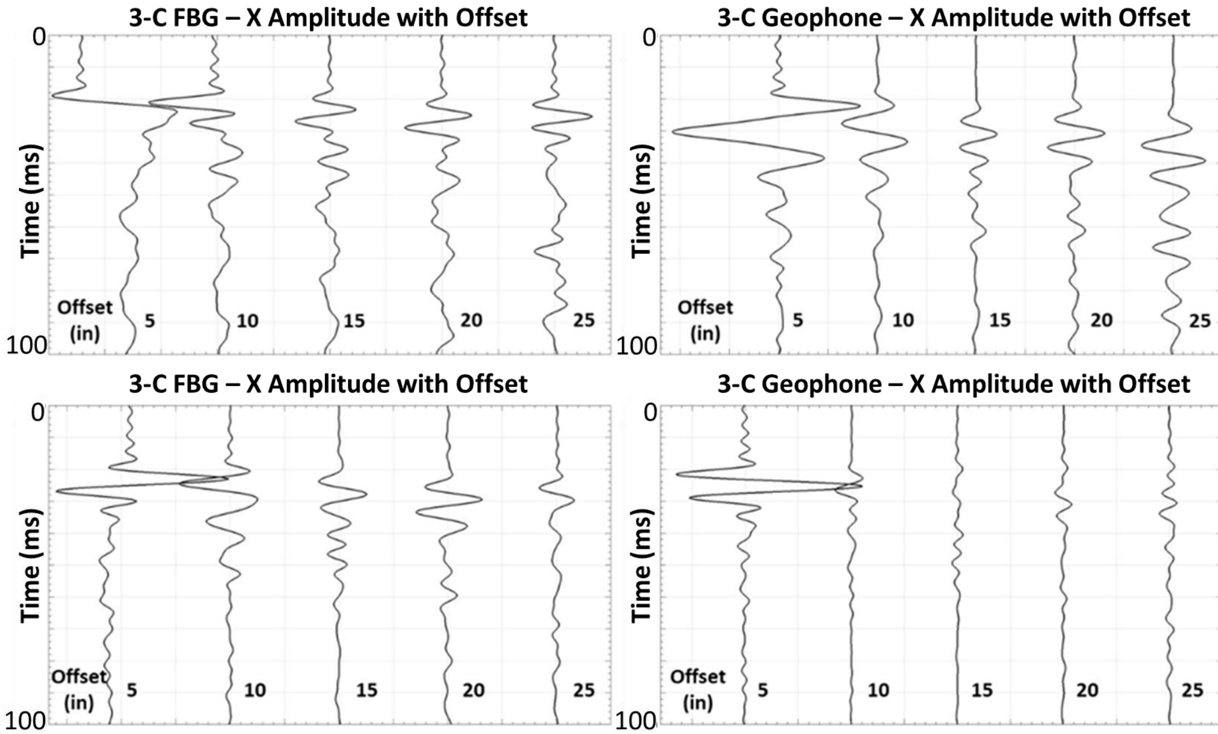

Figure 5.12: Walk-away response for wooden FOS and geophone for the X and Z components.

Next, we compare the multicomponent response at far offset (25 in) in the time and frequency domain. The weight drop results show similar frequency content (Figure 5.13), capturing a peak frequency of around 40 Hz and 90 Hz, however, the amplitudes are significantly different. The 3-C FBG shows the highest amplitude at 40 Hz, whereas the 3-C geophone shows the highest amplitude at 90 Hz. The vibratory source results (Figure 5.14) show more comparable time and frequency responses, where both sensors measure the source frequency at 145 Hz, with both sensors exhibiting harmonics of the source at 290 Hz.

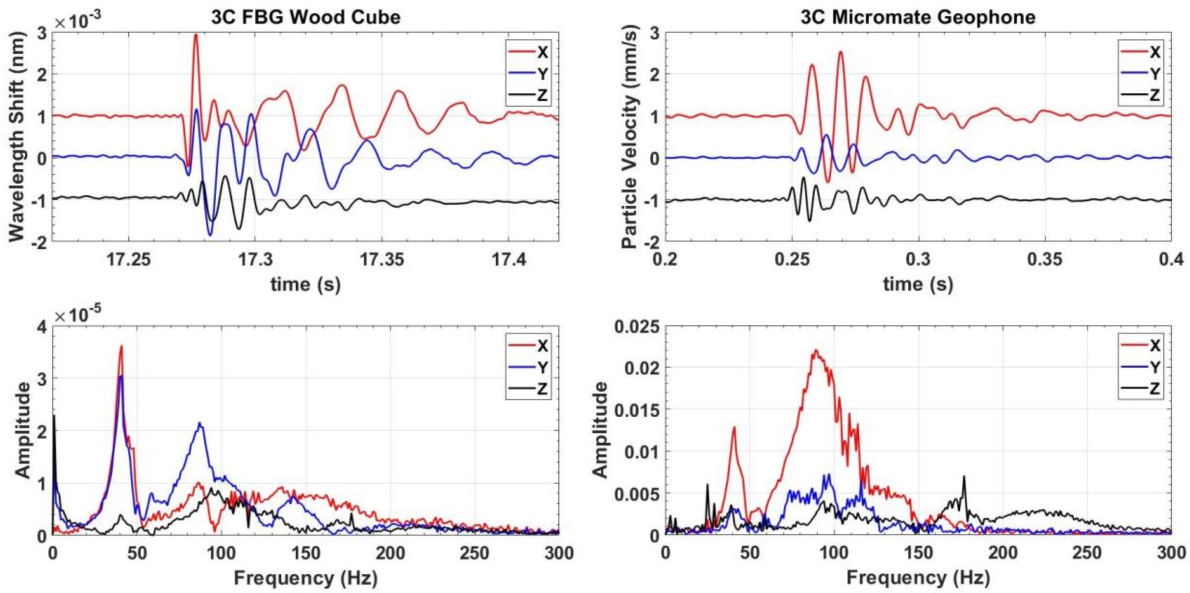

Figure 5.13: Weight drop source results for the 3-C FBG sensor (left) and the 3-C geophone (right) at maximum offset (25 in) (Alfataierge and Stewart, 2019).

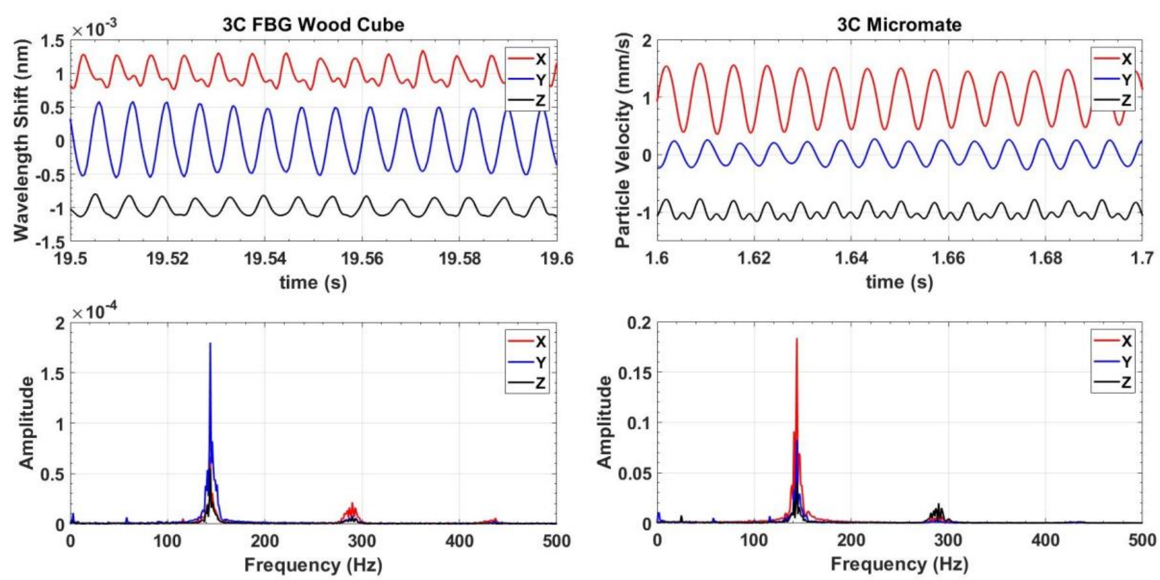

Figure 5.14: Vibratory source results for the 3-C FBG sensor (left) and the 3-C geophone (right) at maximum offset (25 in) (Alfataierge and Stewart, 2019).

Next, hodogram analysis is done on the results presented in Figures 5.13 and 5.14 to evaluate the vector fidelity of the 3-C FBG sensor. Figure 5.15 presents the hodogram results for the 3-C FBG sensor and the 3-C geophone with respect to the weight drop source results presented in Figure 5.13. The results show that there is no positive correlation between the 3-C FBG sensor and the 3-C geophone. The source was offset in the X direction and therefore the hodogram is expected to point towards the source with maximum particle displacement in the X-direction. Which is the case with the 3-C geophone results, but not with the 3-C FBG results. Next, the hodogram analysis is done on the vibratory source data (Figure 5.16). The vibratory source hodogram analysis confirms the observation made with respect to the weight drop source. Finding no positive correlation in the FBG vector response. One possible explanation is considering the variable particle displacement at the geophone, which was placed on the surface, in comparison to the 3-C FBG which was buried beneath the geophone. Therefore, these experiments were reconsidered with mounting the FBGs to the geophone (Figure 5.7c) and burying the sensors. The results of the new setup were still the same, with no positive correlation between the 3-C FBG hodogram results and the 3-C geophone results. Thus concluding that the 3-C FBG sensor lacks vector fidelity.

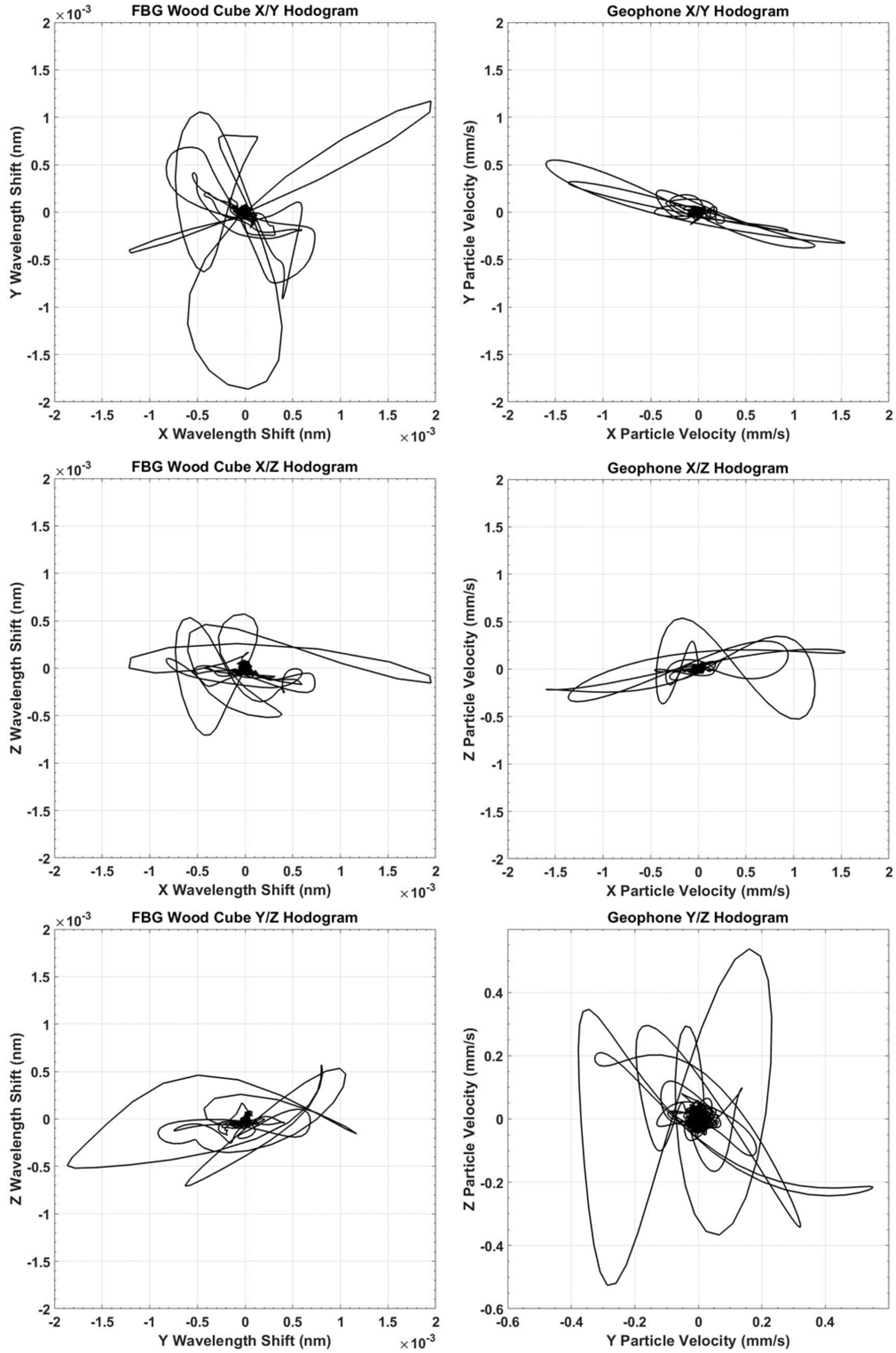

Figure 5.15: Hodogram analysis results for the 3-C FBG sensor (left) and the 3-C geophone (right) with respect to the weight drop source. X/Y, X/Z, and Y/Z hodograms are presented from top to bottom respectively.

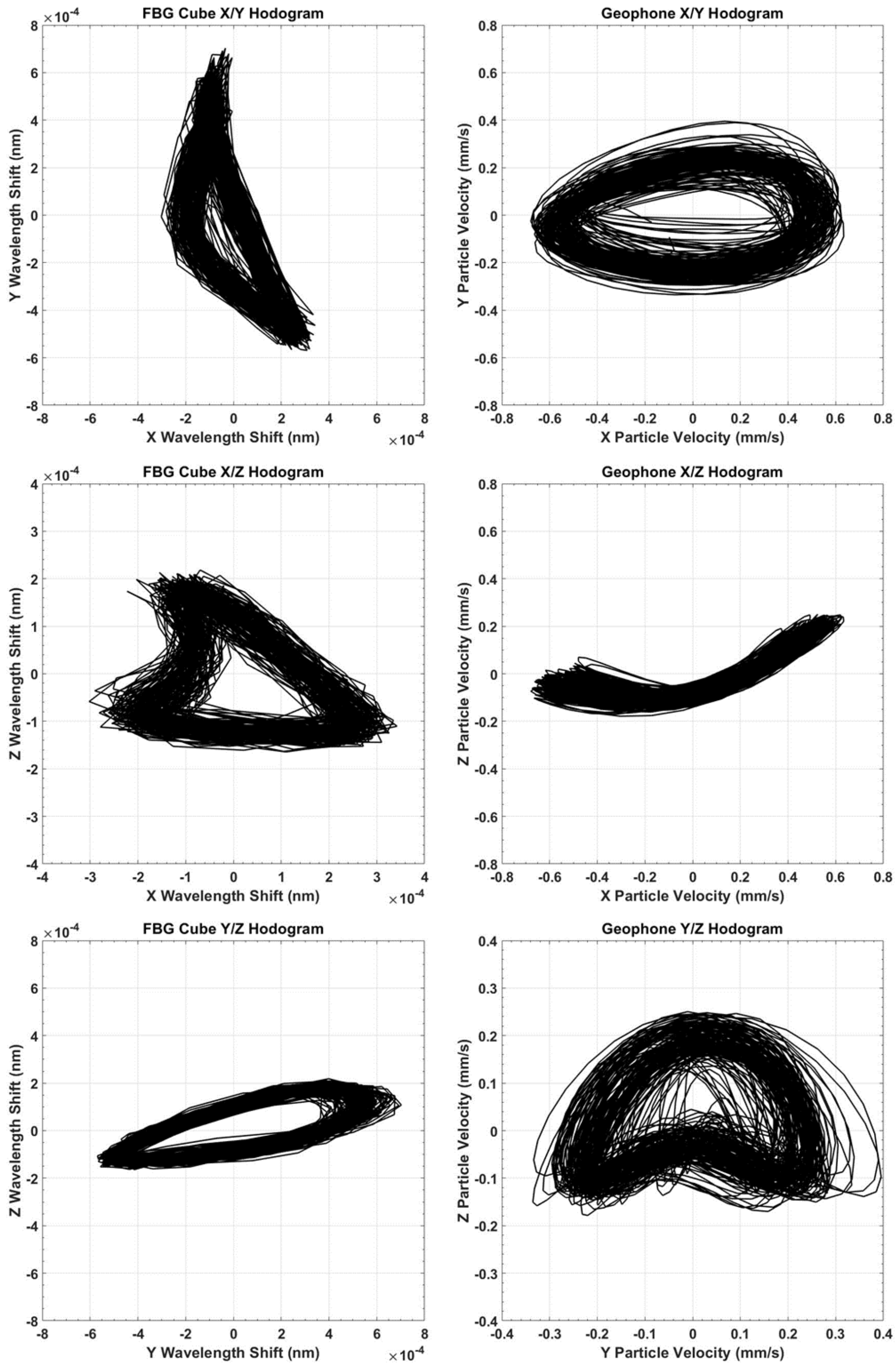

Figure 5.16: Hodogram analysis results for the 3-C FBG sensor (left) and the 3-C geophone (right) with respect to the vibratory source. X/Y, X/Z, and Y/Z hodograms are presented from top to bottom respectively.

Overall, the results show that the 3-C FBG cube can produce comparable multicomponent measurements to a 3-C geophone and that the material of the cube (wood, glass, or aluminum) had no significant influence on the data. The impact source results show that both systems capture a source frequency signature of 40 Hz and 90 Hz, however, the geophone shows a higher amplitude response at 90 Hz. The Vibratory source results show that both systems were able to capture the frequency response of the source around 145 Hz along with the harmonic frequencies. The FBGs demonstrated higher sensitivity to the source harmonic frequencies in the vibratory source measurements. The hodogram analysis shows that the spatial response of each sensor is not identical. In conclusion, we find that it is possible to make multicomponent fiber-optic vibration sensors using FBGs. However, further work is required to better understand why the FBGs lack vector fidelity.

CHAPTER VI

CONCLUSIONS

This chapter summarizes the findings and contributions of this dissertation. The findings are grouped into two categories, field and laboratory observations. Field observations include applications of FOMS in BSI and SSI (Chapters 2 and 3). Laboratory observations include applications of FOMS to a simulated marine environment and multicomponent seismic considerations (Chapters 4 and 5).

6.1. <u>Summary of Field Observations:</u>

A summary of the findings from Chapter 2 and 3 with regards to applications of FOMS in BSI and SSI is presented:

6.1.1. Borehole Seismic Imaging

Seismic data acquisition capabilities of DAS and geophones in a borehole setting were evaluated, with both DAS fiber and geophones cemented behind casing. Two seismic source types were tested, an accelerated weight drop (AWD) and a Vibroseis truck, recorded by the two receiver arrays. The AWD required a high fold (16 for geophone data) to achieve an acceptable signal-to-noise ratio (SNR = 10). Whereas, the Vibroseis source was able to provide significantly better data (SNR = 25) at lower fold (8 for geophone and 32 for DAS). As expected, the SNR in the stack is proportional to the square root of the number of shots.

For DAS, data quality depends on the system's optical parameters. I investigated the parameters using a dual-pulse phase-based DAS interrogator. The optimal gauge length (GL) correlated to about one-quarter of the seismic wavelength (4.5 m). This optimal GL, out of a range from 2 m to 12 m, yielded the highest SNR for the shot gather and provided the highest correlation to geophone results at the corridor stack stage. It was concluded that the AWD source is not optimal for DAS surveying with the purpose of reflection imaging; it is, however, sufficient for check-shot applications. Furthermore, optimizing optical amplifiers and selecting the GL based on seismic wavelength is necessary to obtain optimal data quality.

For FBGs, the feasibility of VSP via FBGs was demonstrated, finding comparable results to a hydrophone array. The field trial showed that a source trigger mechanism is something that must be considered for FBG monitoring systems, as they currently operate on a manual trigger basis.

6.1.2. Surface Seismic Imaging

The application of surface seismic imaging using a surface trenched fiber in a unique geometry was explored. Finding that surface waves were best suppressed using the Zheng-Hu method of surface-wave modeling and subtraction, in comparison to a conventional approach using f-k filters. Also finding that in both cases no reflection events were observable, thus concluding that the proposed processing of the horizontal Smart DAS data for converted-wave imaging would be challenging at least.

In considering the data for surface wave analysis using an MASW approach, it was demonstrated that the final MASW shear-wave velocity model correlated with values published by Bakulin et al. (2019) on similar analysis done on part of the Smart DAS fiber.

Additionally, an application to urban infrastructure monitoring using DAS on telecommunication fibers in an existing telecommunication fiber-optic network was demonstrated. Highlighting the challenges associated with such application that comes from the working with telecommunication fiber-optic connectors. Also, presenting a case for positive identification of train activity on the train rails at the University of Houston campus, and identifying the speed of the train on the rails.

Finally, a field test was presented, demonstrating the feasibility of using an FBG array for surface seismic imaging. Contributing many lessons learned from the experiment on fiber-optic handling and deployment as well as the limitations of the acquisition system.

6.2. Summary of Laboratory Observations

A summary of the findings from Chapters 4 and 5 on the applications of FOMS in a simulated marine environment and considerations of multicomponent FOMS is presented:

6.2.1. Pipeline Flow Assessment and Integrity

Two primary observations were made with regards to the response of FBGs to flow. First, the overall shift in the wavelength correlated with the flow rate, such that an increase in flow resulted in an increase in the wavelength shift. Second, short-term fluctuations in wavelength corresponded to the turbulence in the flow produced by the flow control valve. Similarly, DAS amplitudes corresponded to the turbulence in flow. In conclusion, the fiber-optic sensing system showed considerable promise for monitoring flow in pipes.

6.2.2. Marine Seismic Source Characterization

The fiber optic sensing systems used in this study were able to sense the seismic sources while preserving the frequency response of the source. FBGs were found to be able to detect seismic sources even when uncoupled from solid support and suspended in water. The experiments conducted in this study show that the fiber-optic sensors can be considered as a marine seismic receiver on the ocean floor and potentially as a streamer.

6.2.3. Underwater Communication

A concept for using PZT transducers and a DAS system for underwater communication in a marine environment was demonstrated, showing that such an application would be feasible using frequencies up to 24.5 kHz. Future tests should consider sending coded messages from the transducer and measuring them on the DAS system and decoding them, further demonstrating the feasibility of such an application.

6.2.4. Multicomponent FOMS

Overall, the results showed that FBGs have amplitude and frequency fidelity but lack vector fidelity. Demonstrating that the 3-C FBG sensor produced comparable multicomponent measurements to the 3-C geophones and that the material of the sensor was coupled to (wood, glass, or aluminum) had no significant influence on the data.

6.1. Conclusion of the Dissertation

This dissertation has presented several cases supporting applications of fiber-optic motion sensing in the field (borehole seismic imaging, surface seismic imaging, and infrastructure monitoring) and in the laboratory (pipeline flow assessment and integrity, marine seismic source characterization, underwater communication, and multicomponent FBG sensing). A summary of this work has been discussed in chapter 6, highlighting the contributions of each section. Overall, this dissertation serves as a contribution to academia, as a foundation for future students seeking research in the field of fiber-optic sensing, demonstrating the various applications that can be explored within the domain of fiber-optic sensing. Additionally, findings have contributed to industry, highlighting the importance of optimizing optical parameters prior to seismic data acquisition, demonstrating the effect of gauge length on VSP data, providing a guide to selecting such gauge length, demonstrating novel applications to DAS with MASW, demonstrating the effectiveness of the Zheng-Hu method in suppressing surface waves, providing a relationship between fluid flow in pipelines and the relative change in FBG wavelengths, demonstrating the capabilities of DAS and FBGs in characterizing marine seismic sources, and providing a multicomponent FBG sensor prototype for seismic sensing applications. These are some of the major contributions to this dissertation.

In conclusion, the evidence clearly shows the maturity of fiber-optic sensing systems and the untapped potential and the plethora of applications that can be obtained from a sensing system that has many advantages to conventional electronic sensing systems. Nonetheless, each technology has its limitations and its own challenges. I leave no preference to one technology or one sensing system over the other, the final conclusion is that all these systems are great and each one of them has something to offer. Once you understand the functionality of each system you will see that it is not fair to compare them to one and other, as they are not at the same level, they are not simply "apples and oranges" but rather fruits and vegetables. Each system has its advantages and disadvantages, as each fruit and vegetable have its minerals and vitamins. One cannot live on fruits alone nor vegetables alone, a balanced diet is what we need. Similarly, a balanced diet of fiber-optic sensors and electrical sensors makes for the best geophysical regimen, having the systems complement each other.

CHAPTER VII

FUTURE WORK

Potential for future work is fairly evident in this dissertation with suggestions left for each chapter. With regards to the application of borehole seismic imaging, considerations on depth calibration of the fiber is one topic that needs to be explored, I have suggested a method for approaching this problem but the suggested solution is limited to the presented experiment. For FBGs in borehole seismic sensing, the test that was presented had limited resources, thus with additional funding, such experiment could be done better, having a longer FBG array would have allowed for better imaging and a complete VSP acquisition that could be processed and benchmarked against the hydrophones.

Other applications to surface DAS have been demonstrated by people at Stanford and cited in the dissertation, such work could be reproduced at the University of Houston. The university has access to 27 km of dark fiber that is designated for research, a loop of fiber that crosses many active roads in Houston. That alone has potential for several applications of active and passive seismic monitoring.

Additionally, further experimentation in the laboratory can be done to help establish a stronger relationship between flow and the fiber-optic systems, using a controlled flow loop and introducing multi-phase flow are two options to explore. Further work on the development of fiber-optic marine streamers would be a major contribution.

Future work considering multicomponent FBG sensing can consider the use of 3-C printing technologies to develop a Fiber-Optic Geophone (FOG). A prototype design was created during this dissertation that faced challenges with accommodating a multiplexed FBG geometry. The design presented in Figure 7.1 considers the use of three fibers with a single FBG on each fiber, such design is not favorable, as it would require a three-channel interrogator. Future designs should consider using a quasi-distributed FBG fiber. Other considerations should be made with respect to the termination of the fiber from the sensor structure. This should be done in a way that the fiber is not overstrained or bent beyond the fiber bend-loss radius.

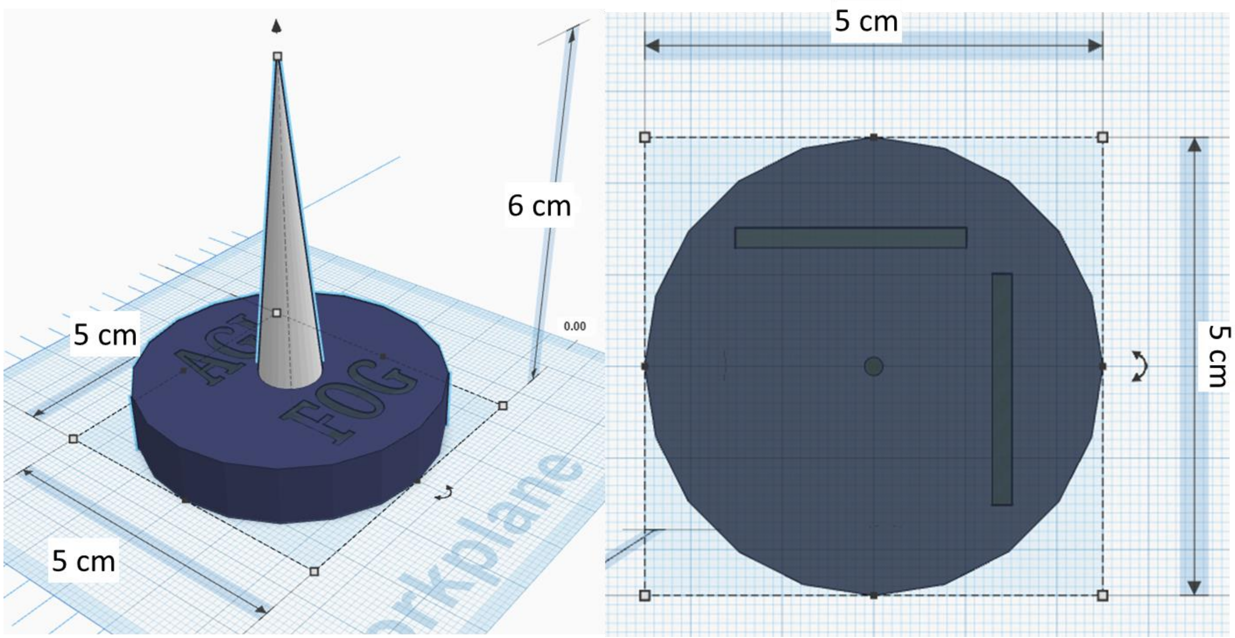

Figure 7.1: 3-C FOG (Fiber-Optic Geophone) prototype.

A model designed for 3D printing to incorporate three FBGs in three orthogonal directions.

BIBLIOGRAPHY

Alfataierge, E., and R. R. Stewart, 2018, Seismic receiver comparison: fiber optic sensors vs. geophones: Poster presented at the HGS Annual Sheriff Lecture.

Alfataierge, E., and R. R. Stewart, 2019, Multicomponent fiber optic sensing: A comparison between FBGs and Geophones: Poster presented at the Annual Dobrin Lecture.

Alfataierge, E., L. Chang, N. Dyaur, R. R. Stewart, and M. Ho, 2018, Fiber optic sensing applications for marine environments: Presented at the SEG Summer Research Workshop.

Alfataierge, E., N. Dyaur, and R. R. Stewart, 2019a, Measuring Flow in Pipelines via FBG and DAS Fiber Optic Sensors: OTC Houston.

Alfataierge, E., N. Dyaur, L. Chang, and R. R. Stewart, 2019b, Marine Seismic Source Characterization Using Fiber Optic Sensors: OTC Houston.

Bakku, S. K., 2015, Fracture characterization from seismic measurements in a borehole: Ph.D. thesis, Massachusetts Institute of Technology.

Bakulin, A., P. Golikov, R. Smith, K. Erickson, I. Silvestrov, and M. Al-Ali, 2017a, Smart DAS upholes for simultaneous land near-surface characterization and subsurface imaging: The Leading Edge, **36**, 1001–1008.

Bakulin, A., P. Golikov, R. Smith, K. Erickson, I. Silvestrov, and M. Al-Ali, 2017b, Smart DAS upholes for near surface model building and imaging with vertical arrays: International Conference on Engineering Geophysics, SEG, Expanded Abstracts, 252-255.

Bakulin, A., I. Silvestrov, and R. Pevzner, 2018a, Surface seismic with DAS: Looking deep and shallow at the same time: SEG Technical Program Expanded Abstracts, 16-20.

Bakulin, A., P. Golikov, K. Erickson, I. Silvestrov, Y. S. Kim, R. Smith, and M. Al-Ali, 2018b, Seismic imaging of vertical array data acquired using smart DAS uphole acquisition system: SEG Technical Program, SEG, Expanded Abstracts, 4050-4054.

Bakulin, A., P. Golikov, R. Smith, K. Erickson, I. Silvestrov, and M. Al-Ali, 2018c, Smart DAS uphole acquisition system for near-surface characterization and imaging: SEG Technical Program, SEG, Expanded Abstracts, 201-205.

Bakulin, A., I. Silvestrov, and R. Pevzner, 2019, Surface seismic with DAS changes land acquisition: Middle East Oil and Gas Show and Conference, SPE, 1-12.

Baker, E. T., Jr., 1979, Stratigraphic and hydrogeologic framework of part of the coastal plain of Texas: Texas Department of Water Resources Report 236, 43.

Buck, A., 2017, The importance of mass flow measurement and the relevance of coriolis technology, https://www.bronkhorst.com/blog/the-importance-of-mass-flow-measurement-and-the-relevance-of-coriolis-technology-en/, accessed: January 3, 2017.

Biondi, B., E. Martin, S. Cole, M. Karrenbach, and N. Lindsey, 2017, Earthquakes analysis using data recorded by the Stanford DAS array: 87th International Exposition and Annual Meeting, SEG, Expanded Abstracts, 2752-2756.

Cole, S. and M. Karrenbach, 2019, MASW analysis of active-source and passive DAS fiber-optic data: 89th International Exposition and Annual Meeting, SEG, Expanded Abstracts, 968-973.

Cheng, D., X. Zhao, M. Willis, R. Zhou, M. Zhang, and D. Quinn, 2019, Channel decimation and impact on DAS VSP data processing: 89th International Exposition and Annual Meeting, SEG, Expanded Abstracts, 5350- 5354.

Crawford, D., 2014, APC vs. UPC: What's the difference?, https://www.belden.com/blog/data-centers/upc-or-apc, accessed 12 November 2019.

Dean, T., T. Cuny, and A. Hartog, 2016, The effect of gauge length on axially incident P-waves measured using fibre optic distributed vibration sensing: Geophysical Prospecting, **65**, 184-193.

Dean, T., and D. Sweeney, 2019, The effect of land seismic recording system noise levels on survey productivity: 81st EAGE Conference and Exhibition, Expanded Abstracts.

Ellmauthaler, A., D. A. Barfoot, M. E. Willis, X. Wu, C. Erdemir, O. Barrios, D. Quinn, and S. Shaw, 2016, Depth calibration for DAS VSP – Lessons learned from two field trials: 86th International Exposition and Annual Meeting, SEG, Expanded Abstracts, 632 - 636.

Fernandez, A., F. Berghmans, B. Brichard, P. Mégret, M. Decréton, M. Blondel, and A. Delchambre, 2001, Multi-component force sensor based on multiplexed fibre Bragg grating strain sensors: Measurement Science and Technology, **12**, 810-813.

Fang, G., Y. E. Li, Y. Du, J. H. Yin Ma, E. Martin, and D. Yu, 2018, Near-surface monitoring enabled by distributed acoustic sensing: An example of the Stanford Array data: 88th International Exposition and Annual Meeting, SEG, Expanded Abstracts, 2677-2681.

Gordon, A., D. Lawton, K. Hall, B. Freifeld, T. Daley, and P. Cook, 2018, Depth registration of VSP DAS fibre: 88th International Exposition and Annual Meeting, SEG, Expanded Abstracts, 5427 - 5431.

Dean, T., A. Hartog, and B. Frignet, 2015, Seismic without sensors - distributed vibration sensing: ASEG, Extended Abstracts, 1-4.

FBGS, 2017, TR-TSC-PR2017_39: Temperature and Strain calibration test report.

Hayward, P., 2018, Personal discussion on: "Interrogating telecommunication fibers".

Hardeman-Vooys, H. K., M. P. Lamoureux, 2019, Analytic models of distributed acoustic sensing data for straight and helical fibre: GeoConvention, 1-4.

Hartog, A., 2017, An Introduction to Distributed Optical Fibre Sensors. CRC Press.

Hecht, J. (1999). City of Light: The Story of Fiber Optics. New York: Oxford University Press.

Hornman, J. C., 2017, Field trial of seismic recording using distributed acoustic sensing with broadside sensitive fiber-optic cables: Geophysical Prospecting, **65**, 35-46.

Hu H., M. Senkaya and Y. Zheng, 2019, A novel measurement of the surface wave dispersion with high and adjustable resolution: Multi-channel nonlinear signal comparison: Journal of Applied Geophysics, **160**, 236-241.

Hu H. and Y. Zheng, 2019, Data-driven dispersive surface-wave separation using high-resolution dispersion estimation, Presented at the SEG Near Surface Modeling and Imaging Workshop in Manama, Bahrain.

Innanen, K. A., D. Lawton, K. Hall, K. L. Bertram, M. B. Bertram, and H. C. Bland, 2019, Design and deployment of a prototype multicomponent distributed acoustic sensing loop array: 89th International Exposition and Annual Meeting, SEG, Expanded Abstracts, 953-957.

Ivanov, J., R. D. Miller, and G. Tsoflias, 2008, Some practical aspects of MASW analysis and processing: Symposium on the application of geophysics to engineering and environmental problems, **21**, 1186-1198.

Kersey, A. D., M. A. Davis, H. J. Patrick, M. LeBlanc, K. P. Koo, C. G. Askins, M. A. Putnam, and E. J. Friebele., 1997, Fiber Grating Sensors: Journal of Lightwave Technology, **15**, 8, 1442-1463.

Krohn, D., 2015, Fiber Optic Sensors: Fundamentals and Applications.

Kuvshinov, B. N., 2016, Interaction of helically wound fibre-optic cables with plane seismic waves: Geophysical Prospecting, **64**, 671-688.

LeBlanc, Michel, 2000, Acoustic sensing using free and transducer-mounted fiber Bragg gratings: Fourteenth International Conference on Optical Fiber Sensors.

Lim, I. C. N., and P. Sava, 2016, Multicomponent distributed acoustic sensing: 86th International Exposition and Annual Meeting, SEG, Expanded Abstracts, 5597-5602.

Lim, I. C. N., and P. Sava, 2017, High-resolution multicomponent distributed acoustic sensing, 87th International Exposition and Annual Meeting, SEG, Expanded Abstracts, 941-946.

Lim, I. C. N., and P. Sava, 2018, Multicomponent distributed acoustic sensing: Concept and theory: Geophysics. **83**, 2, 1-8.

Martin, E., B. Biondi, M. Karrenbach, and S. Cole, 2017, Continuous subsurface monitoring by passive seismic with distributed acoustic sensors – the “Stanford Array” experiment: 15th International Congress of the Brazilian Geophysical Society, 1366-1370.

Martin, E., and B. Biondi, 2017, Ambient noise interferometry across two-dimensional DAS arrays: 87th International Exposition and Annual Meeting, SEG, Expanded Abstracts, 2642-2646.

Martin, E., and B. Biondi, 2018, Eighteen months of continuous near-surface monitoring with DAS data collected under Stanford University: 88th International Exposition and Annual Meeting, SEG, Expanded Abstracts, 2642-2646.

Mateeva, A., J. Mestayer, B. Cox, D. Kiyashchenko, P. Wills, J. Lopez, S. Grandi, K. Hornman, P. Lumens, A. Franzen, D. Hill, and J. Roy, 2012, Advances in Distributed Acoustic Sensing (DAS) for VSP: SEG Technical Program Expanded Abstracts: 1-5.

McDonald, M., 2019, Personal discussion on: “Principles of Helios DAS”.

Mestayer, J., B. Cox, P. Willis, D. Kiyashchenko, J. Lopez, M. Costello, S. Bourne, G. Ugueto, R. Lupton, G. Solano, D. Hill, and A. Lewis, 2011, Field Trials of Distributed Acoustic Sensing for Geophysical Monitoring: International Exposition and Annual Meeting, SEG, Expanded Abstracts, 4253-4257.

Nobel, J. E., P. W. Bush, M. C. Kasmarek, and D. L. Barbie, 1996, Estimated depth to the water table and estimated rate of recharge in outcrops of the chicot and Evangeline aquifers near Houston, Texas: USGS Water-Resources Investigations Report 96-4018, 1-19.

Qiao, X., Z. Shao, W. Bao, Q. Rong, 2017, Fiber Bragg Grating Sensors for the Oil Industry: Sensors, **17**(429), 1-34.

Somerville, M., 2012, Flow measurement via novel fiber Bragg grating optical sensor: M.S. thesis, University of Delaware.

Shroyer, B., Dria, D., 2017, Fiber-Optic Completion and Deployment: Presented at the Fiber-Optics Workshop, SPE.

Smith, R., A. Bakulin, and M. Jervis, 2019, Performance of a hybrid seismic monitoring system with buried receivers for an onshore carbonate reservoir: Current status and way forward: SEG Technical Program Expanded Abstracts, 5234-5238.

Stewart, R. R., and J. P. Disiena, 1989, The values of VSP in interpretation: The Leading Edge. **8**, 16-23.

Stewart, R. R., 1984, VSP interval velocities from traveltime inversion: Geophysical Prospecting. **32**, 4, 608-628.

Suresh, R., S. C. Tjin, and S. Bhalla, 2009, Multi-component force measurement using embedded fiber Bragg grating: Optics and Laser Technology, **41**, 431-440.

The Nobel Foundation. (2009). Press Release. The Nobel Foundation. Retrieved from https://www.nobelprize.org/nobel_prizes/physics/laureates/2009/press.html

Toko, J., 2017, LIOS DTS Services: Presented at the Fiber-Optics Workshop, SPE.

Willis, M., D. Barfoot, A. Ellmauthaler, X. Wu, O. Barrios, C. Erdemir, S. Shaw, D. Quinn, 2016, Quantitative quality of distributed acoustic sensing vertical seismic profile data: The Leading Edge. **35**, 7, 605-609.

Willis, M., A. Ellmauthaler, M. LeBlanc, W. Palacios, and X. Wu, 2018, Comparing distributed acoustic sensing, vertical seismic profile data acquired with single- and multi-mode fiber optic cables: SEG Technical Program Expanded Abstracts, 4674-4678.

Williams, J., 2012, Distributed acoustic sensing for pipeline monitoring: Pipeline & Gas Journal, **239**, 7.

Williams, J., 2017, The use of DAS in other industries: Infrastructure monitoring and beyond: Presented at the 87th Annual International Meeting, SEG.

Wu, X., M. E. Willis, W. Palacios, A. Ellmauthaler, O. Barrios, S. Shaw, and D. Quinn, 2017, Compressional- and shear-wave studies of distributed acoustic sensing acquired vertical seismic profile data: The Leading Edge, **36**, 987–993.

Zheng Y. and H. Hu, 2017, Nonlinear signal comparison and high-resolution measurement of surface wave dispersion, BSSA, **107**, 3, 1551-1556.

APPENDICES

APPENDIX A

DAS USER OPERATIONS MANUAL

INTRODUCTION

This manual has been compiled using the supporting materials provided by Fotech and experience gained through using the equipment. With this manual, you will be able to operate the equipment, acquire data, and display the data. We recommend looking over the entire document prior to operating the equipment and not to rely on the Quick Setup Guide.

The Quick Setup Guide guides the user to quickly record data under the assumption that all acquisition parameters have been preset. In Hardware Setup, we guide the user on handling and deploying the Helios Theta Interrogator for acquisition. In Software Setup, we discuss accessing the Helios Theta unit via the web browser and navigating the software interface for acquisition and data display. In Data Extraction, we discuss the necessary steps to extract recorded data from the unit. In Demo, we discuss setting up the unit for a quick demonstration of the capabilities of the unit.

QUICK SETUP GUIDE

In this section, we go over a quick setup of the Fotech Helios Theta interrogator, starting with instructions on connecting the equipment, then starting the system, and finally accessing the onboard software via an internet browser. We will further discuss the necessary steps to optimizing the optical parameters and recording data. Further setup details will be discussed in the following chapters.

1. Ensure that all connections on the back of the unit are secure and are connected as illustrated.

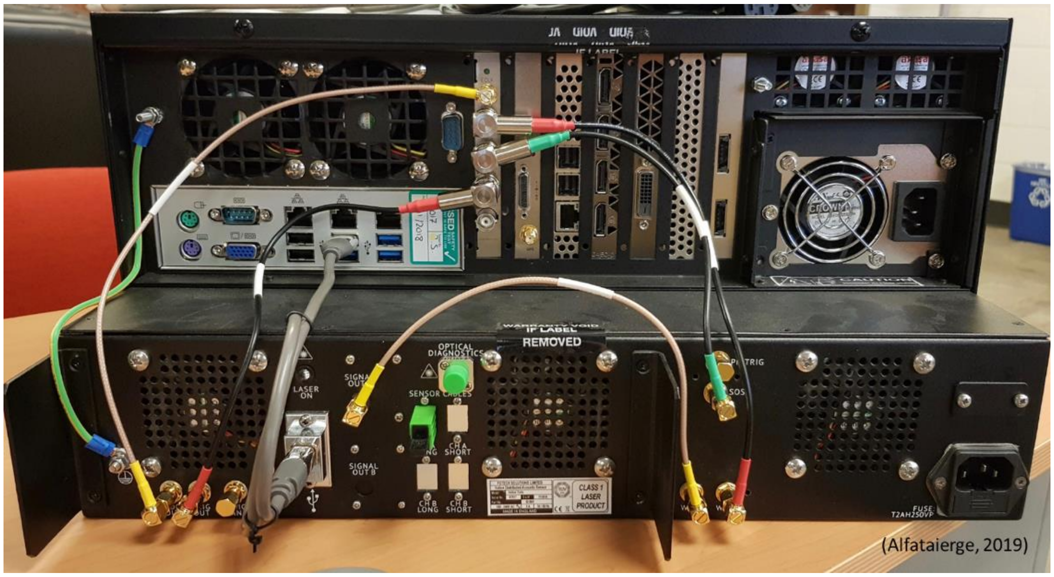

2. Turn on the unit by pressing on the upper power switch (PC power), then press on the lower power button (laser power).

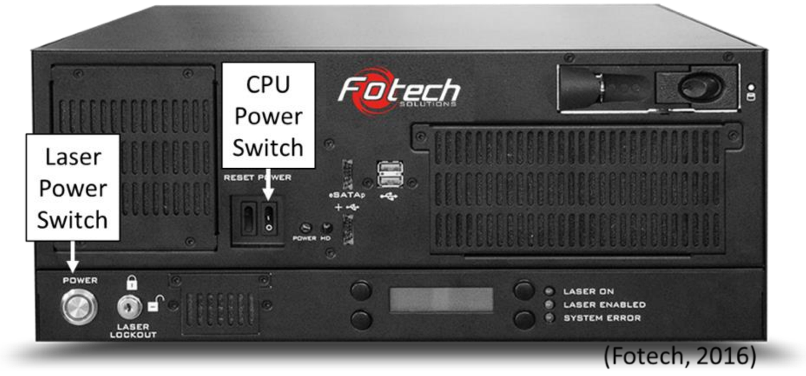

3. As the laser is powering up, make sure that the status button shows all rectangles.

4. Connect the ethernet cable to the ethernet port on Laptop.
5. Launch the internet browser on the Laptop.
6. Type the unit IP address in the browser bar (192.168.33.60)
7. Log in (User: administrator, Password: password)

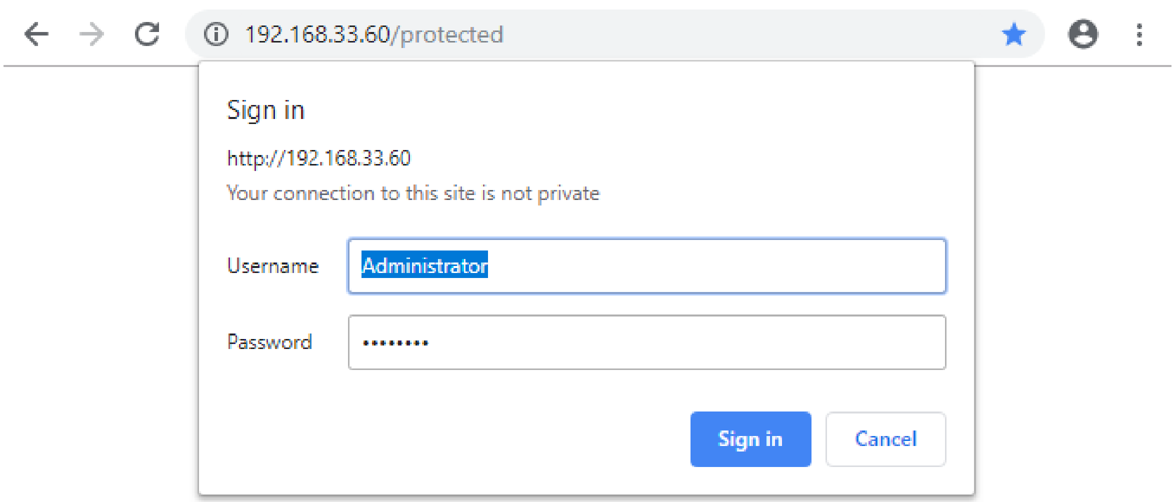

You are now logged into the user interface and can start optimizing the unit once it has fully started up.

8. Navigate to the optical settings
9. Make sure the fiber length exceeds the amount of fiber that will be interrogated.
10. Make sure to set the digitizer voltage to 4v as to not overpower the digitizer.
11. Set the EDFA values to the factory recommended settings.
12. Disable logging

13. Access the Raw Fiber Shot display
14. Enable Oscilloscope mode
15. Physically unlock the laser using the key, then Enable laser and recording on the software.

We have now completed the process for starting the system, we will now wait for the FBG to tune. once the amplitudes have stabilized, we can proceed with optimizing the optical parameters.

16. Change the Pulse Repetition Frequency (PRF) based on the desired frequency bandwidth. Note in Fidelity mode the frequency bandwidth is 1/3 the PRF.
17. Change Pulse Width (P_w) and Pulse Gap (P_g) to achieve the desired Gauge-length (G_L). You may use the following equation to calculate the G_L.

$$G_L = V\left(\frac{P_w + (P_w * P_g)}{4}\right) \text{ where } V = \frac{C}{n}$$

G_L: Gauge Length (m), P_w: Pulse Width (ns), P_g : Pulse Gap (%),

V : Speed of Light in Fiber (m/s), C : Speed of Light in Vacuum (m/s)

n : Fiber Refractive Index

18. Change the Digitizer voltage and EDFA values to get the average backscatter amplitude at 2/3 of the scale. While ensuring that your data does not clip. (Note: Digitizer voltage will apply large shifts in the amplitudes, while EDFA values will apply small shifts. Also, EDFA 2 and 3 should always be equal.)

The system should now be optimized and ready for acquisition. You can now proceed to the Phase-Polar display or Acoustic Display (if theta is disabled). The next step is to set up the system for recording.

19. Specify the file name and data location for recording and choose the parameters to be recorded (i.e. raw, phase, acoustic, …), then enable logging to start recording. This information is accessed through data logging settings.

This concludes the quick setup guide for setting up the system and recording. Additional details on each step will be provided in the following chapters, as well as optional settings that are available.

HARDWARE SETUP

In this section, we will discuss the hardware setup of the Helios Theta unit and the various components of the device.

A simplified diagram of the internal system of the Helios Theta interrogator is shown in figure A.1. The system consists of two chains, a transmitting chain and a receiving chain. The transmitting chain consists of the various components of the laser pulser, EDFA 1, and the connected fiber sensor. Each EDFA (Erbium-doped Fiber Amplifier) is followed by an optical filter, the amplifier is necessary to increase the power of the laser pulse, while the filter filters any sidelobe that is enhanced during the amplification process (you can think of these as optical magnifiers and FBG filters). The receiver chain consists of the optical fiber sensor, EDFAs 2 and 3, and the Output backscatter signal. Here the transmitted signal interacts with the fiber to reflect backscattered energy that is diverted by the optical switch towards EDFAs 2 and 3. EDFAs 2 and 3 perform a two-step amplification and filtration process to enhance the measured backscatter signal. This is done in two steps rather than using one larger amplifier in order to minimize the amplifier generated noise. Finally, the optical signal is sensed by the optical detector and digitized to an output signal. The parameters of the laser and the EDFAs are all controlled digitally via the software interface. These parameters are tested during the acquisition process to determine the best combination of parameters for the tested application and fiber geometry.

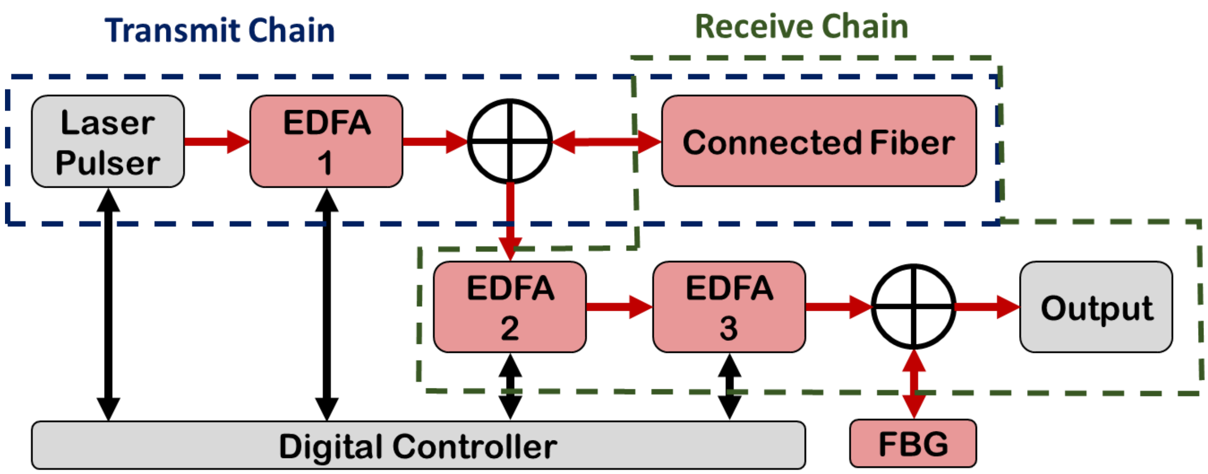

Figure A.1: Simplified diagram of the interrogator system.
We start with a laser pulse generated from the laser pulser and sent through EDFA-1 to the optical switch, the signal then is diverted do the connected fiber sensor. The backscatter is diverted from the optical switch to EDFAs 2 and 3 and to another optical switch. The second optical switch allows for diagnostics via the FBG, otherwise, the signal is detected by the optical detector and output as the raw backscatter signal.

The Helios Theta interrogator consists of two major components, a Linux OS CPU and a Laser, these are highlighted in Figure A.2. These two systems are connected by a set of external cables. It is important to always check that these cables are securely connected and to follow the layout shown in Figure A.2.

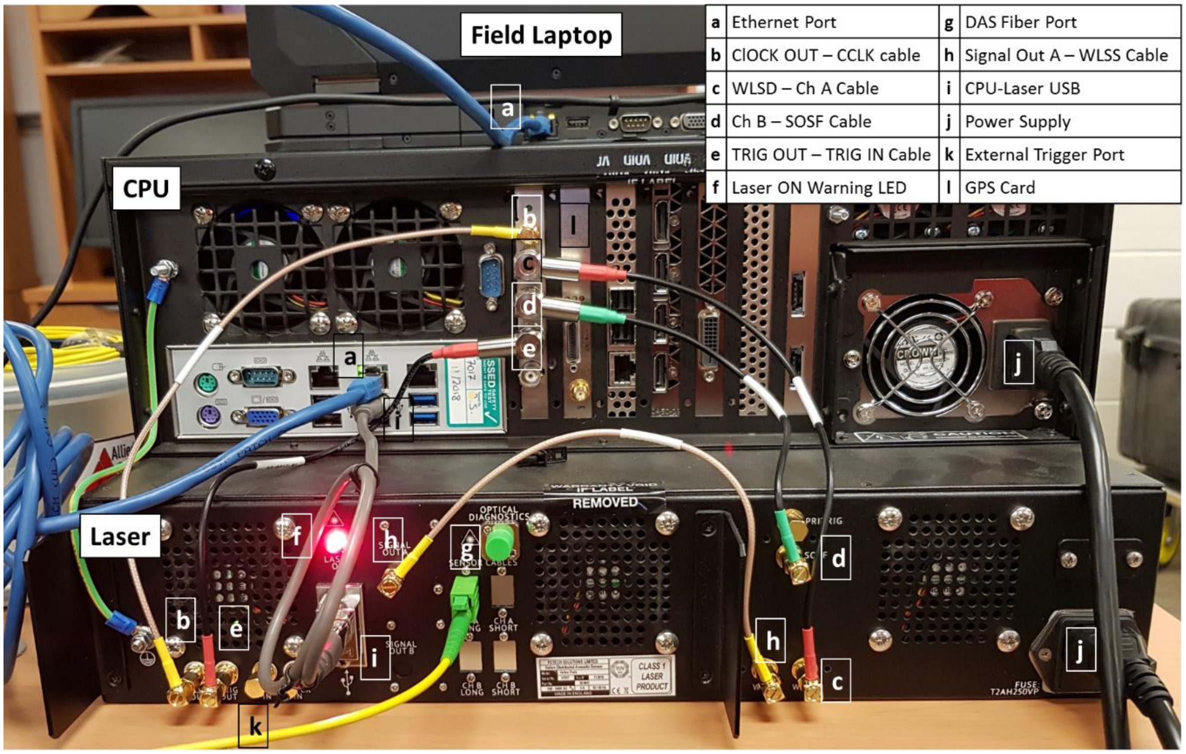

Figure A.2: An annotated image of the rear connections of the Helios Theta interrogator.
It is important that all connections are checked and made secure prior to operation, in order to avoid any complications or contamination of the acquired data.

Things to note:

- When transporting the equipment for short-distance transport, you may leave all the cables connected except for the CPU-Laser communication USB (Figure A2i). Otherwise, it is best to disconnect all cables to avoid breaking any of the connectors.
- Always protect the optical port by plugging the cap in when there is no fiber connected.
- Make sure that the connectors are clean prior to connecting them.
- The Ethernet cable should always be connected to the center port.

Next, we will go over detailed steps for setting up the hardware:

1. Connect all external cables in the back of the interrogator in accordance with Figure A.2.
2. Power up the interrogator CPU and the field laptop.
3. Power up the laser unit.
4. Connect the Ethernet cable between the field laptop and the CPU.
5. As the laser is powering up, the interrogator IP address will be shown, additionally, a display of rectangles will be shown representing the system checkup. Make sure that all 7 rectangles are shown, if any are represented with a "_" then that is an indicator that there is a system malfunction. Most probably, it would be due to a loose connection in one of the cables. To troubleshoot, ensure all connections are correct and tightly secured, then reboot the system.

6. In field acquisition, there is an optional GPS antenna that can be connected to the GPS card. The GPS antenna is used to acquire the GPS clock time and not an accurate GPS location, so general guidelines of GPS deployment are not mandatory.

At this point, the system should be up and ready for the next step of software access and setup.

SOFTWARE SETUP

In this section, we discuss the software interface of the Helios Theta unit, going over the necessary steps to access the software, the various settings that must be set prior to recording, and the optional settings that can be set during recording. The following steps are a continuation of the previous steps done to get the system up and running.

1. Make sure the IP address of the field laptop is set to match the interrogator IP address.

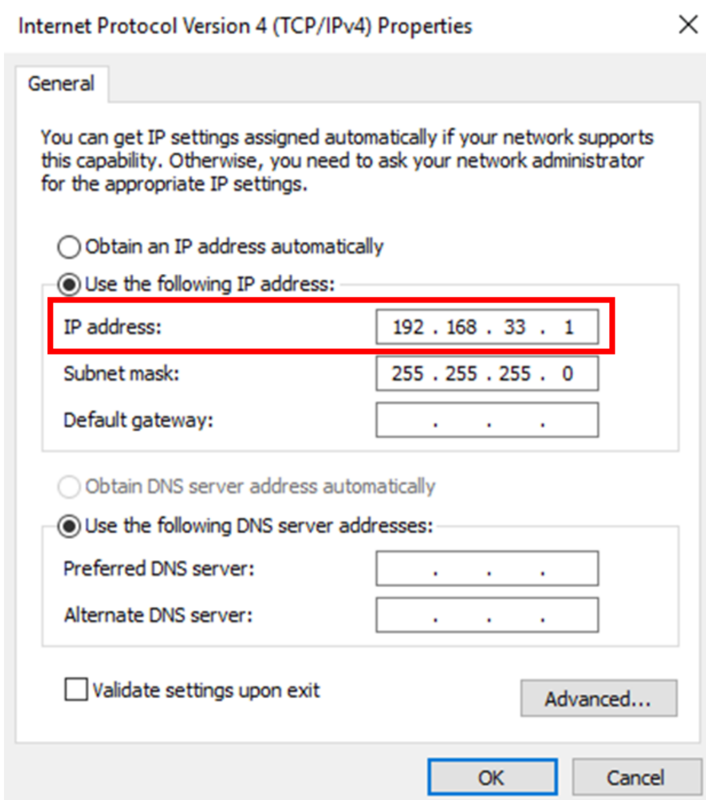

2. Access the internet browser and type the IP address of the interrogator (192.168.33.60)
3. Log in using the administrator credentials (User: administrator, Password: password)

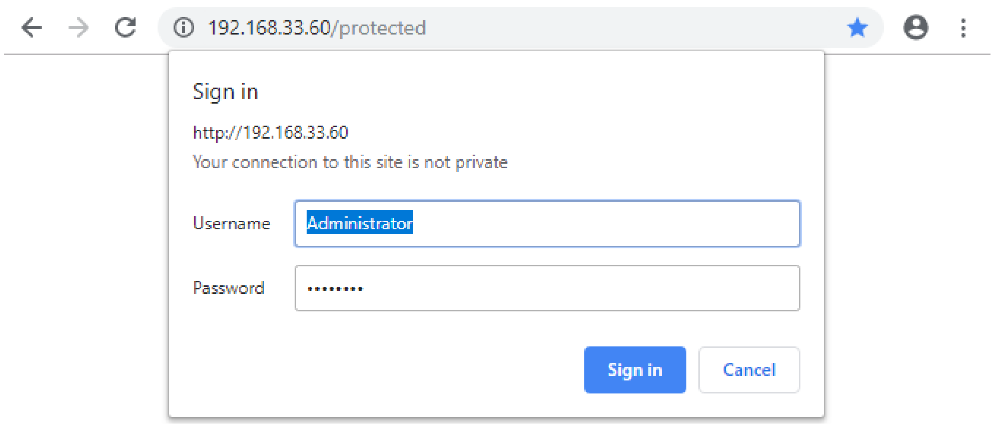

You are now logged into the user interface and the following display should be visible.

The next steps will go over setting up the interrogator for recording and optimizing the optical parameters.

4. Unlock the laser using the physical key. This will change the *Helios Controls* so they are pressable.

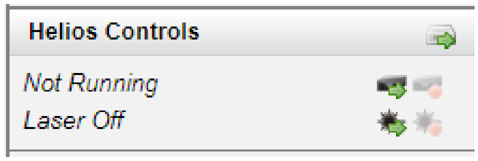

5. Press on Admin > Optical channel properties, to set the optical parameters.

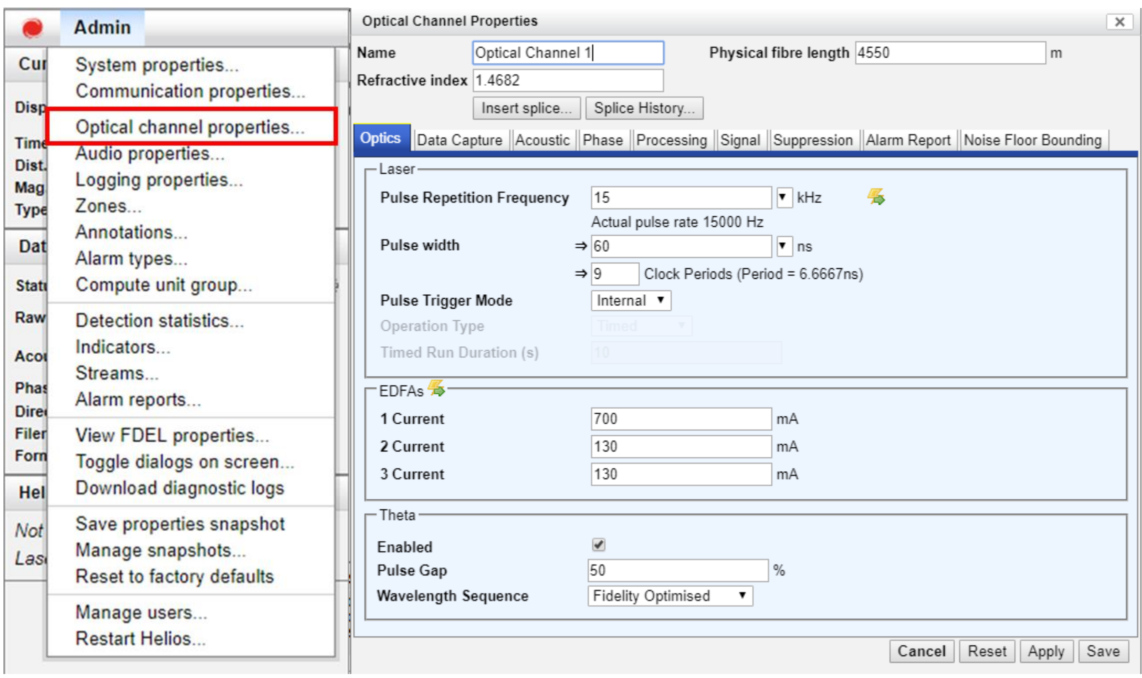

6. Set the *Physical fiber length* to exceed the expected amount of fiber connected for interrogation.

7. Select the *Pulse Repetition Frequency* (PRF) based on the desired frequency bandwidth. The fiber length will dictate the maximum PRF that can be selected. The system will display an error if the user attempts to select a PRF higher than the maximum allowed for the given fiber length. Use the following table to assist in selecting the PRF.

Table A.1: Key Pulse Repetition Frequencies

Key Pulse Repetition Frequencies	
Fiber Length (m)	Max PRF (kHz)
5	20
10	10
20	5
25	4
50	2

8. Select the *Pulse width* P_w with respect to the desired gauge-length. If Theta is disabled the gauge-length (G_L) is roughly one-tenth the pulse width, otherwise, use the equation in figure A.3 to compute the G_L.

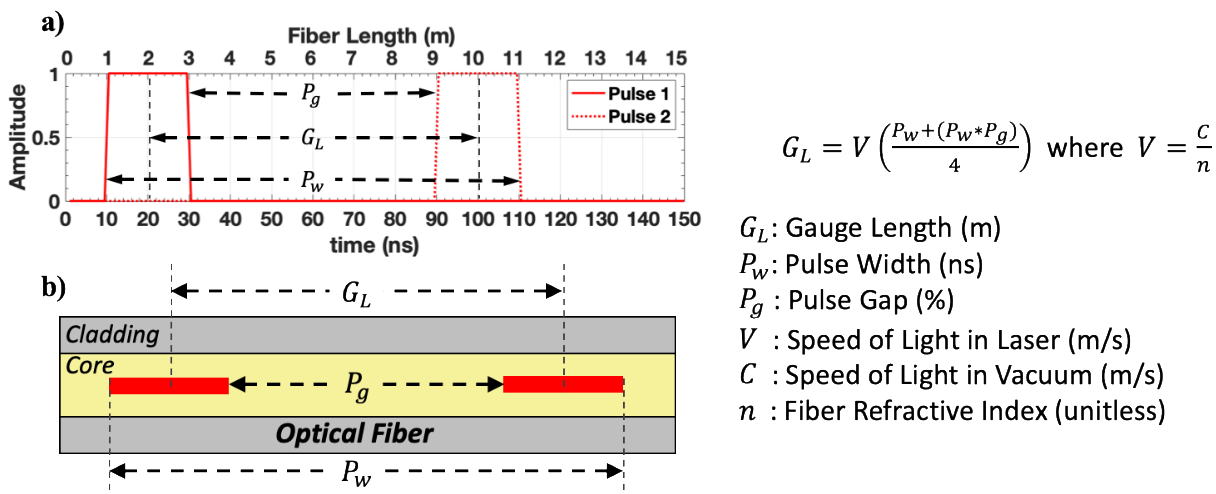

Figure A.3: Illustration of gauge-length (G_L) and equation for computing the G_L in Theta mode with respect to the Pulse Width (P_w) and Pulse Gap (P_g).

9. The *Pulse Trigger Mode* can be changed if using an external trigger, otherwise, leave it on internal.

10. Next, set the EDFA values to the default manufacturer recommended values. This can be found on the unit specification sheet. For the AGL Helios Theta H7017 the values are:

Table A.2: Manufacturer recommended EDFA values

Interrogator Mode:	**Theta**	**HSi**
Pulse Repetition Frequency:	2 kHz	5 kHz
Pulse Width:	100 ns	100 ns
EDFA 1:	590	300
EDFA 2 and 3:	130	130

11. In Theta mode (recommended mode for seismic acquisition), the Fidelity Optimized mode defines the frequency bandwidth to one-third the PRF.

12. Next step is to set the *Data Capture* parameters

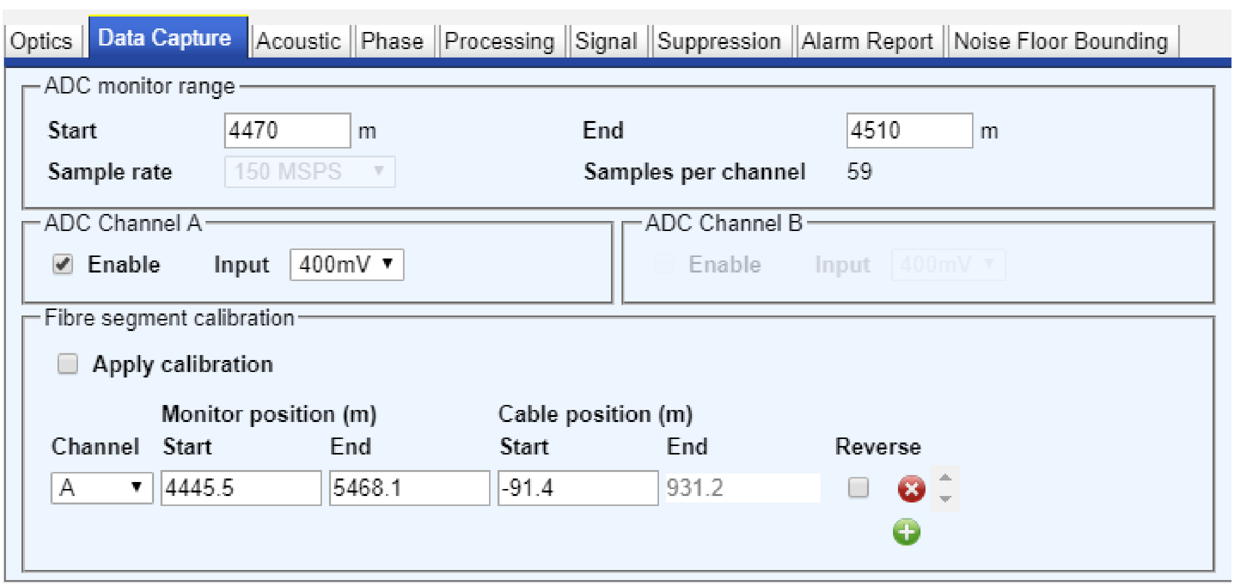

13. The *ADC monitor range* specifies the section of fiber you would like to display and record. When setting up the interrogator set these values to cover the entire fiber. Once the settings have been optimized you may refine the range to the section of fiber you are interested in.

14. The *ADC Channel A* is the voltage sensitivity of the digitizer, this should be set to the maximum value (4 V) when first calibrating the system, we will later change this value to optimize the raw backscatter.

15. The *Acoustic* tab is only applicable in the case of HSi recording mode.

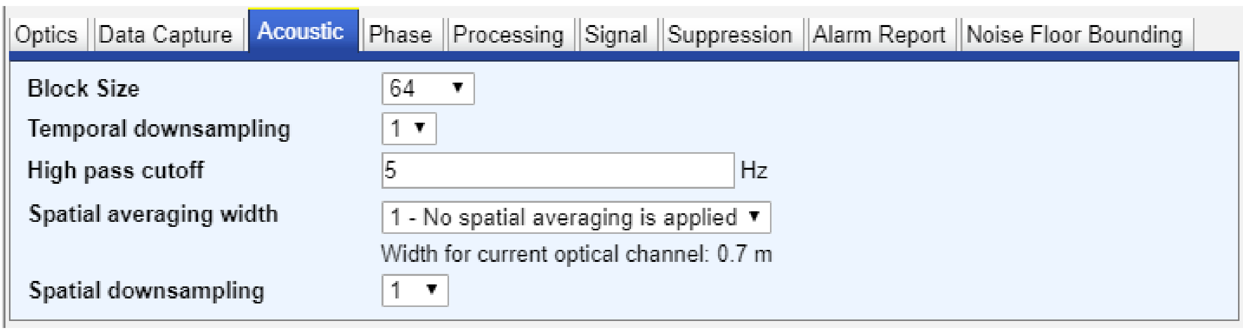

16. *Phase* settings can be set to perform basic optical processing to the data. The *Variational* method of *Phase unwrapping* has been recommended by Fotech as the more stable option. *Spatial downsampling* will decrease the number of channels and should not be confused with the gauge-length which we already went over in step 8. *Temporal downsampling* will decimate the time samples that are output, a low-pass /high-cut filter can also be applied to decrease the frequency bandwidth. These settings primarily influence the size of the output data, more sampling = larger file size.

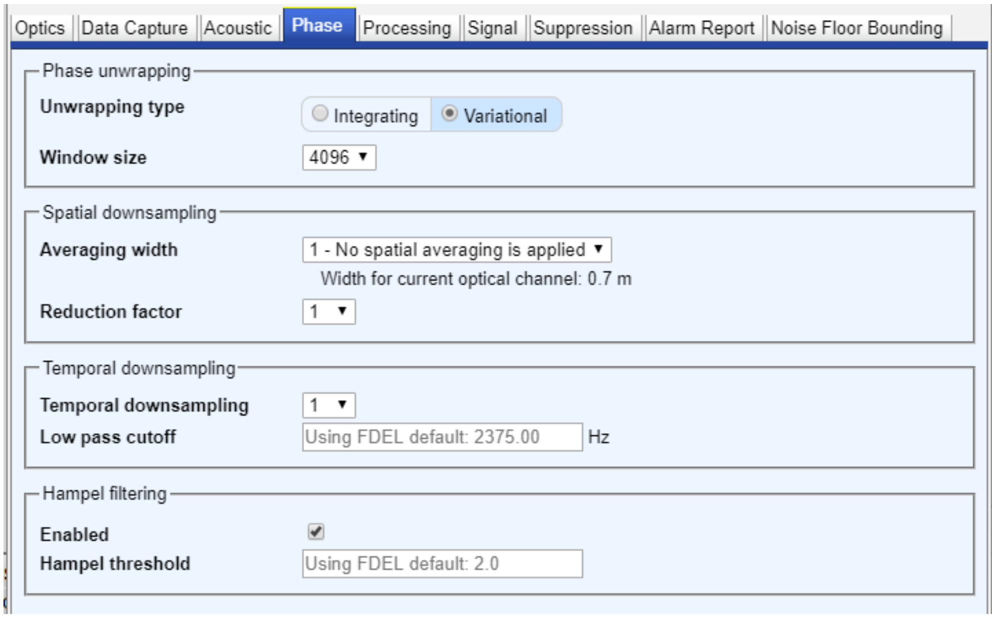

17. In *Processing* settings, the user can specify visual processing parameters as well as a low-cut frequency filter. It is important to note the value of the low-cut filter for later data analysis. The sound field settings influence the frequency of displaying data in real-time, this is limited by the screen capabilities to display data at high frequency and the graphics card to load the data fast enough. Given a large *Update rate*, the status bar will show an error related to dropping shots which correlates to laser shots not being displayed.

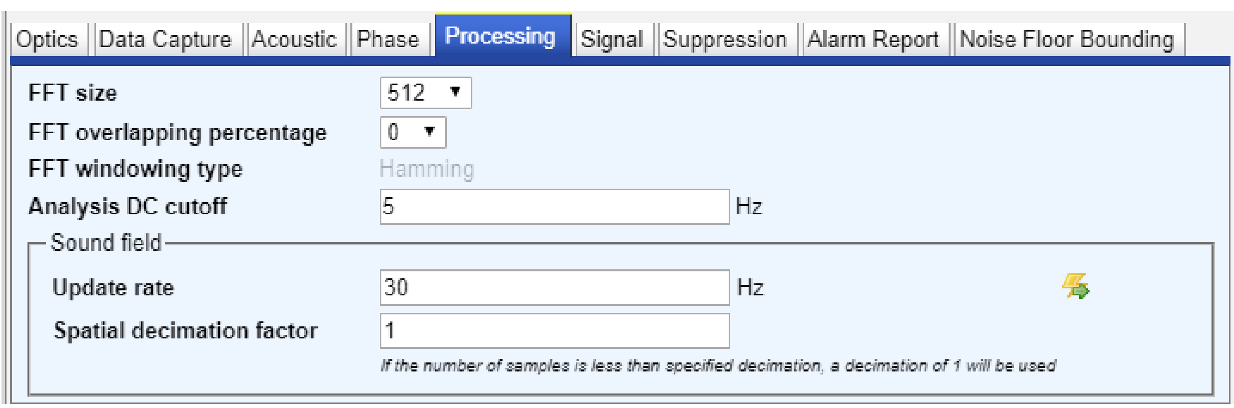

18. Other settings are not of high relevance to seismic acquisition, more information is available in the documentation and supporting material given by Fotech.

19. The next step is to change the display to *Raw Fibre Shot* by pressing on the display tab. Then enabling Oscilloscope mode.

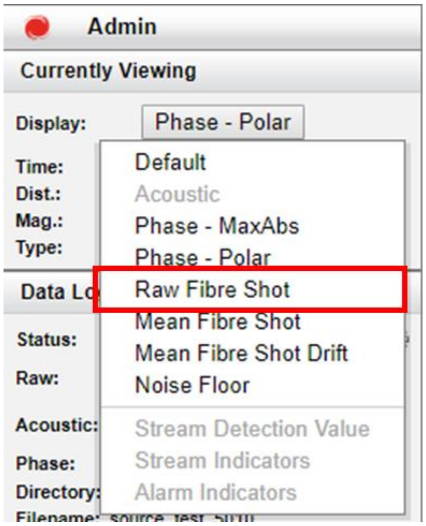

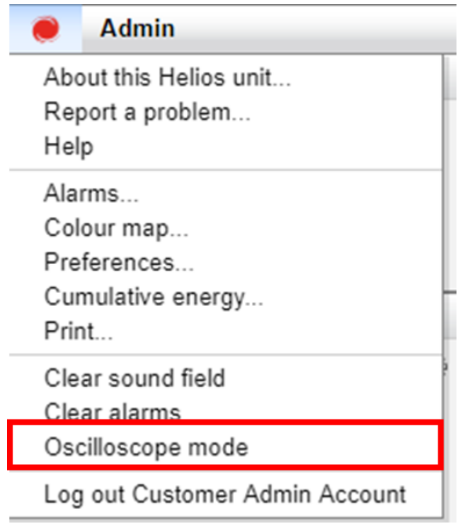

20. The next step is to disable logging prior to enabling the laser, otherwise, the calibration process will be recorded. This is done by pressing the following icon and then unchecking all logging parameters.

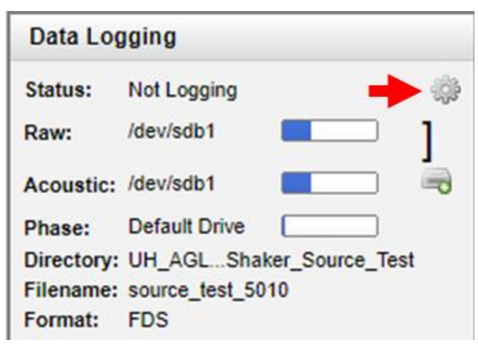

21. We are now ready to enable the laser and logging for display by pressing on the following icons. Note: make sure the fiber is connected with proper care as instructed in the sensor setup section.

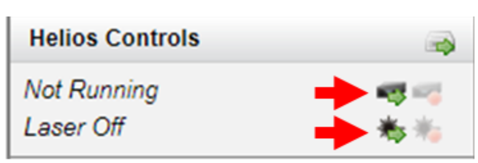

22. The system will now work on calibration and tuning the internal FBG and the laser. During this process, the backscatter spectrum will fluctuate. This process may take up to 15 min. Once it is complete the error message *FBG tuning* will go away and the orange LED on the front display of the Laser unit will turn off.

    Note: The AGL Helios Theta (H7017) requires a minimum of 1 km of fiber for the FBG to tune. We have been provided with a 4.5 km fiber spool that should be used during acquisition.

23. Once the FBG has tuned and the backscatter has stabilized (as seen below), we can proceed with optimizing the backscatter.

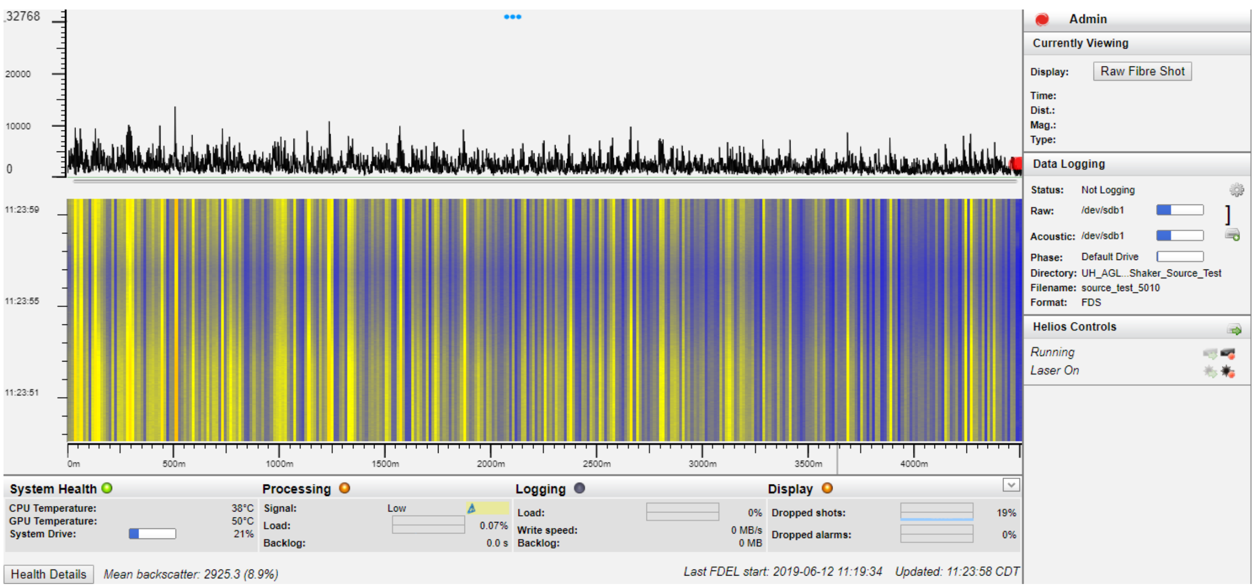

24. To optimize the backscatter, we will change the EDFA and ADC values iteratively to push the average backscatter amplitudes to two-thirds the amplitude spectrum (as seen below).

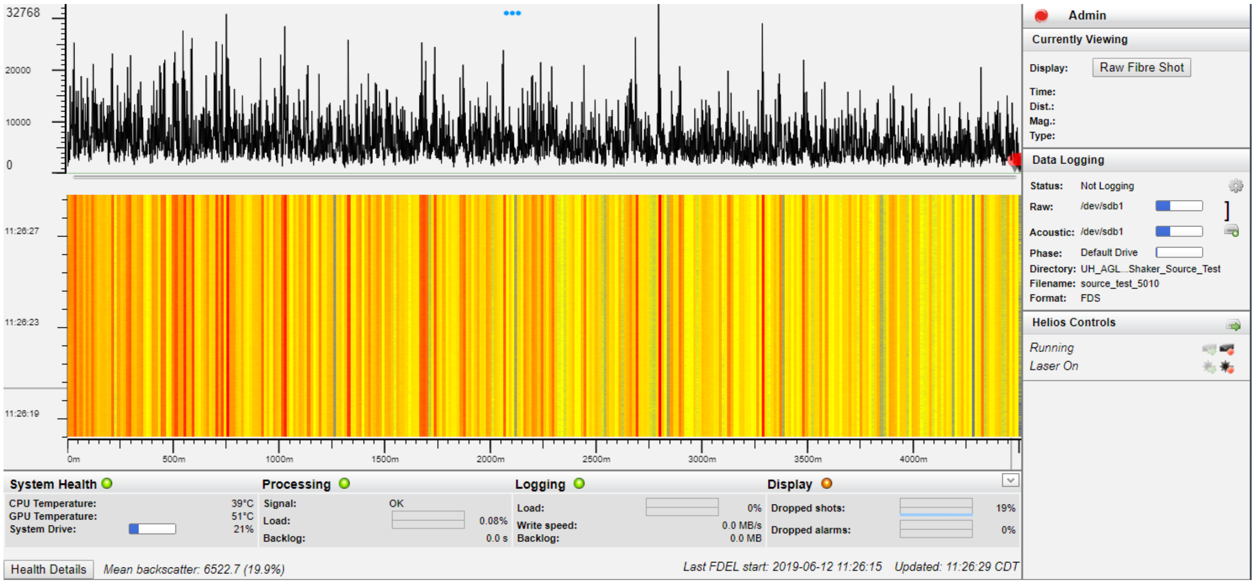

25. When optimizing the backscatter, we want to avoid clipping the data as shown below, this will result in data loss.

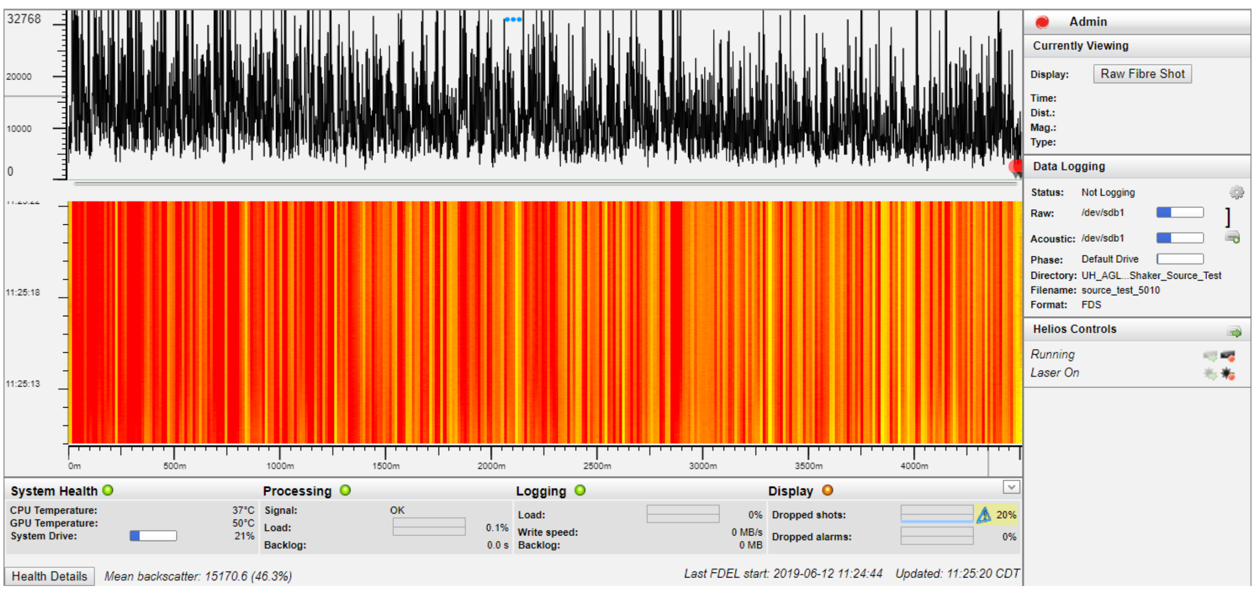

With this, the system should now be optimized and ready for acquisition. You can now proceed to the Phase-Polar display or Acoustic Display (if theta is disabled).

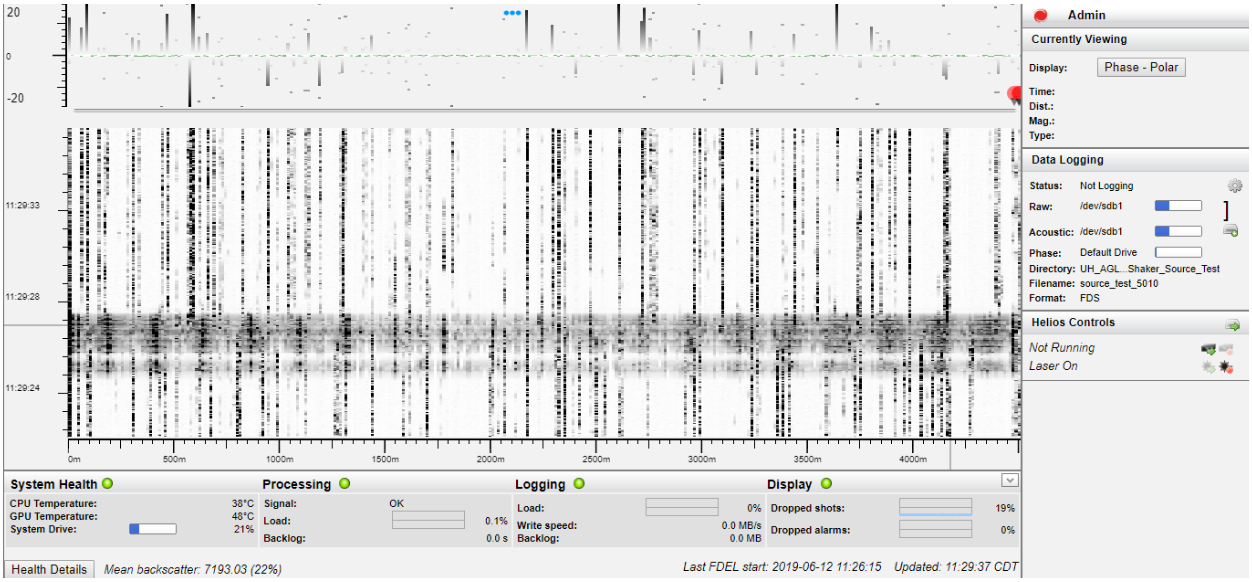

To set up the system for recording we will go back to the *Data Logging* settings and select the desired recording parameters (raw, acoustic, phase, etc.) and specify the file name and save location. It is recommended to use the internal Fotech file format (FDS) for raw recording. Saving the raw data allows for more optical processing options but at the price of a larger file size. While saving the desired parameter (acoustic or phase) results in smaller files but less processing options. Note: use the logging icon under *Helios Controls* to start and stop recording when using the internal trigger option.

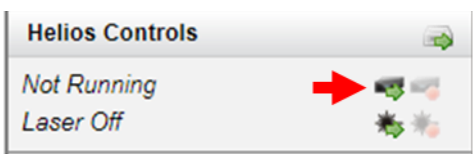

For additional information and support please refer to the training materials provided by Fotech or access the internal user's manual help portal.

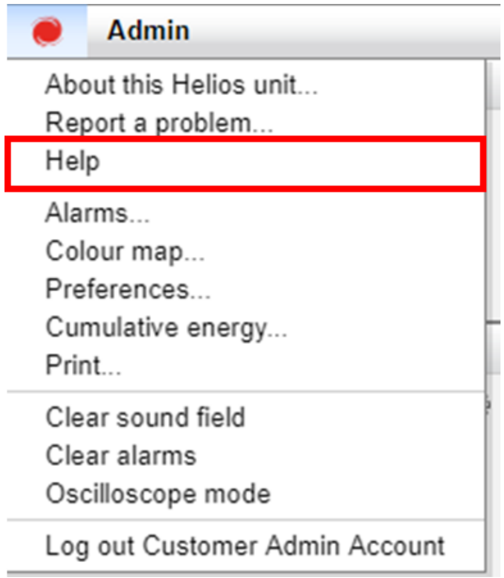
Admin
About this Helios unit...
Report a problem...
Help
Alarms...
Colour map...
Preferences...
Cumulative energy...
Print...
Clear sound field
Clear alarms
Oscilloscope mode
Log out Customer Admin Account

DATA EXTRACTION

This chapter will go over the necessary steps to extract DAS data from the Helios Theta Interrogator. The process requires minimal experience with operating a Linux operating system. First, the Helios unit must be connected to a screen, a mouse, and a keyboard.

1. Open a Terminal window, by right-clicking the desktop and then clicking on Terminal.
2. Sign in to Super User mode by typing *su* in the terminal.
3. Password: *fotechf00*
4. Type *lsblk* to view mounted drives
5. Type *cd* to change directory to the location where data has been saved as specified on the Helios recording parameters.
6. Connect a storage device to the Helios unit.
7. Mount the drive using the following command "*mount /dev/sdc1 /media/*"
8. Use the following command to copy the data "*cp -rf /opt/Fotech/data/HeloisData /media/*"
9. When done, use the following command to unmount the drive prior to unplugging it "*umount /dev/sdc1*"

Alternatively, you may navigate to your drive location and data location and copy the data using the desktop manager, similar to Microsoft operating systems.

DEMO

In this section, we will go over setting up the system for the purpose of demonstrating DAS technology and showcasing the Helios Theta interrogator capabilities. We recommend setting up this demonstration to AGL guests or students who are being introduced to fiber-optic sensing and/or are new to DAS.

First, start up the system and set it up following instructions in the Software Setup chapter. Have the fiber spool connected to the system during this process. We will use the fiber spool to perform the illustrations.

1. The first option is to set up the system for HSi mode, in this mode, there will be minimal delay in the sound playback that will be illustrated. The second option is to use the Theta mode, in this mode, there is a significant reduction in background noise but there is a consequence of a delay in the playback recording time.

2. Press on the three dots on the top of the page

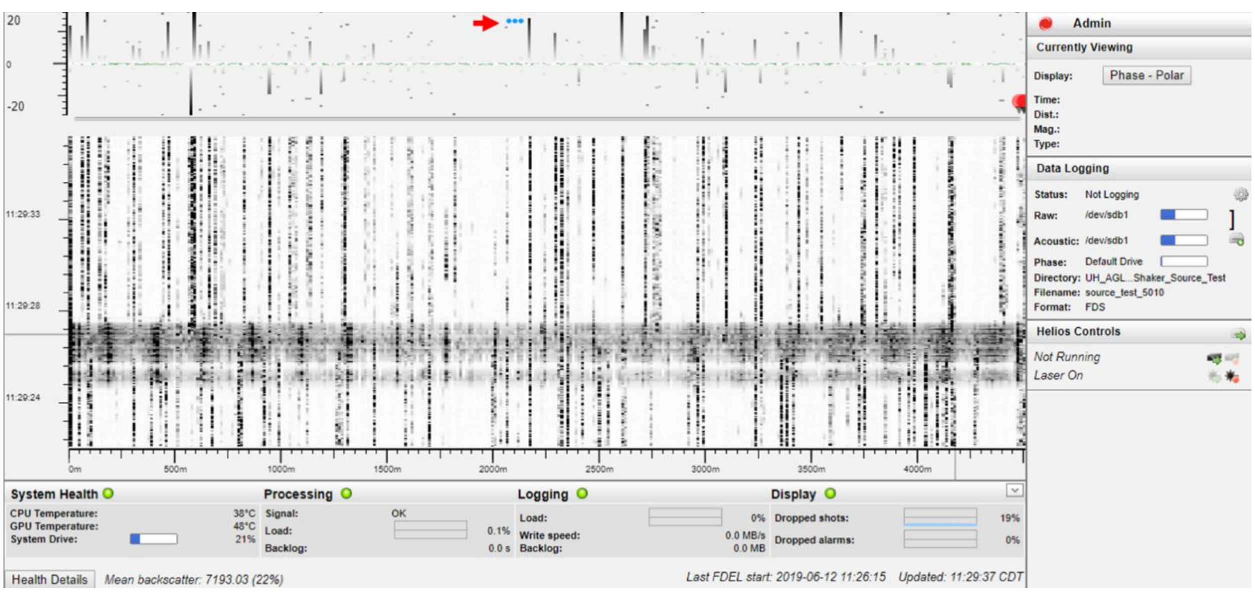

3. Press on the speaker icon, this will launch the following page and start playing sound waves of the recorded signal. Make sure the speaker is on. The left panel is the time response at the selected location, and the right panel is the corresponding frequency spectrum.

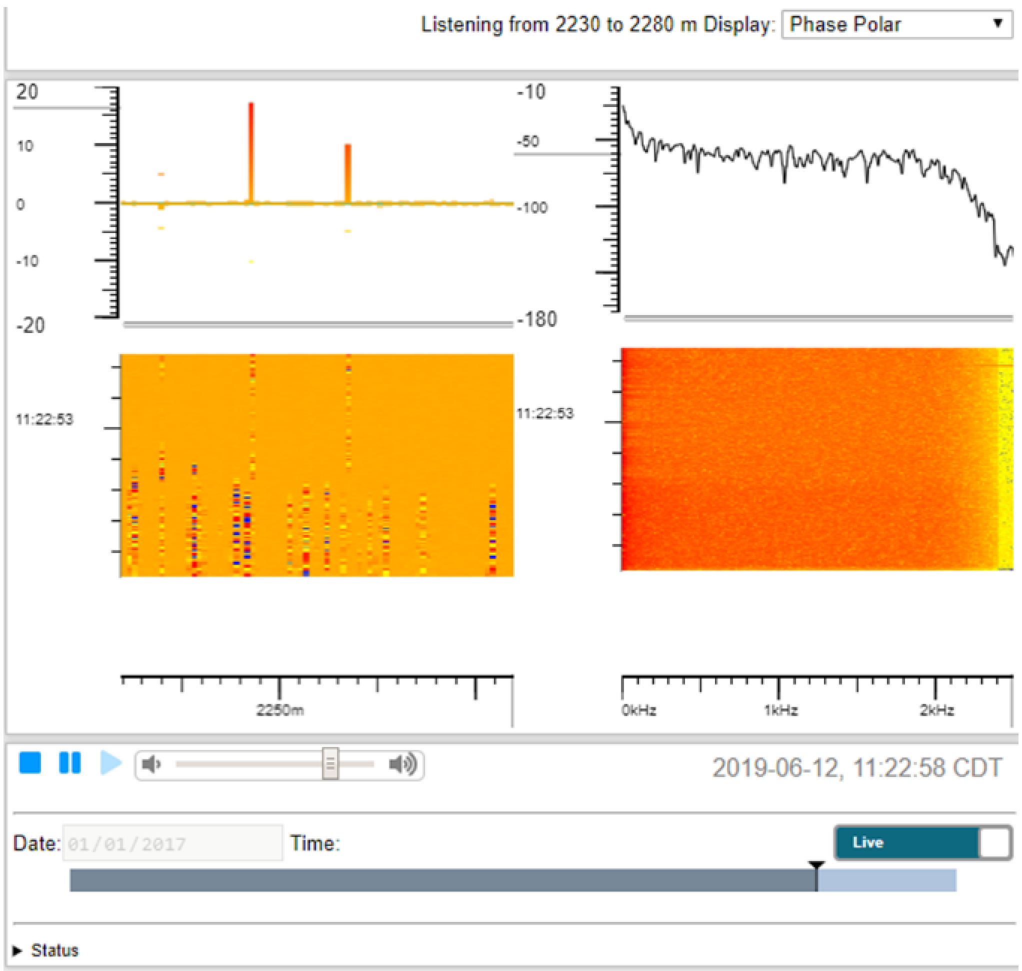

4. A small icon will pop up on the main window that is a marker for the channel that is being played back. You may move this to a location with the highest SNR.

5. For the illustration, you will now tap on the fiber spool and wait for the sound to playback. Also, you will observe horizontal amplitude signals in the waterfall display.

APPENDIX B

FBG USER OPERATIONS MANUAL

INTRODUCTION

This manual has been compiled using the supporting materials provided by FBGS and experience gained through using the equipment. With this manual, you will be able to operate the equipment, acquire data, and display the data in MATLAB. We recommend looking over the entire document prior to operating the equipment and not to rely on the Quick Setup Guide.

The Quick Setup Guide guides the user to quickly record data under the assumption that all acquisition settings are preset. In Hardware Setup, we guide the user on handling and deploying the FAZT Interrogator for acquisition. In Software Setup, we discuss launching the FBG software (Femtosense) for acquisition and go over the settings to manipulate prior to recording data. Under Sensor Setup, we discuss the FBG sensors and how to set them up for data acquisition. Finally, we will go over some of the MATLAB codes that have been generated by Ezzedeen Alfataierge for displaying the FBG data and some processing codes.

Please refer to the User Guide provided by FBGS for any further information.

QUICK SETUP GUIDE

In this section, we outline a quick setup of the FAZ I4 interrogator, accessing the Femtosense software, selecting your FBG sensors, and recording data.

1. Power up the FAZ I4 interrogator
2. Connect Ethernet cable to Ethernet port on Laptop
3. Launch Femtosense software on Laptop
4. Connect to FAZ I4 interrogator using its IP address 192.168.33.12

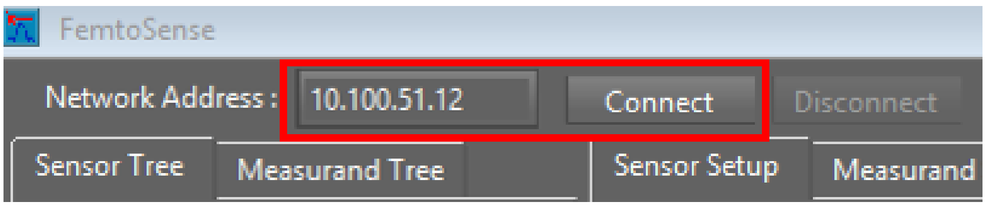

5. Select Fiber in the Sensor Tree under the corresponding channel of which the fiber has been connected

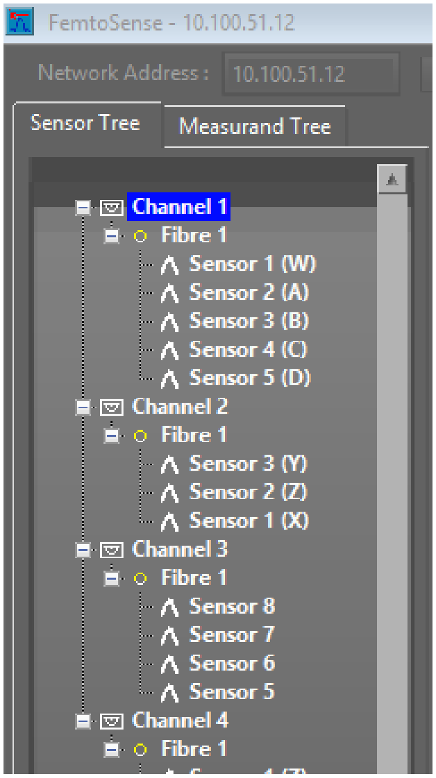

6. Select FBG sensors you would like to record

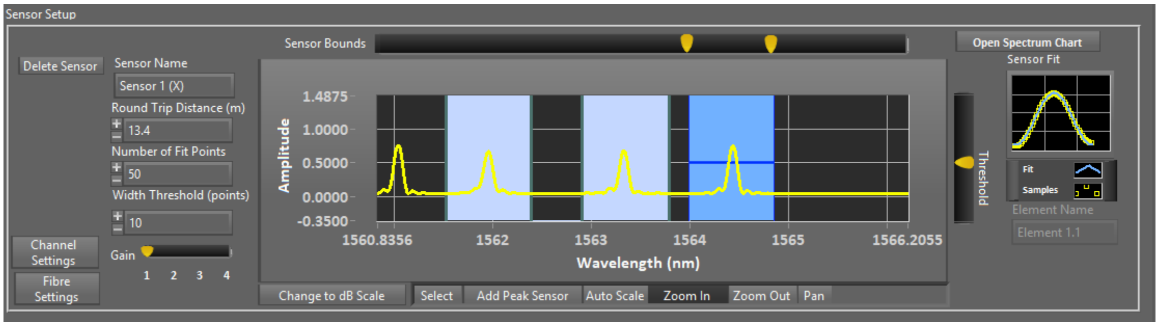

7. Specify the location of file and name, then click Save Peaks to start recording

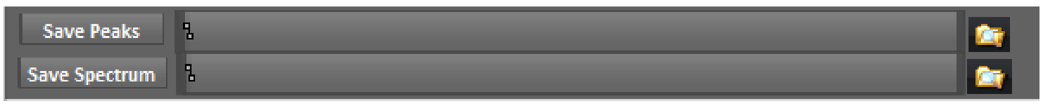

8. Press on Finish recording when you are done

HARDWARE SETUP

In this section, we will discuss how to physically set up the FAZ I4 interrogator and FBG sensors.

Safety:

Please refer to the FAZT User Guide provided by FBGS for a full safety disclaimer.

CAUTION: Invisible Laser Radiation - Do not view directly with optical instruments (magnifiers). Viewing the laser output with certain optical instruments (e.g., eye loupes, magnifiers, and microscopes) within a distance of 100 mm may pose an eye hazard. Laser power up to 100 mW at 1.55 μm could be accessible if an optical connector is open or fiber is broken. Use of controls, adjustments, and procedures other than those specified herein may result in hazardous laser radiation exposure.

Handling:

The interrogator is an expensive and delicate piece of equipment. When transporting the equipment make sure to label it as fragile and to include foam protection inside the packaging.

Always keep the fiber ports clean and protected using proper cleaning and protection tools that are available.

Fiber ports should always be capped when not in use. When in use, place the protective cap in a safe and clean place, so it doesn't get lost or dirty.

Through experience, environmental noise around the interrogator can contaminate the data. Trying to minimize noise around the interrogator or isolating the interrogator from the environment will help increase the quality of the acquired data.

Components:

The main hardware components consist of the following:

- FAZT Interrogator.
- Power Cable and Inverter.
- Ethernet Cable.

Auxiliary components that should be present include:

- Laptop/ PC with Femtosense Software installed.
- Fiber-optic connector cleaner.
- FBG Fiber-optic cable(s).

In remote field deployment, the following equipment would be necessary:

- Power supply: Battery and Battery inverter.
- Canopy Tent

Setup:

The figure below shows the proper setup of the equipment for acquisition in a laboratory environment (Figure A.1). First, the user must place the interrogator on a stable surface, connect the power supply, turn on the device using the flip-switch on the back, and enable the laser using the red button. Second, connect the Ethernet cable between the interrogator and the PC unit to establish communication. Once the LED status is blue then the system is ready to connect. The interrogator can now be accessed using the Femtosense software, which will be explained in the next chapter.

Figure B.1: Hardware Setup
Field laptop equipped with Femtosense software is connected to the FAZT Interrogator via an ethernet cable. The FAZT Interrogator is powered by a 12V power source. The interrogator can interrogate up to four fibers simultaneously through the four channels visible on the front of the equipment.

SOFTWARE SETUP

In this section, we discuss how to set up the Femtosense software for Acquisition and go over the key parameters that must be adjusted based on the objective of acquisition. Additional information can be found in the FAZT User Guide, including information on installing the software for the first time.

After completing the Hardware Setup,

Setup the interrogator time to local time:

1. **Launch** the SetIxTime.vi code located on the desktop of the field laptop
2. **Enter** the FAZT Interrogator IP Address 192.168.33.12
3. **Press** Update Time

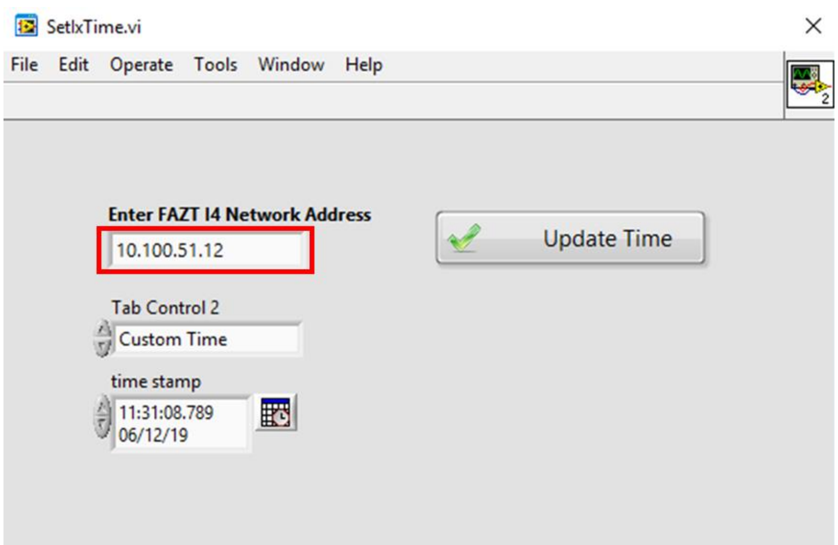

The SetIxTime.vi code has been developed by FBGS and sent to AGL through Bram Van Hoe, to fix an issue with the interrogator clock having incorrect time and date reference. This step must be completed every time the interrogator is rest. If the user does not care about the correct time and date, then this step could be skipped.

Connecting to the Interrogator:

1. **Launch** Femtosense software.

2. **Type** the FAZT interrogator IP Address 192.168.33.12 in the Network Address box, then **click** connect. (if an error window pops up saying "Unable to connect to the specified Interrogator" and the IP address is correct. Then try rebooting the system)

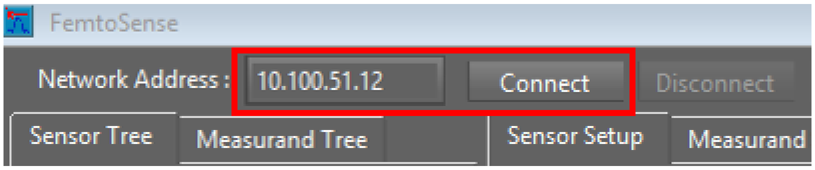

3. You are now connected to the interrogator and can see the wavelength spectra for each channel.

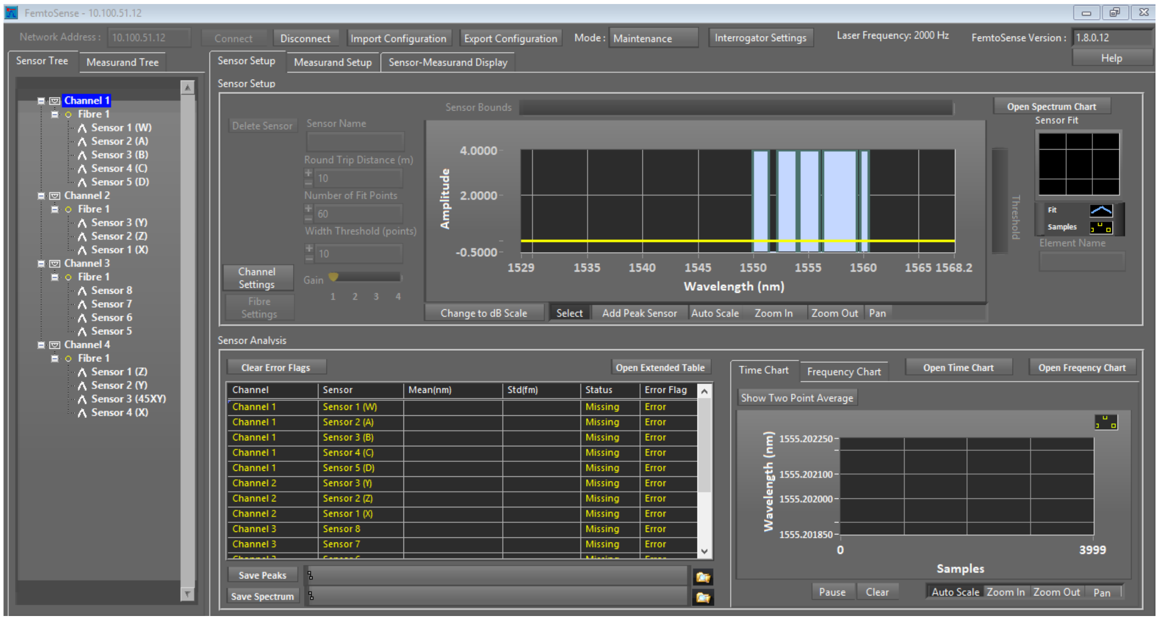

Defining FBG sensors:

Now that you have connected to the interrogator you can view the wavelength spectra of up to four connected fibers in each channel. The channel labels correspond to their labels on the interrogator. If your fiber is connected into the channel and you do not see any response in the wavelength spectrum, then it is possible the fiber is broken. Similarly, if you are expecting to see five FBG peaks but only see three, then the fiber is broken somewhere between the third and fourth FBG.

1. **Select** the <u>channel</u> in which the fiber has been connected.

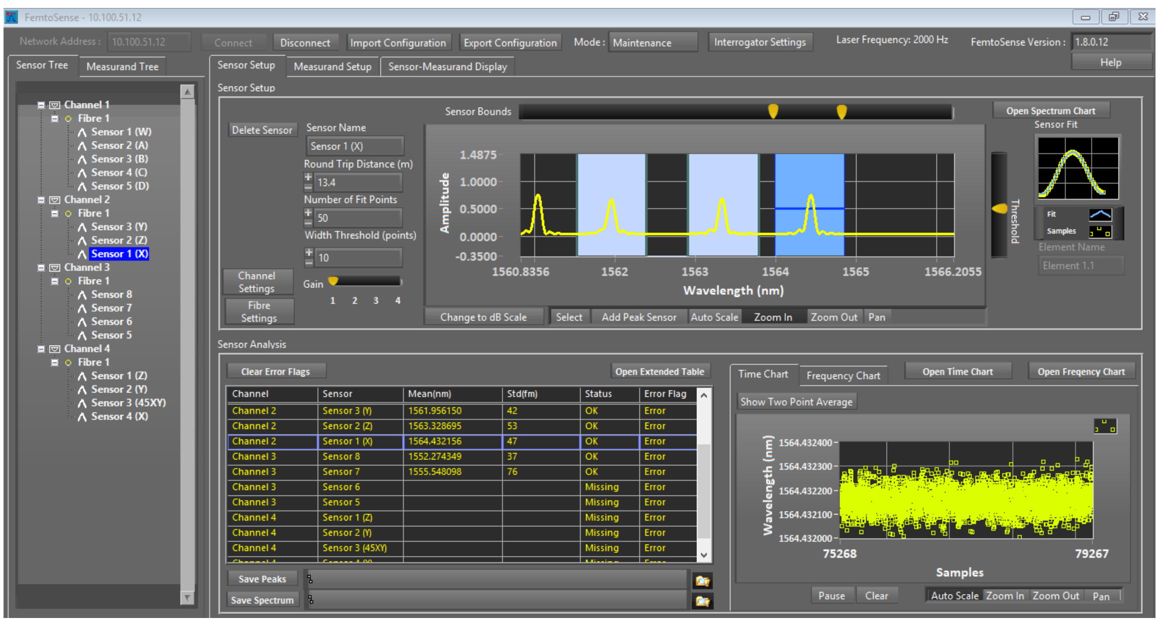

You should now see peaks in the wavelength spectrum that correspond to each FBG sensor as seen above.

2. **Click** on <u>Add Peak Sensor</u> to define the boundary of a single FBG sensor.

3. **Adjust** the <u>Sensor Bounds</u> by dragging the yellow icons. You want the bounds to encompass the peak along with its side lobes and have enough space to accommodate the expected FBG shift from the experiment. The bounds must not include more than one peak or overlap with another bound.

4. **Adjust** the Threshold by dragging the yellow icon. The optimal threshold is half the peak amplitude, it should be high enough to avoid the sidelobe energy and low enough to capture the peak while accommodating for amplitude change during the experiment.
5. **Enter** the approximate round trip distance in meters from the fiber connector to the selected FBG sensor.
6. **Adjust** the Number of Fit Points, Width Threshold, and Gain, such that the Sensor Fit is good.
7. You may change the Sensor name as desired.
8. Repeat these steps until all FBG sensors of interest have been defined.

Note: Only defined sensors will be recorded. You do not have to define all FBGs in a fiber.

Determining FBG Location:

If you have not been supplied with the FBG fiber specification sheet which includes the expected FBG nominal wavelengths and their geometry along the fiber, then you may map the FBG wavelengths using some small experiments.

1. Find the FBG marking along the fiber (the two black marks).

2. Gently place your finger on the FBG and observe the wavelength shift response. A gentle shift in the wavelength will be observed in correspondence to the temperature change introduced by the warmth of your finger.

3. Another approach is to pinch the fiber before and after the FBG. Pinching the fiber will disturb the laser path and eliminate all peaks past the pinched area. CAUTION: if done improperly, you can break the fiber. This method is not recommended, especially with bare fiber.

Interrogator Settings:

The following settings can be manipulated under the interrogator setting tab.

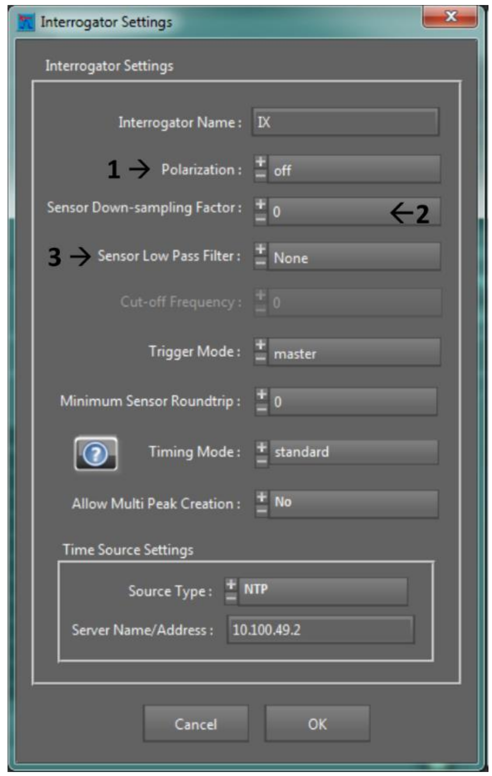

1. **Polarization**

   The polarization could be enabled only when using the interrogator at 1kHz. This option pulses the laser in two different polarizations to more accurately capture the response of the FBG.

2. **Sensor Down-sampling Factor**

   Down-sampling will reduce the number of samples being recorded in time, thus decreasing the frequency bandwidth and time sampling rate. It is best not to down-sample unless recording for long periods of time.

   At 1 kHz the frequency bandwidth is 0-500 Hz with a sampling rate of 1 ms

   At 2 kHz the frequency bandwidth is 0-1000 Hz with a sampling rate of 0.5 ms

3. **Sensor Low Pass Filter**

   A low pass filter will cut frequencies higher than the specified value and pass frequencies lower than the specified value. Applying a low pass filter at the bandwidth boundary helps reduce the sampling noise seen in the data.

Recording Data:

Once all the FBG sensors have been defined and all the desired settings have been selected, data can be recorded by clicking on Save Peaks, after selecting the file name and location using the file icon. The saved file will be an ASCII file, I recommend using (.fbg) as the file extension.

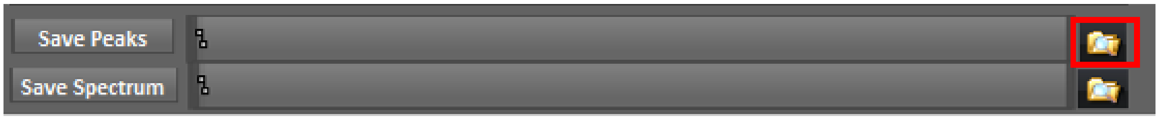

Save Spectrum will save a binary file which contains the entire wavelength spectrum, whereas Save Peaks will only save the wavelength shift relative to each defined FBG sensor in ASCII format.

Note: Always take a screenshot of the Sensor Analysis table to have as a reference for the sensor and channel names relative to the mean wavelengths. This is important for identifying the data later during processing as this information is not properly defined in the data.

Live Multi-Sensor Display:

During acquisition, you may wish to monitor multiple sensors at once, you can do so through the Sensor-Measurand Display tab. There you can drag up to six sensors into the display and simultaneously monitor them.

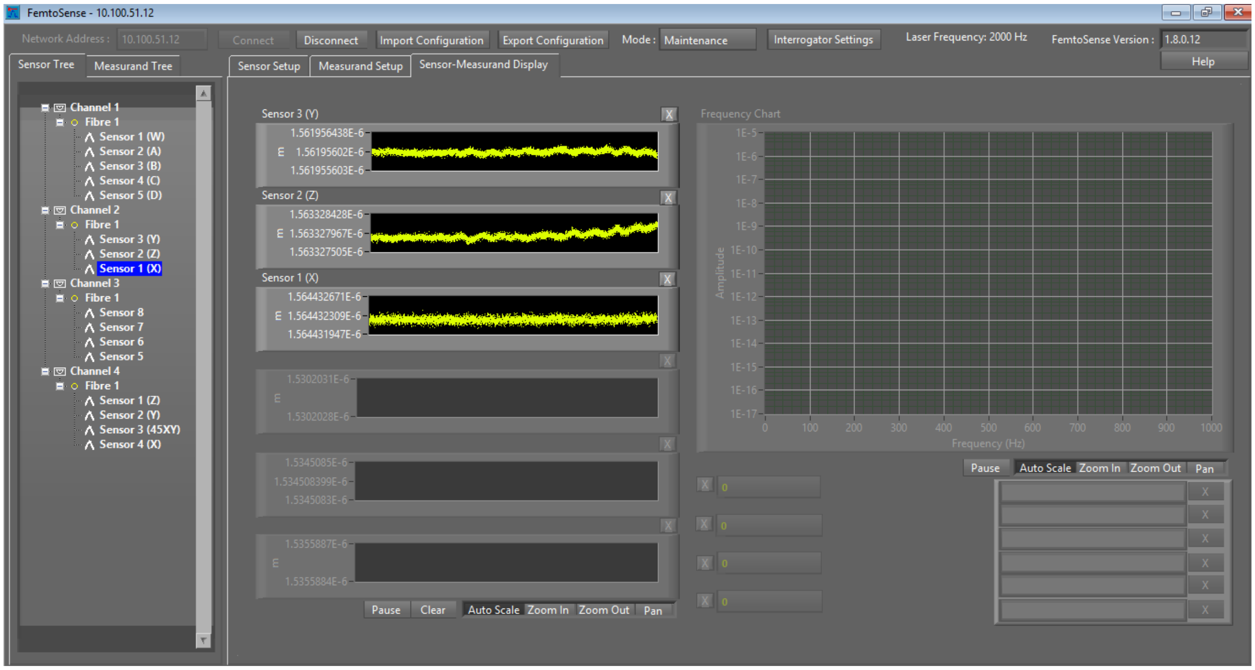

SENSOR SETUP

In this section, we will discuss handling the FBG fibers and how to best deploy them for acquisition. The first and most important thing to note is that fiber and especially bare fiber is extremely sensitive, mishandling the fiber will lead to breaking it and losing all sensors past the broken end. A broken fiber may be repaired using a fusion splice device, only if there is enough fiber lead to splice together. Note that, splicing the fiber degrades the amplitude of the FBG peak in the wavelength spectrum. Therefore, we must always handle the fibers with care and be careful not to bend them to their breaking point. We have lost several fibers during past experiments and hope you may learn from our mistakes.

FBGS recommended gluing the FBG fiber on to the structure we would like to measure. This is not favorable, as it is a permanent installation, and is not applicable for surface seismic where the structure of interest is sediments in the land case or water in the marine case. Through laboratory experimentation, we find that taping the FBG sensor yields an acceptable response that is comparable to gluing (Figure B.2).

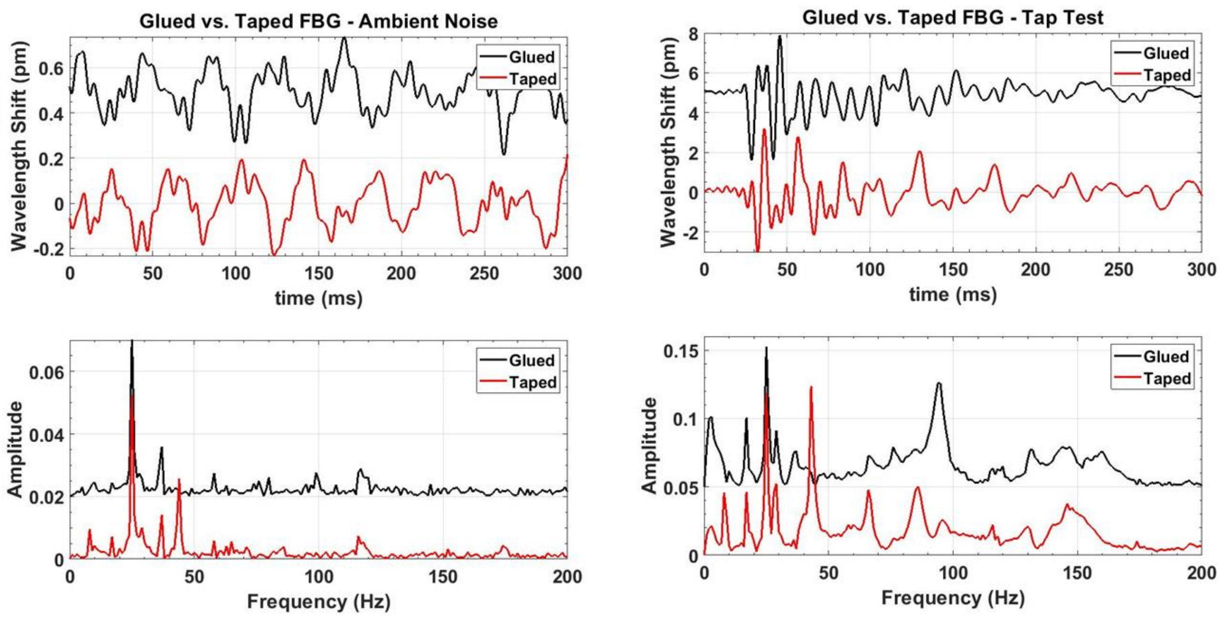

Figure B.2: Glued vs. Taped FBG test results for ambient noise (left) and a tap test (right) with respect to two FBGs mounted on PVC pipe in a laboratory setting.
The FBGs are roughly 20 cm apart (Alfataierge et al., 2019a).

A few things to note when mounting the FBG:

1. Make sure to secure the fiber before and after the FBG, as any strain on the fiber near the FBG is transferred and will show up in the data.
2. Make sure to secure the fiber near and around the connection to the interrogator. Any movement of the fiber near the connector introduces noise into the data. This is particularly important in field deployment where the wind will waive the fiber around and contaminate the FBG data.
3. Make sure the surface you are securing the FBG to is clean and flat. Otherwise, any sediment or grains that push on the fiber will influence the measurements.

DATA MANIPULATION ON MATLAB

In this section, we will look at the MATLAB scripts that have been generated by Ezzedeen Alfataierge to display and manipulate the FBG data.

Data Loading in MATLAB

The following code has been constructed using the MATLAB data import tool for data with four FBG sensors. This is an example of how to load the FBG data into MATLAB to display and process.

<table>
<tr><th>Description</th><th>MATLAB Code</th></tr>
<tr><td>Create Function</td><td><pre>function [t,S1,S2,S3,S4] = iFBG(filename)
%IMPORTFILE Import numeric data from a text file as column vectors.
%   [T,S1,S2,S3,S4] = IFBG(FILENAME) Reads data from text file
%   FILENAME for the default selection.
%
% Example:
%   [t,S1,S2,S3,S4] = iFBG('3-C_FBG_Cube_Test_1.fbg');</pre></td></tr>
<tr><td>Setup Parameters to Read ASCII file</td><td><pre>%% Initialize variables.
delimiter = '\t';
startRow = 1;
endRow = inf;
%% Format for each line of text:
formatSpec =
'%*s%f%*s%*s%*s%*s%f%*s%*s%*s%f%*s%*s%*s%f%*s%*s%*s%f%*s%
[^\n\r]';</pre></td></tr>
<tr><td>Read Data</td><td><pre>%% Open the text file.
fileID = fopen(filename,'r');
%% Read columns of data according to the format.
dataArray = textscan(fileID, formatSpec, endRow(1)-startRow(1)+1,
'Delimiter', delimiter, 'TextType', 'string', 'EmptyValue', NaN,
'HeaderLines', startRow(1)-1, 'ReturnOnError', false, 'EndOfLine',
'\r\n');
for block=2:length(startRow)
    frewind(fileID);
    dataArrayBlock = textscan(fileID, formatSpec, endRow(block)-
startRow(block)+1, 'Delimiter', delimiter, 'TextType', 'string',
'EmptyValue', NaN, 'HeaderLines', startRow(block)-1, 'ReturnOnError',
false, 'EndOfLine', '\r\n');
    for col=1:length(dataArray)
        dataArray{col} = [dataArray{col};dataArrayBlock{col}];
    end
end
%% Close the text file.
fclose(fileID);</pre></td></tr>
<tr><td>Output each FBG response in nm, and time vector in seconds</td><td><pre>%% Allocate imported array to column variable names
ut = (1e-9)*dataArray{:, 1};
S1 = (1e9)*dataArray{:, 2};
S2 = (1e9)*dataArray{:, 3};
S3 = (1e9)*dataArray{:, 4};
S4 = (1e9)*dataArray{:, 5};
t = ut-ut(1);</pre></td></tr>
</table>

The following script can be used to call on the created function to read the data and display it.

Description	MATLAB Code
Call function to read data from file "5100.fbg"	`[t,S1,S2,S3,S4] = iFBG('5100.fbg');`

Assign the sampling rate and compute time boundaries for display	`dt = 0.0005;  % FBG Sampling Rate (s)`
	`start1 = 10;  % FBG Start Time (s)`
	`l = 4;    % Record Length to display from Start Time (s)`
	`tstart = start1/dt; % Start time (Sample)`
	`% tend = numel(t);   % End time sample to display entire record (start1=dt)`
	`tend = (start1+l)/dt; % End time (Sample)`

Compute the 1st degree polynomial trend lines (linear trend) of the data for each sensor. This is used to approximate the temperature response and later subtract it from the data.	`% Compute FBG Data Trendlines`
	`tL1 = polyfit(t(tstart:tend),S1(tstart:tend),1);      % Linear Fit for S1`
	`tS1 = polyval(tL1,t(tstart:tend));                     % Generate fit curve`
	`tL2 = polyfit(t(tstart:tend),S2(tstart:tend),1);      % Linear Fit for S2`
	`tS2 = polyval(tL2,t(tstart:tend));                     % Generate fit curve`
	`tL3 = polyfit(t(tstart:tend),S3(tstart:tend),1);      % Linear Fit for S3`
	`tS3 = polyval(tL3,t(tstart:tend));                     % Generate fit curve`
	`tL4 = polyfit(t(tstart:tend),S4(tstart:tend),1);      % Linear Fit for S4`
	`tS4 = polyval(tL4,t(tstart:tend));                    % Generate fit curve`
	`tL5 = polyfit(t(tstart:tend),S5(tstart:tend),1);      % Linear Fit for S5`
	`tS5 = polyval(tL5,t(tstart:tend));                     % Generate fit curve`

Generate a figure with subplots displaying the response of each sensor and the corresponding linear trend.	`% Plot FBG S2-S5 Time Response`
	`figure; hold on;`
	`dx1 = subplot(4,1,1);`
	`plot(t(tstart:tend),S2(tstart:tend),'k',t(tstart:tend),tS2,'-.r')`
	`ylabel('Sensor 2')`
	`dx2 = subplot(4,1,2);`
	`plot(t(tstart:tend),S3(tstart:tend),'k',t(tstart:tend),tS3,'-.r')`
	`ylabel('Sensor 3')`
	`dx3 = subplot(4,1,3);`
	`plot(t(tstart:tend),S4(tstart:tend),'k',t(tstart:tend),tS4,'-.r')`
	`ylabel('Sensor 4')`
	`dx4 = subplot(4,1,4);`
	`plot(t(tstart:tend),S5(tstart:tend),'k',t(tstart:tend),tS5,'-.r')`
	`ylabel('Sensor 5')`
	`xlabel('time (s)')`
	`linkaxes([dx1,dx2,dx3,dx4],'x')`

To compute the frequency spectrum for each sensor you may use the following function. The record length must be one second, otherwise, the function will be wrong.

Description	MATLAB Code

Create function called Highcut_Filt	`function [ f, trace_f, trace_F0] = Highcut_Filt(  t_s, trace, dt, F0, trace_trend )`
	`%HIGH_CUT SUMMARY`
	`%   Preform High Cut filter to "trace" at F0`
	`% t_s = time;`
	`% trace = trace;`
	`% trace_trend = trace_trend;`

Compute the Frequency Spectrum via FFT for the given FBG trace.
The trace trend must be subtracted to get amplitudes relative to the change in the wavelength.
	`%% Compute and Graph the Frequency Spectrum`
	`if nargin==4`
	`    Tt1S1 = polyfit(t_s,trace,1);   % Linear Fit for Test1 Sensor1`
	`    trace_trend = polyval(Tt1S1,t_s);    % Generate fit curve`
	`end`
	
	`% Computing Frequency Parameters and Spectra`
	`nfft = numel(t_s);          % Number of Elements in (t) = nfft`
	`df = 1/ (dt*nfft);                   % Frequency Step`
	`sF = dt*ifft(trace-trace_trend)*nfft; % Computing Trace Frequency Spectrum`
	`f = [0:nfft/2 -(nfft/2-1):-1]*df;   % Complete Frequency Spectrum`

Apply Highcut Filter in on the data.
This is recommended to reduce the sampling noise in the data.
	`%% Highcut Filter`
	`% Matrix Allocation`
	`trace_f(1:nfft) = 0;`
	`for i = 1: nfft/2+1`
	`    if f(i) <= F0`
	`        trace_f(i) = sF(i);`
	`    else`
	`        trace_f(i) = 0;`
	`    end`
	`    if i>=2                    % Computing negative frequencies`
	`        trace_f(nfft+2-i)=conj(trace_f(i));`
	`    end`
	`end`
	`dw = 2*pi/(dt*nfft);         % Standard definition of dw`
	`trace_F0 = fft(trace_f)*dw/(2*pi);    % Converting s1F to the time domain`
	`% trace_f_dB = 20*log10(abs(trace_f)/abs(trace_f(1)));`

Plot the trace and its frequency spectrum after highcut filter.	`%%  Plot Frequency Spectrum after Highcut`
	`figure; hold on;`
	`subplot(2,1,1);`
	`plot(t_s,trace_F0,'k')`
	`xlabel('time (s)')`
	`ylabel('Relative Wavelength (pm)')`
	`subplot(2,1,2)`
	`plot(f(1:nfft/2),abs(trace_f(1:nfft/2)),'b')`
	`% plot(f(1:nfft/2),trace_f_dB(1:nfft/2),'b')`
	`xlabel('Frequency (Hz)')`
	`ylabel('Amplitude')`
	`axis([0 F0 0 inf])`

APPENDIX C

ZVSP PROCESSING OF DAS DATA VIA VISTA

This appendix discusses the processing steps that were done to process ZVSP DAS data using Schlumberger's VISTA seismic data processing software, aided by figures of the VISTA workflows for reproducibility. The general workflow that was shown in Chapter 2 is followed (Figure 2.3). First, the data (which is in SEG-Y format) is imported into the software and the headers are checked to ensure proper import, we ensure that the channel, shot-point, field-record, and field-station numbers are populated with the appropriate values. These headers are essential for generating the proper sorting for the records. Other headers such as source parameters and well parameters can also be populated but they are not essential to the processing outcome.

Next, the data is displayed and interpreted for the well top and bottom locations along the fiber (Figure 2.6), this is typically done in the field but we found that in our case it was not done accurately. We use a few events in the data to help identify and interpret the well top and bottom: the first event that helps identify and well top and bottom is the tube waves, the tube waves propagate down and up the borehole (assuming that the well is fluid-filled from top to bottom). If the fiber is deployed in a loop geometry then the first-break arrivals can be used to identify the well bottom by picking the maximum first-break point to be the well bottom. Additionally, the well top can be identified by the first-break arrivals (assuming that the fiber was recorded all the way to surface). The first arriving waves from the surface to the depth that corresponds to the source offset will be refractions and not direct-waves, thus the travel-time will decrease from surface to the source-offset depth point then increase from thereon. So picking the earliest first-break time should be at the depth that is equal to the source-offset. These events can also be used to depth calibrate the DAS data.

Once the well top and bottom have been interpreted, we proceed with the first processing workflow (Figure C.1) which is applied to looped fiber data in order to separate the fiber runs using the well top and bottom interpretations. In this workflow bad traces are killed, then the headers are edited to calibrate the depth values with respect to the well top and bottom depths, then the data is separated to extract the first fiber run from the data.

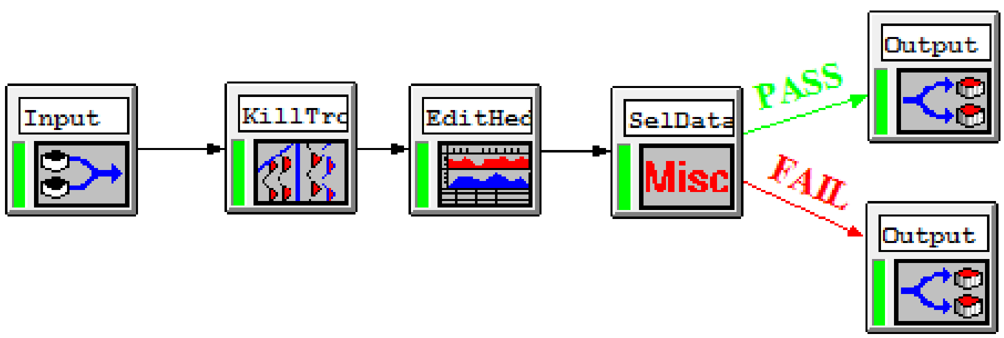

Figure C.1: Fiber Run Separation Workflow

DAS data will usually exhibit common-mode noise (CMN), this is witnessed by horizontal events in the data. These events correspond to instrument noise that is generated at the interrogator. Given that this noise is constant across the fiber but variable in time, it can be subtracted from the data by using a large median filter. In our data, a median filter using 399 traces was used (which corresponds to half the total trace number) to enhance the CMN then subtract it from the data (Figure C.2). The next steps are done using the interactive processing tools in VISTA, where we import the source and receiver geometry to the headers, accounting for any well deviation, and incorporating the calibrated depth measurements to the fiber length. We then pick the first breaks and export them for velocity analysis. During the velocity analysis, first-break picks (FBP) may be adjusted to account for bad interval velocity values. The adjusted FBP are then used to compute a velocity profile and a time-to-depth curve. These are the first products of ZVSP.

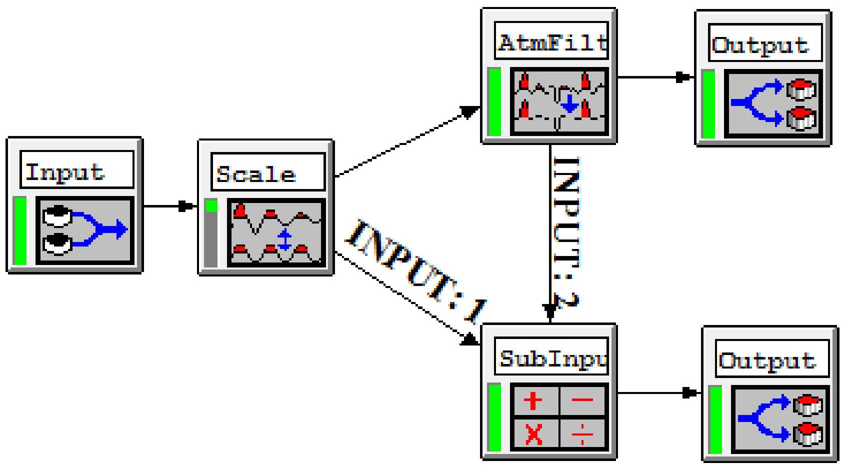

Figure C.2: Common-Mode Noise Suppression Workflow

Next, the FBP are used to separate the downgoing (DG) wavefield from the data using a median filter (Figure C.3). The data is first flattened on the FBP and bulk-shifted to some time (150 ms in our case). Then a mean scaling is applied to account for variable trace amplitudes. After a median filter is applied with a relatively large window (79 traces in our case), this is typically tested to select the optimal median window that enhances and isolates the DG wavefield. The output of the median filter is then subtracted from the scaled data, and both data are un-flattened back to the field-record time (FRT). With this, we have successfully separated the DG wavefield from the data and what is left contains the up-going (UG) wavefield along with DG shear and tube waves. The DG wavefield can now be used for attenuation analysis as a secondary product of VSP, this option is available in an interactive processing tool in VISTA.

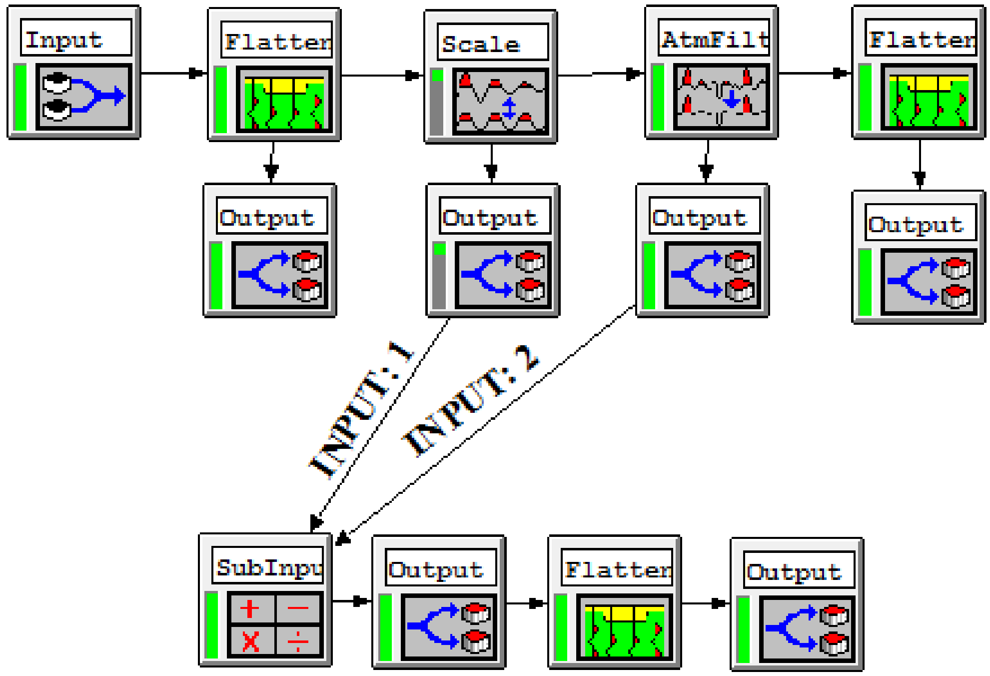

Figure C.3: Wavefield separation workflow

The next processing step is deconvolution, this consists of a two-step workflow (Figure C.4) and an iterative analysis to select the optimal deconvolution parameters. Since the DG wavefield represents the source wavelet as it is propagating in depth, it is used as the deconvolution operator. We first test the deconvolution parameters on the DG wavefield by deconvolving it from itself, where the optimal parameters will result in a zero-phase wavelet with minimal side-lobes. In our study, we used a 500 ms design window with a 20 ms taper, an operator of ±500 ms with 1% pre-whitening and a 50 ms taper.

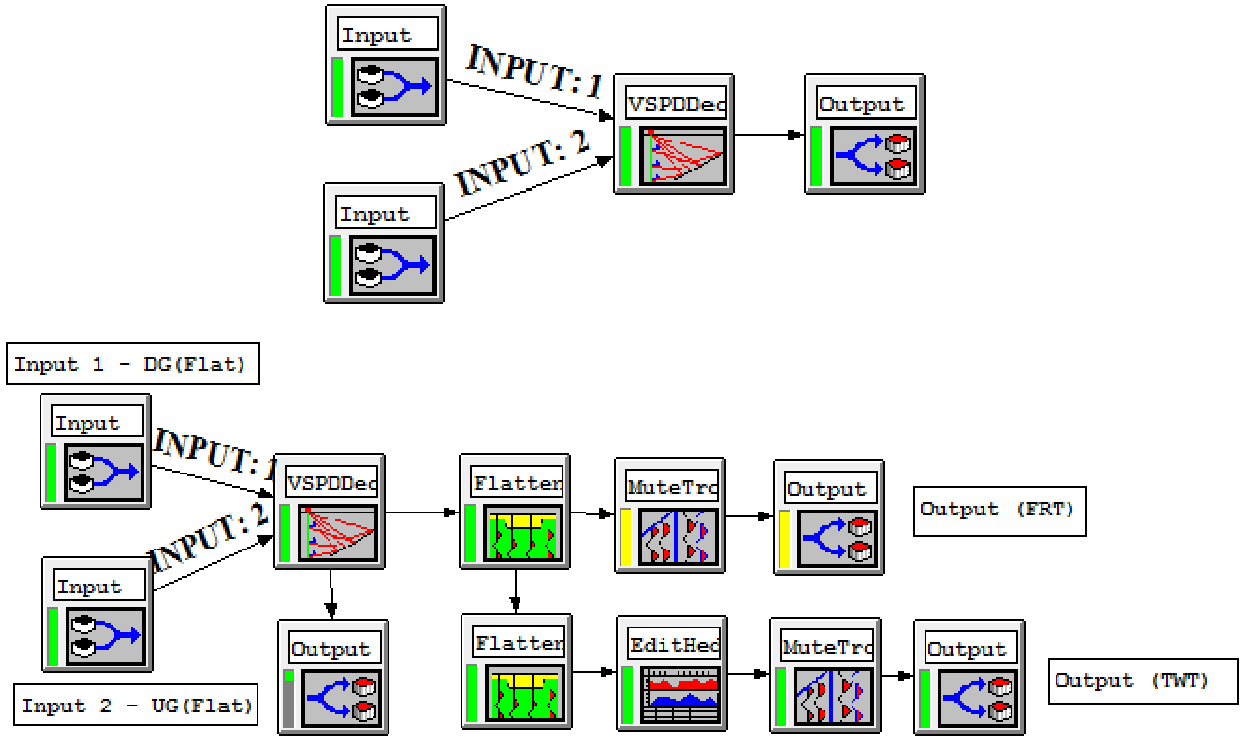

Figure C.4: Deconvolution workflows

The final workflow (Figure C.5) consists of multiple special processing steps that are applied to enhance the UG wavefield and suppress any other wavefields (shear and tube waves) which we will consider as noise. Prior to initiating this workflow, an f-k filter (filter in the frequency-wavenumber domain) is interactively designed on the deconvolved UG data in two-way time (TWT). Here the UG waves should appear flat in the time domain and thus any linear dipping events will be isolated in the f-k domain and easy to cut out. The filter is designed by interpreting the linear events visible in the f-k domain and saving the filter design file which is then applied in the workflow. The data is then flattened to FRT to apply gain corrections for spherical divergence and transmission loss, followed by NMO corrections using the velocity profile that was created earlier, then application of a top-mute at the FBP. Next, the data undergoes two processing paths to output two stack sections, a corridor-stack and a shot stack. The corridor-stack is designed by applying a corridor mute to the data that only captures 100 ms of data from the first break and then the full record towards the end of the well, whereas the shot stack encompasses the entire record. In theory, the shot stack will contain the primary reflections along with multiples, while the corridor-stack will represent the primary reflections only. During this process, an Ormsby filter (band-pass) is applied to the data that corresponds to the source sweep frequency band, in our case a tapered band of 8-16-80-120 Hz was applied. With this, we conclude the processing of the DAS data for ZVSP and use the produced stacks to compare to surface seismic data and well log synthetic data.

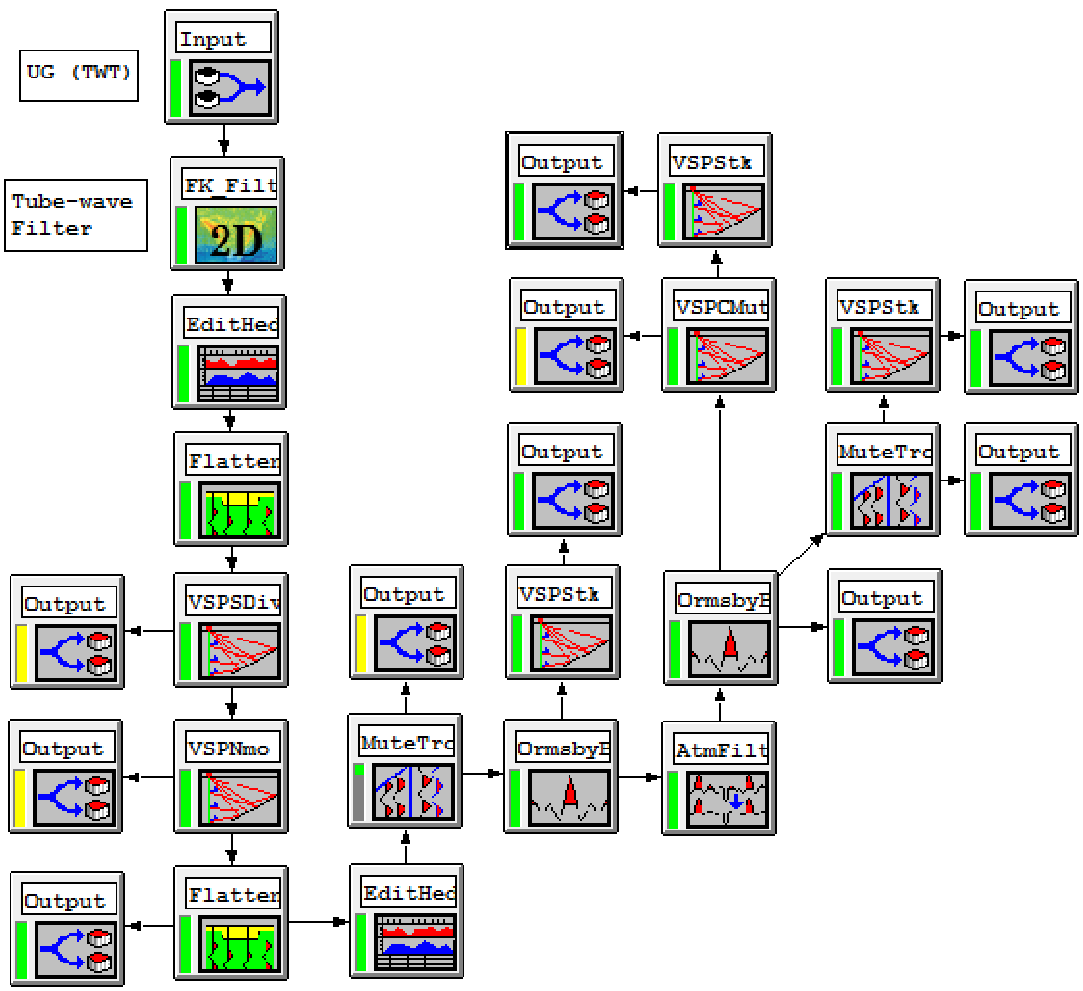

Figure C.5: Special processing workflow

To recap, data was imported in SEG-Y format and the headers were checked. The data were then interpreted for the well top and bottom and the information was used to correct fiber geometry and extract the fiber run (for looped fiber geometry). Then CMN was suppressed by median filter and subtraction. Followed by FBP and wavefield separation, to produce the first products of VSP (velocity profile, time-depth curve, and attenuation analysis). We then deconvolved the DG wavefield from the data and designed an f-k filter to enhance the UG wavefield. Finally, we apply the f-k filter, gain, and NMO corrections to the data, followed by a band-pass filter and various mutes to produce our two final products of a corridor-stack and a shot stack.

APPENDIX D

INFLUENCE OF COUPLING ON FBG SENSING

Fiber coupling is a major issue when it comes to fiber-optic sensing. Similar to coupling with any sensing technology, the sensor must be coupled to the medium of which it is sensing. With geophones, this is accomplished using spikes that are coupled to the ground, and in some extreme cases, the geophones are buried to achieve better coupling. Therefore, the argument of coupling makes perfect sense. With fiber, however, the fibers are sensitive to multiple things in the environment (temperature, strain, pressure, vibrations, etc.), the fiber effectively interacts with the environment making it very sensitive. Thus, coupling fiber helps minimize environmental sensitivities and focus the sensing on the coupled medium. The question arises to how couple the fibers to the medium? The general recommendation is permanent installation, to glue or cement the fibers to the structure that will be measured. So in DAS applications the fiber is typically clamped to pipes and cemented or buried, while in FBG applications the FBG is glued to the structure of interest.

In the geophysical domain, permanent installation is not favorable, retrievable systems allow for repeated use and leaving sensors in the ground is not environmentally friendly. Therefore, we test the influence of coupling on measurements in a laboratory environment to better evaluate the value of coupling. The testing was done with regards to FBGs and not DAS, as DAS is influenced by the gauge length and would require large strands of fiber to be tested, while FBGs are point sensors that can easily be tested in the laboratory.

First, we compare the response of several tests on two FBGs, one glued and one taped to a PVC pipe. First, the response of each sensor to the ambient noise is presented (Figure D.1). Finding that the taped FBG response was comparable to the glued FBG. Both FBGs display fluctuations between 0.2-0.3 picometers (pm) and the dominant frequency of the ambient noise was around 25 Hz. The taped FBG shows higher sensitivity to a secondary ambient noise frequency around 45 Hz.

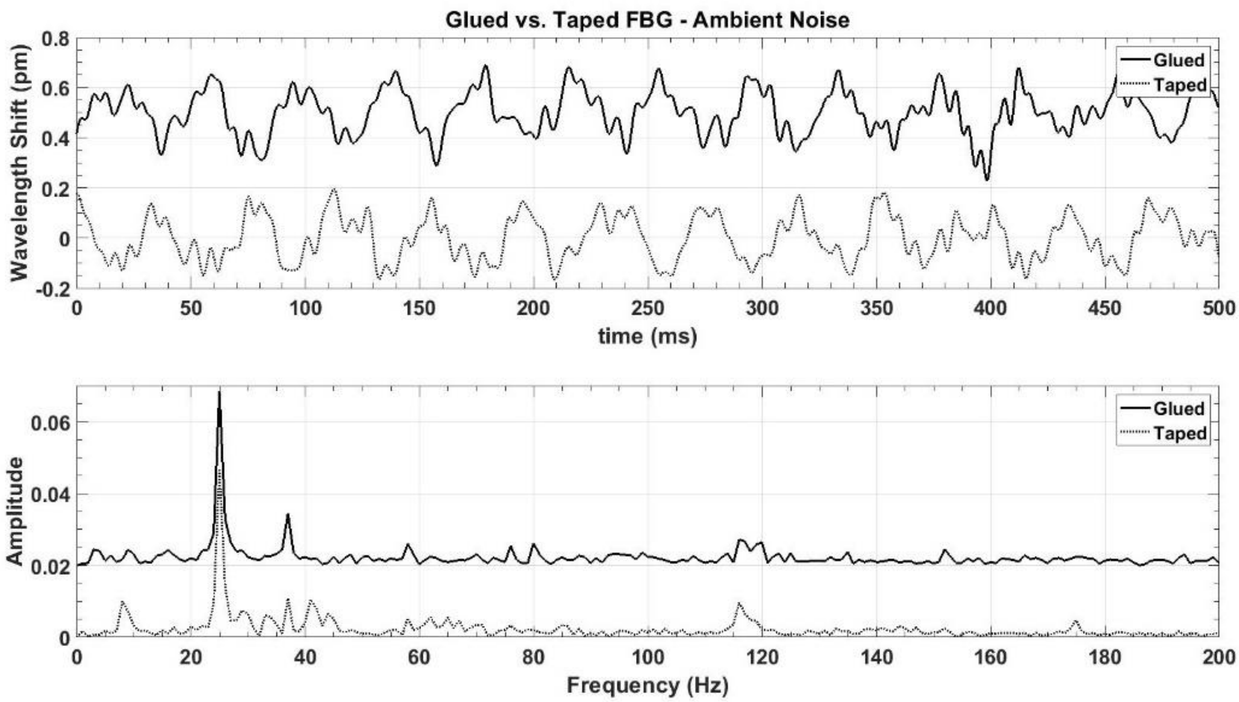

Figure D.1: Comparison of a glued (-) and taped (-.) FBG response to ambient noise. Results show that the amplitude and frequency response is comparable. Glued FBG time response is shifted 0.5 pm and frequency response is shifted 0.02 for display purpose (Alfataierge et al., 2019a).

Next, a tap test is considered, tapping on the PVC pipe to compare the response of each FBG to a wavefield, noting that the FBGs were located 20 cm apart. The results show that both FBGs exhibit a maximum wavelength shift around 3 pm, the variation in the wavefield and frequency spectrum is attributed to the FBGs being in different locations, with the Glued FBG closer to the source tap location (Figure D.2).

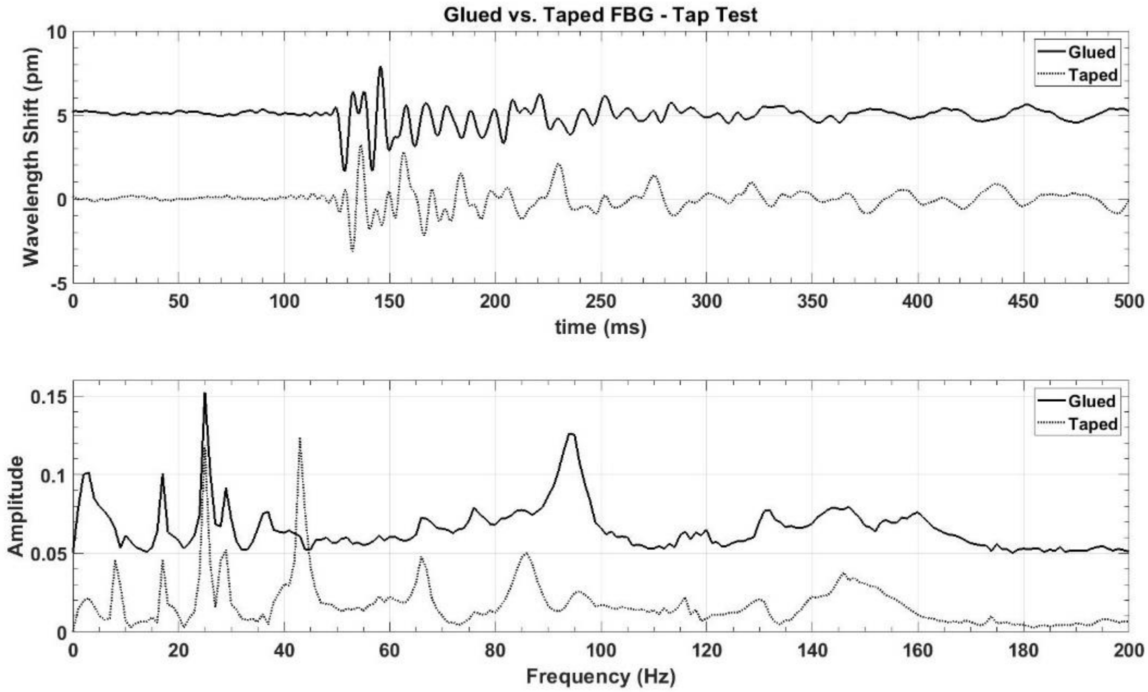

Figure D.2: Comparison of a glued (-) and taped (-.) FBG response to a tap test. The time curve shows that both FBGs capture the tap response with peak fluctuations of 3 pm. Glued FBG time response is shifted 5 pm for display purposes (Alfataierge et al., 2019a).

In conclusion, the results show that although the coupling does influence measurements, taping the FBG sensor is acceptable for our applications in comparison to gluing them. We note that taping is a temporary solution that provides acceptable measurements while gluing the sensor would provide superior measurements.

APPENDIX E

INFLUENCE OF MATERIAL ON 3-C FBG

This appendix discusses the influence of materials on the measurements of the 3-C FBG introduced in Chapter 5. The measurements provided in this section have all been acquired at different times in similar settings, thus this is not a fair comparison of materials in a single experiment, rather than a discussion of the influence of materials on the measurement of the 3-C FBG sensor in comparison to a 3-C geophone. Thus, using the geophone measurements as the benchmark to the expected sensing response. Figure 5.7 illustrates the three materials that were tested, a) a wooden cube, b) a glass cube, and c) an aluminum geophone case.

A vibratory source was used to introduce a mono-frequency signal to compare the response of each sensor. The results of the wooden and glass cube show little to no influence of the material on the measurements (Figure E.1). In both setups, the 3-C FBG sensor produced a similar response that was comparable to the geophone measurement with regards to amplitude and frequency. The only observation is that the glass cube results show higher sensitivity to the source harmonics. The slight discrepancy between the geophone and FBG measurements is attributed to two things, the setting (i.e. the geophone was placed on top of the buried FBG cube) and the measurement type (the FBG is measuring strain while the geophone is measuring particle velocity or displacement).

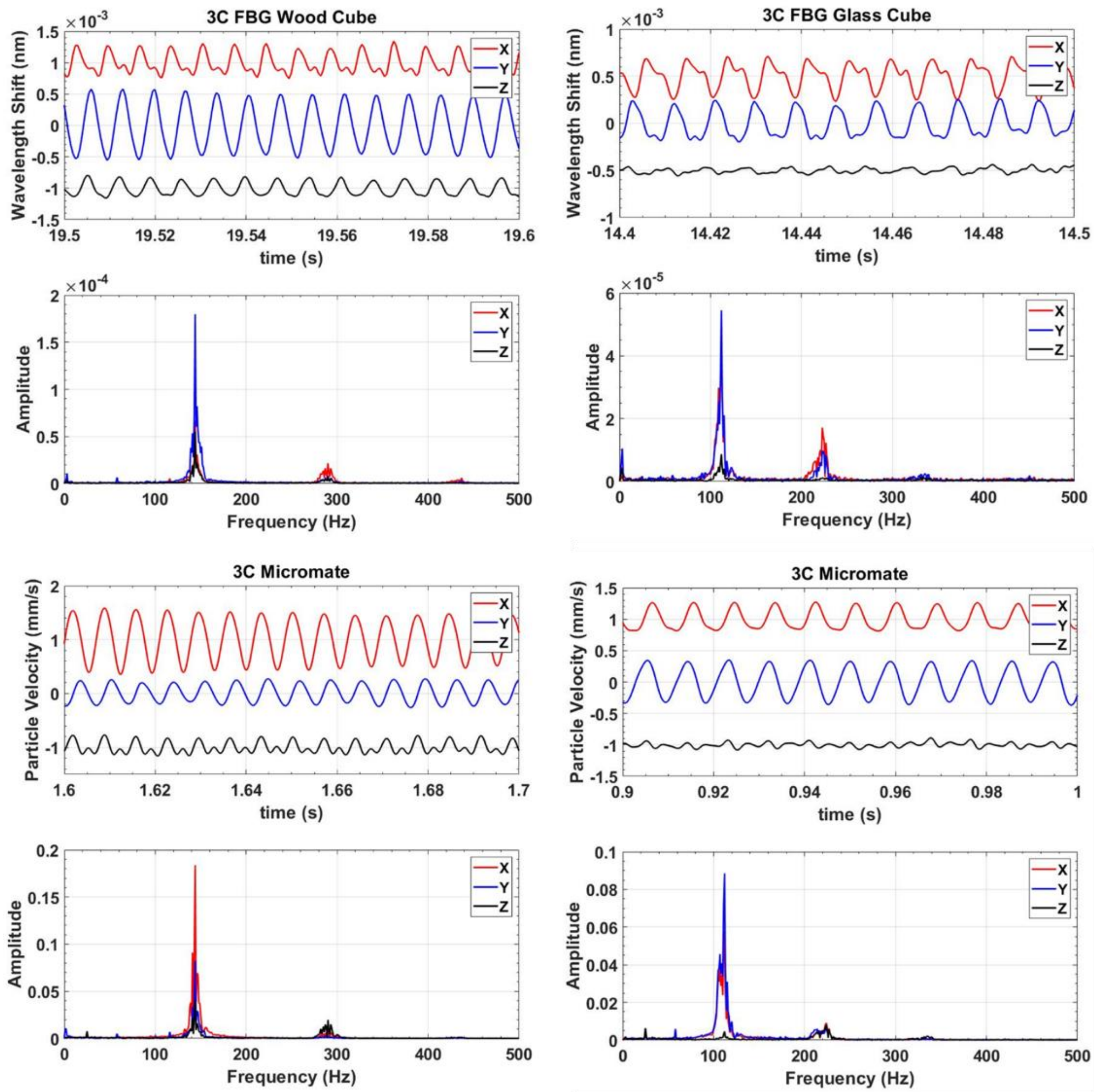

Figure E.1: Measurements from a vibratory source comparing the response of the 3-C FBG (top) to the 3-C Geophone (bottom) with respect to the wooden cube (left) and the glass cube (right) (Alfataierge and Stewart, 2019).

Results with respect to the 3-C FBG mounted on the 3-C geophone casing are shown in Figure E.3. They show a similar response to the previous results with the wooden and glass cube, with the 3-C FBG preserving the frequency response of the source and some minor discrepancy in amplitude observed. The 3-C FBG also exhibits low-frequency noise that is possibly a residual temperature response in the record that was not effectively processed from the data.

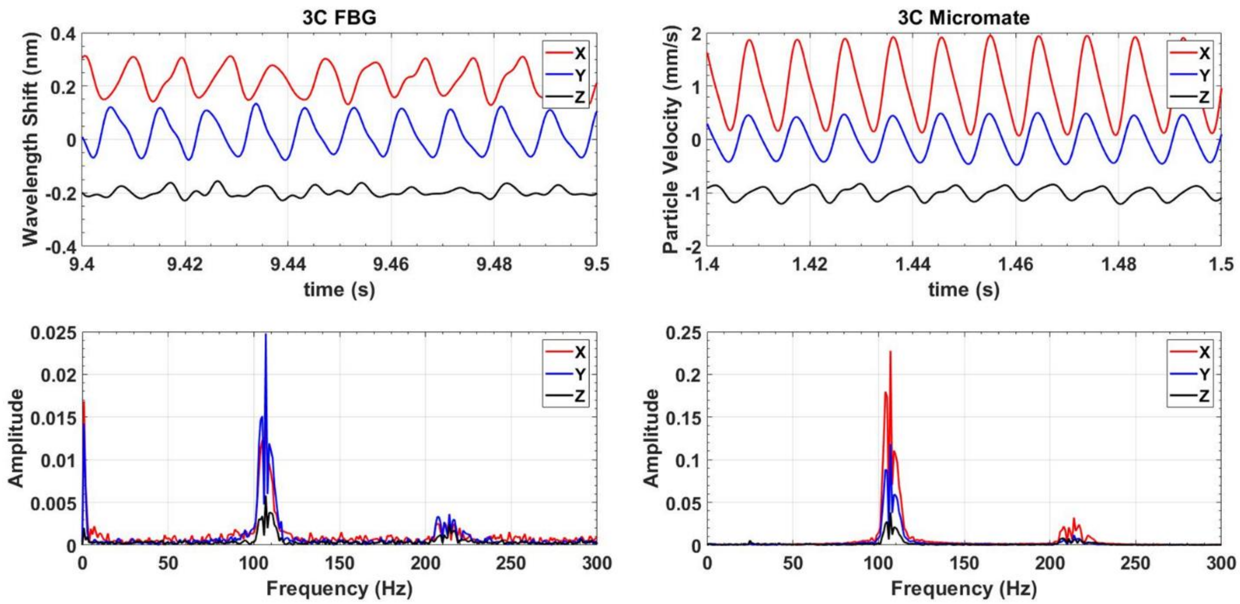

Figure E.2: Measurements from a vibratory source comparing the response of the 3-C FBG (left) to the 3-C geophone (right) with respect to the FBGs mounted on the geophone.

In conclusion, the results show that materials have no significant influence on the FBG measurements. This is due to the investigated frequencies having a wavelength that is significantly larger than the sensor, thus the wavefield does not interact with the material the FBG is coupled to. It is possible that if the investigated seismic frequencies had wavelengths at the order of the cube size, then material influence may be observed.